BASE ISOLATION OF A CHILEAN MASONRY HOUSE:

A COMPARATIVE STUDY

A Thesis

by

RACHEL LYNN HUSFELD

Submitted to the Office of Graduate Studies of
Texas A&M University
in partial fulfillment of the requirements for the degree of

MASTER OF SCIENCE

May 2008

Major Subject: Civil Engineering

BASE ISOLATION OF A CHILEAN MASONRY HOUSE:

A COMPARATIVE STUDY

A Thesis

by

RACHEL LYNN HUSFELD

Submitted to the Office of Graduate Studies of
Texas A&M University
in partial fulfillment of the requirements for the degree of

MASTER OF SCIENCE

Approved by:

Chair of Committee,	Paul N. Roschke
Committee Members,	Jose Roesset
	Ozden Ochoa
Head of Department,	David Rosowsky

May 2008

Major Subject: Civil Engineering

ABSTRACT

Base Isolation of a Chilean Masonry House: A Comparative Study.

(May 2008)

Rachel Lynn Husfeld, B.S., Valparaiso University

Chair of Advisory Committee: Dr. Paul N. Roschke

The objective of this study is to reduce the interstory drifts, floor accelerations, and shear forces experienced by masonry houses subject to seismic excitation. Ambient vibration testing was performed on a case study structure in Maipú, Chile, to identify characteristics of the system. Upon creating a multiple degree-of-freedom (MDOF) model of the structure, the effect of implementing several base isolation techniques is assessed. The isolation techniques analyzed include the use of friction pendulum systems (FPS), high-damping rubber bearings (HDRB), two hybrid systems involving HDRB and shape memory alloys (SMA), and precast-prestressed pile (PPP) isolators.

The dynamic behavior of each device is numerically modeled using analytical formulations and experimental data through the means of fuzzy inference systems (FIS) and S-functions. A multiobjective genetic algorithm is utilized to optimize the parameters of the FPS and the PPP isolation systems, while a trial-and-error method is employed to optimize characteristic parameters of the other devices.

Two cases are studied: one case involves using eight devices in each isolation system and optimizing the parameters of each device, resulting in different isolated periods for each system, while the other case involves using the number of devices and device parameters that result in a 1.0 sec fundamental period of vibration for each base-isolated structure. For both cases, the optimized devices are simulated in the numerical model of the case study structure, which is subjected to a suite of earthquake records.

Numerical results for the devices studied indicate significant reductions in responses of the base-isolated structures in comparison with their counterparts in the fixed-base structure. Metrics monitored include base shear, structural shear, interstory

drift, and floor acceleration. In particular, the PPP isolation system in the first case reduces the peak base shear, RMS floor acceleration, peak structural shear, peak interstory drift, and peak floor acceleration by at least 88, 87, 95, 95, and 94%, respectively, for all of the Chilean earthquakes considered. The PPP isolation system in the second case (yielding a 1.0 sec period) and the FPS isolation systems in both cases also significantly reduce the response of the base-isolated structure from that of the fixed-base structure.

DEDICATION

To Dag and my family. You have been a tremendous inspiration to me.

ACKNOWLEDGEMENTS

I would like to thank my committee members, especially my committee chair, Dr. Paul Roschke, for their guidance throughout my graduate study.

I gratefully acknowledge the technical support from the University of Chile. I particularly appreciate the assistance offered by Drs. Maria Moroni, Mauricio Sarrazin, Ruben Boroschek, and Maximiliano Astroza. In addition, I am thankful for the experimental support from Pedro Soto.

I owe a debt of gratitude to Ernesto Herbach who provided the structural drawings and specifications for the case study structure and arranged the site visits to the structure.

I also thank Dr. Juan Carlos de la Llera for providing a wealth of information about the precast-prestressed pile device that he developed.

I extend my thanks to the many fellow students I have worked with in the office. I have enjoyed sharing our ideas, cultures, and friendship with each other.

Finally, I am extremely grateful to the National Science Foundation for providing a Graduate Research Fellowship which enabled my graduate study.

NOMENCLATURE

ANFIS	Adaptive Neuro-Fuzzy Inference System
CuAlBe	Copper-Aluminum-Beryllium
DOF	Degree-of-Freedom
FFT	Fast Fourier Transform
FIS	Fuzzy Inference System
FPS	Friction Pendulum System
FRB	Fiber-Reinforced Bearing
GA	Genetic Algorithm
GDP	Gross Domestic Product
HDRB	High-Damping Rubber Bearing
LRB	Lead Plug Rubber Bearing
MDOF	Multiple Degree-of-Freedom
M_W	Moment Magnitude
M_S	Richter Magnitude
NiTi	Nickel-Titanium
NSGA-II	Non-Dominated Sorting Genetic Algorithm II
NSGA-II CE	Non-Dominated Sorting Genetic Algorithm II with Controlled Elitism
PGA	Peak Ground Acceleration
PPP	Precast-Prestressed Pile
PSD	Power Spectral Density
RC	Reinforced Concrete
RMS	Root-Mean-Squared
SMA	Shape Memory Alloy

TABLE OF CONTENTS

Page

Page

LIST OF TABLES

Page

LIST OF FIGURES

Page

Page

Page

Page

Page

Page

Page

Page

Page

Page

1. INTRODUCTION

1.1. General

The largest earthquake ever instrumentally recorded occurred in southern Chile on May 22, 1960. The moment magnitude (M_W) 9.5 earthquake was followed by a series of earthquakes, tsunamis, flooding, and landslides in Chile and in places as far away as Hawaii and Japan. The Chilean government estimated that two million people were homeless and over 58,600 houses were completely destroyed by the earthquake and related events (Stroker 2008). Fig. 1 shows severely damaged homes after the 1960 Chile earthquake. The U. S. National Geophysical Data Center (NGDC) predicts that "it is only a matter of time until Chile once again has a 'world-class' earthquake whose impact, like the 1960 Chile event, will be felt around the world."

Fig. 1. Damaged houses after 1960 Chile earthquake (www.ngdc.noaa.gov)

Since 1900, Chile has experienced over 75 earthquakes with Richter magnitude (M_S) 7.0 or greater (Servicio Sismológico 2007). The most recent was the M_W 7.7 earthquake in Antofagasta, Chile, on November 14, 2007, which resulted in the total

---

This thesis follows the style of the *Journal of Structural Engineering.*

destruction of over 1,200 houses (Saez 2007).

On a continuing basis significant earthquakes occur throughout the world. These earthquakes have a major impact on society. Recent examples include the M_S 7.7 earthquake in Gujarat, India, in 2001; the M_S 6.6 earthquake in Bam, Iran, in 2003; the M_W 9.1 2004 Indian Ocean earthquake; the M_S 7.7 earthquake in Kashmir, Pakistan, in 2005; and the M_W 8.0 earthquake in Peru in 2007 (Mikhail 2000). Together these earthquakes have killed hundreds of thousands of people and caused millions to be left homeless.

In response to the extensive damage that earthquakes often cause to buildings and, in particular, to housing structures, many techniques, including passive, semi-active, and active control systems have been proposed to mitigate the effect of seismic damage. As a contribution to these efforts this study considers the use of passive control systems, specifically base isolation systems in Chilean masonry houses.

Due to its strong financial institutions and sound governmental policy, Chile has one of the most stable economies in South America (CIA 2008). From 2000 to 2006 Chilean growth in real GDP ranged from 2 to 6% due to high copper prices, significant export earnings from forestry, fishing, and mining, as well as growing domestic consumption. Chile has maintained a low rate of inflation and a decreasing rate of unemployment. Foreign investment in gas, water, electricity, and mining has also strengthened Chile's economy (CIA 2008). Because many employment opportunities are available in the major cities, the Chilean government is enabling urbanization with the construction of low-cost housing. Minimization of construction time and cost are often the top priorities of those who design and construct the low-cost housing.

However, because of the seismicity of Chile as evidenced by its many earthquakes, and the damage resulting from the earthquakes, seismic protection procedures are being considered for structures in Chile. In particular, the use of base isolation techniques could offer significant benefits to structures in Chile. To this end, the goal of this study is to illuminate the benefits of several base isolation systems on the

seismic performance of low-cost houses in Chile. It is the hope of the author that the information in this report could be of use to Chilean engineers.

Although this study focuses on masonry houses that are located in Chile, results of this study are applicable to houses constructed in other countries as well. After an introduction to the most commonly-used construction technique for low-cost Chilean houses, confined masonry, an overview of the application of base isolation techniques in Chile is included.

1.2. Confined Masonry Construction

Confined masonry is a common construction technique used in housing structures in Chile. In this technique, masonry walls are confined by reinforced concrete members on two or more edges. The masonry walls are the main load-bearing elements, as they transmit both gravity loads and lateral loads to the foundation (Murty et al. 2006). Construction of a typical confined masonry low-cost housing structure in Maipú, Chile, is shown in Figs. 2 and 3. As can be seen in Fig. 2, masonry walls are constructed prior to pouring of concrete for the confining members. Fig. 3 shows construction of a house with the same floor plan as that which is analyzed in this study. The housing layout consists of a 110 m^2 two-story dwelling designed to be occupied by two families who are separated by interior partitions. This particular floor plan was selected for study because it is constructed throughout Chile. Many thousands of homes similar to the case study structure are in the planning and construction stages in the greater Santiago area.

Fig. 2. Confined masonry construction in Maipú, Chile

Moroni et al. (2004) identify the deficiencies of confined masonry walls as: (1) limited in-plane shear strength; (2) limited ductility; (3) lack of tie columns at all wall openings, thus reducing the shear strength and displacement capacity; (4) excessive distance between tie columns or lack of tie beams that may cause out-of-plane damage; and (5) shear cracks that propagate through the tie columns and reduce the wall stiffness and resistance capacity. They conclude that despite these deficiencies, most confined masonry buildings have "appropriate seismic behavior" (Moroni et al. 2004). However, Moroni et al. (1996) explain that seismic codes are developed to ensure serviceability requirements for frequent moderate earthquakes and life safety for major earthquakes, thereby allowing extensive damage to occur in major earthquakes as long as collapse is prevented.

Moroni et al. (1996) analyze the performance of several three- and four-story confined masonry buildings subjected to a number of earthquake records from a Chilean earthquake on March 3, 1985, and from a Mexican earthquake on September 19, 1985. They conclude that the confined masonry buildings analyzed have different seismic behavior depending on the source mechanism of the earthquake. The structures studied experience severe damage and nearly collapse when subjected to the epicentral Chilean

records, whereas they experience low or moderate damage when subjected to the Mexican records. It should be mentioned, however, that these buildings were designed according to the *NCh2123.c90* and *NCh433.of72* codes, instead of the current *NCh2123.of97* and *NCh433.of96* codes.

Fig. 3. Confined masonry house near completion

Past earthquakes and experimental testing have shown that most damage to confined masonry buildings results from shear failure of the masonry, without plastification of the columns (Moroni et al. 1996). It has been concluded from a study of experimental data that appreciable in-plane stiffness degradation occurs after the first shear cracking of the walls (Moroni et al. 1996). In the structure studied, the author anticipates that shear cracking in the wall segments adjacent to the large openings in the front of the structure could be of concern. This failure mode is evident in the dwellings shown in Figs. 4-6, which show damaged masonry structures after Chilean earthquakes, such as the M_S 7.8 1985 Melipilla earthquake and the M_S 7.8 magnitude 2005 Tarapacá earthquake (Astroza et al. 2005b).

Fig. 4. Three-story partially reinforced masonry building; Ñuñoa, Chile, on March 3, 1985

Fig. 5. Three-story partially confined masonry building; Melipilla, Chile, on March 3,1985

Fig. 6. Masonry house at Huara, Chile, after Tarapacá earthquake on June 13, 2005

1.3. Base Isolation in Chile

In 1992, the first base-isolated structure in Chile was constructed (see Fig. 7). The structure is a four-story reinforced concrete and masonry low-cost house in Santiago that is supported by eight high-damping rubber bearings (HDRBs). Moroni et al. (1998) used accelerometers to measure the response of the structure to several small earthquakes and one moderate earthquake over a period of several years and also performed experimental tests on the structure. In addition to monitoring the base-isolated building, Moroni et al. (1998) monitored a nearby, identical building that was constructed without using bearings to isolate the structure. Data collected on responses of the two buildings to at least 24 earthquakes show that the isolation system has a strong positive effect on the dynamic characteristics of the isolated building. That is, the peak accelerations were reduced in the longitudinal and transverse directions for the

base-isolated structure compared to the fixed-base structure. However, residents of the base-isolated building experience noticeable vibrations when large vehicles travel nearby. In addition, the response of the structure to the most severe earthquake it has experienced (an M_S 5.9 earthquake on February 22, 1996) resulted in reduction of the horizontal response accelerations while the vertical component of ground acceleration was amplified considerably by the isolation system (Moroni et al. 1998).

Fig. 7. Base-isolated structure studied by Moroni et al. (1998)

Several larger-scale structures have since been constructed in Chile using base-isolation techniques (De la Llera et al. 2004), including a hospital and the Engineering Faculty building at the Universidad Católica. The hospital building is isolated using rubber bearings with and without lead cores. The isolators for the hospital building were placed at the top of the basement, thus avoiding construction of an extra floor slab. The Engineering Faculty building (shown in Fig. 8) was isolated using rubber bearings with and without lead cores, and steel-teflon-elastomer sliders (De la Llera et al. 2004). While seismic protection of hospital and academic buildings has often been pursued,

improving the performance of housing structures subjected to moderate or severe earthquakes remains to be a concern in Chile and in many countries around the world.

Fig. 8. Base-isolated Engineering Faculty building at the Universidad Católica (De la Llera et al. 2004)

2. REVIEW OF LITERATURE AND RELEVANT TOPICS

2.1. General

Seismic isolation aims to decouple a structure from the horizontal components of ground motion. As a result, isolation devices reduce the seismic demand placed upon a structure itself, rather than increasing the earthquake resistance of the structure. In order to significantly reduce dynamic responses due to seismic loads, isolation devices can be inserted between a structure and its foundation. This approach lowers the natural frequency of a structure, and thereby increases its fundamental period (Naeim and Kelly 1999). Seismic isolation theory shows that the reduction of seismic loading by an isolation system for a relatively stiff low-rise structure is influenced primarily by the ratio of the isolated period to the fixed-base period. According to Kelly (2002), because the fixed-base period of a masonry block or brick building is approximately 1/10 sec, an isolation period of 1 sec or longer would significantly reduce the seismic loads on the structure and would not require the design for a large displacement of the isolator. Note that the design value for isolator displacement could be large for a near-fault earthquake if the ground motion has displacement pulses with durations in the range of 1 – 3 sec (Jangid and Kelly 2001).

In this study, the dynamic behavior of a number of isolation devices are modeled through the use of fuzzy inference systems (FIS) and S-functions in MATLAB, based on experimental and analytical force-displacement data for each device. The creation and use of a FIS and an S-function are explained after an introduction to the seismic isolation devices.

2.2. Seismic Isolation Devices

2.2.1. Friction Pendulum System

One common method of seismic isolation is the use of friction pendulum systems (FPS). An FPS is a curved sliding surface that produces a restoring force against displacement due to its geometry. The weight of the structure is carried on spherical sliding or rolling devices that move relative to each other when the ground motion

exceeds a threshold level. The friction between the slider and the spherical surface generates damping in the isolator, while the curved surface provides a restoring force (Naeim and Kelly 1999). The radius of curvature can be used to control the apparent stiffness of the isolation system and the period of the motion of the supported structure.

Advantages of the use of an FPS include the generation of restoring forces, simple numerical modeling, linearity of the stiffness over a moderate range of horizontal displacement, and an isolated structure that has a constant period regardless of the mass supported by the FPS bearings (Kim et al. 2006). Additional advantages include the repeatability of its cyclic behavior, stability of physical properties, durability, reduced height from that of other isolation systems, separation between the restoring and dissipating behaviors, and the ability to control the fundamental period of vibration and deformation capacity by altering simple geometric properties (Almazan and De la Llera 2003). The latter property of FPS bearings has caused them to be used in situations where the displacement due to seismic motion or the required fundamental period of the structure exceeds limits attainable through the use of other isolation systems (Zayas and Low 2000). Fig. 9 shows an FPS bearing with dual rollers (Kim et al. 2006).

Fig. 9. FPS bearing with dual rollers

One disadvantage of an FPS is that relatively large base displacements can occur depending on the severity of the earthquake. Another disadvantage is that uplift can be a

concern because damage due to large compressive forces on re-engagement following uplift can occur. Also, if FPS bearings are used in conjunction with HDRBs, uplift of the structure could cause damage to the HDRBs. Roussis and Constantinou (2006) recently developed a new isolation device that consists of two orthogonal opposing concave beams connected by a sliding mechanism that allows tension to develop in the bearing. By allowing tension to develop in the bearing, uplift is prevented. A review of the passive devices, including friction dampers, most commonly installed within the framing of building structures is presented by Symans et al. (2008).

2.2.2. Elastomeric Bearings

Another method of seismic isolation is the use of elastomeric bearings. Multilayer elastomeric bearings involve the vulcanization bonding of sheets of rubber to thin steel reinforcing plates. The steel plates allow the bearings to be stiff enough vertically to support the vertical load of the structure, while remaining flexible in the horizontal direction (Naeim and Kelly 1999). Two common types of elastomeric bearings are high-damping rubber bearings (HDRBs) and lead plug rubber bearings (LRBs). HDRBs (see Fig. 10) involve the use of rubber compounds with increased damping properties while LRBs have a lead plug in the center of the bearing to give additional damping when the lead deforms (Naeim and Kelly 1999).

De la Llera et al. (2004) summarize the results of a testing program conducted on more than 260 full-scale isolators. They conclude that the elastomeric compounds can be accurately represented by testing reduced-scale specimens. Although primarily referring to hospitals and other large structures, De la Llera et al. (2004) state that seismic isolation is both a technically and economically feasible option for building design in Chile. In addition to testing elastomeric isolators, several numerical models have been proposed to model the hysteretic behavior of HDRBs and LRBs. Pan and Yang (1996) and Hwang et al. (2002) each proposed an analytical formulation for elastomeric bearings. These models are described in Section 5.3.

One advantage of HDRBs is that because of their high level of damping, there is usually no need for adding supplemental damping devices to the isolation system. On the other hand, a significant disadvantage of HDRBs and LRBs is the relatively high cost associated with manufacturing, testing, and installing the devices in low-cost housing structures. Circular bearings are typically more expensive than rectangular bearings, and testing of the bearings is often required due to the variability of rubber properties.

Fig. 10. HDRB subject to shear loading

Kelly (2002) performed experimental testing on elastomeric isolators that used fiber reinforcing plates instead of the typical steel reinforcing plates. The purpose of this study was to determine the feasibility of using fiber reinforcement to produce low-cost and lightweight elastomeric isolators for use in housing, schools, or other public structures in highly seismic regions of the world. The study concluded that it is possible to produce a fiber-reinforced strip isolator that matches the behavior of a steel-reinforced isolator. The fiber-reinforced bearing (FRB) is significantly more lightweight and can be manufactured more easily than a traditional steel-reinforced isolator. Production of strips of FRBs would make the manufacturing process less expensive by avoiding the use of circular molds and allowing the strips to be cut to the appropriate size on-site. In addition, rectangular isolators would be more easily applied than circular bearings in structures that use walls as the lateral-resisting system. The use of fiber reinforcement instead of steel reinforcement would allow strips to be cut from a large specimen using a

standard saw, and the lighter weight isolators would be easier to lift into place than conventional isolators.

In this study, the effect of using HDRBs with steel plates is analyzed for the model housing structure. It is anticipated that the HDRBs will reduce the accelerations and base shear in comparison with the fixed-base structure while increasing the base displacement. Although traditional HDRBs are used to base-isolate the structure considered in this study, results of the study could be applied to the behavior of the house isolated using FRBs because the FRBs can be produced to closely match the behavior of traditional steel-reinforced HDRBs.

2.2.3. Hybrid Base Isolation

As mentioned previously, base isolation systems typically reduce the acceleration of the structure while increasing its base displacement. In addition to FRBs and HDRBs, the use of SMAs has been suggested for application in the seismic protection of buildings in recent years (Bruno and Valente 2002). SMAs can be introduced in a traditional base isolation system in order to, at least theoretically, eliminate plastic deformation of the structure. In the current study, in addition to studying the effect of base isolation using HDRBs, two hybrid base isolation systems, including the combined use of HDRBs and shape memory alloys (SMAs) are analyzed.

Other researchers, including Dolce et al. (2007), classify the components of an isolation system as isolators and auxiliary devices. Isolators decouple the building from the horizontal components of ground motion by allowing large horizontal displacements to occur, while auxiliary devices dissipate energy and/or re-center the structure when these functions are not performed by the isolator devices. For the hybrid base isolation cases, an array of HDRBs serves as isolators, while the SMA wires can be classified as auxiliary devices.

SMAs, including nickel-titanium (NiTi) and copper-aluminum-beryllium (CuAlBe), among others, are a certain class of metals that can undergo large strains and recover their initial shape at the end of the deformation process (Dolce et al. 2007).

SMAs are characterized as exhibiting superelasticity at high temperatures and the shape memory effect at low temperatures (Andrawes and DesRoches 2007). Due to the superelasticity of SMAs, the original deformation resulting from the application of load is recovered upon removal of the load. The shape memory effect causes SMAs to recover their undeformed shape upon being reheated. Throughout the deformation and recovery processes, which involve phase changes between the austenite and martensite phases, SMAs dissipate energy. Although the use of SMA wires could increase the energy dissipation of the hybrid system over that of an HDRB system, here the primary role of the SMA wires in the hybrid system is to re-center the structure. NiTi is the SMA that is considered in this study because of the ability of the alloy to undergo large strains (up to approximately 8% according to Bruno and Valente 2002), and due to the availability of experimental data, which are incorporated into the structural model through creation of a FIS. However, the moderate sensitivity of SMAs to ambient temperature changes should be considered (Andrawes and DesRoches 2007). Torra et al. (2007) discuss the temperature sensitivity of CuAlBe and NiTi in terms of the Clausius-Clapeyron coefficient.

Fig. 11 shows the stress-strain relationship for a sample of 0.5 mm diameter CuAlBe wire, which exhibits superelastic behavior similar to that of NiTi (Ozbulut et al. 2006). The area of the hysteretic curve in this diagram represents the amount of energy that the wire dissipates in one cycle of displacement. Also, it can be seen that the wire has no residual stress upon unloading, i.e. the loading/unloading curve always returns to the origin.

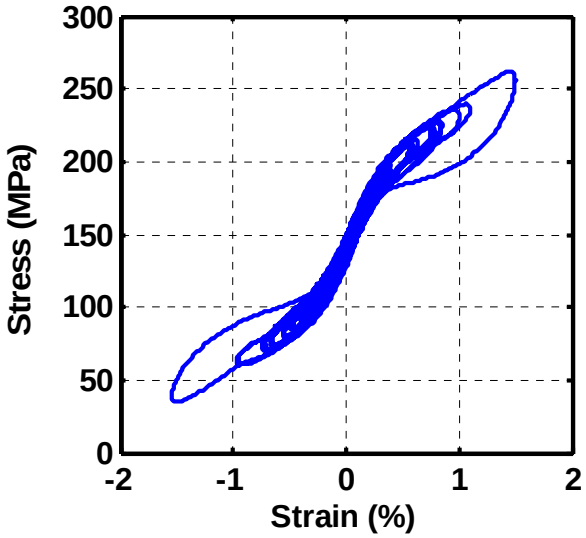

Fig. 11. Stress-strain diagram for CuAlBe (Ozbulut et al. 2006)

Previous research related to base isolation devices that incorporate the use of SMAs has been performed. Wilde et al. (2000) performed a numerical study on the use of a rubber bearing and SMA bar isolation system for application to highway bridges. The isolation system between the bridge pier and deck used SMA bars to control the displacement of the bridge deck and provide additional energy dissipation. The relative displacement of the bridge deck was decreased due to the isolation system, while the shear force transmitted to the pier and the acceleration response of the bridge were increased due to the isolation system. Dolce et al. (2007) performed shake table tests on reinforced concrete (RC) frames isolated using steel-teflon sliding bearings and SMA wire loops and concluded that SMA-based isolation systems are able to protect non-structural elements even under strong earthquakes due to their strongly softening behavior. This behavior limited the maximum interstory drift of the RC frames to a lower value than the other isolation systems considered, which included rubber-based, steel-based, and hybrid SMA and steel base isolation systems (Dolce et al. 2007). However, Dolce et al. (2007) noted that although the isolation system involving steel-

teflon sliding bearings and SMA-based devices produced favorable base displacement and base shear quantities, the resulting floor accelerations were often quite high.

Torra et al. (2007) performed a finite element analysis on the use of SMA dampers in family homes. The dampers were modeled as braces in a steel-framed two-story house and were capable of reducing the maximum displacement amplitude resulting from the El Centro earthquake by a factor of 2; they also dissipated 50% of the energy transmitted to the structure. Torra et al. (2007) did not discuss the affect of SMA dampers on the acceleration response of the structure. Song et al. (2006) provide a review of additional applications of SMAs in civil engineering.

In the structural model that is discussed in what follows, the hybrid HDRB and SMA isolation systems are simulated using two different configurations. One configuration is that shown in Fig. 12, in which two bundles of superelastic SMA wires extend diagonally from the top steel cover plate to the bottom steel cover plate. One-half of the total number of wires could be installed on one side of the bearing, with the other half on the opposite side of the bearing. Using this configuration, each HDRB remains unconnected to adjacent HDRBs. Another configuration is to connect the SMA wires diagonally from the bottom of one HDRB to the top of the adjacent HDRB, as shown in Fig. 13. The wires extend a sufficient length to avoid excessive strains, but in an attempt to reduce the cost of the system, the SMA wires do not extend the entire length of the diagonal. It is assumed that each wire is connected to a rigid link element that attaches it to the HDRBs. The assumption of a rigid link element has also been made by other researchers (McCormick et al. 2007).

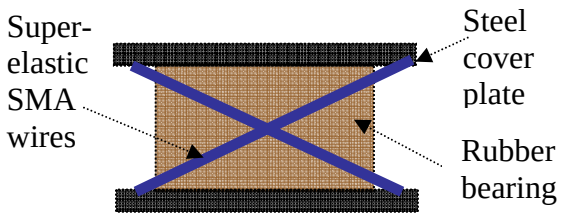

Fig. 12. Hybrid HDRB+SMA configuration (HDRB+SMA1)

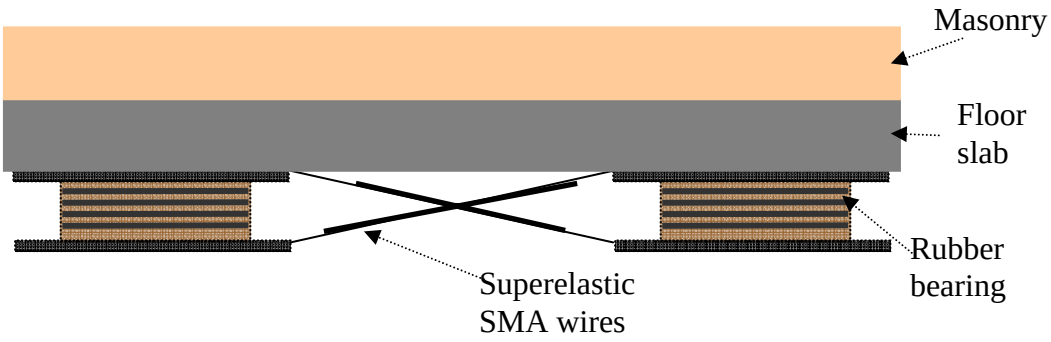

Fig. 13. Hybrid HDRB+SMA alternative configuration (HDRB+SMA2)

2.2.4. Kinematic Self-Centering Isolators

Pinochet et al. (2006) developed a kinematic isolator as an economical method for the seismic protection of low-cost housing. In Chile, as in many countries, low-cost housing is frequently located on the perimeter of big cities, where poor soil conditions are common. The proposed device can serve as a pile foundation in areas with poor soil conditions by transferring the load of the structure to layers of soil having larger bearing capacities.

Fig. 14 shows the components of the kinematic isolator (Pinochet et al. 2006), which is also known as a precast-prestressed pile (PPP). The kinematic isolator serves as a pile foundation with a central prestressed cable and rolling steel surfaces at the top and bottom ends. Energy dissipation occurs in the isolator through the yielding of unbonded ductile rebars that are grouted to the bottom capital of the device, and through friction between the central prestressed cable and the duct in which it is located. Self-centering behavior is achieved through the device geometry and the force in the prestressed cable. Thus, the force-displacement or stress-strain curve for the kinematic isolator exhibits hysteresis similar to that of the superelastic SMA wire.

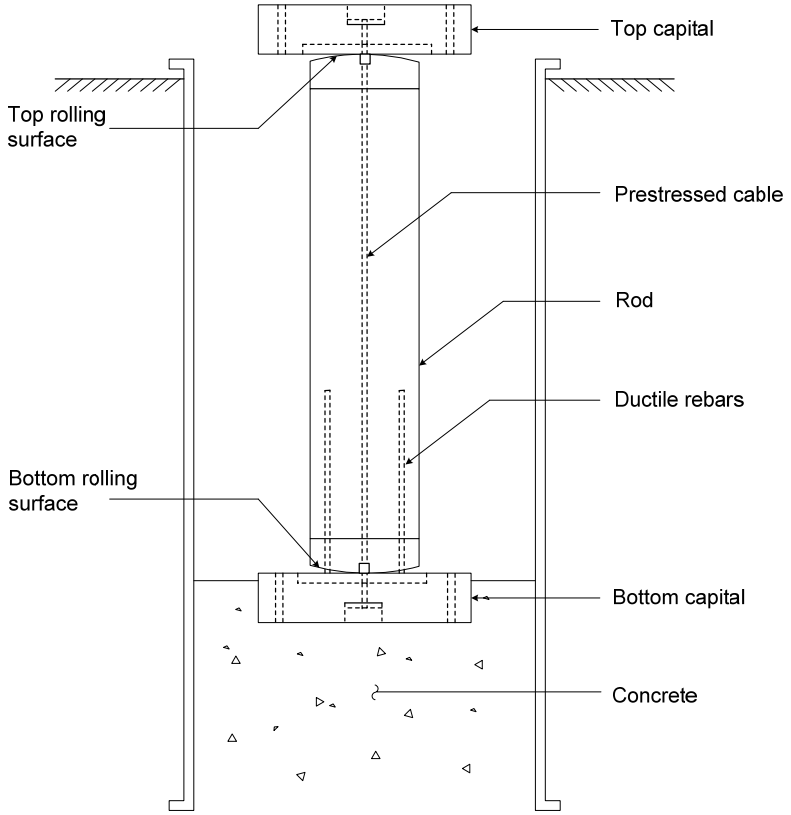

Fig. 14. Kinematic isolator (Pinochet et al. 2006)

An analytical formulation, computational implementation, parametric study, and experimental study of the device are discussed by Pinochet et al. (2006). In the current study, the formulation proposed by Pinochet et al. (2006) is utilized after modifying the model to account for the friction between the central prestressed cable and its duct. This change was suggested by Besa et al. (2008), who used additional experimental data to provide further validation of the analytical model proposed by Pinochet et al. (2006).

Jünemann et al. (2008) developed a 3D analytical formulation of the behavior of the PPP isolator. The 3D formulation was validated through comparisons with the 2D formulation developed by Pinochet et al. (2006) and with an ANSYS finite element model of the PPP isolator. Jünemann et al. concluded that because the lateral stiffness of

the PPP isolator is small, the devices are appropriate for seismic isolation of lightweight structures, such as houses.

One consideration associated with the PPP isolator is the uplift of the structure caused by the device. The uplift is more significant using a flat rolling surface than a spherical rolling surface. Another consideration is to design the PPP such that the tension in the central prestressed cable does not exceed the ultimate allowable stress in the cable. The kinematic isolator is anticipated to be more economical than other devices because the materials that comprise the device: concrete, steel reinforcement, steel prestressed tendon, and concrete conduit, are readily available and do not require special testing procedures before installation. According to Pinochet et al. (2006), the cost of using PPP isolation devices in Chile is approximately 25-50% of the cost of a typical rubber bearing isolation system.

2.3. Computational Approach

2.3.1. Fuzzy Logic

Fuzzy logic is a manner in which an input space is mapped to an output space through the means of if-then rules. The main advantage of fuzzy logic is that it can relatively easily handle imprecise data and complex nonlinearities (*MATLAB/Simulink* 2007). To use fuzzy logic, a fuzzy inference system (FIS) is created to link the input space to the output space. The first step in creating a FIS is to select the input and output parameters. To model the dynamic behavior of a seismic isolation device, the output parameter of concern is the force exerted by the device on the structure. The inputs are usually displacement and velocity, and sometimes one more input is required. Displacement is a necessary input to model the force-displacement behavior of the device, while velocity is used to provide sufficient data to model hysteresis of the force-displacement behavior. Note that hysteretic devices can have several possible force values for a given displacement value. Using velocity as an input enables the FIS to determine the appropriate force value associated with the corresponding displacement. For each additional input and output that is used in a FIS, the computational time

increases exponentially. Using three or less inputs and one output can be executed within a reasonable computational time. Fig. 15 shows the typical inputs and outputs for a FIS of an isolation device.

Fig. 15. Example inputs and output for a FIS of an isolation device

Upon selecting the desired input and output variables, a large set of training data of numerical values of input and output quantities is required to create the FIS. In this study, the FISes are created using 50,000 or more data points, such that a plot of the displacement and velocity data points uniformly covers all quadrants of the graph. The data should be experimental or, alternatively, created using an accurate analytical model of the device. Each data point should include values for each of the input and output parameters.

The type of inference must then be chosen for the FIS. Sugeno-type inference (*MATLAB/Simulink* 2007) is used in this research. Also, the number and type of membership functions for each input variable are chosen. In this trial-and-error procedure, a membership function is used to assign the degree of membership of each data point to the data set (*MATLAB/Simulink* 2007). Through this process, a series of IF [ ], THEN [ ] statements are formed which map the relationship of the input variables to the output variables. The training process for the FIS involves the use of one-half of the data, while the other half is utilized for checking the FIS. After checking the FIS, the training process is complete and the FIS is created. Graphs that result from the training process for each FIS are included in subsequent sections.

At this step, the FIS must be validated on a completely different set of data. In this application, the validation data set involves random displacement data that are different than those used for training. Here, random data are utilized for both creating and validating the FIS. This is done because the earthquake excitation(s) for the base-isolated system are random in nature. Upon making a comparison of the force-displacement output from the FIS validation with the actual experimental or analytical data, the level of accuracy of the FIS can be determined. Often the training and validation procedures are repeated several times to refine the prediction capabilities of the FIS.

The most significant advantage of using fuzzy logic to represent dynamic behavior of seismic isolation devices is that numerical simulation of the devices becomes modular. For example, upon creating a FIS that accurately represents the behavior of a 30 cm diameter HDRB made from a certain rubber compound, the FIS can be used to represent the behavior of the HDRB subjected to any earthquake, or in any structure with the same vertical load on the bearing. There is no need to perform additional experimental testing to modify the FIS. In addition, upon training and validation of a FIS, the computational implementation using the FIS model of the device is often significantly more favorable than utilizing complex analytical models to simulate the device. Therefore, if the device is to be used in several numerical simulations, use of a FIS instead of a complex analytical model can save significant computational time.

On the other hand, the most important limitation of a FIS is that it is only applicable for the range of data for which it was trained. Therefore, for example, a HDRB FIS that has been trained for displacements ranging from -20 to 20 cm cannot be used in a situation in which it is displaced -30 cm. That is, the FIS is unable to extrapolate to a larger range of input data. Likewise, extrapolation of analytical formulations beyond their known range of application also requires caution. Kim et al. (2006) discuss additional applications of fuzzy logic.

2.3.2. S-Functions

S-functions are a manner in which code-oriented computer routines written by the user can be incorporated in the graphical interface of Simulink (*MATLAB/Simulink* 2007). In this study, S-functions are written to model the FPS and the PPP devices, based on analytical models that were previously mentioned. Simulink is used to perform dynamic analyses of the fixed-base and base-isolated structures. For the cases using FPS bearings or PPP devices, the FPS or PPP S-function is used to evaluate the analytical model and predict a restoring force from the device at each time interval.

2.3.3. Numerical Simulation

MATLAB 7.4, Simulink, and a set of toolboxes for Simulink are utilized for the numerical simulation and computations in the work that follows. MATLAB and Simulink (*MATLAB/Simulink* 2007) are used jointly to numerically simulate dynamic response of a lumped-mass model of the case study structure to external seismic excitation. The analysis sequence is represented by Fig. 16. Incorporation of the isolation devices is achieved through free-body diagrams and application of equilibrium at each degree-of-freedom (DOF), as shown in Fig. 17, where the isolated structure is represented as a three DOF model. The stiffness, damping, and mass of each floor are represented by k_i, c_i, and m_i, respectively, while the absolute displacement, velocity, and acceleration are represented by u_i, $\dot{u}_i$, and $\ddot{u}_i$, respectively. The ground acceleration is noted by $\ddot{u}_g(t)$, the force exerted by each device on the structure as F_{device}, and the number of isolation devices by n. Fig. 17 shows a free body diagram for the ground floor level. Free body diagrams for the first and second floors are similar.

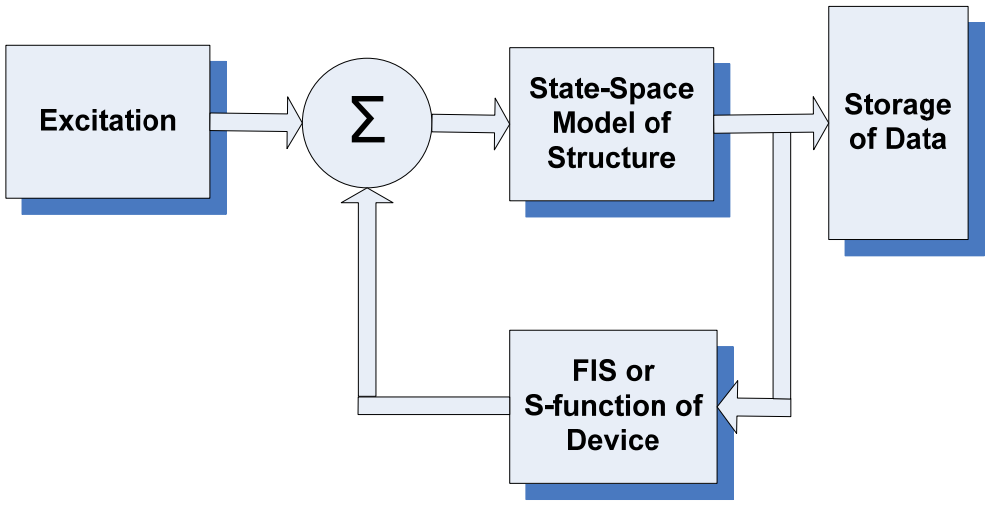

Fig. 16. Sequence of numerical simulation

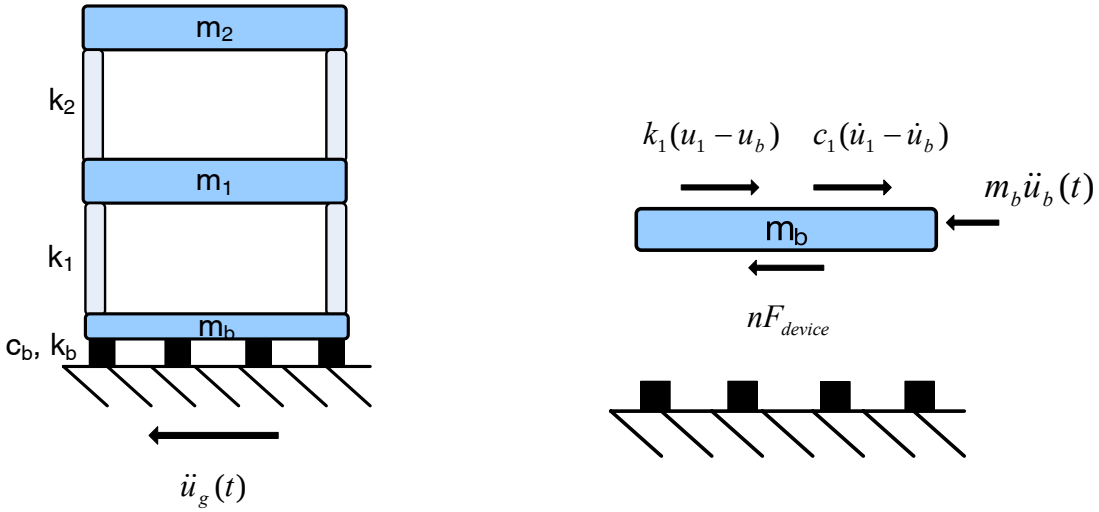

(a) (b)

Fig. 17. MDOF structure (a) Lumped-mass model and (b) Example free body diagram

2.3.4. Genetic Algorithm

The use of a genetic algorithm (GA) for optimization was first proposed by Holland (1975). GAs are a robust trial-and-error approach to optimization that consider

a population of solutions, or ‘configurations,’ at each generation. They utilize a training process that involves crossovers and mutations of the parent population. The solutions are characterized using objective functions, which in this study are performance indices related to predicted quantities such as base displacement, acceleration of each floor, and base shear. All of the performance indices except those related to base displacement are normalized with respect to the fixed-base case. For the normalized performance indices, values less than unity indicate a reduction in response from that of the fixed-base structure. Penalty functions, which penalize a solution for exceeding threshold values, can also be implemented in the GA. For example, a penalty function for solutions with peak base displacements larger than 20 cm is applied in this study. Fig. 18 shows the sequence of GA optimization.

Previously, Kim and Roschke (2006) pursued concurrent optimization of four objective functions using a non-dominated sorting genetic algorithm (NSGA-II). Narayanan and Azarm (1999) used multiobjective GAs to optimize the design of a truss and a vibrating platform. Shook (2006) describes the progression of research in the GA field as it relates to structural control.

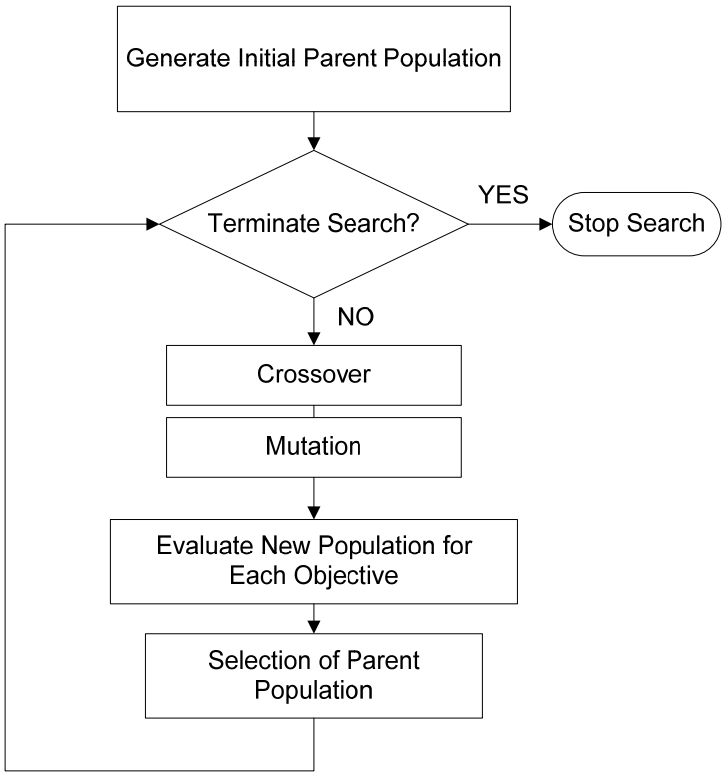

Fig. 18. Sequence of GA optimization (Shook 2006)

In this study, the multiobjective non-dominated sorting genetic algorithm with controlled elitism (NSGA-II CE) created by Deb (2001) is utilized to optimize the design parameters of the FPS and PPP isolation systems. For example, the FPS design parameters include the radius of curvature and the coefficient of friction of the sliding surface. After the optimization procedure for the FPS has been completed, the results are verified using a manual method as the process involves optimizing only two parameters of the device. The PPP optimization is much more complex as it involves optimization of five parameters: the initial prestressing force of the central cable, the radius of the top and bottom spherical rolling surfaces, the length of the pile, the stiffness of the central cable, and the diameter of the ductile rebar embedded at the base of the PPP isolator. Each optimization, including the GA and the trial-and-error optimizations, are performed using an earthquake motion generated using RSPMatch, described in the

following sub-section. Selected optimal devices are then included in the analyses of the structure subjected to a suite of earthquake motions. The performance indices that result from these analyses are used to make design decisions about relative merits of each base-isolation option.

2.4. Earthquake Selection

The isolation systems are designed using an earthquake motion that is based on a code-stipulated response spectrum for the base-isolated structure. There are several methods to create an earthquake acceleration time-history to fit a design response spectrum. Most commonly-used methods create an artificial time-series from white noise and adjust the record to conform to the required response spectra (Hancock et al. 2006). However, the disadvantages of using these methods are that the artificial records are dissimilar to real earthquake ground motions in the number of cycles, phase content, and duration (Hancock et al. 2006). The result is that it can take a large number of analyses to obtain stable estimates of the inelastic response of the structure. Another approach is to scale pairs of recorded horizontal ground motion time histories in the time domain using the *Uniform Building Code UBC-94* or *UBC-97*. This can lead to extremely conservative acceleration values with no physical meaning, which greatly exaggerate higher modal participation in the building response (Naeim and Kelly 1999).

The method used in this study to generate a suitable earthquake was developed by Hancock et al. (2006). This technique adjusts an acceleration time-history in the time domain by adding wavelets to an acceleration signal recorded from an actual earthquake. Hancock et al. (2006) modified the program developed by Abrahamson (1992) which uses the technique of Lilhanand and Tseng (1987, 1988). Details have been coded into a program named RSPMatch2005b. Using this program, existing earthquake acceleration-time histories are modified to match the inelastic design spectrum specified by the general Chilean seismic code, *NCh433.Of1996*, and the elastic design spectrum specified by the Chilean seismic code for isolated structures, *NCh2745.Of2003* (Instituto Nacional de Normalización 2003b). The Arias intensity (Arias 1970), which is proportional to the

integral over time of the acceleration time-history squared, of the resulting motion is then checked with that of the original motion for fidelity.

3. MODEL OF CASE STUDY STRUCTURE

3.1. General

To create a numerical model of the 110 m^2 two-story dwelling described previously, ambient vibration testing was performed to determine salient dynamic characteristics of the structure. The case study structure is representative of a housing layout that is commonly constructed in thousands of homes that are currently under construction in the vicinity of Santiago, Chile. This layout is also constructed in other parts of Chile. The ambient vibration method can be applied to perform system identification of a structure (Wenzel and Pichler 2005). Testing involves measuring the response of a structure resulting from ambient vibration over an extended period of time. In this study, the velocity of the structure was measured. Excessive vibration in the surrounding area, such as the use of a jackhammer to construct a neighboring house, can cause high frequency data to be collected which would require more filtering to be applied to the data. The data collected in this study were filtered only by the data collection devices themselves.

3.2. Ambient Vibration Testing

3.2.1. Ambient Vibration Measurements

Ambient vibration testing of the structure was performed in Maipú, Chile, on May 24, 2007, to determine its fundamental natural frequencies and periods. Four SS-1 Ranger seismometers manufactured by Kinemetrics were used to record the velocities of the structure. A 16-bit Daqbook 200 with DBK 18 by IO Tech was utilized with a laptop computer as the data acquisition system. A 20 min test was recorded with a sampling rate of 200 Hz. No external excitation was applied to the structure. The orientations and locations of the seismometers are shown in Fig. 19, where seismometers 1, 2, and 3 were on the second floor concrete slab, while seismometer 4 was located outside of the house on the soil at ground level. The longitudinal and transverse directions of motion are also identified in Fig. 19. A schematic of the test set-up and a

typical seismometer are shown in Figs. 20 and 21, respectively. Figs. 22 and 23 show front and back views of the structure that was tested.

The two-story structure is constructed of confined masonry and will serve as the residence of two families. An interior vertical partition bisects the house and provides separate living spaces for each family. The cantilevered portion of the second story can be seen in Fig. 22. Also, the larger number of wall openings in the longitudinal direction than in the transverse direction should be noted. Fig. 23 shows the openings in the longitudinal direction in the rear of the structure and the fence that is loosely attached to the back wall of the structure.

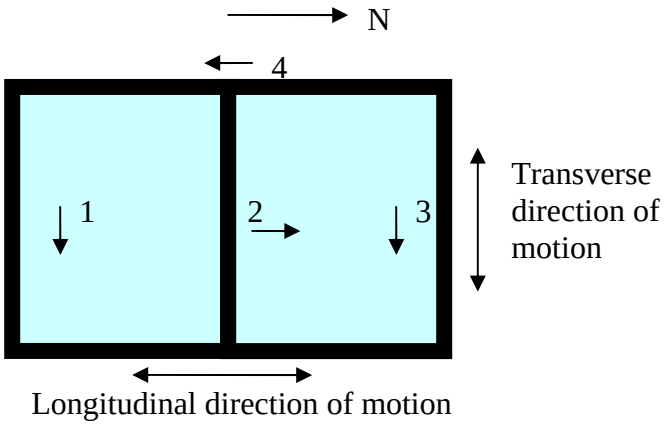

Fig. 19. Second floor plan view and locations of seismometers

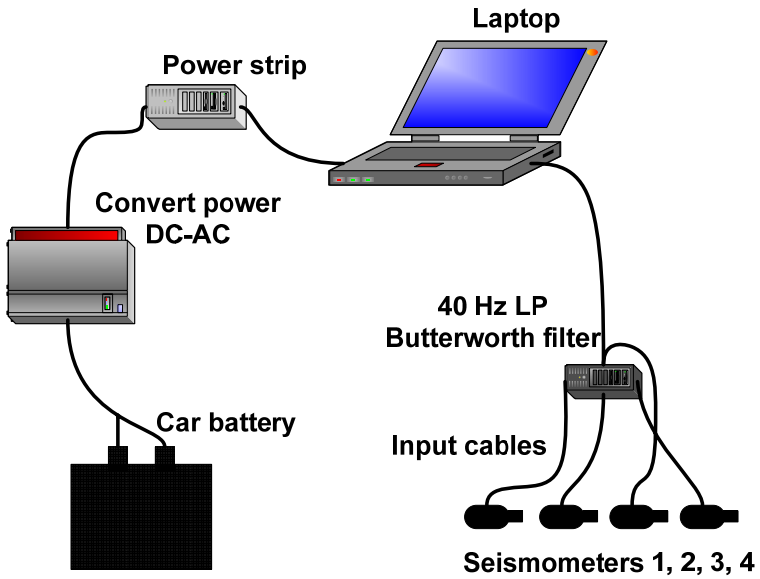

Fig. 20. Schematic of test set-up

Fig. 21. Typical seismometer

Fig. 22. Front view of test structure

Fig. 23. Back view of test structure

3.2.2. Ambient Vibration Results

Fig. 24 shows a time-history of the microvibration record for each of the four seismometers, labeled S1–S4, which correspond to locations marked 1-4 in Fig. 19. Some of the peaks result from construction traffic close to the test site. The power spectral density (PSD) for each seismometer is included in Fig. 25. The close correspondence in the transverse direction between seismometers 1 and 3, which are both aligned in the transverse direction, is apparent. Fig. 25(d) shows the response of the soil beneath the foundation of the case study structure. The soil is gravely in the top few meters. The influence of the soil on the seismic performance of the structure is not considered in the present study. Fig. 26 shows the correlation between seismometers over the range of frequencies from 0 to 25 Hz.

The natural frequencies and periods are determined using a non-parametric system identification technique based on power spectra, transfer, and coherency functions (Boroschek et al. 2003). The structural periods are identified from the power spectral peaks and correlation analysis.

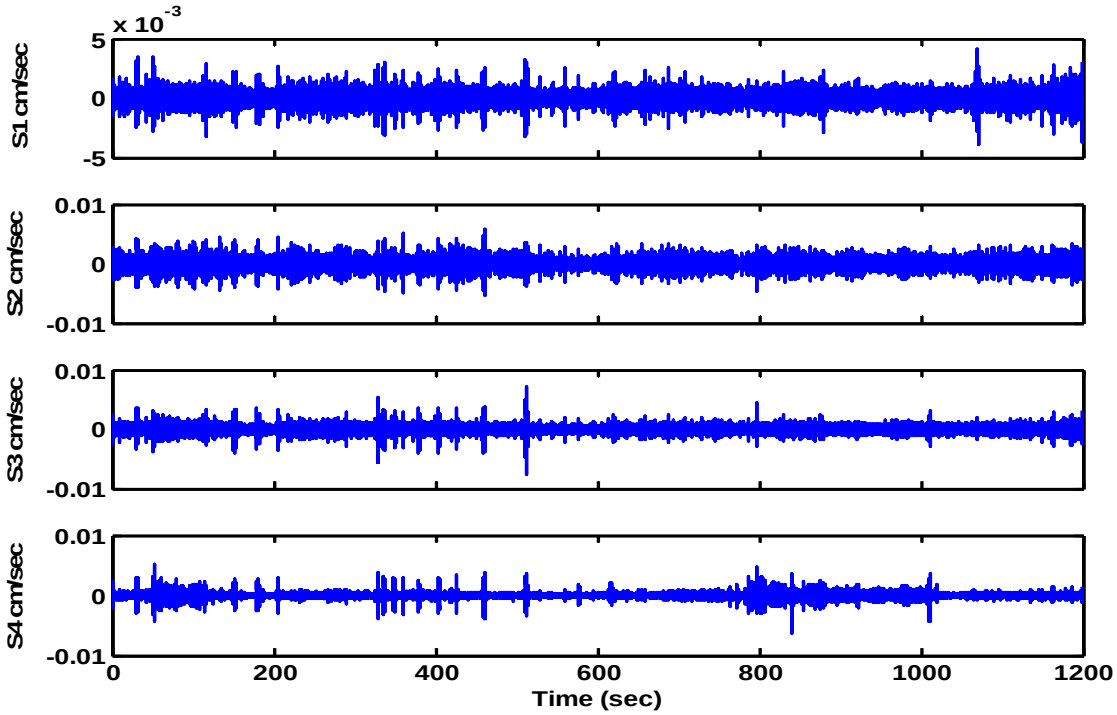

Fig. 24. Time-history of microvibration data

Based on Figs. 25 and 26, it can be concluded that the natural frequencies corresponding to the first mode of the structure in the transverse and longitudinal directions are approximately 16 Hz and 13 Hz, respectively. The 16 Hz natural frequency corresponds to a period of 0.063 sec in the transverse direction, while the 13 Hz natural frequency corresponds to a period of 0.077 sec in the longitudinal direction. As expected, these periods are slightly less than those measured by Astroza et al. (2005a) for three- and four-story confined masonry buildings. These periods are also approximately the same as those measured from microvibration testing on a four-family house with nearly the same layout as that of the two-story house reported here. The natural frequencies of the second mode of the structure can also be estimated. Based on the PSD spectra, the natural frequencies of the second mode in the transverse and longitudinal directions are approximated as 20 Hz and 24 Hz, respectively. These values are confirmed by an initial finite element analysis of the structure.

(a)

(b)

(c)

(d)

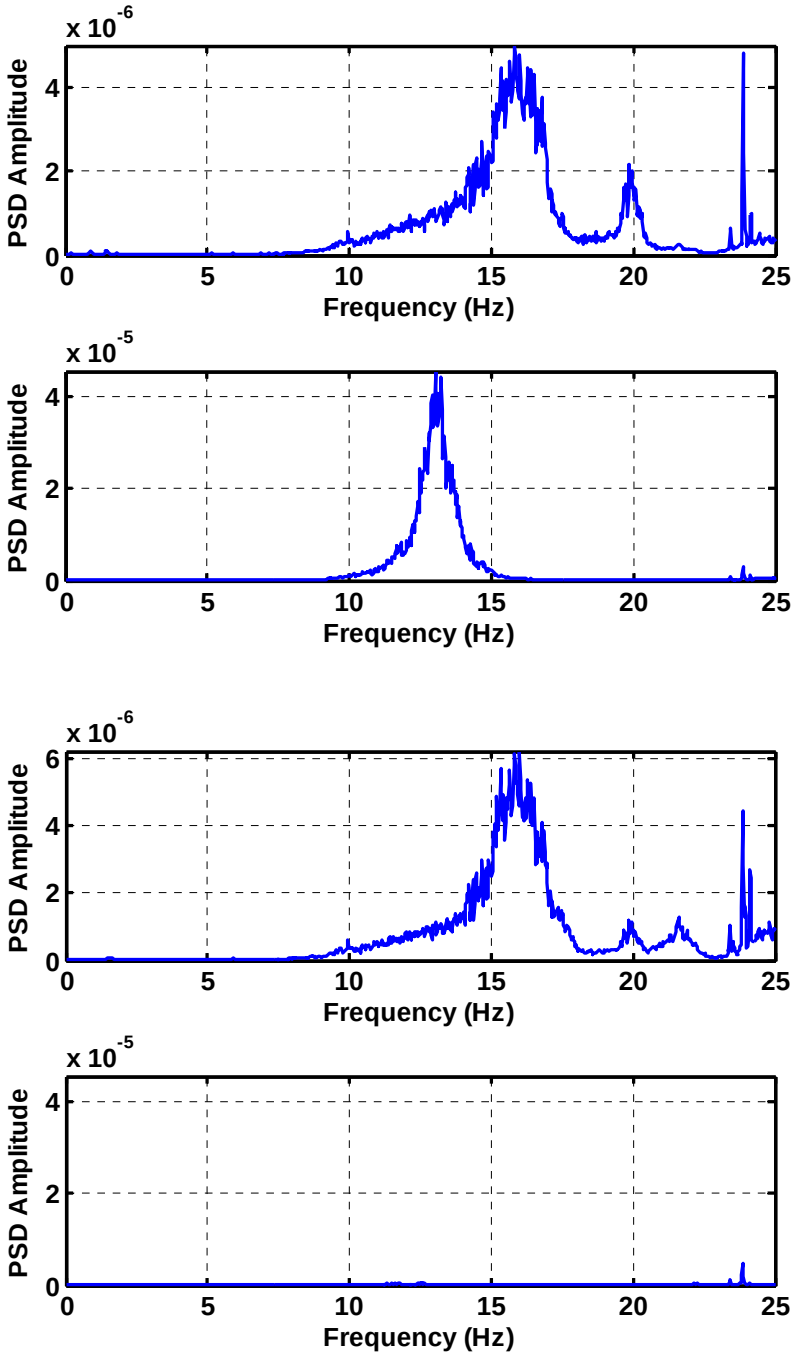

Fig. 25. Power spectral density for seismometer (a) 1, (b) 2, (c) 3, and (d) 4

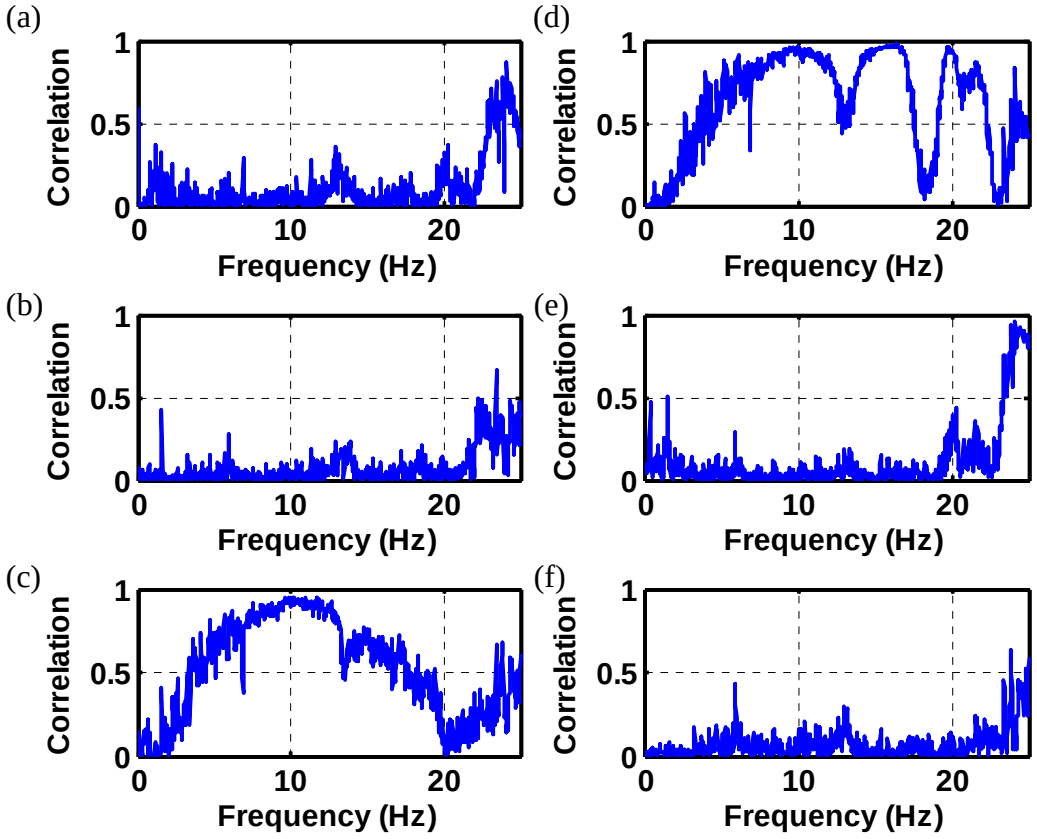

Fig. 26. Correlation between seismometers (a) 1 and 2, (b) 1 and 4, (c) 2 and 4, (d) 1 and 3, (e) 2 and 3, (f) 3 and 4

3.2.3. Estimation of Equivalent Viscous Damping

An estimation of the equivalent viscous damping of the structure is made using the bandwidth method, in which f_1 and f_2 are the frequencies associated with one-half the amplitude of the frequency peak (Boroschek et al. 2003). The formulation for the equivalent viscous damping is:

$$\psi = 0.5A\left(1-0.375A^2\right) \tag{1}$$

where:

$$A = \frac{f_2^2 - f_1^2}{f_2^2 + f_1^2}, f_1 < f_2 \quad (2)$$

Using this method, the equivalent viscous damping of the structure in the transverse and longitudinal directions are approximately 5.77% and 3.82%, respectively. The difference in the equivalent viscous damping in the two directions is likely due to the strong sensitivity of the bandwidth method to the amplitude of the PSD. This sensitivity is also noted by Boroschek et al. (2003). For the interested reader, Boroschek and Yañez (2000) include more information related to ambient vibration testing.

3.3. Structural Model

3.3.1. Overview

The two-family structure considered in this case study is analyzed using a multiple degree-of-freedom (DOF) model. The goal of numerical simulation with the model is to be able to analyze the effect of implementing the base isolation devices on the seismic behavior of the structure. The traditionally-constructed fixed-base house is modeled as a two DOF structure [see Fig. 27(a)], while the base-isolated structure is modeled using three DOFs [see Fig. 27(b)]. The necessity of adding a third DOF for the modified structure is due to the fact that in order for a base isolation strategy to be implemented, the two-family house must have a reinforced concrete (RC) slab-on-grade. It should be noted that seismic behavior of the house only in the longitudinal direction is considered in this study (see Fig. 19).

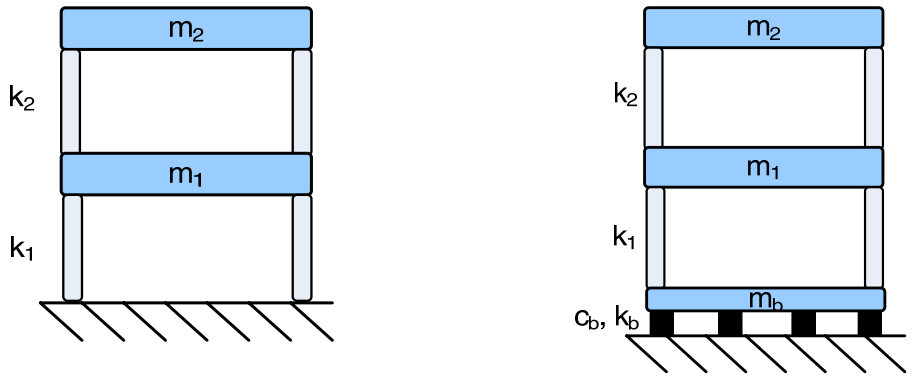

(a) (b)

Fig. 27. Lumped-mass models of (a) Fixed-base and (b) Base-isolated structures

3.3.2. Mass Calculations

The mass of a 12 cm thick RC slab-on-grade is included in the total mass of the base-isolated structure. As required by Instituto Nacional de Normalización (1996) 5.5.1, 25% of the live load on the structure is also included in mass calculations for the fixed-base and isolated structures. Table 1 shows the calculated mass of each floor for the fixed-base and base-isolated cases. The only difference in the mass calculations for the two structures is that the fixed-base case does not include the mass of a RC slab-on-grade, while the base-isolated case does. Detailed calculations are included in Appendix A. The total mass of the fixed-base and base-isolated structures are estimated as 67,370 and 83,877 kg, respectively. These calculations are made using the structural plans and unit weights included in the project specifications.

Table 1. Mass Calculations (kg) by Floor for Fixed-Base and Base-Isolated Cases

Floor	**Fixed-Base**	**Base-Isolated**
	Mass (kg)	
Base:		
Slab-on-grade	N/A	16,508

Table 1. Continued

Floor	Fixed-Base	Base-Isolated
	Mass (kg)	
Columns	1,768	1,768
Walls	5,991	5,991
25% live load	2,752	2,752
	10,511	**27,018**
1st Floor:		
1st Floor slab	16,888	16,888
Columns	2,158	2,158
Beams	5,506	5,506
Walls	13,344	13,344
25% live load	2,815	2,815
	40,711	**40,711**
2nd Floor:		
Columns	390	390
Beams	4,258	4,258
Walls	10,247	10,247
Roof	768	768
25% live load	485	485
	16,148	**16,148**
Total Mass of Structure	**67,370**	**83,877**

3.3.3. Stiffness Calculations

The classic equation of motion:

$$[M]\{\ddot{X}\}+[C]\{\dot{X}\}+[K]\{X\}=\{F\} \tag{3}$$

is applied to the two DOF model of the fixed-base structure to determine the stiffness values for each floor. In this equation, $[M]$, $[C]$, and $[K]$ are the mass, damping, and stiffness matrices, respectively; $\{\ddot{X}\}$, $\{\dot{X}\}$, and $\{X\}$ are the acceleration, velocity, and displacement vectors, respectively; and $\{F\}$ is the external force vector. Writing these matrices out, the equation of motion is:

$$\begin{bmatrix} m_1 & 0 \\ 0 & m_2 \end{bmatrix} \begin{Bmatrix} \ddot{x}_1 \\ \ddot{x}_2 \end{Bmatrix} + \begin{bmatrix} c_1 + c_2 & -c_2 \\ -c_2 & c_2 \end{bmatrix} \begin{Bmatrix} \dot{x}_1 \\ \dot{x}_2 \end{Bmatrix} + \begin{bmatrix} k_1 + k_2 & -k_2 \\ -k_2 & k_2 \end{bmatrix} \begin{Bmatrix} x_1 \\ x_2 \end{Bmatrix} = \begin{Bmatrix} F_1 \\ F_2 \end{Bmatrix} \tag{4}$$

This equation can be solved for the general form when [*C*] = [0] and {*F*} = {0}. It should be noted that solving the equation of motion for the undamped, free vibration case yields the same stiffness values as that of the solution involving a small amount of damping. For the undamped, free vibration case, the solution of Eq. (4) is (Hart and Wong 2000):

$$\omega_1^{\,2} = \frac{\left[\left(k_1 + k_2\right) m_2 + k_2 m_1\right] - \sqrt{\left[\left(k_1 + k_2\right) m_2 + k_2 m_1\right]^2 - 4 m_1 m_2 k_1 k_2}}{2 m_1 m_2} \tag{5}$$

In order to solve Eq. (5) for the values of k_1 and k_2, the ratio between the two values is calculated based on the amounts of masonry walls and RC columns per floor. These amounts are normalized with respect to the ratio of the concrete and masonry shear moduli. This assumption is consistent with findings by Moroni et al. (2000), which identify wall density as an appropriate indicator in determining the seismic vulnerability of a confined masonry structure. The result is that the first and second floors account for approximately 57% and 43% of the stiffness of the structure, respectively. This distribution is reasonable because the first floor has a larger area of masonry walls and concrete columns due to the vertical distribution of the masses (see Fig. 28). Using calculated values for m_1 and m_2, ω_1 = 13 Hz (longitudinal direction), and the ratios between the stiffnesses, it follows from Eq. (5) that $k_1 = 4.33 \times 10^8$ N/m and $k_2 = 3.24 \times 10^8$ N/m.

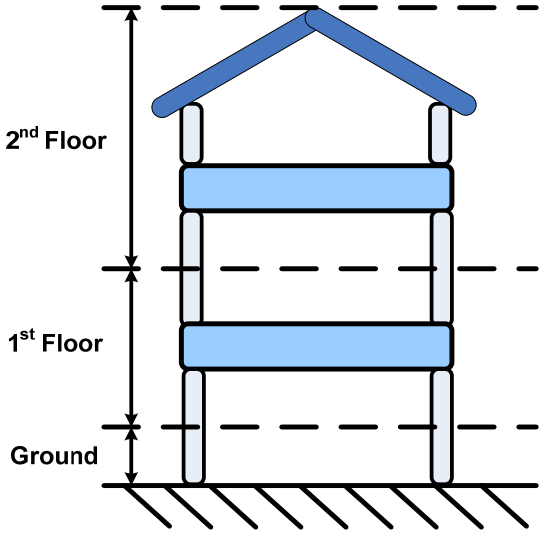

Fig. 28. Distribution of mass per floor

3.3.4. Damping Calculations

Next components of the damping matrix of the structure are calculated using stiffness-proportional damping as follows (Chopra 2001):

$$[C] = a_1[K] \tag{6}$$

where:

$$a_1 = \frac{2\zeta_1}{\omega_1} \tag{7}$$

and the natural frequency in the longitudinal direction of the first mode ω_1 = 13 Hz, as measured by the ambient vibration testing. $[K]$ is the stiffness matrix as defined in Eq. (4), and the damping ratio ζ_1 is taken to be 3.82% (see Section 3.2.3). Stiffness-proportional damping is applied to enable the fixed-base and base-isolated structures to have the same structural damping. The additional damping for the base-isolated structure is included in the models of each isolation device. Final calculated values for $[C]$ of the fixed-base structure in terms of N and m are as follows:

$$[C] = \begin{bmatrix} 7.08\times10^{5} & -3.03\times10^{5} \\ -3.03\times10^{5} & 3.03\times10^{5} \end{bmatrix} \tag{8}$$

4. EARTHQUAKE SELECTION

4.1. General

After the fixed-base structure has been selected and discussed, and its fundamental dynamic properties have been determined by means of experimental tests and numerical analyses, time-histories of earthquake excitations that are used to evaluate the dynamic behavior of the structure need to be determined. These excitations are selected to conform to standard seismic codes that govern the design of low-cost houses constructed in Chile.

Two construction scenarios are investigated: fixed-base and base-isolated cases. For the base-isolated cases there are five different seismic reduction strategies investigated, as outlined in Section 2. In preparation for their implementation, this section describes creation of a set of envelopes that define an acceleration spectrum for various levels of excitation and damping, and then uses a wavelet method to modify the time history of a Chilean earthquake to create an acceleration time-history that matches the design spectrum. The resulting acceleration time-history is used in the optimization of the parameters of each base isolation technique. Although the design spectrum for each of the base-isolated cases is somewhat different due to different damping levels of each system, the same earthquake time-history is utilized for all cases by conservatively using the design spectrum with the lowest damping ratio. A similar procedure is followed for the fixed-base structure and is described in detail in the following sub-section.

Frequently an inelastic design response spectrum is used for a fixed-base structure, thus allowing inelastic deformations in the superstructure under a strong motion earthquake loading. On the other hand, an elastic design response spectrum is typically utilized for a base-isolated structure because the superstructure is intended to remain elastic when it is subjected to seismic loading (Naeim and Kelly 1999). The use of an elastic design response spectrum for a base-isolated structure also results in an appropriate design of the isolation system. In this study, the earthquake motion generated using the elastic design response spectrum for each base-isolated structure is

applied to both the fixed-base and base-isolated structures to allow a suitable comparison to be made between the two cases. However, an inelastic design response spectrum is developed for the fixed-base structure and included in this section to allow comparison with the elastic response spectrum of the base-isolated structure.

4.2. Design Response Spectra

4.2.1. Fixed-Base Structure

Design of a structure for seismic loads is based on one or more response spectra that represent the response of an infinite array of structures with varying stiffness, mass, and damping ratios. Frequency content and amplitude of the response spectrum generally correspond to an envelope of response spectra from a family of earthquakes that are credible events for the site. For this study, the Chilean seismic code *NCh433.Of96* (Instituto Nacional de Normalización 1996) is the building code that is utilized to generate the inelastic design response spectrum for the fixed-base structure, that is, the two-family structure constructed traditionally. This code governs the earthquake-resistant design of fixed-base buildings in Chile. Design response spectra were created for a house constructed in Maipú, Chile, and a house constructed in Valparaíso, Chile. The purpose of creating a design response spectrum for the Valparaíso house is to show how a more severe seismic zone and weaker soil type strongly influence the seismic design of the structure. The house in Valparaíso is in seismic zone III and assumed to be in soil type III. On the other hand, the house constructed in Maipú is in seismic zone II and assumed to be supported by soil type II, based on soil boring logs performed in September, 2004, by civil engineer Mr. Hector Ventura on a construction site in the Alberto Blest Gana subdivision in Maipú.

NCh433.Of96 equation 6-8 [Eq. (9)] is used to calculate the design spectrum, taking into account the seismic resistance of the structure. The spectral acceleration is as follows:

$$S_a = \frac{IA_0\alpha}{R^*} \tag{9}$$

where I is the importance factor, A_0 is the maximum effective acceleration, α is the amplification factor for each mode of vibration *n*, and R^* is a reduction factor based on the construction material. Including the reduction factor R^* in the denominator of the equation for spectral acceleration causes the design response spectrum to be inelastic because it accounts for inelastic deformations in the superstructure.

The amplification factor is calculated using *NCh433.Of96* equation 6-9 [Eq. (10)]:

$$\alpha = \frac{1 + 4.5\left(\frac{T_n}{T_0}\right)^p}{1 + \left(\frac{T_n}{T_0}\right)^3} \tag{10}$$

where T_n is the period of vibration for mode *n*, and T_0 and *p* are parameters based on the soil type.

Finally, *NCh433.Of96* equation 6-11 is used to calculate R^* as follows:

$$R^* = 1 + \frac{NR_0}{4T_0R_0 + N} \tag{11}$$

where *N* is the number of stories in the building, R_0 is a modification factor based on the structural material, and T_0 is as defined previously.

In summary, constants for the Maipú and the Valparaíso houses are defined in Table 2.

Table 2. Values of Constants for *NCh433.Of96*

	Maipú House	Valparaíso House
Category of structure	C	C
Importance factor, *I*	1	1
Seismic zone	II	III
Soil type	II	III

Table 2. Continued

	Maipú House	Valparaíso House
A_0/g	0.3	0.4
T_0	0.3	0.75
p	1.5	1
N	2	2
R_0	3	3
R^*	2.07	1.55

NCh433.Of96 defines a Category *C* structure as one dedicated to private living or public use that does not belong to categories *A* or *B*, which include buildings used in case of catastrophe and buildings whose content is of great value. The importance factor (*NCh433.Of96* Table 6.1) corresponds directly to the category of the structure. The seismic zone for cities in Chile is specified in *NCh433.Of96* Table 4.1, while the soil type classification is based on the descriptions in *NCh433.Of96* Table 4.2.

It should be noted that *NCh433.Of96* does not place an upward limit on the value of S_a/g, and the percentage of damping of the structure is not directly taken into account in the design response spectrum. In contrast *NCh2369.Of2003* (Instituto Nacional de Normalización 2003a), which governs the earthquake-resistant design of industrial facilities, does place an upper limit on S_a/g, and requires an estimation of the structural damping.

The design response spectra (based on *NCh433.Of96*) for the fixed-base houses in Maipú and Valparaíso are created using the values in Eqs. (9)-(11) over a range of periods from 0 to 6 sec, and are included in Fig. 29. It can be seen that the Valparaíso house has a much more severe design response spectrum than the Maipú house, based on the stronger seismic zone and weaker soil in Valparaíso.

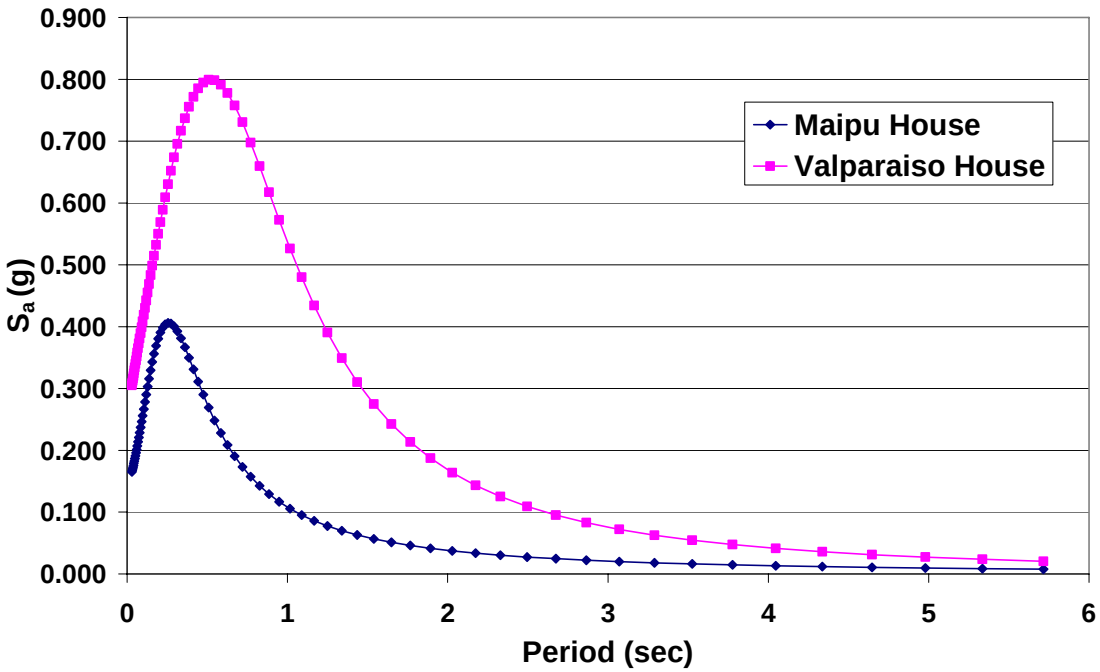

Fig. 29. *NCh433.Of96* Inelastic design response spectra for fixed-base structure

4.2.2. Base-Isolated Structure

The design response spectra for a fixed-base structure as outlined in the previous section allow inelastic response of the superstructure under a strong earthquake. By contrast, design response spectra for base-isolated Chilean structures that allow only elastic behavior of the structure are created according to *NCh2745.Of2003*. The spectra considered in the discussion that follows are created using the base design spectrum from Fig. 1 in *NCh2745.Of2003*, which is reproduced here as Fig. 30. This baseline figure is for a structure located in seismic zone II and having 5% damping. For any other seismic zone or damping ratio, the figure must be scaled by a factor of Z, which depends on the seismic zone, and divided by the appropriate damping ratio B_D. That is:

$$S_a = S_{a_{baseline}} \frac{Z}{B_D} \tag{12}$$

This equation applies only at periods greater than the target isolated period. For periods less than the target isolated period, the baseline spectral acceleration is multiplied by Z, without dividing by the damping ratio B_D. For this reason, the target isolated period of the structure should be determined in order to create the elastic design spectrum. Eq. (12) does not include division by the resistance factor R because it assumes that the superstructure remains elastic. This process is applied to create design spectra for the Maipú and Valparaíso houses, and is discussed in what follows.

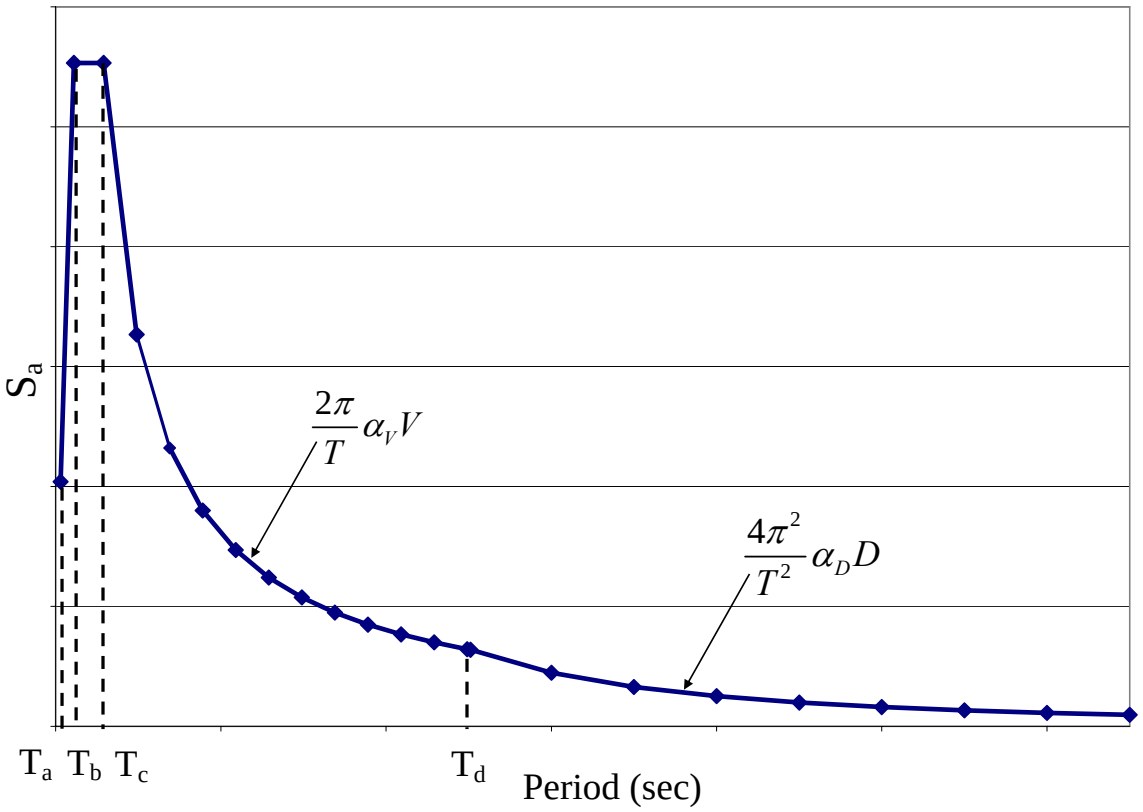

Fig. 30. *NCh2745.Of2003* base design spectrum, zone II, soil type I, 5% damping

For the Maipú house (seismic zone II), Z = 1. On the other hand, for the Valparaíso house (seismic zone III), Z = 5/4. Damping of the superstructure is estimated

as 5%, the value specified in Table 5.5 of *NCh2369.Of2003* for masonry structures. As mentioned in Section 3, the ambient vibration tests resulted in an estimated 3.82 and 5.77% damping, β_D, of the structure in the longitudinal and transverse directions, respectively. The values for B_D in Eq. (12) that correspond to each value of β_D are listed in Table 2 of *NCh2745.Of2003*. Figs. 31 and 32 show response spectra for the Maipú and Valparaíso houses, respectively, based on assumed damping values of 10, 15, and 20%, and an isolated period of 2.0 sec. For β_D values of 10, 15, and 20% of critical damping, the corresponding B_D values are 1.37, 1.67, and 1.94. From Figs. 31 and 32 it can be seen that there is not a significant difference in the design response spectrum for these damping levels. For this reason, the design response spectrum using 10% damping is conservatively utilized in the sections that follow to generate the adjusted earthquake acceleration-time history using RSPMatch2005b. Figs. 33 and 34 show the effect of maintaining the same damping ratio (10%) while changing the value of the isolated period of the structure. It can be seen that a longer isolated period of the structure yields a response spectrum with higher spectral acceleration values. In this study, each isolation system is optimized using an earthquake generated from a response spectrum based on the period of the structure isolated using that system.

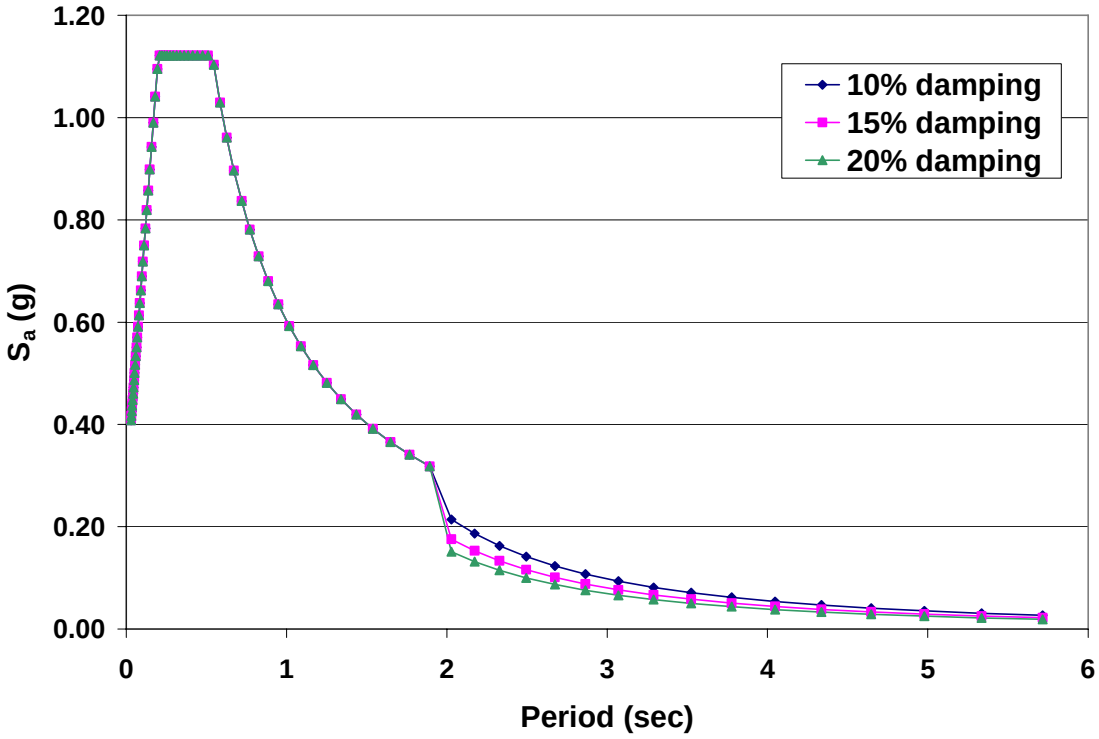

Fig. 31. Elastic response spectrum for the Maipú house for various damping levels

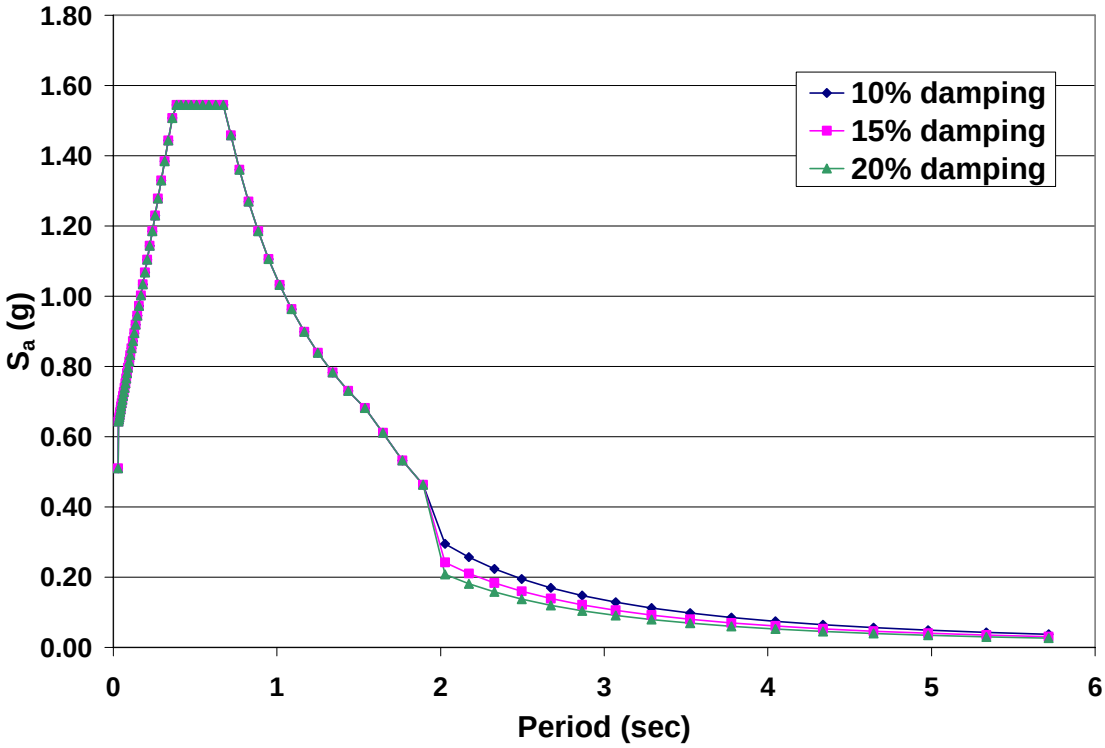

Fig. 32. Elastic response spectrum for the Valparaíso house for various damping levels

Based on a comparison of Fig. 29 with Figs. 31 and 32, it is evident that the base-isolated house is designed to withstand significantly higher spectral accelerations than the fixed-base house because the design response spectrum for the base-isolated house is based on elastic analysis, while the fixed-base house allows the use of an inelastic design response spectrum. However, only the earthquake motion generated using the elastic design response spectrum is applied to the fixed-base and base-isolated structures. Use of the acceleration-time record based only on the elastic design response spectrum enables an adequate comparison to be made between the fixed-base and base-isolated structures.

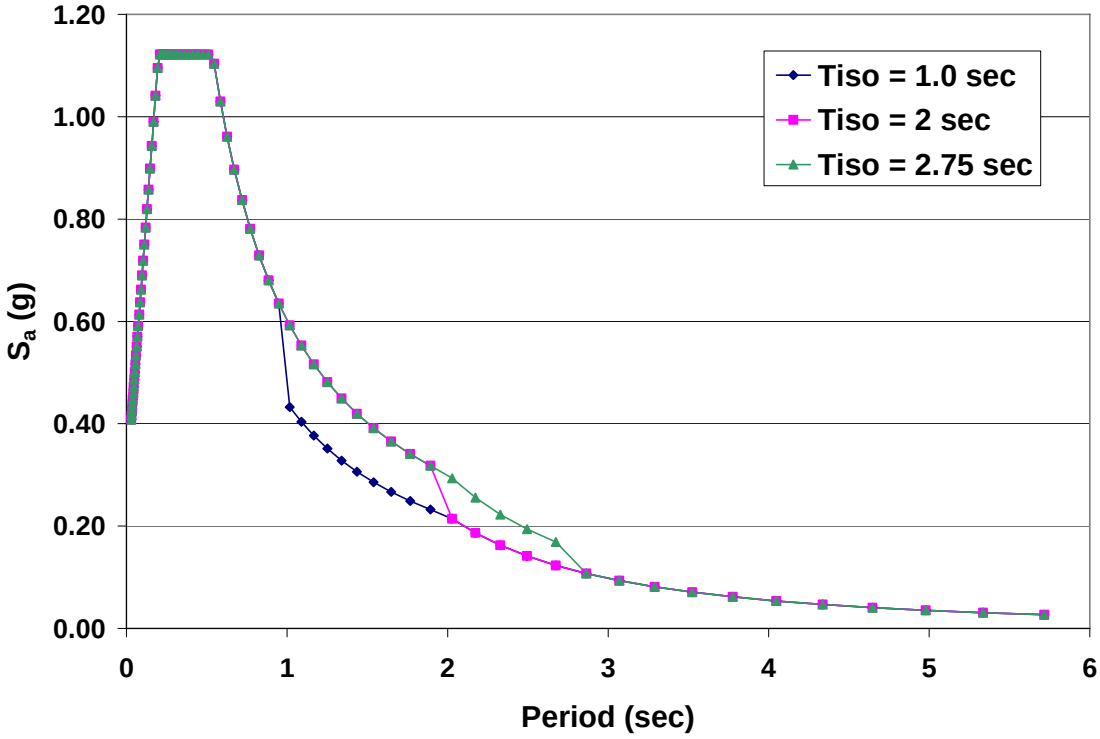

Fig. 33. Elastic response spectrum for the Maipú house for various T_{iso}

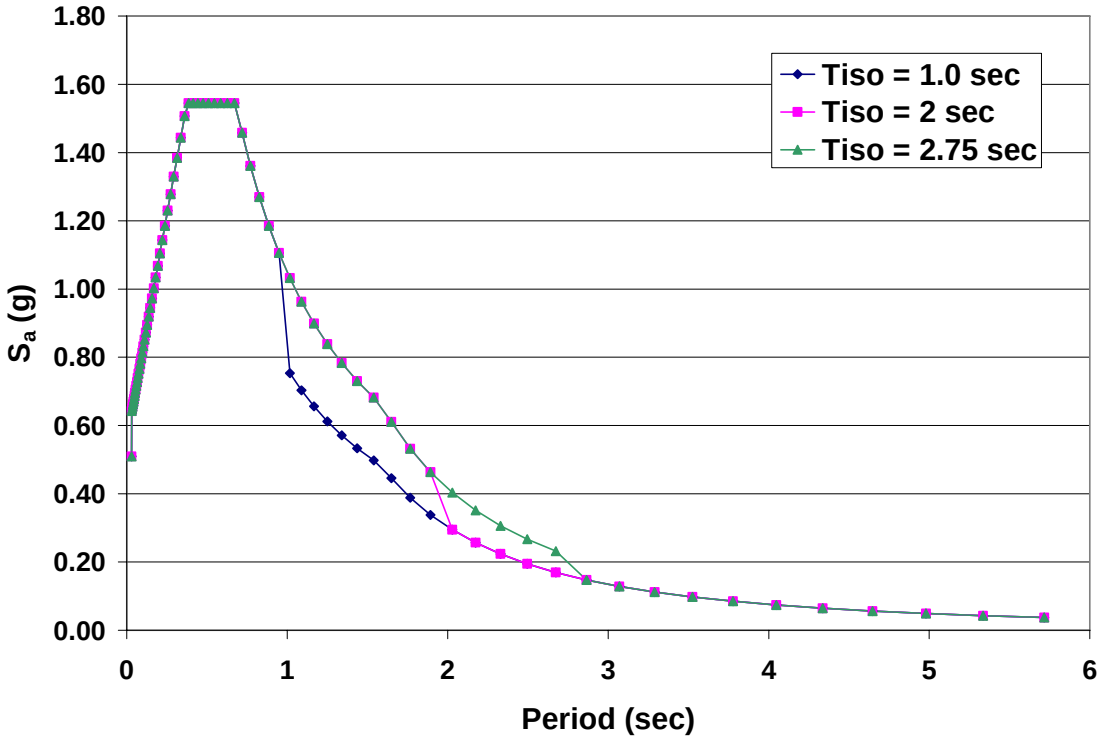

Fig. 34. Elastic response spectrum for the Valparaíso house for various T_{iso}

4.3. Generation of Earthquake Ground Motion

4.3.1. Background

In the study at hand, an analysis of the Maipú house that takes into account nonlinear aspects of the base isolation devices is required. In order to perform dynamic analyses of a structure supported by these devices, a time-series of ground accelerations must be generated that is compatible with the specified design response spectrum. For the reasons discussed in Section 2.4, an approach developed by Hancock et al. (2006) that adjusts an acceleration time-history in the time domain is utilized. The modifications made by Hancock et al. (2006) to the program developed by Abrahamson (1992) use wavelets to prevent drift in the velocity or displacement time-series that correspond to the acceleration time-series. In addition, the theory that is implemented in

a computer program named RSPMatch2005b allows the acceleration record to be simultaneously matched to a target spectrum that has different levels of damping.

There are a number of methods that use wavelets to adjust accelerograms to have a closer match to a target response spectrum. The continuous wavelet transform (CWT) has been used by Mukherjee and Gupta (2002) and Suarez and Montejo (2003, 2005) to decompose the original acceleration time-history into a number of time series with energy in frequency bands that do not overlap. Then the time-histories are scaled using an iterative procedure so that they produce a spectrum-compatible ground motion when added together. However, the adjusted accelerograms have noticeably different amplitudes and frequency contents from the original accelerogram. The wavelet method developed by Lilhanand and Tseng (1987, 1988), which is used by RSPMatch2005b, employs the response of elastic single degree-of-freedom (SDOF) systems to determine the wavelets, instead of the CWT. As a result, the accelerograms are made spectrum-compatible with smaller adjustments than those used by the CWT (Hancock et al. 2006). Based on its promising results to date, RSPMatch2005b is selected in the current study to generate an acceleration time-history to match each design response spectrum, using a set of time-histories of ground accelerations that have been recorded in Chile as a starting point.

4.3.2. Earthquake Time History from RSPMatch2005b

RSPMatch2005b requires three input files to generate an output file of the ground acceleration time-history (see Fig. 35). The first file defines the target spectrum, which includes the periods and spectral accelerations associated with a single or multiple damping levels. The target design spectra used here (see Figs. 29 and 31) are generated using the Chilean seismic codes, as described previously. Only the design spectra for the house in Maipú are utilized.

The second file required contains a seed accelerogram. The accelerogram to be adjusted is from a recorded significant seismic event that preferably occurred in a geographical region that is reasonably close and similar to the site of the housing

structure that is being studied. Moreover, to minimize the amount of adjustment required by wavelets, the seed accelerogram should have a spectral shape and amplitude that is similar to that of the target accelerogram. Based on the User Manual for RSPMatch2005 (unpublished, November 2005), the spectral shape can be matched using the root-mean-squared (RMS) difference between the spectrum of the normalized record and the target spectral acceleration. The amplitude can be adjusted by linear scale factors of 10 without causing a bias in the response, if the seed acceleration records are selected to match the spectral shape (Watson-Lamprey and Abrahamson 2006).

The third file required is an input file that specifies many parameters for the analysis by RSPMatch2005b, including the number of passes made by the program, the maximum number of iterations, the tolerance, the type of wavelet model to use, and the frequency range for spectral matching, among others. Samples of each of the three files required to run RSPMatch2005b are included in Appendix B.

Output from RSPMatch2005b includes the modified acceleration time-history, the spectral response for the periods which were requested to be matched, and the average and maximum misfit for each iteration. It is very important to check the output of RSPMatch2005b. The User Manual for RSPMatch2005 (unpublished, November 2005) suggests verifying the output of RSPMatch2005b by plotting the adjusted spectral acceleration and corresponding displacement with those from the target spectrum. An additional check of the RSPMatch2005b output is made by plotting the Arias intensity, which is a measure of the energy content introduced into the record. These checks of the output from RSPMatch2005b are made using a commercial software program called SeismoSignal (SeismoSoft 2006).

Fig. 36 shows the target and computed response spectra for the fixed-base structure, where the ‘target’ is that specified by *NCh433.Of96* and the ‘computed’ is the response spectrum based on the earthquake time-history resulting from the RSPMatch2005b analysis. Fig. 37 shows the original and adjusted acceleration time-histories for the fixed-base structure, where the ‘original’ acceleration time-history is that of the earthquake motion used for training and the ‘adjusted’ acceleration time-

history is that which results from the iterative procedure. Fig. 38 is a plot of the original and adjusted Arias intensity. Similarly, Figs. 39-41 show the response spectra based on *NCh2745.Of2003*, acceleration time-histories, and Arias intensity, respectively, for the base-isolated structures with an isolated period of 1.5 sec, Figs. 42-44 for the structures with an isolated period of 2.0 sec, and Figs. 45-47 for the structures with an isolated period of 2.75 sec. All of the earthquakes generated for the base-isolated structures with different isolated periods are based on response spectra that conservatively assume 10% damping.

The earthquake used for training by RSPMatch2005b in the fixed-based case is the 1985 Chilean earthquake as measured at an orientation of 290° in Laligua, Chile. The earthquake is not scaled. For the base-isolated cases, the S80E component of the 1985 Chilean earthquake as measured in Llolleo, Chile, is utilized. The earthquake is scaled by a factor of 1.5 to speed convergence. Three passes were made by RSPMatch2005b in each of the cases shown. The basic file relationships related to the use of RSPMatch2005b and its output are shown in Fig. 35, while a more detailed file relationship flow chart is included as Fig. 48.

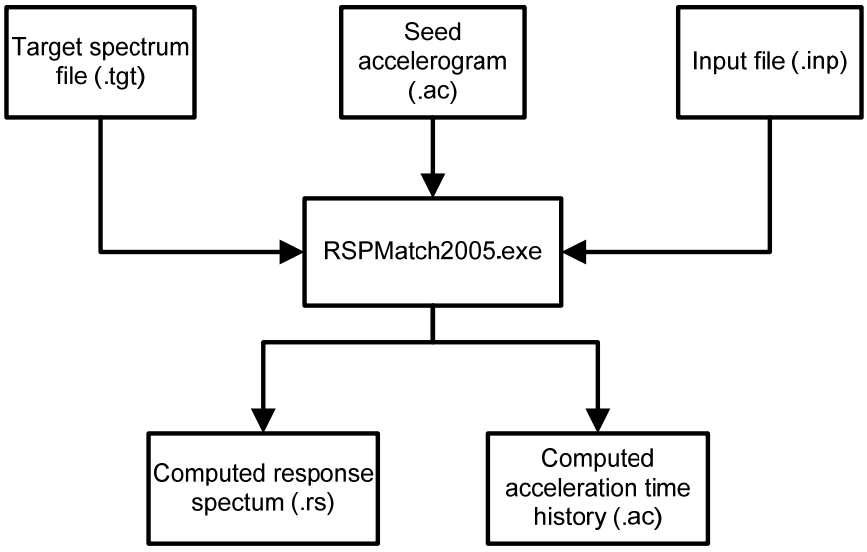

Fig. 35. Basic file relationship for RSPMatch2005b

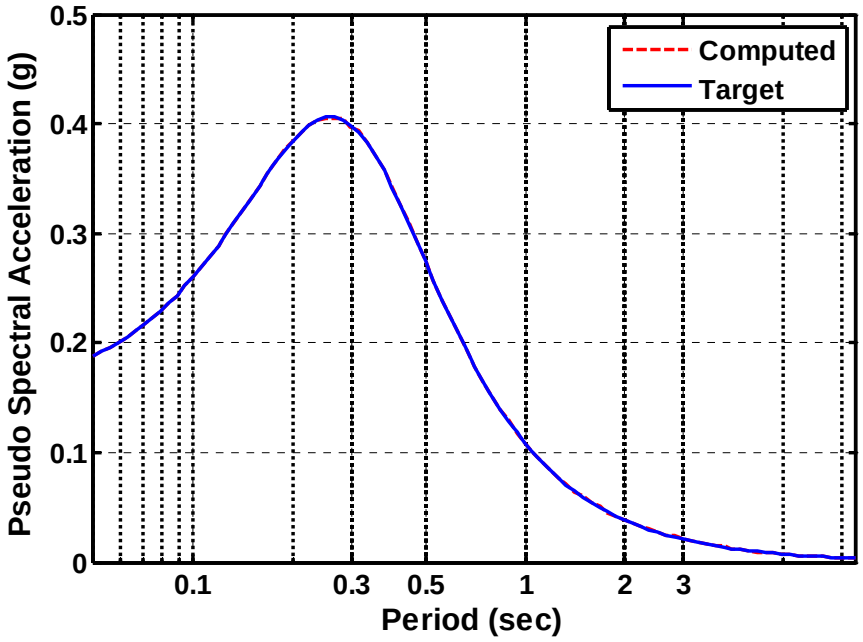

Fig. 36. Response spectrum, Maipú fixed-base, 5% damping

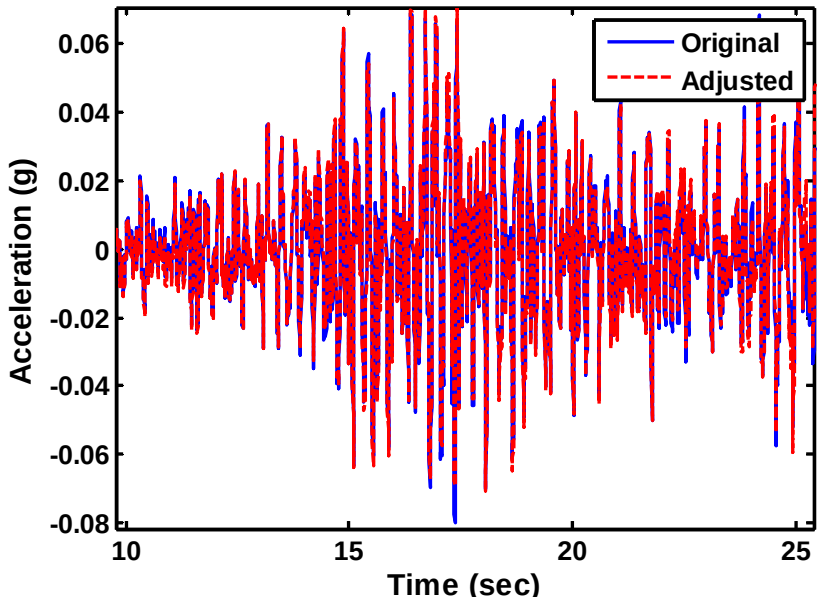

Fig. 37. Time history, Maipú fixed-base, 5% damping

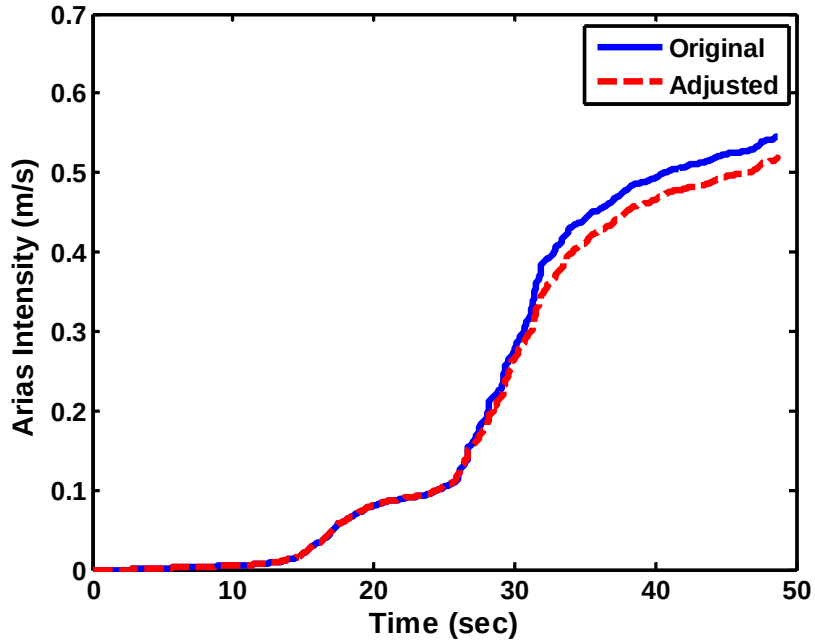

Fig. 38. Arias intensity, Maipú fixed-base, 5% damping

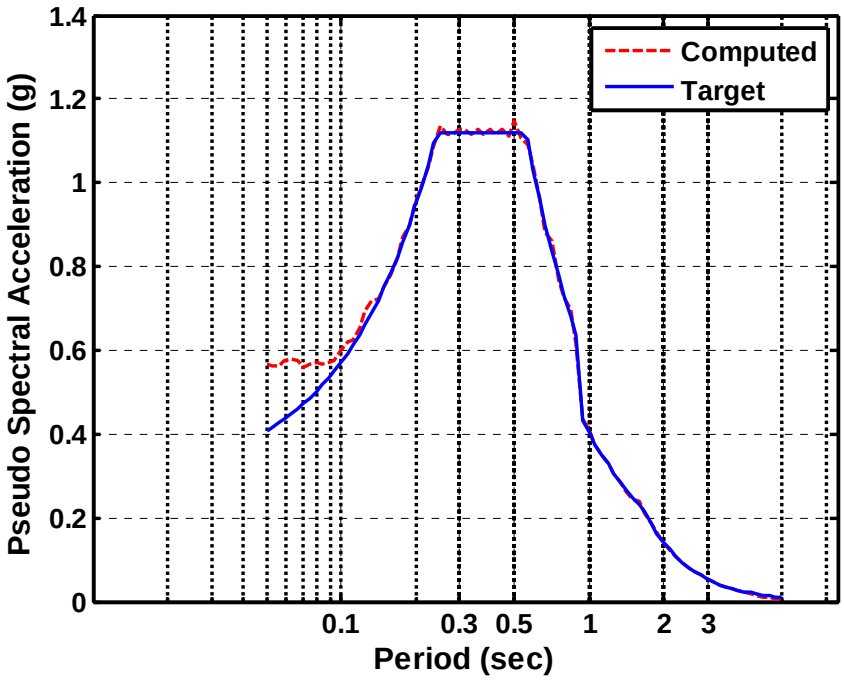

Fig. 39. Response spectrum, Maipú base-isolated, 10% damping, T_{iso} = 1.0 sec

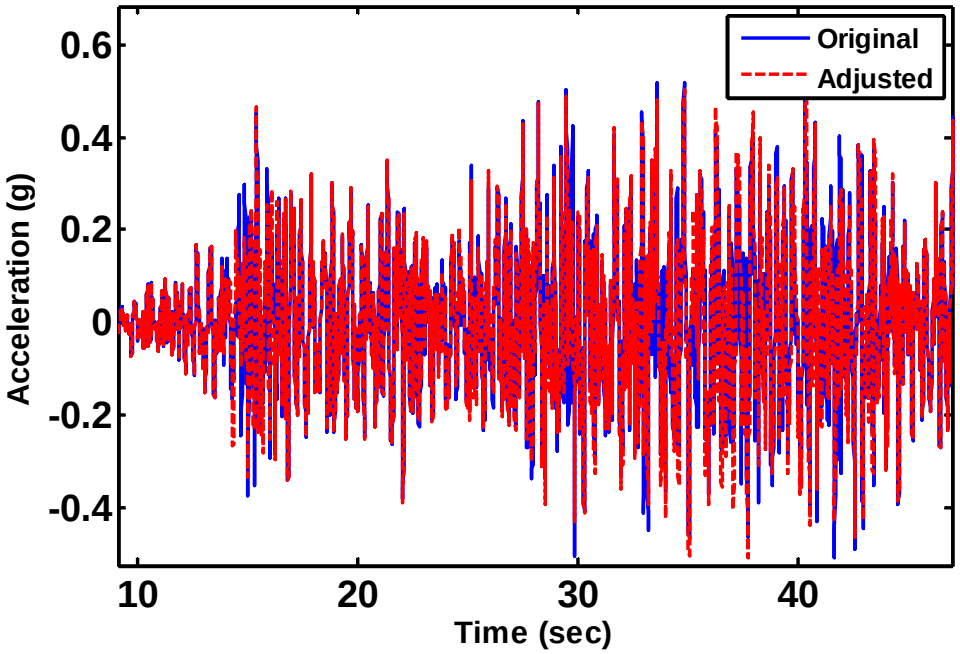

Fig. 40. Time history, Maipú base-isolated, 10% damping, T_{iso} = 1.0 sec

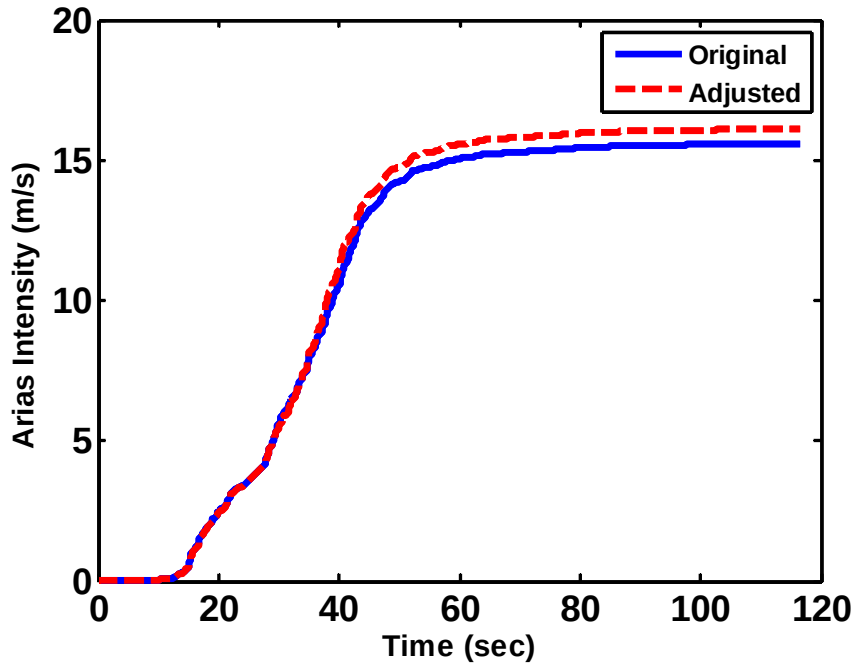

Fig. 41. Arias intensity, Maipú base-isolated, 10% damping, T_{iso} = 1.0 sec

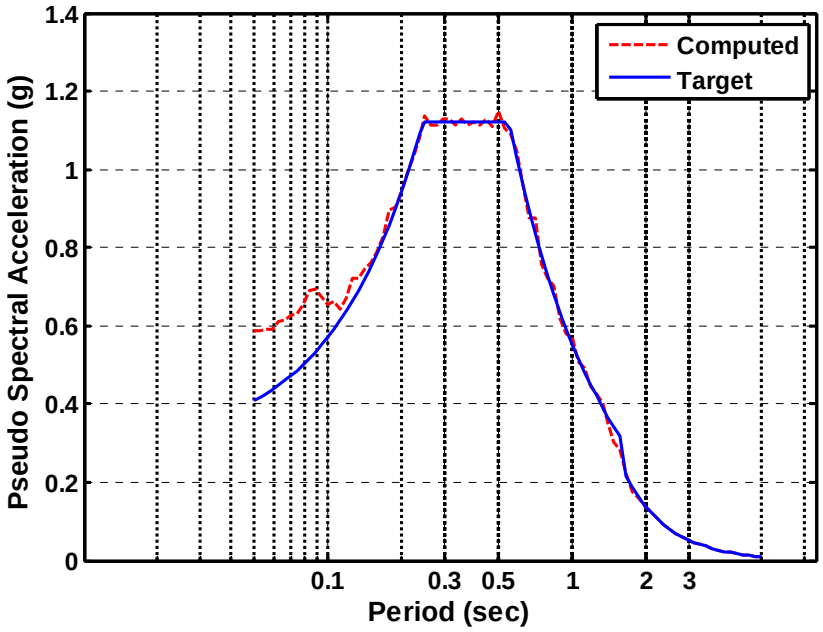

Fig. 42. Response spectrum, Maipú base-isolated, 10% damping, T_{iso} = 2.0 sec

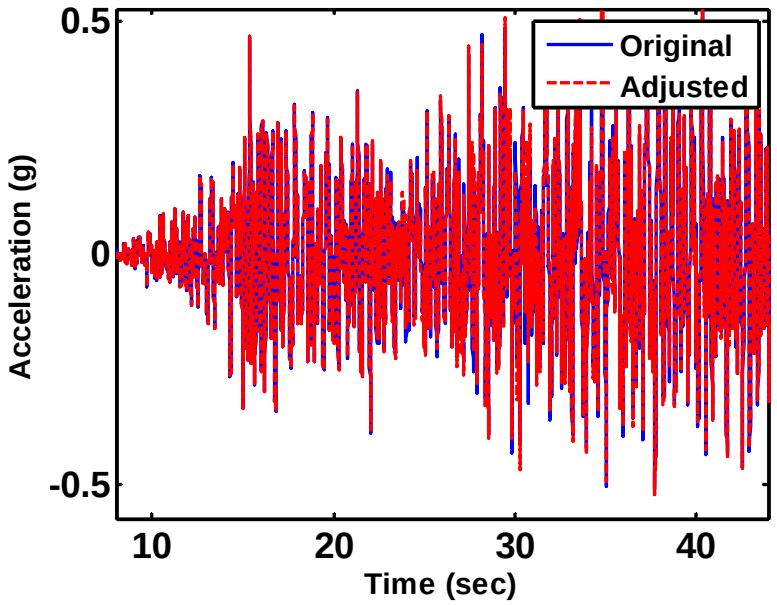

Fig. 43. Time history, Maipú base-isolated, 10% damping, T_{iso} = 2.0 sec

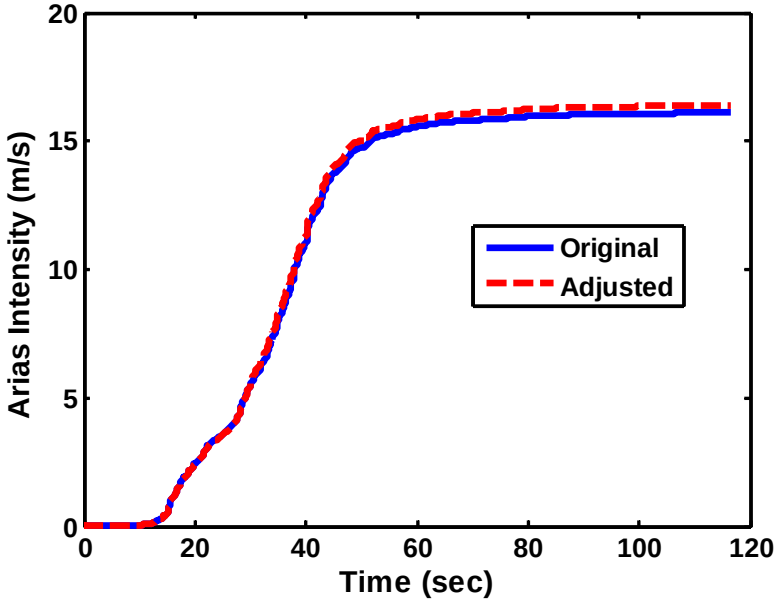

Fig. 44. Arias intensity, Maipú base-isolated, 10% damping, T_{iso} = 2.0 sec

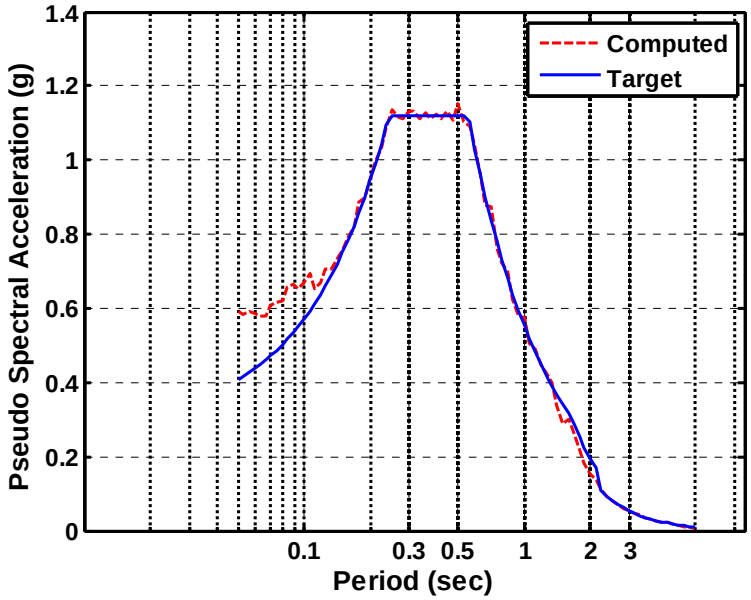

Fig. 45. Response spectrum, Maipú base-isolated, 10% damping, T_{iso} = 2.75 sec

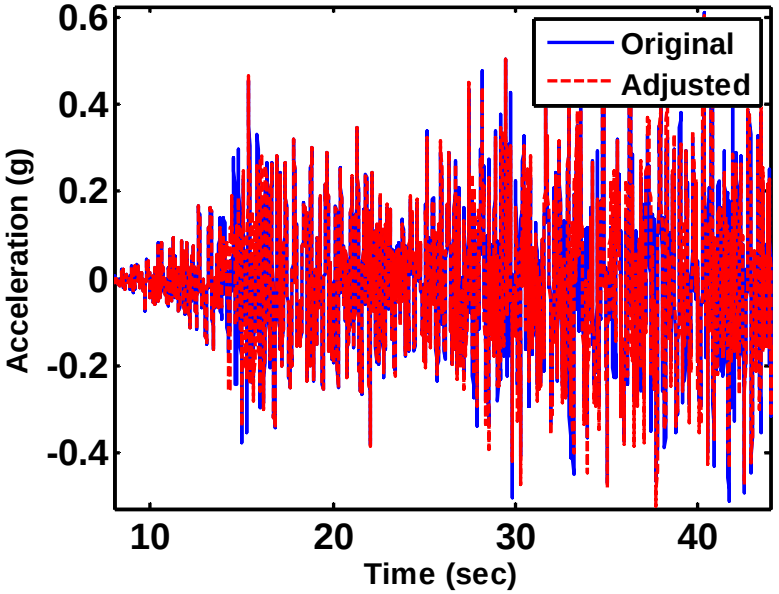

Fig. 46. Time history, Maipú base-isolated, 10% damping, T_{iso} = 2.75 sec

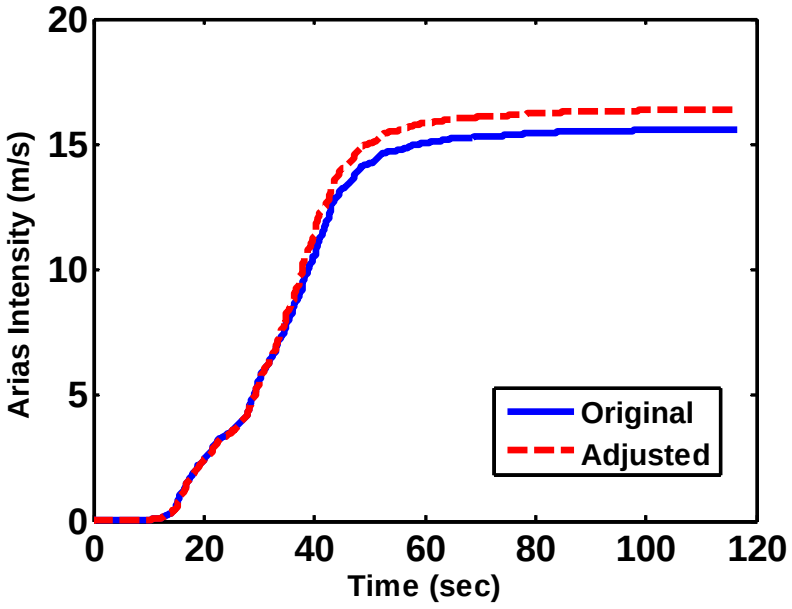

Fig. 47. Arias intensity, Maipú base-isolated, 10% damping, T_{iso} = 2.75 sec

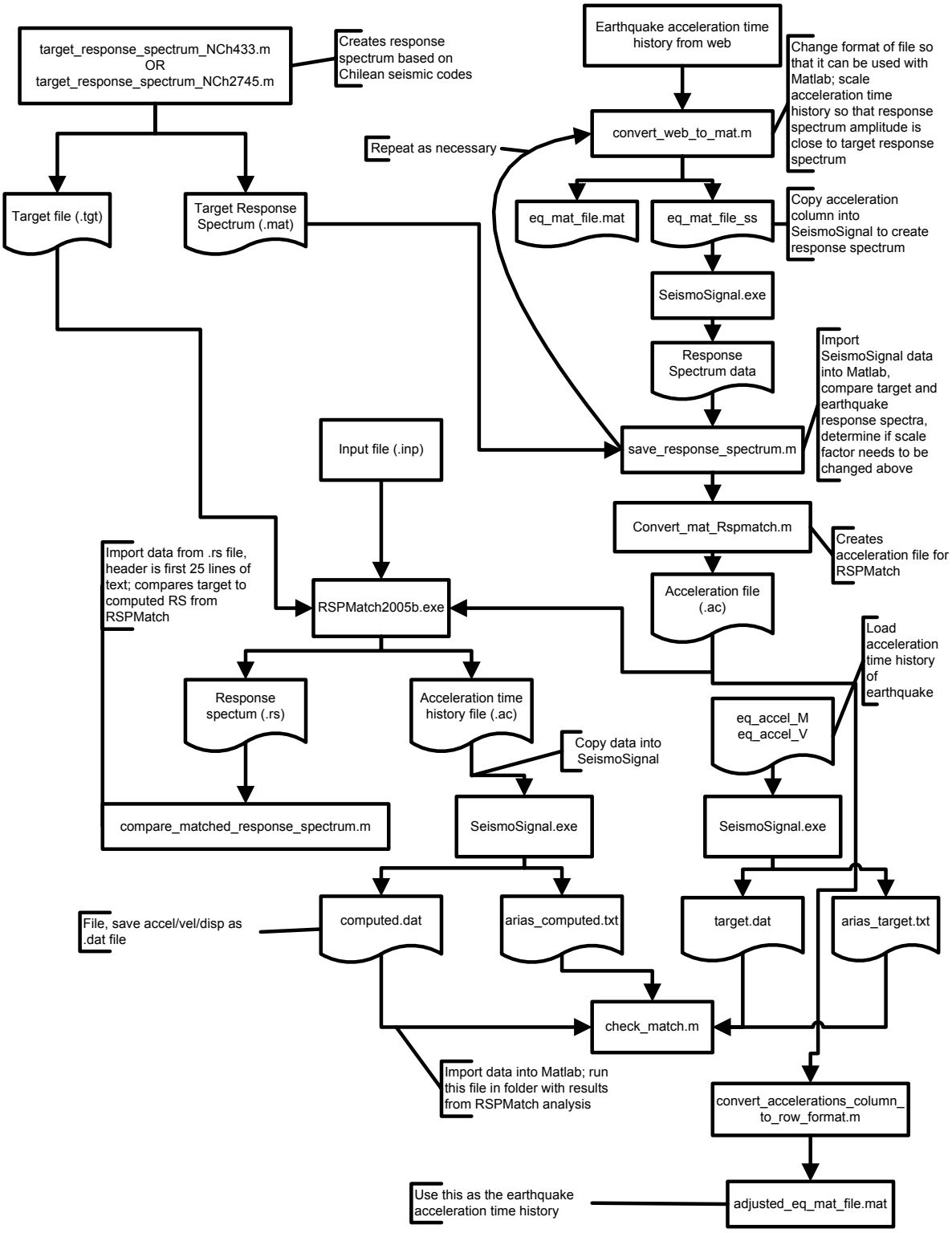

Fig. 48. File relationships used with RSPMatch2005b

4.4. Earthquake Ground Motions Utilized

4.4.1. Device Optimization

The earthquakes generated using RSPMatch2005b to match the design response spectra based on the Chilean seismic codes are used for optimization of each base isolation system and simulation of the fixed-base case. These earthquake ground acceleration time-histories are shown in Figs. 49-52. As previously mentioned, the ground motions are generated using various isolated periods of the structure because optimization of each isolation system can result in a different isolated period. The difference between the acceleration time-histories for the base-isolated structures with different isolated periods is hardly noticeable. The peak ground acceleration (PGA) values range from 0.561 to 0.604 *g* for the acceleration time-histories of the base-isolated structures.

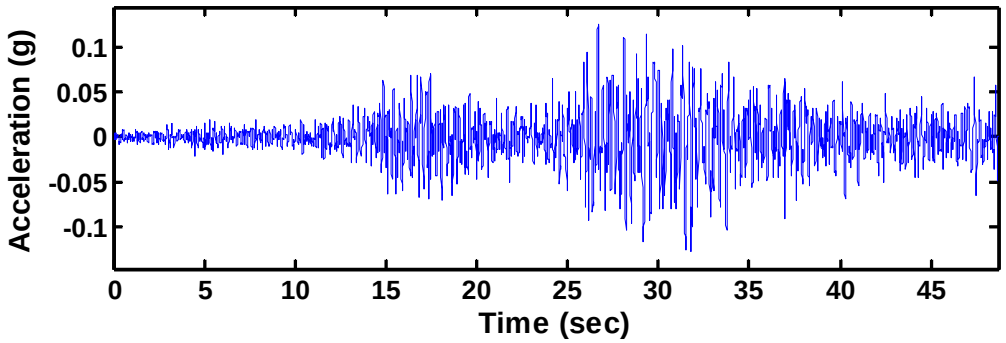

Fig. 49. Acceleration time-history for fixed-base case

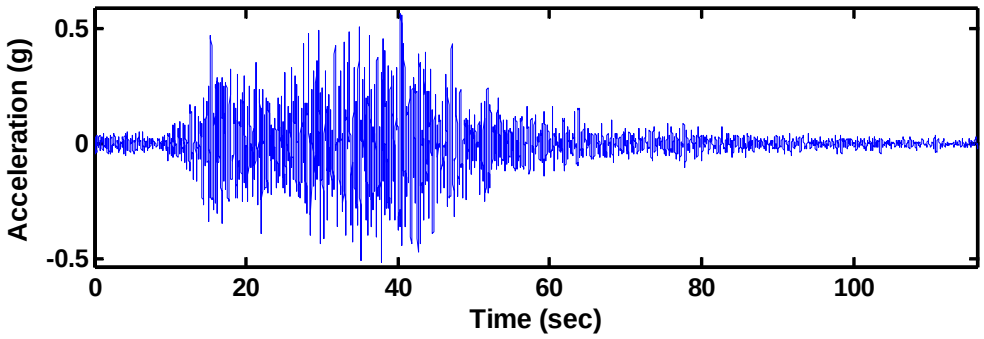

Fig. 50. Acceleration time-history for base-isolated cases with T_{iso} = 1.0 sec

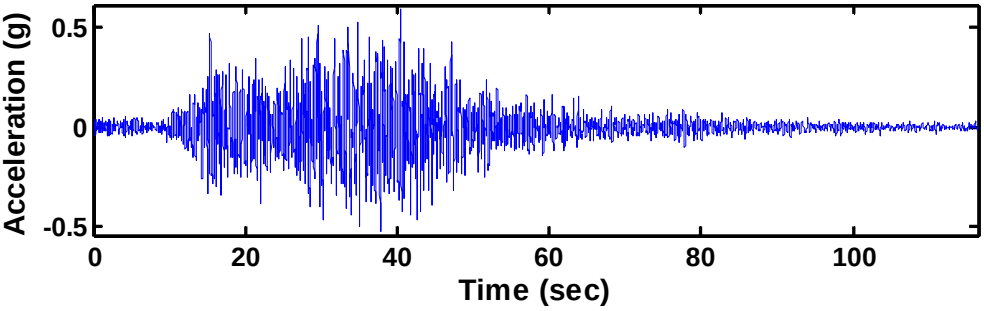

Fig. 51. Acceleration time-history for base-isolated cases with T_{iso} = 2.0 sec

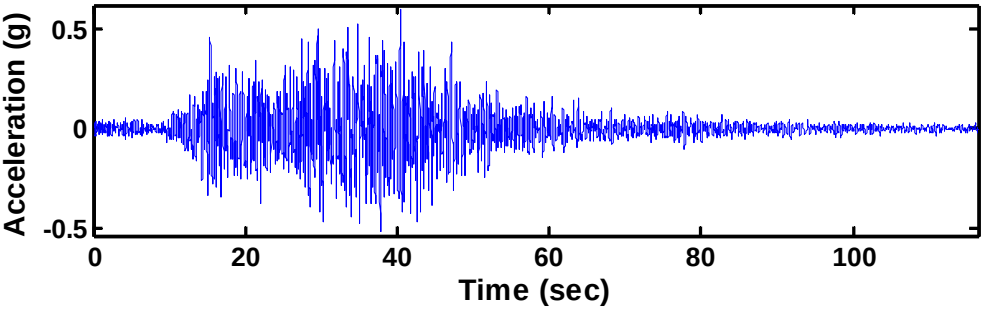

Fig. 52. Acceleration time-history for base-isolated cases with T_{iso} = 2.75 sec

4.4.2. Comparison of Devices

To make a comparison of the performance for each isolation system and a recommendation of the most appropriate device for the case-study structure, a suite of earthquake time-histories is used to test the performance. Each earthquake is applied to the fixed-base and base-isolated structures and their dynamic responses are tabulated according to a set of metrics discussed in subsequent sections. The earthquake time-histories utilized in the analysis are listed in Table 3, along with their PGA value. The earthquake acceleration time-histories are plotted in Figs. 53-59. The RSPMatch earthquake using *NCh2745.Of2003* and T_{iso} = 2 sec is included as Fig. 51. It should be noted that the Mexico City, Kobe, and Northridge earthquake acceleration time-histories are scaled by a factor of one-half.

Fig. 60 shows the response spectrum for each earthquake considered in the analyses. The diversity of the earthquakes selected is evident, as the suite of ground motions includes earthquakes with high acceleration content at short periods and earthquakes with relatively high acceleration content at long periods. The magnitude of the peak pseudo spectral acceleration also varies among the suite of earthquakes. Three of the earthquakes occurred in Chile, one in Mexico, two in California, and one in Japan. The remaining earthquake, the RSPMatch earthquake, was generated using the 1985 Llolleo, Chile, earthquake. There is also diversity among the suite of earthquakes in the distance of the ground motion measurement to the epicenter of the earthquake.

Table 3. Earthquakes Used in Analyses

Earthquake	PGA (g)
1981 Chile LPAN	0.527
1985 Llolleo, Chile N10E	0.653
2005 Tarapacá, Chile EW	0.720
1940 El Centro S00E	0.348
RSPMatch based on *NCh2745*, T_{iso} = 2 sec	0.592
1985 Mexico City SCT N90E	0.083

Table 3. Continued

Earthquake	PGA (g)
1995 Kobe NGA1106 KJM000	0.411
1994 Northridge NGA1085 SCE018	0.414

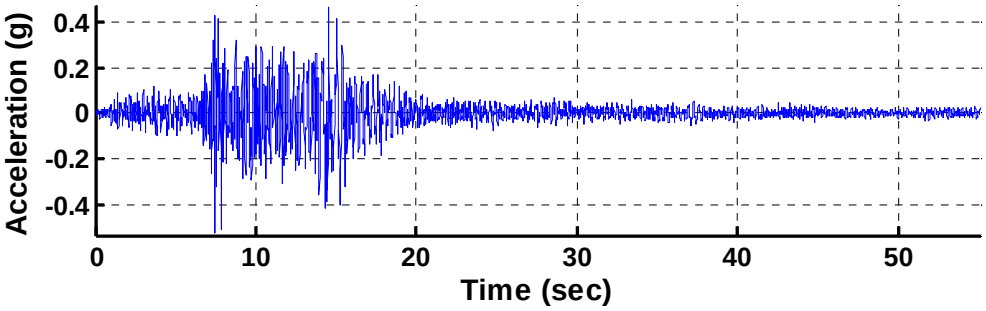

Fig. 53. Acceleration time-history for 1981 Chile earthquake LPAN

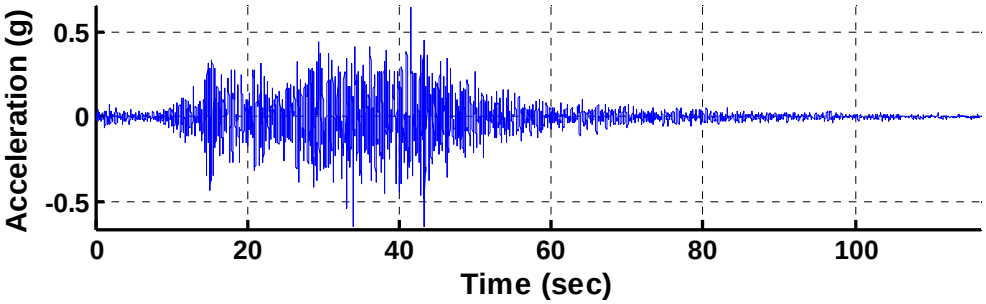

Fig. 54. Acceleration time-history for 1985 Llolleo, Chile, earthquake N10E

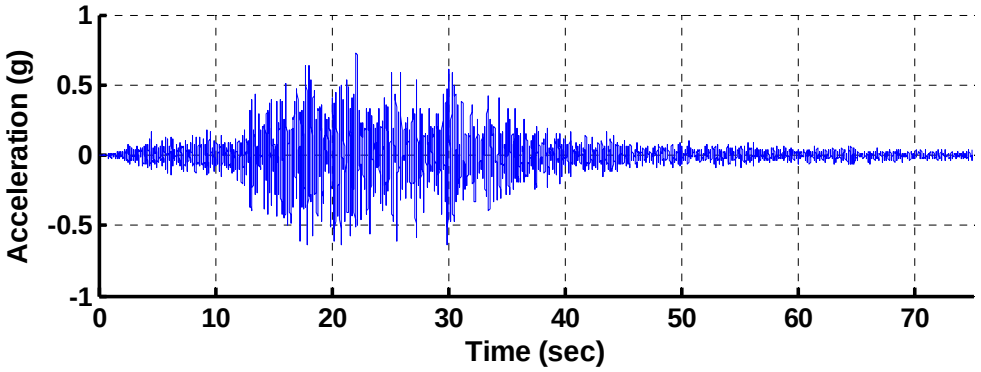

Fig. 55. Acceleration time-history for 2005 Tarapacá, Chile, earthquake EW

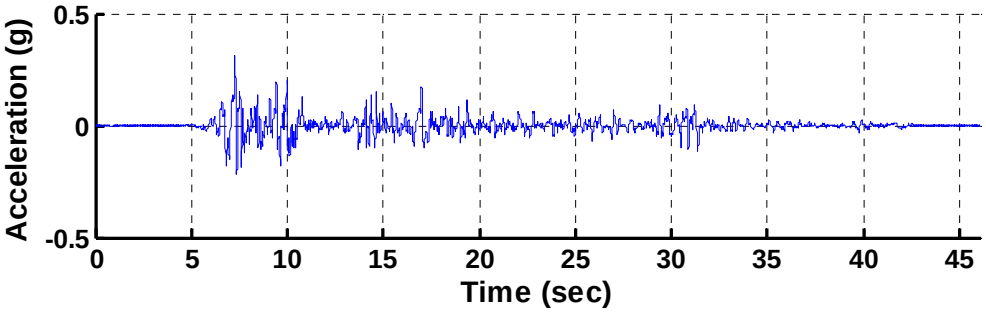

Fig. 56. Acceleration time-history for 1940 El Centro earthquake S00E

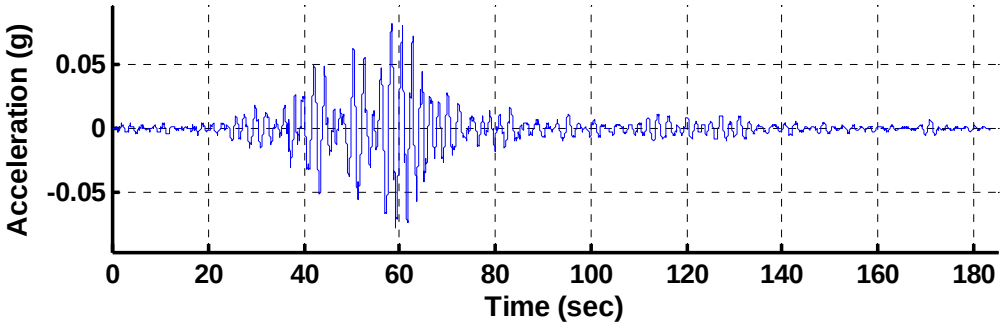

Fig. 57. Acceleration time-history for scaled 1985 Mexico City earthquake SCT N90E

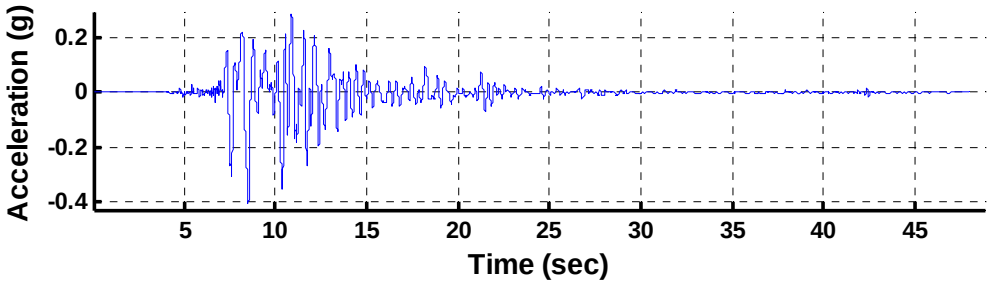

Fig. 58. Acceleration time-history for scaled 1995 Kobe earthquake NGA1106 KJM000

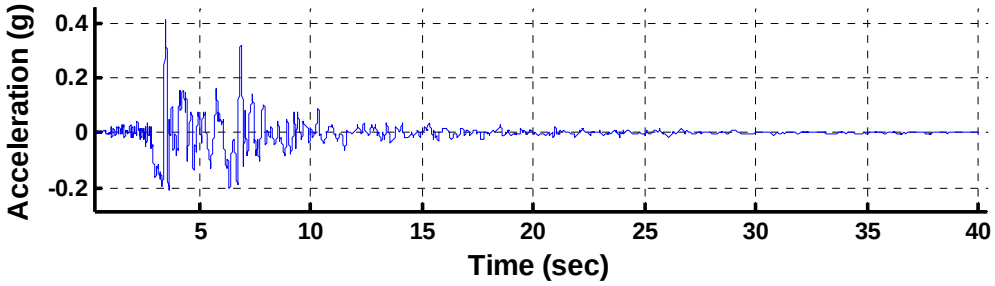

Fig. 59. Acceleration time-history for scaled 1994 Northridge earthquake NGA1085 SCE018

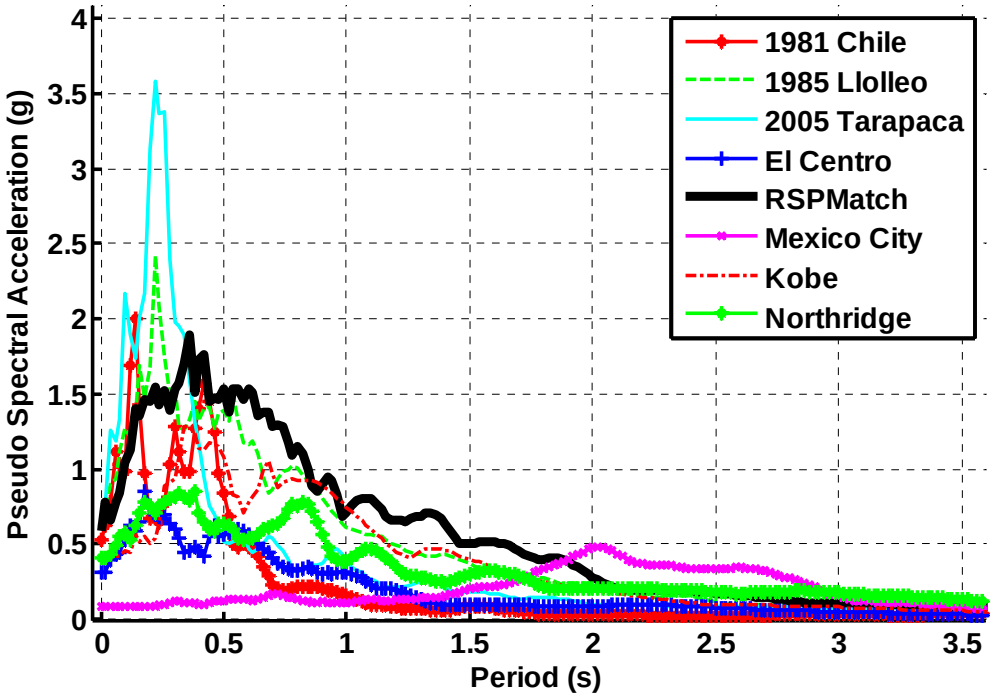

Fig. 60. Response spectrum for each earthquake

4.4.3. Near-Fault Motions

While early seismic isolation research was based on the fact that most strong ground motion records through the 1970s had very low spectral accelerations in the long period range, records collected from lakebed sites in the 1985 Mexico City earthquake raised the issue of possible resonance (Jangid and Kelly 2001). In addition, since the 1970s, a number of earthquake records from near-source sites have been collected. According to Jangid and Kelly (2001), near-fault ground motions have pulse-type displacements, contain significant energy at high frequencies, and have real and pseudo-velocity spectra that are quite different. In this study, the Northridge and Kobe earthquakes meet these requirements. Records collected from the Northridge and Kobe earthquakes have been identified as near-fault earthquakes by other researchers (Chopra and Chintanapakdee 2001). Although the 1985 Mexico City earthquake is not classified as a near-fault earthquake, the ground motion is characterized by containing an

extremely high amount of energy. From Fig. 60, it is evident that the scaled Mexico City earthquake has high spectral accelerations at long periods. Figs. 61-70 show the pseudo-velocity and velocity spectra for the 1985 Llolleo, Chile, RSPMatch, and scaled Mexico City, Kobe, and Northridge earthquakes. The significant differences in the pseudo-velocity and velocity spectra for the Kobe and Northridge earthquakes are evident. The high velocities of the Northridge earthquake at long periods are also evident in Fig. 70.

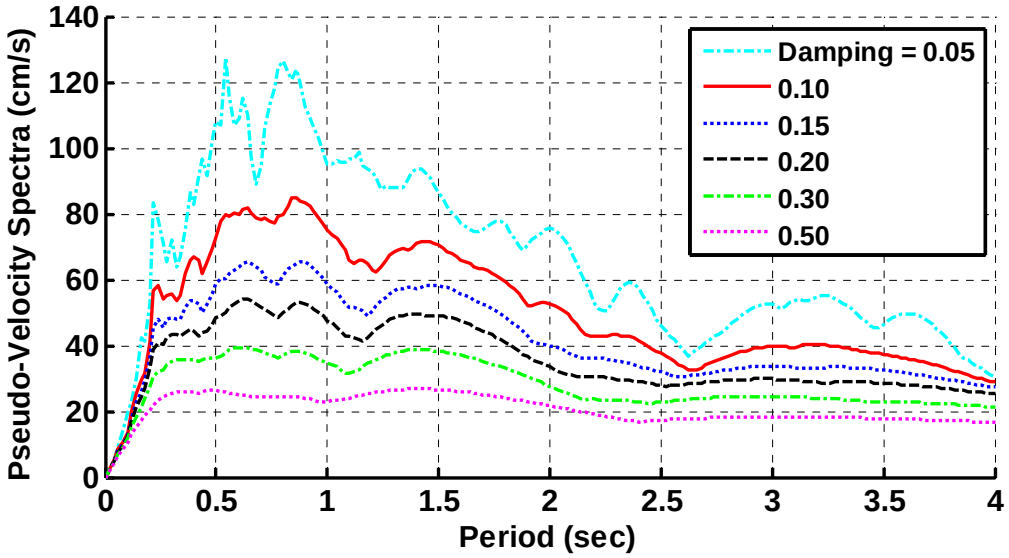

Fig. 61. Pseudo-velocity spectrum for 1985 Llolleo, Chile, earthquake

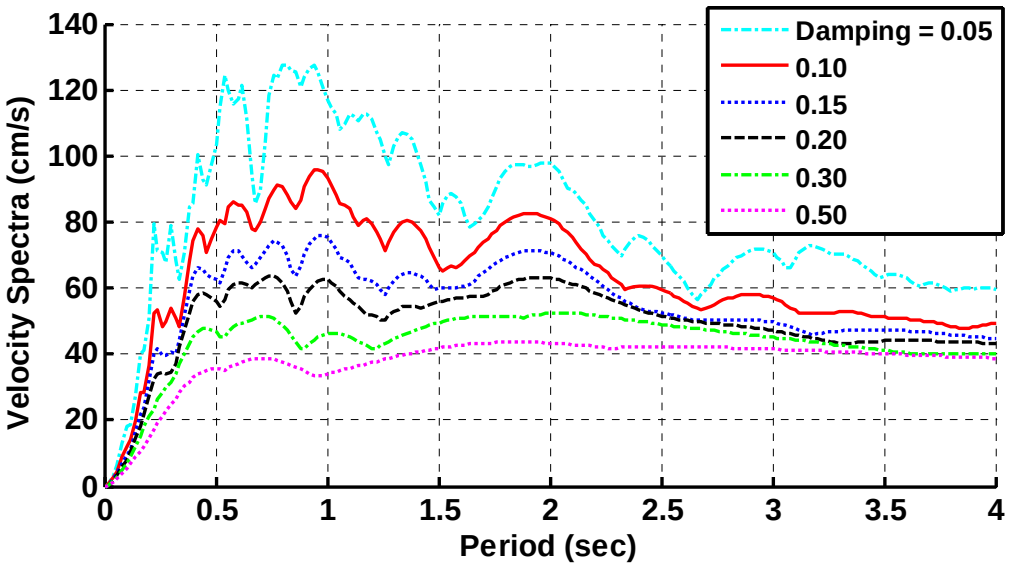

Fig. 62. Velocity spectrum for 1985 Llolleo, Chile, earthquake

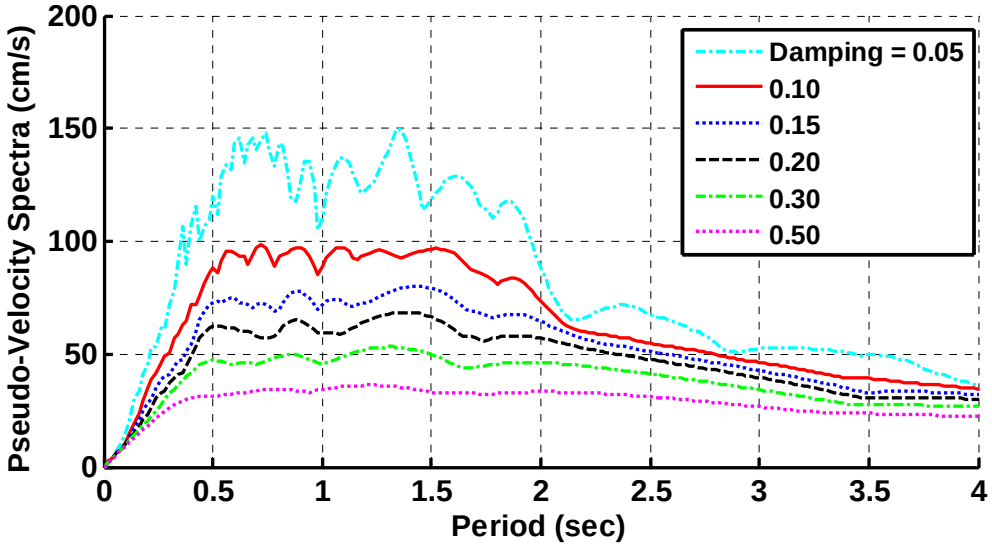

Fig. 63. Pseudo-velocity spectrum for RSPMatch earthquake

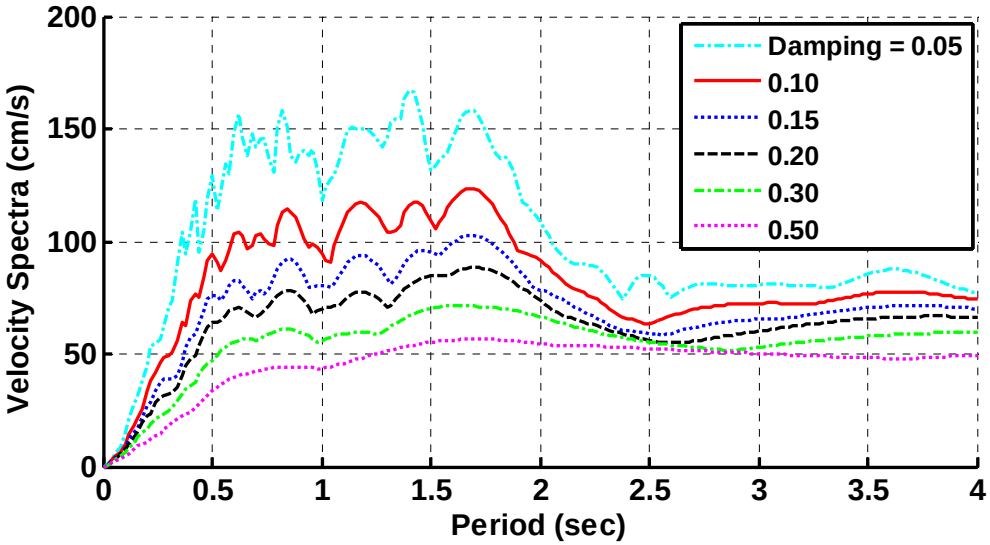

Fig. 64. Velocity spectrum for RSPMatch earthquake

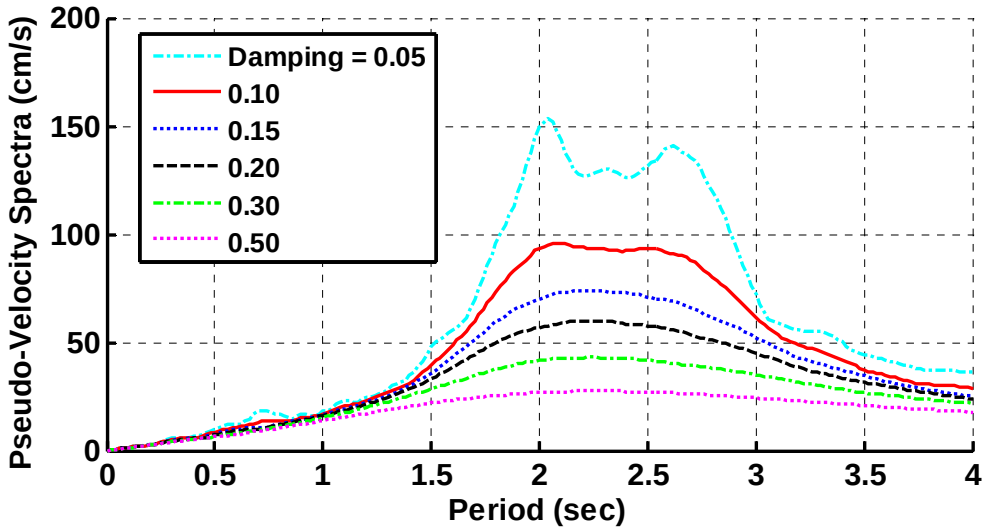

Fig. 65. Pseudo-velocity spectrum for 1985 Mexico City earthquake

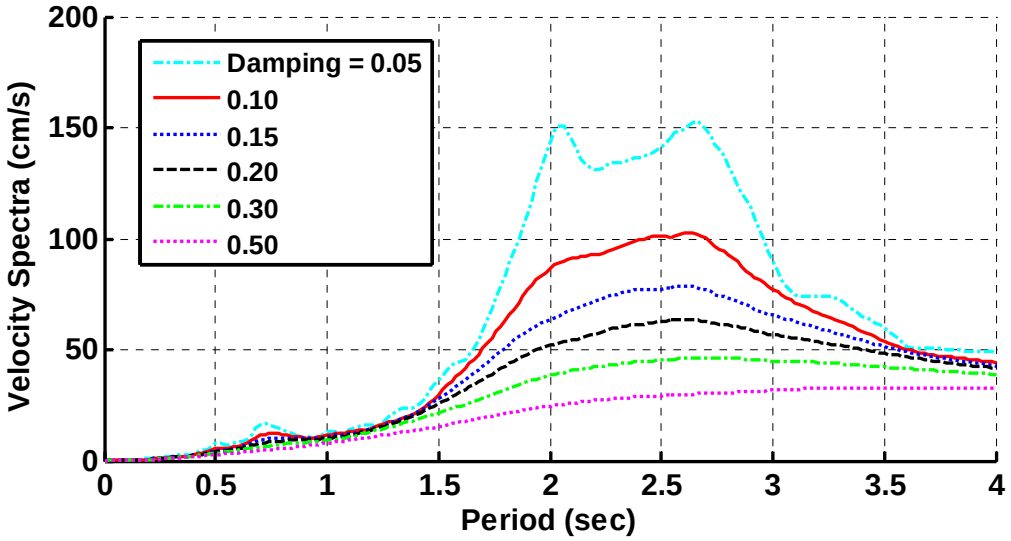

Fig. 66. Velocity spectrum for 1985 Mexico City earthquake

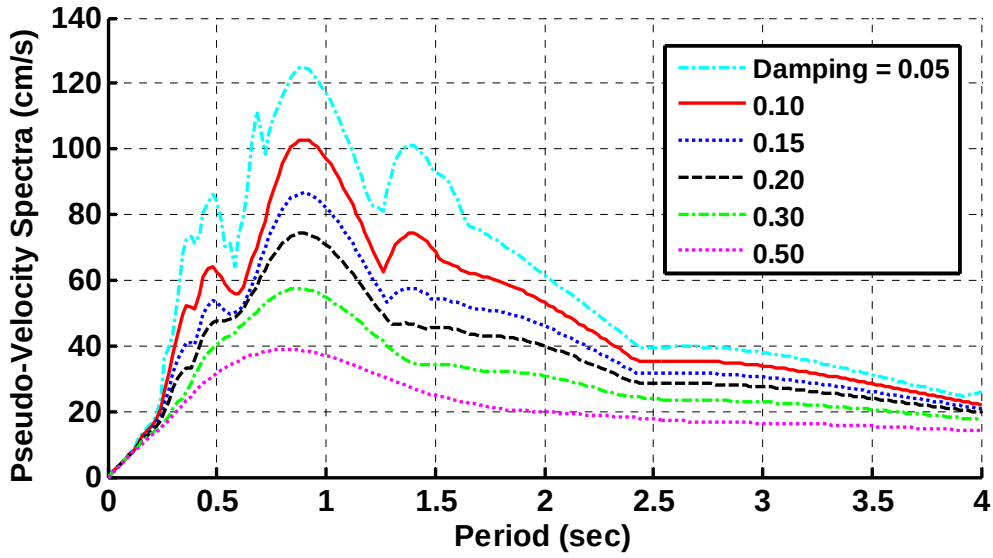

Fig. 67. Pseudo-velocity spectrum for Kobe earthquake

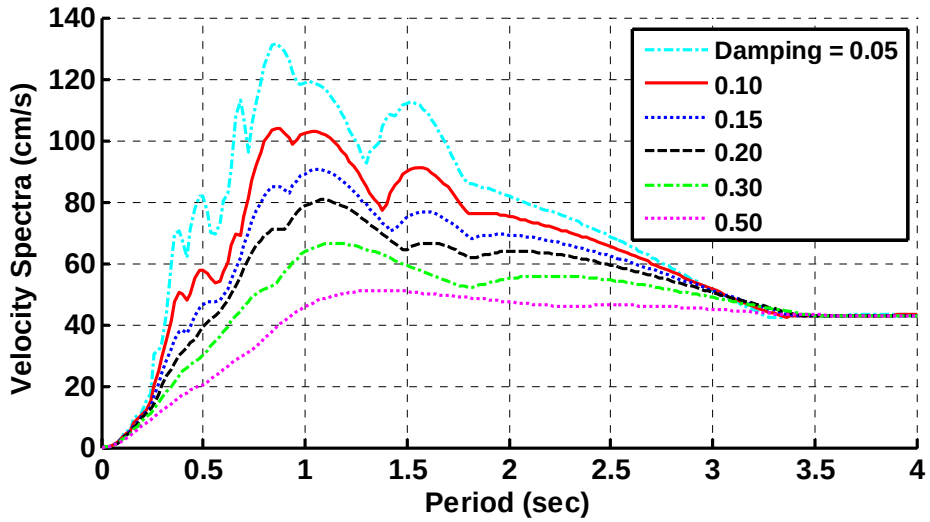

Fig. 68. Velocity spectrum for Kobe earthquake

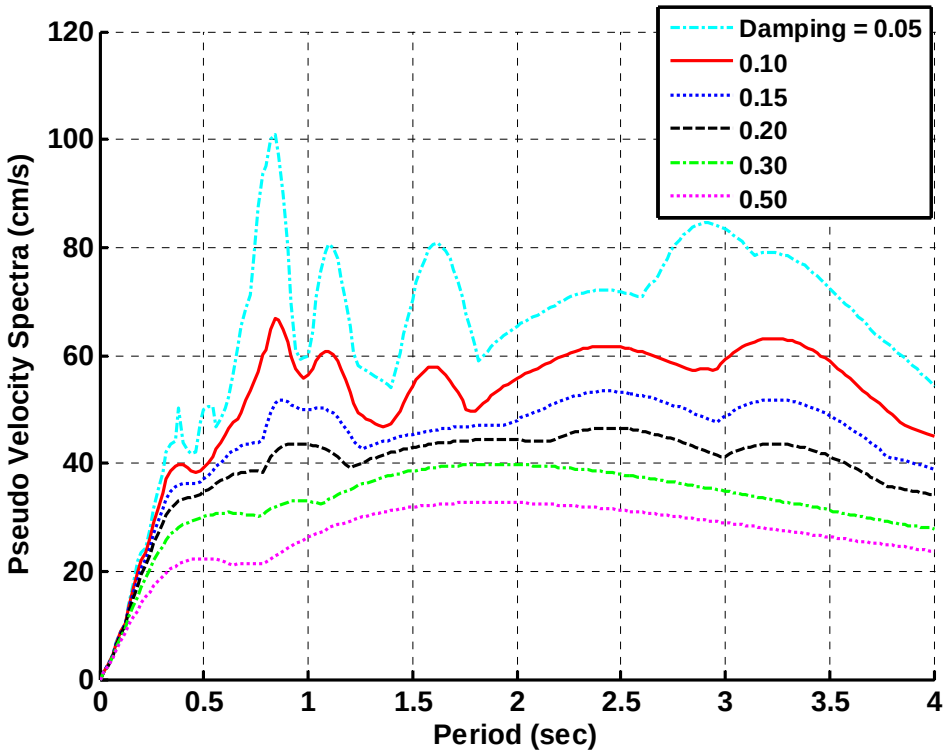

Fig. 69. Pseudo-velocity spectrum for Northridge earthquake

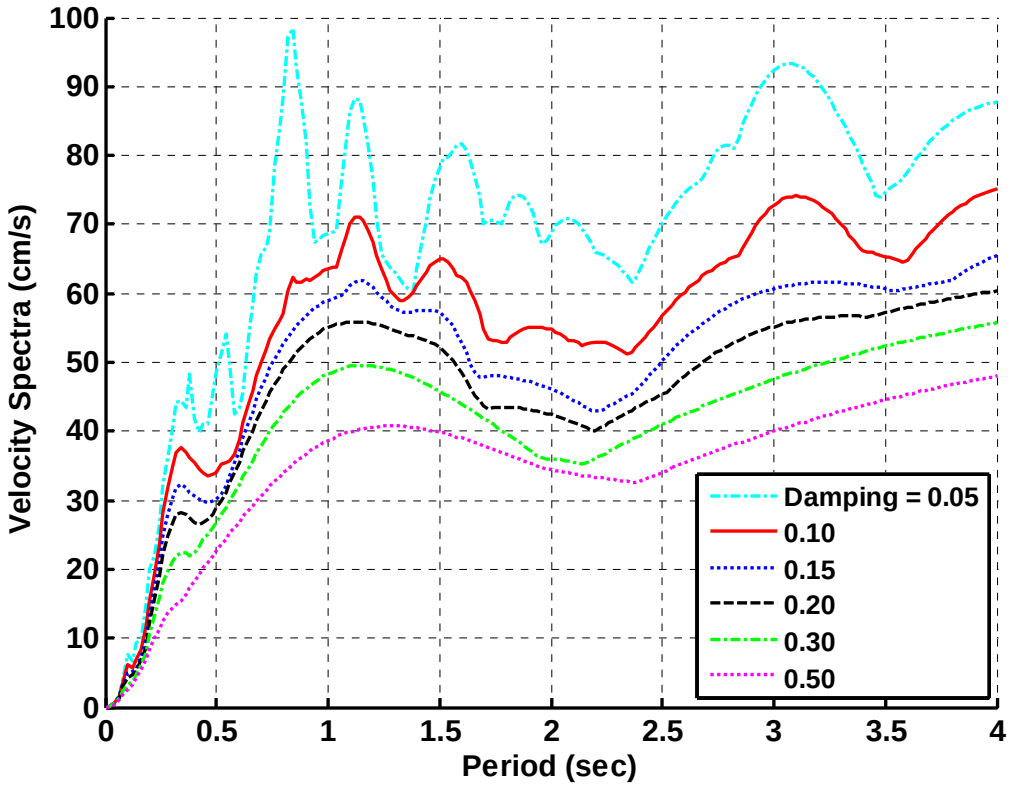

Fig. 70. Velocity spectrum for Northridge earthquake

5. NUMERICAL MODEL OF EACH DEVICE

5.1. General

Descriptions of the numerical model of the FPS, HDRB, hybrid HDRB+SMA systems, and PPP isolation systems are included in this section. The FPS and PPP devices are numerically simulated in MATLAB using S-functions, while the other devices are modeled using FISes. S-functions are utilized to model the FPS and PPP devices due to the availability of analytical formulations to model nonlinear behavior of the devices. Since the other devices are modeled using experimental data, the use of FISes based on the experimental data is more appropriate.

5.2. FPS Model

The effect of implementing FPS isolators to ameliorate response of the structure is investigated first. An FPS is a mechanical device in which lateral motion of the structure is resisted by a friction force at the sliding interface and a restoring force generated when the structure moves up a curved bearing surface (see Fig. 9).

Two expressions, one linear and one nonlinear, have been developed to represent the external force acting on the FPS. Both expressions are based on the force diagram shown in Fig. 71 (Kim et al. 2006), where F is the external force acting on the FPS, W is the weight of the mass supported by the FPS bearing, R is the radius of the spherical bearing surface, θ is the angle of rotation, F_f is the friction force, S is the normal force acting on the FPS at the interface with the articulated slider, u is the horizontal component of displacement, and v is the vertical component of displacement.

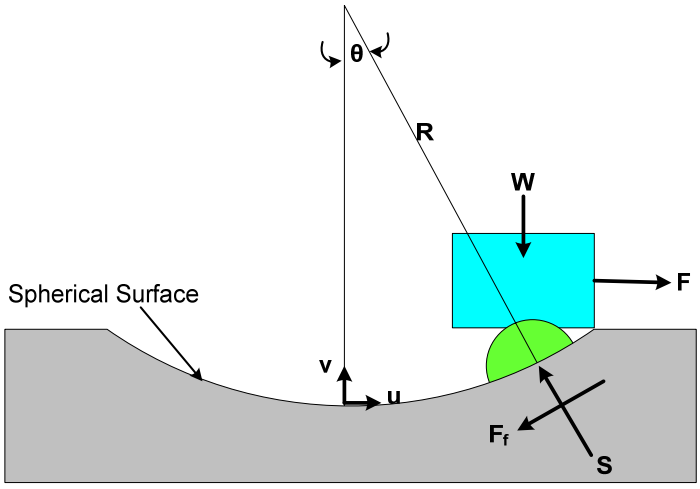

Fig. 71. FPS force diagram

The linear equation for the external force acting on the FPS is reported by Tsopelas et al. (1996) and is included as Eq. (13).

$$F = \frac{W}{R\cos\theta}u + \frac{F_f}{\cos\theta} \tag{13}$$

where the terms are as previously defined. For small displacements, i.e. peak displacements less than $0.2R$ (Tsopelas et al. 1996), the equation can be simplified to the form (Kim et al. 2006):

$$F = \frac{W}{R}u + \text{sgn}(\dot{u})W\mu \tag{14}$$

where $\dot{u}$ is the horizontal velocity, μ is the coefficient of friction, and the remaining parameters are as previously defined. The expression *sgn* is the signum function, which indicates a positive or negative sign of its argument.

The nonlinear expression developed by Kim et al. (2006) for the horizontal force acting on an FPS as a function of horizontal displacement is included as Eq. (15). This expression can be applied for both small and large displacements.

$$F = W\left[\frac{u + \text{sgn}(\dot{u})\mu\sqrt{R^2 - u^2}}{\sqrt{R^2 - u^2} - \text{sgn}(\dot{u})\mu u}\right] \tag{15}$$

where the parameters are as previously defined. This expression is only valid for $R \geq u$, and for an FPS with a spherical surface. Eq. (15) is programmed into the S-function formulation for the FPS device so that the force calculations are accurate for both small and large horizontal displacements. In order to use Eq. (15) in numerical simulations with an S-function, the instantaneous inputs u and $\dot{u}$ are required and the output of the function is the predicted restoring force F of the FPS.

It is also important to monitor the uplift caused by an FPS. Using small displacement assumptions, the vertical displacement of the structure due to motion by the FPS is:

$$\delta_v = R\left[1 - \cos\left(\sin^{-1}\frac{u}{R}\right)\right] \tag{16}$$

where u and R are as defined previously (Naeim and Kelly 1999). It can be seen that the uplift of the system does not depend on the coefficient of friction of the sliding surface, but rather it depends solely on the radius of curvature of the surface.

5.3. HDRB Model

There have been relatively few analytical models of HDRBs that can be used to perform time-history analyses of isolated structures. One analytical model, proposed by Pan and Yang (1996), uses two equations with a total of 11 parameters (b_1 to b_{11}) to represent the restoring force and the damping force of a high damping elastomeric isolation bearing. These parameters are determined from cyclic loading tests on the elastomeric bearing. The restoring force calculation yields a skeleton curve of the shear force-displacement loop [Eq. (17)], while the damping force calculation results in the proper hysteretic loop area [Eq. (18)]. Superposition of the two forces results in the total shear force in the bearing [Eq. (19)]. It should be noted that both Eqs. (17) and (18) are independent of the loading history of the bearing, but are dependent on the displacement $x(t)$ and velocity $\dot{x}(t)$ at time t. Additional mathematical models that describe the behavior of an HDRB have been proposed by Kikuchi and Aiken (1997) and Hwang and Ku (1997), but are not used in this study.

$$F_1\left(x(t),\dot{x}(t)\right)=\left[b_1+b_2x^2(t)+b_3x^4(t)+\frac{b_4}{\cosh^2\left(b_5\dot{x}(t)\right)}+\frac{b_6}{\cosh\left(b_7\dot{x}(t)\right)\cosh\left(b_8x(t)\right)}\right]x(t) \tag{17}$$

$$F_2\left(x(t),\dot{x}(t)\right)=\left[\frac{b_9+b_{10}x^2(t)}{\sqrt{b_{11}^2+\dot{x}^2(t)}}\right]\dot{x}(t) \tag{18}$$

$$F\left(x(t),\dot{x}(t)\right)=F_1\left(x(t),\dot{x}(t)\right)+F_2\left(x(t),\dot{x}(t)\right) \tag{19}$$

Hwang et al. (2002) modified the hysteretic model for elastomeric bearings that was originally proposed by Pan and Yang (1996). Modifications made by Hwang et al. (2002) take into account the Mullins effect and the scragging effect of an HDRB, which are dependent on the loading history of the bearing. The Mullins effect is the stress softening that occurs between cycles (Mullins 1987). Scragging is a deformation-dependent phenomenon that restarts every time the isolator is taken to a new larger deformation (De la Llera et al. 2004). In this phenomenon, the area of the force-displacement changes with each cycle. The calculation is still separated into restoring force and damping force components, but it uses constants a_1 to a_{10}. Again, the constants are determined from experimental cyclical testing of a particular rubber compound, and they are functions of the rubber compound, Mullins effect, scragging, frequency, temperature, and axial load (Hwang et al. 2002). The formulation is included as Eqs. (20)-(22), where Eq. (22) is the same as Eq. (19) from Pan and Yang's model (1996); that is, the two force components are superimposed. The variables $x(t)$ and $\dot{x}(t)$ are as previously defined. De la Llera et al. (2004) apply the model proposed by Hwang et al. (2002) to the behavior of a 60 cm diameter LRB.

$$F_1\left(x(t),\dot{x}(t)\right)=K\left(x(t),\dot{x}(t)\right)x(t)$$

$$=\left[a_1+a_2x^2(t)+a_3x^4(t)+\frac{a_4e^{a_9\int_0^t F\left(x(t),\dot{x}(t)\right)dx(t)}}{\cosh^2\left(a_5\dot{x}(t)\right)}\right]x(t) \tag{20}$$

$$F_2\left(x(t),\dot{x}(t)\right) = C\left(x(t),\dot{x}(t)\right)\dot{x}(t)$$
$$= \left[\frac{a_6 + a_7 x^2(t)}{\sqrt{a_8^2 + \dot{x}^2(t)}}\right]\left(1 + e^{a_{10}\int_0^t F\left(x(t),\dot{x}(t)\right)dx(t)}\right)\dot{x}(t) \tag{21}$$

$$F\left(x(t),\dot{x}(t)\right) = F_1\left(x(t),\dot{x}(t)\right) + F_2\left(x(t),\dot{x}(t)\right) \tag{22}$$

In this study, the analytical model proposed by Pan and Yang (1996), namely Eqs. (17)-(19), is utilized to model the HDRBs due to the availability of experimental data from previous research using this model. The parameters used to model the HDRBs are based on laboratory tests discussed by Jankowski (2004) and Jankowski et al. (1998).

5.4. Hybrid HDRB+SMA Model

5.4.1. General

The HDRB device, the model of which is discussed in Section 5.3, is utilized as a component of the hybrid HDRB+SMA systems. The other component of the hybrid systems is SMA wires. Although the use of SMA wires could increase the energy dissipation of the hybrid system over that of the HDRB system, the primary role of the SMA wires in the hybrid system is to re-center the structure after the excitation from an earthquake ceases. NiTi is the SMA material that is considered in this study because of the alloy's ability to undergo large strains, and due to the availability of experimental data from testing.

For numerical simulation of the base-isolated structure that is equipped with one of the two hybrid HDRB+SMA devices, the SMA wires are modeled using two different configurations. One configuration of the wires is that shown in Fig. 12 of Section 2. Using this configuration, each HDRB is not connected to adjacent HDRBs. Another configuration considered is to connect the SMA wires diagonally from the bottom of one HDRB to the top of the adjacent HDRB (see Fig. 13 of Section 2 and Fig. 72 below). The wires do not extend the entire length of the diagonal, and are assumed to be rigidly connected to a link element that connects them to each HDRB.

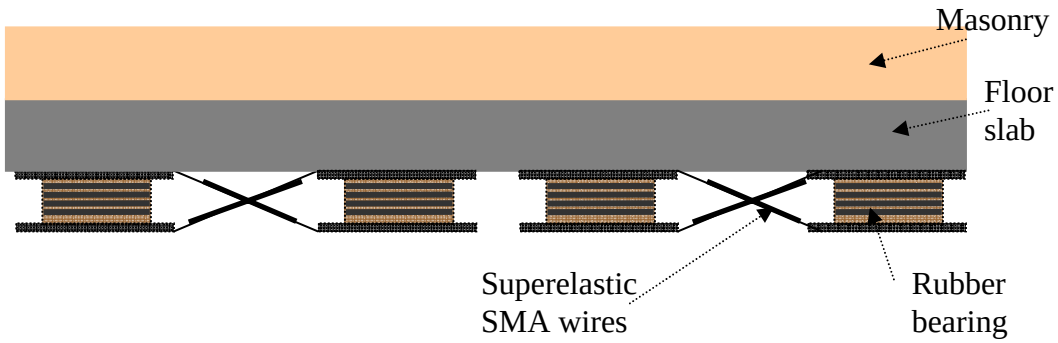

Fig. 72. Hybrid HDRB+SMA2 elevation view

5.4.2. FIS Training and Validation

Development of the SMA FIS is based on experimental testing of 1 mm diameter NiTi wire in tension at Texas A&M University. The wire was tested at various frequencies with a sinusoidal displacement that imposed up to 7% strain and a strain rate of 0.6 1/sec on the wire. The data that were collected from tensile tests are modified to represent the behavior of an SMA cross-brace in which only one of the two sets of diagonal wires is in tension during motion. This modification is made by duplicating the set of data and reversing the sign of the duplicated data to represent the second set of diagonal wires in the cross-brace (Shook et al. 2008).

The data used for training of the SMA FIS, representing an SMA cross-brace with one wire in each diagonal, is shown in Fig. 73. The SMA FIS uses strain and strain rate as inputs to calculate the stress in the SMA. Shook et al. (2008) explain that although previous researchers used prestress and ambient temperature in addition to

strain and strain rate as inputs in neuro-fuzzy modeling of SMA wires, these effects are not included as inputs to the FIS here because the SMA wires are not prestressed and because the austenite finish temperature of the SMA wires is within a range sufficient for civil engineering applications.

The FIS is created using three membership functions for the strain input and four for the strain rate input, 200 epochs, a step size of 0.003, a step size increase rate of 1.2, and a step size decrease rate of 0.8. The membership functions are of type 'gbellmf,' which indicates the use of generalized bell-shaped membership functions. Plots of the initial and final membership functions for each input variable are shown in Fig. 74. The variation of step size throughout the total number of epochs used for training is shown in Fig. 75. The FIS resulting from the training process is included in Fig. 76. The training plots are included as Figs. 77 and 78, where Fig. 78 is a zoomed-in view of the last plot of Fig. 73.

Using the FIS developed for a NiTi cross-brace comprised of one wire in each diagonal, the result of a cross-brace comprised of many wires is calculated by multiplying the output from the FIS representing a one-wire cross-brace by an integer number representing the total number of wires in the brace that are in tension at any given time.

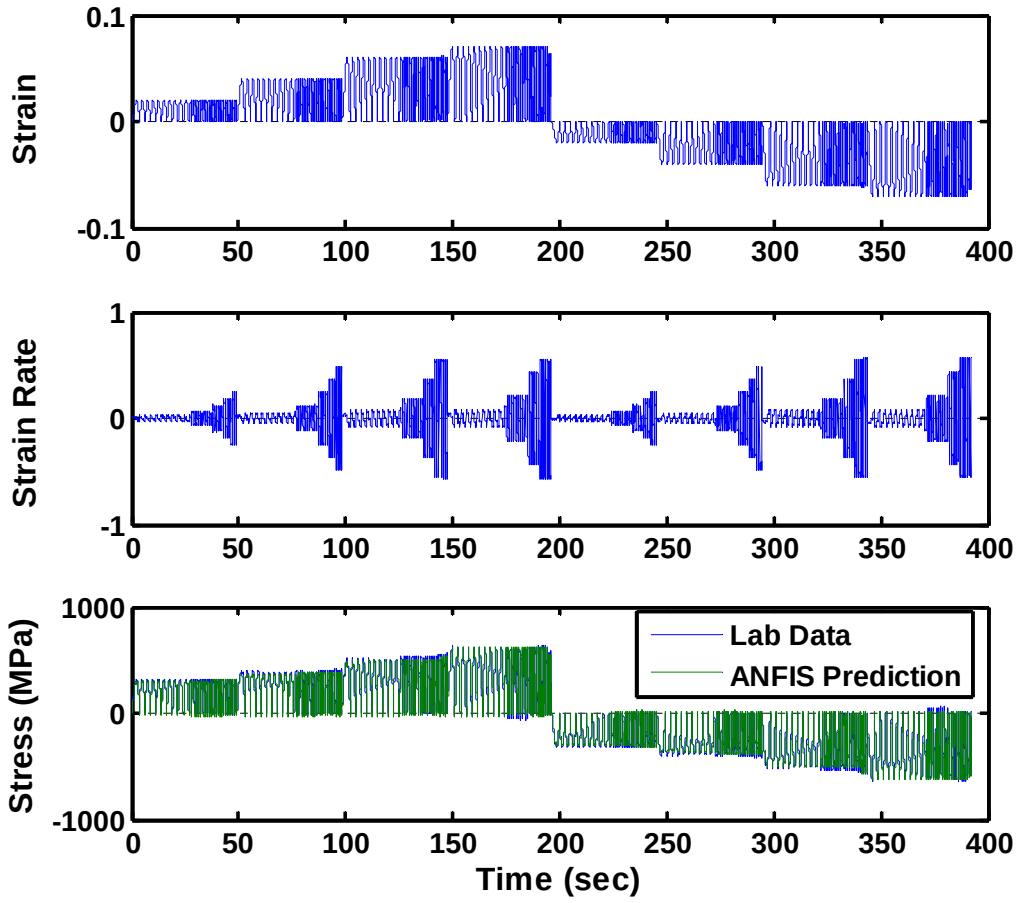

Fig. 73. NiTi SMA training data

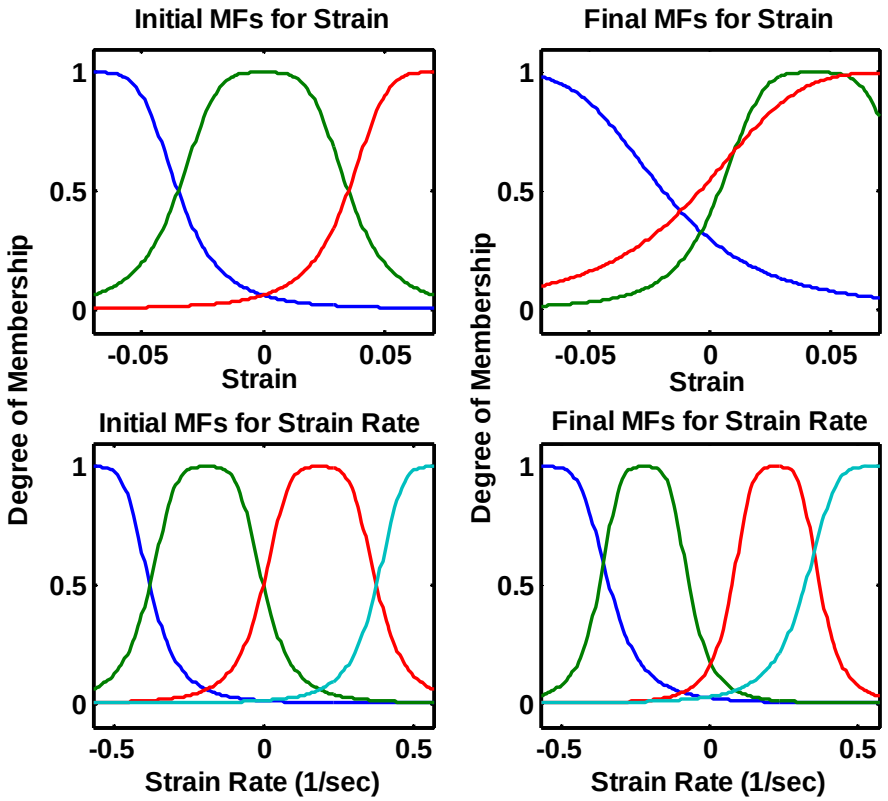

Fig. 74. Membership functions before and after training for NiTi SMA FIS

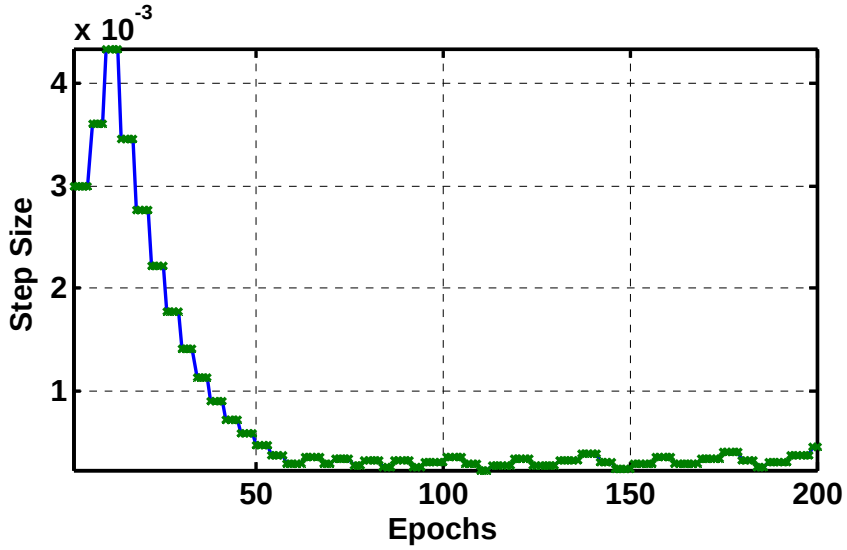

Fig. 75. Step size alterations throughout training for NiTi SMA FIS

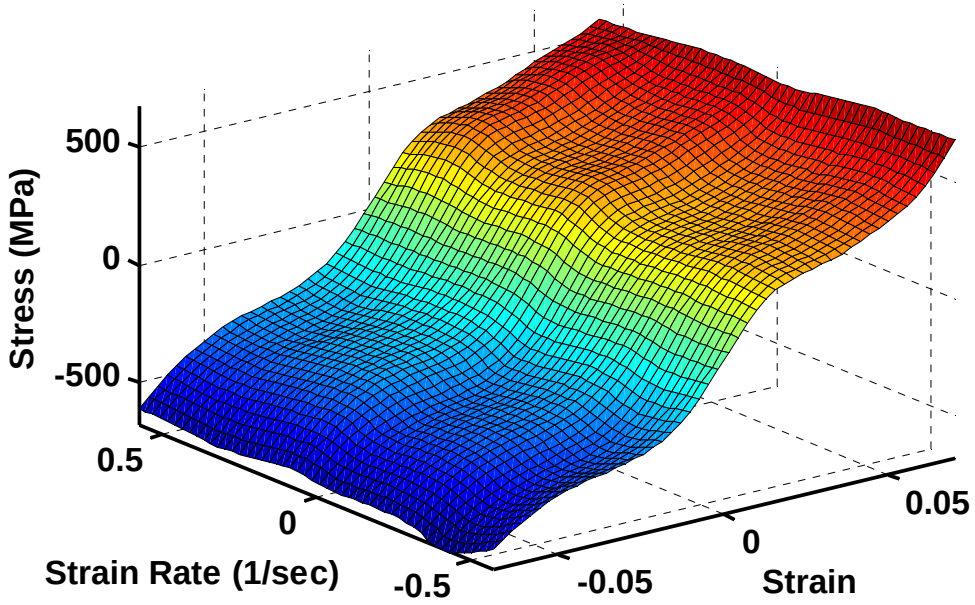

Fig. 76. Fuzzy surface for 1 mm diameter NiTi SMA wire

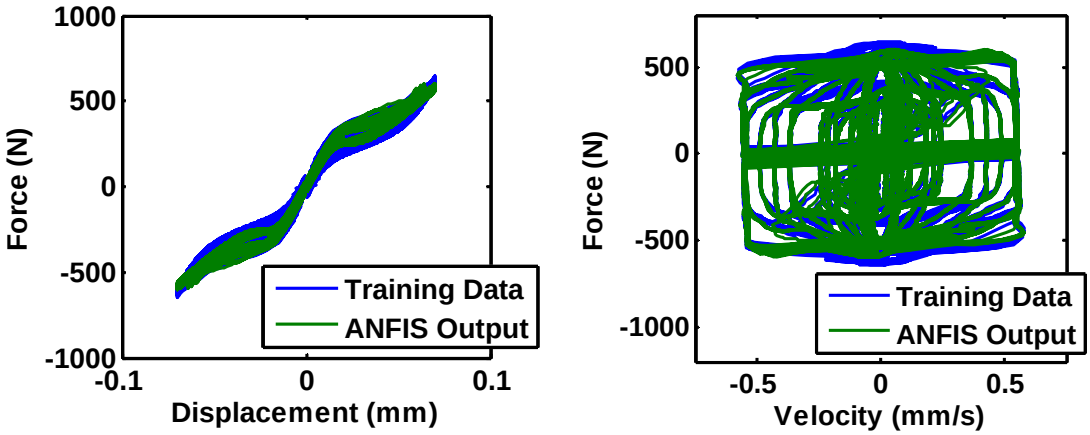

(a) Force-displacement (b) Force-velocity

Fig. 77. Training results for NiTi SMA FIS

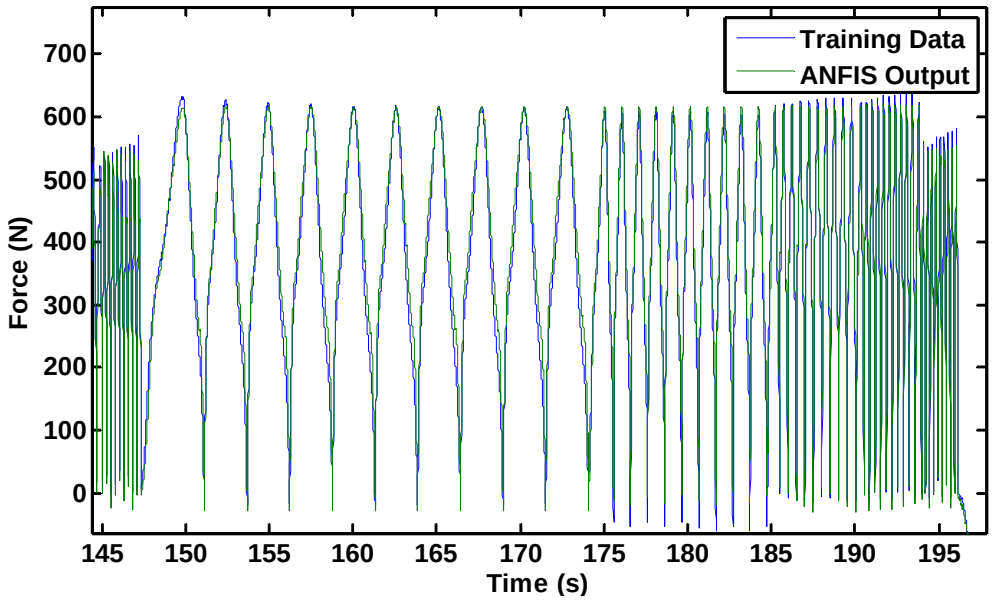

Fig. 78. Training force results for NiTi SMA FIS

5.5. PPP Model

Pinochet et al. (2006) developed a PPP isolator as an economical method for the seismic protection of low-cost housing. The PPP is a reinforced concrete pile with ends that are confined by steel rolling surfaces. PPP elements are joined together by a central prestressed cable that elongates due to relative lateral displacement between the top and bottom capitals. A lateral restoring force is generated both by the geometry of the element and the horizontal projection of the cable force. Ungrouted ductile rebar can be included at the base of the device to provide energy dissipation upon yielding. The analytical model, validated using experimental data, is developed with extensive detail in Pinochet et al. (2006). Fig. 79 shows three DOFs that are identified for each of the components of the PPP, including the top capital, top rolling surface, rod, bottom rolling surface, and bottom capital.

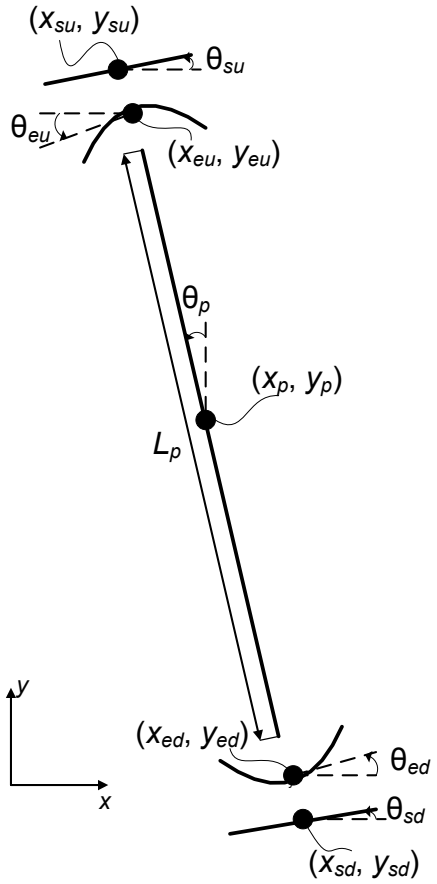

Fig. 79. Free body of PPP components (Pinochet et al. 2006)

Three main assumptions are made in the development of an analytical model of the PPP device. The assumptions are that the vertical rod is rigid in axial deformation and bending, the deformed shape of the cable is considered as piecewise linear (angle changes only occur at the four outer locations identified in Fig. 79), and tension in the cable is constant along its length (Pinochet et al. 2006). The horizontal restoring force of the device is determined after applying kinematic, action-deformation, and equilibrium constraints. The resulting equation for the force vector is included as Eq. 23 (Pinochet et al. 2006).

$$Q_i = V,_{q_i}^T + L_d^T \left[V,_{q_d}^T - Q_d \right] + \left[G,_{q_i}^T + L_d^T G,_{q_d}^T \right] f_n(q_n, z) \tag{23}$$

where $V,_{q_i}$ and $V,_{q_d}$ are the Jacobians of the internal energy relative to the independent and dependent coordinates, L_d is the kinematic transformation matrix between the independent and dependent coordinates, Q_d is the known vector of dependent forces, $G,_{q_i}$ and $G,_{q_d}$ are components of a vector that accounts for the deformations associated with the ductile passive reinforcement and other components at the rolling interface, and $f_n(q_n, z)$ represents the inelastic forces of the inelastic elements (Pinochet et al. 2006). Further information related to the formulation of these quantities is included in the paper by Pinochet et al. 2006.

Pinochet et al. (2006) validate their analytical model by testing nine half-length PPP elements with various rolling surfaces and steel cap thicknesses. The PPP elements tested were half-length because they had identical top and bottom rolling surfaces and thus had a point of inflection at the center of the element. Based on the testing, Pinochet et al. (2006) conclude that the analytical model is capable of representing the actual behavior of non-linear PPP isolators. They also conclude that the PPP isolators are rate-independent.

In this study, a modified form of the analytical equations developed by Pinochet et al. (2006) is used in numerical simulations. The original model is modified to account for friction between the central prestressed cable and its duct. This change was suggested by Besa et al. (2008) upon performing experimental testing on eight full-scale PPP isolators. The effect of friction between the central cable and its duct is taken into account by utilizing the following equations (Besa et al. 2008):

$$\widetilde{F} = F + \mu N_S sign(\dot{q}) \tag{24}$$

where:

$$N_S = T\cos\phi_S \tag{25}$$

and

$$\phi_S = \tan^{-1}\left(\frac{x_{su} - x_{eu}}{y_{su} - y_{eu}}\right) \tag{26}$$

where $\widetilde{F}$ and F are the corrected and uncorrected lateral force in the device, respectively, μ is the coefficient of friction, and $\dot{q}$ is the horizontal velocity of the top capital. In addition, T is the cable tension at the time considered, and ϕ_S is the angle of the cable with respect to the vertical direction. As in the analytical formulation developed by Pinochet et al. (2006), x_{eu} and y_{eu} are the current coordinates of the center of the top rolling surface, and x_{su} and y_{su} are the current coordinates of the center point of the rolling plate of the top capital. The coefficient of friction μ is assumed to be 1.8% in this study, as suggested by Besa et al. (2008).

Besa et al. (2008) also suggest that the model can be improved by using the Menegotto-Pinto model for the ductile rebar that is located at the base of the PPP element. In addition, Besa et al. conclude that the effect of flexibility in the interaction between the metal rolling surface and the plate in the top capital should be taken into account if the thickness of the rolling surface is less than 12 mm. This study uses an elastic-perfectly plastic model for the ductile rebar (as done by Pinochet et al. 2006) and assumes that the thickness of the top rolling surface is 12 mm or greater.

Jünemann et al. (2008) conduct a three-dimensional analytical study of the behavior of the PPP isolators. They conclude that using the analytical formulation by Pinochet et al. (2006) for the *x*- and *y*-directions independently results in an unconservative estimate of the force in the central prestressed cable. To compensate for the unconservative calculation of the cable force, Jünemann et al. suggest increasing the calculated cable force by 30%. This suggestion is applied in the current study when considering the maximum allowable tension in the central prestressed cable.

6. DEVICE OPTIMIZATION

6.1. General

The parameters of each of the isolation systems are optimized using a genetic algorithm or a trial-and-error approach. Specifically, the FPS and PPP isolation systems are optimized using genetic algorithms, while the HDRB, HDRB+SMA1, and HDRB+SMA2 isolation systems are optimized by trial-and-error. The parameters optimized are factors related to the geometry and state of the devices. As will be discussed in Section 7, two comparisons are made, including one comparison in which the parameters of each device are optimized and a second comparison in which the device parameters are selected to yield a fundamental period of 1.0 sec for the isolated structure. This section discusses the selection of parameters for the first comparison, in which an effort is made to use eight devices in each isolation system due to the layout of the case study structure.

The objectives used in the optimizations are:

- Peak base shear
- Peak base displacement
- Root-mean-squared base displacement
- Root-mean-squared absolute floor acceleration

These objectives are critical in evaluating the ability of an isolation system to minimize damage that could occur in the structure. The peak base shear is an indicator of the seismic force induced at the base of the structure. For the fixed-base case, the structure must withstand this force, while for the isolated case, the isolation devices need to be able to withstand this force. The peak base shear is closely related to the peak absolute floor acceleration because of the relative stiffness of the house, and thus the peak absolute floor acceleration is not utilized as an optimization objective. The peak base displacement is an important parameter to minimize because the isolators must be able to be displaced by this amount. In addition, precautions must be made to avoid damage to piping due to the base displacement, which does not occur in the fixed-base case. The RMS base displacement is used as an optimization parameter because it

quantifies the entire base displacement record. The RMS absolute floor acceleration is important because it is an indicator of the comfort of the building inhabitants throughout the duration of the seismic motion.

6.2. Overview of NSGA-II CE

Deb et al. (2002) discuss the advantages of using NSGA-II for multiobjective genetic algorithm optimization instead of traditional multiobjective evolutionary algorithms (EAs). NSGA-II is an approach that addresses the criticisms of traditional EAs, which include computational complexity, nonelitism, and the need for specifying a sharing parameter (Deb et al. 2002). The NSGA-II CE algorithm is applied in this study through the use of MATLAB and Simulink (2007).

The initial population for the GA optimization is generated randomly. The GA optimization process involves applying crossovers and mutations to the initial parent population to create a child population. The parent and child populations are then evaluated based on each objective function. NSGA-II uses Pareto fronts, crowding distances, and controlled elitism to create a new parent population (Shook 2006). A chromosome, which is a string of values, is created to tabulate each solution in the population. Each chromosome consists of the design parameters being optimized, values for each optimization function, rank, and crowding distance. An example chromosome is included as Fig. 80.

Parameter 1	Parameter 2	Parameter *n*	J_1	J_2	J_3	J_4	Rank	Crowding Distance

Fig. 80. Example GA chromosome

6.3. Objective Functions

The effectiveness of each set of parameters for a given isolation device is quantified in terms of objective functions. The objective functions in this study (also referred to as performance indices) are peak base shear (J_1), peak base displacement (J_2), RMS base displacement (J_3), and RMS absolute floor acceleration (J_4) of the case study structure. J_2 and J_3 are not normalized with respect to the fixed-base case because it does not experience base displacement. However, because J_1 and J_4 are normalized, values of J_1 and J_4 that are less than unity indicate a reduction in response from that of the fixed-base case. The objectives are defined as follows (Narasimhan et al. 2006):

$$J_1 = \frac{\max_t \left| V_{0,isolated} \right|}{\max_t \left| V_{0,fixed} \right|} \tag{27}$$

$$J_2 = \max_t \left| d_i \right| \tag{28}$$

$$J_3 = \max \left| \sigma_d(t) \right| \tag{29}$$

$$J_4 = \frac{\max_f \left| \sigma_{a,isolated}(t) \right|}{\max_f \left| \sigma_{a,fixed}(t) \right|} \tag{30}$$

where V_0 is base shear, d_i is the peak displacement of any isolator, $\sigma_d(t)$ is the RMS base displacement, and $\sigma_a(t)$ is the RMS acceleration. The subscripts *t*, *i*, and *f* refer to all time, isolators, and floors, respectively.

6.4. GA Optimization Terminology

6.4.1. Crossovers and Mutations

Crossovers and mutations are modifications of the parent chromosomes to produce the next generation of solutions. A crossover involves the exchange by two parent chromosomes of equal amounts of information to produce two children (Shook 2006). A chromosome in the previous generation is termed a parent, while a

chromosome in the current generation is termed a child. In this application, all individuals in the parent population are subjected to a crossover to produce the child population. At the end of the crossover operation, the parent and child populations have the same number of chromosomes.

Mutations occur by altering data at random after the completion of the crossover operations. This operation prevents the generation cycle from stagnating. Here 20% of each child population is mutated before it is pooled with the parent population. Only one value of the chromosome is altered in a single mutation.

6.4.2. Pareto Fronts and Crowding Distances

Two critical characteristics of all GAs are the exploitation of current solutions and the exploration of new solutions. Contrary to other GAs such as Pareto-Archived Evolution Strategy and Strength Pareto Evolutionary Algorithm, NSGA-II CE allows the entire population to be evaluated at each generation instead of creating an archived set of optimal solutions that are safe from elimination (Shook 2006). This reduces the exploitive nature of NSGA-II CE while greatly increasing its explorative nature.

A front is a group of non-dominated individuals in the current population. A rank is an integer value assigned to a front. The 1^{st} front is completely non-dominated; that is, each individual of the front has no superior when all objectives are considered. After determination of the 1^{st} front, the 2^{nd} and 3^{rd} fronts are determined. Fig. 81 (Shook 2006) illustrates the members of each front with respect to objectives 1 and 2.

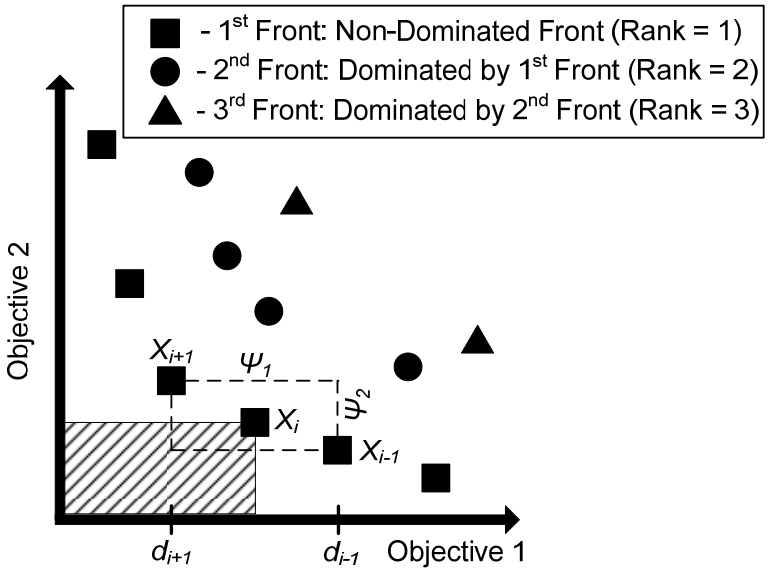

Fig. 81. Pareto fronts (Shook 2006)

Crowding distances, which differentiate members of a given front, are values that quantify the density of solutions surrounding a single solution in a given Pareto front. For multiobjective optimizations, the densities are quantified as follows (Shook 2006):

$$\psi_k = \sum_{j=1}^{J} \left(d_{i-1} - d_{i+1} \right) \tag{31}$$

$$\varphi = \sum_{k=1}^{K} \psi_k \tag{32}$$

where φ is the crowding distance of an individual with respect to all Pareto fronts, ψ is the crowding distance of a single individual with respect to members of the k^{th} Pareto front, J is the total number of optimization objectives, K is the number of Pareto fronts, and d is the distance (measured from the origin) as indicated in Fig. 81. The entire pool of solutions is sorted into Pareto fronts prior to computation of crowding distances. The crowding distance is cumulative among all objectives. Among two solutions within the same rank, the solution with the larger crowding distance is considered superior. This practice promotes strong diversity of the population. A minimum number of solutions in

each front are required to prevent all solutions of a population from evolving into a single front.

6.4.3. Diversity and Controlled Elitism

Two types of diversity are sought in this study, namely, longitudinal and lateral diversity (see Fig. 82). Lateral diversity occurs by maintaining a population with multiple Pareto fronts, which prevents solutions from converging too quickly to a local Pareto front (Shook 2006). NSGA-II CE ensures that individuals from a specified number of fronts are maintained in the population through the use of controlled elitism.

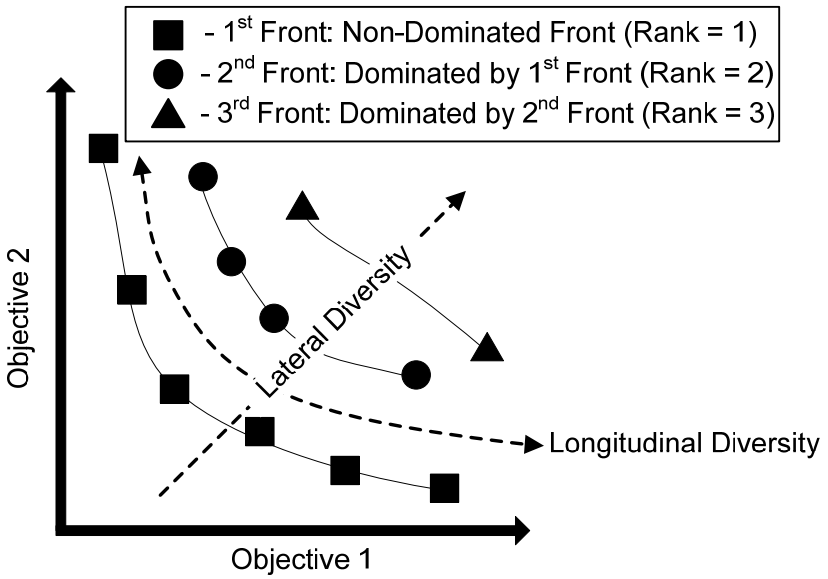

Fig. 82. Lateral and longitudinal diversity (Shook 2006)

According to Deb and Goel (2001), forcing dominated solutions to coexist in a population is an effective manner in which to avoid early convergence, particularly in a multiobjective GA. This practice is termed controlled elitism. The number of solutions in each front is specified as follows (Shook 2006):

$$n_i = N\frac{1-r}{1-r^K}r^{i-1} \tag{33}$$

where n_i is the number of individuals allowed in rank i, N is the total number of individuals in the population, K is the desired number of fronts, and r is a user-defined parameter between 0 and 1 that influences diversity. Four fronts and an r value of 0.5 are used in this study. An r value close to 1 produces a uniform distribution of solutions, while an r value close to 0 yields a more exponential distribution of solutions. Shook (2006) discusses the results of several optimization examples to compare NSGA-II CE with its predecessor NSGA-II (without controlled elitism).

6.5. FPS Optimization

6.5.1. FPS GA Optimization

GA optimization is performed to optimize the radius of curvature and coefficient of friction of the sliding surface of the FPS bearings, assuming that eight FPS bearings are used to isolate the case study structure. The proposed layout of the bearings, which is applicable for all of the cases using eight isolators, is shown in Fig. 83. The optimization is performed for the FPS bearings using the earthquake generated by RSPMatch for a structure with an isolated period of 2 sec (see Figs. 42-44 and Fig. 51). Subsequently, the GA results are verified using a manual procedure. To perform the optimization, the ranges of appropriate values for the parameters are determined.

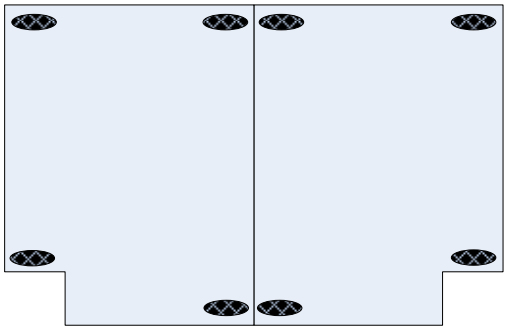

Fig. 83. Proposed locations of isolators

Jangid (2000) performed an analysis of the optimal coefficient of friction for sliding isolation systems. Based on his study, Jangid (2000) concluded that there exists a coefficient of friction at which the RMS acceleration is at a minimum. At coefficient of friction values higher than this value, the RMS acceleration increases. However, research by Jangid (2000) shows that the value of RMS base displacement is not at a minimum at the same coefficient of friction value as that which minimizes the RMS acceleration. Jangid (2000) also concluded that the optimum friction coefficient of the sliding system increases with the number of stories of the structure and it increases with earthquakes of higher intensities.

In addition, Jangid (2005) studied the optimal coefficient of friction for FPS bearings subject to near-fault motions. He concluded that coefficient of friction values of 0.05 to 0.15 are optimal under near-fault motions. These values for the coefficient of friction limit bearing displacement values without significantly compromising acceleration values of the superstructure (Jangid 2005). Mosqueda et al. (2004) also discuss values for the coefficient of friction of an FPS sliding system.

In this study, the ranges used for optimization are 0.001 to 0.15 for the coefficient of friction of the sliding system, and 0.1 to 10 m for the radius of curvature. Fig. 84 shows the Pareto fronts after 20 generations of the FPS optimization for pairs of the four objectives. A total of 150 generations were computed, but only results after 20 generations are shown here due to early convergence to a group of potentially optimal solutions. The population size of each generation is 30, which indicates that 30 solutions are evaluated in each generation. Each solution is assigned a rank based on the Pareto fronts (see Section 6.4.2). The amount of lateral and longitudinal diversity of solutions in each plot of objective pairs varies greatly. The lack of longitudinal diversity in the plots of J_4 vs. J_1 and J_3 vs. J_2 is attributed to the almost linear relationship between the objectives of each pair. Floor acceleration and base shear are related through the structural mass, while there also appears to be a strong relationship between peak and RMS base displacement. Other pairs of objectives lack lateral diversity due to

convergence to a group of potentially optimal solutions. This convergence explains why several of the 30 solutions in each generation coincide in the plots.

Fig. 85 shows the solution results from the 1st to the 20th generation. The results do not show a clear evolution to a single optimal solution because several solutions exist that yield similar values of the performance indices used as objective functions. Some of these solutions even exist in the 1st generation. Based on the population at the 20th generation, the optimal parameters selected for the FPS are a coefficient of friction μ = 0.03 and a radius of curvature R = 3.5 m. This solution is identified in Figs. 84 and 85. It should be noted that because peak base displacement and RMS base displacement are competing objective functions with peak base shear and RMS absolute floor acceleration, there is no single solution that minimizes all of the objective functions. Therefore, the selected values of μ and R minimize the peak base shear (J_1) and RMS absolute floor acceleration (J_4) while resulting in acceptable values for the peak base displacement (J_2) and RMS base displacement (J_3).

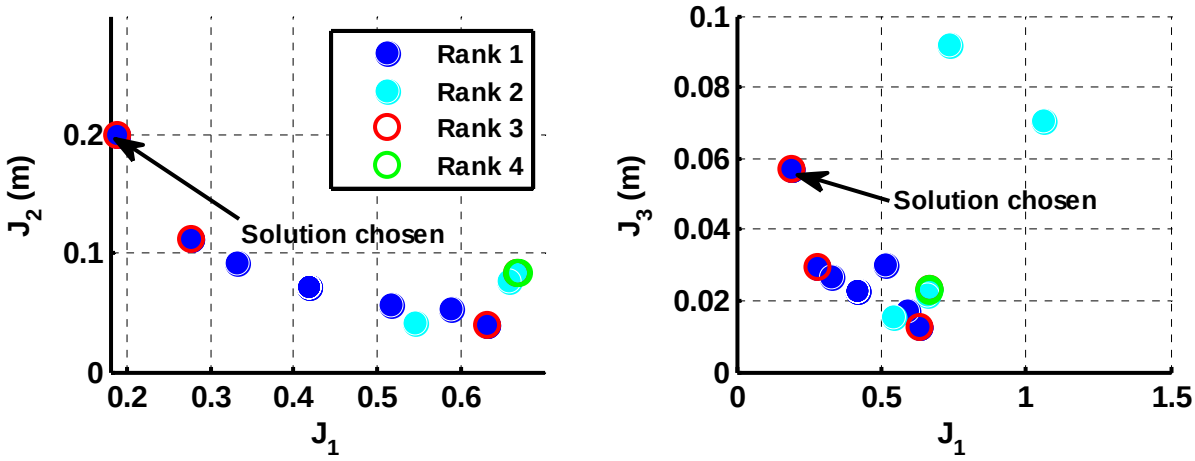

Fig. 84. FPS Pareto fronts after 20 generations

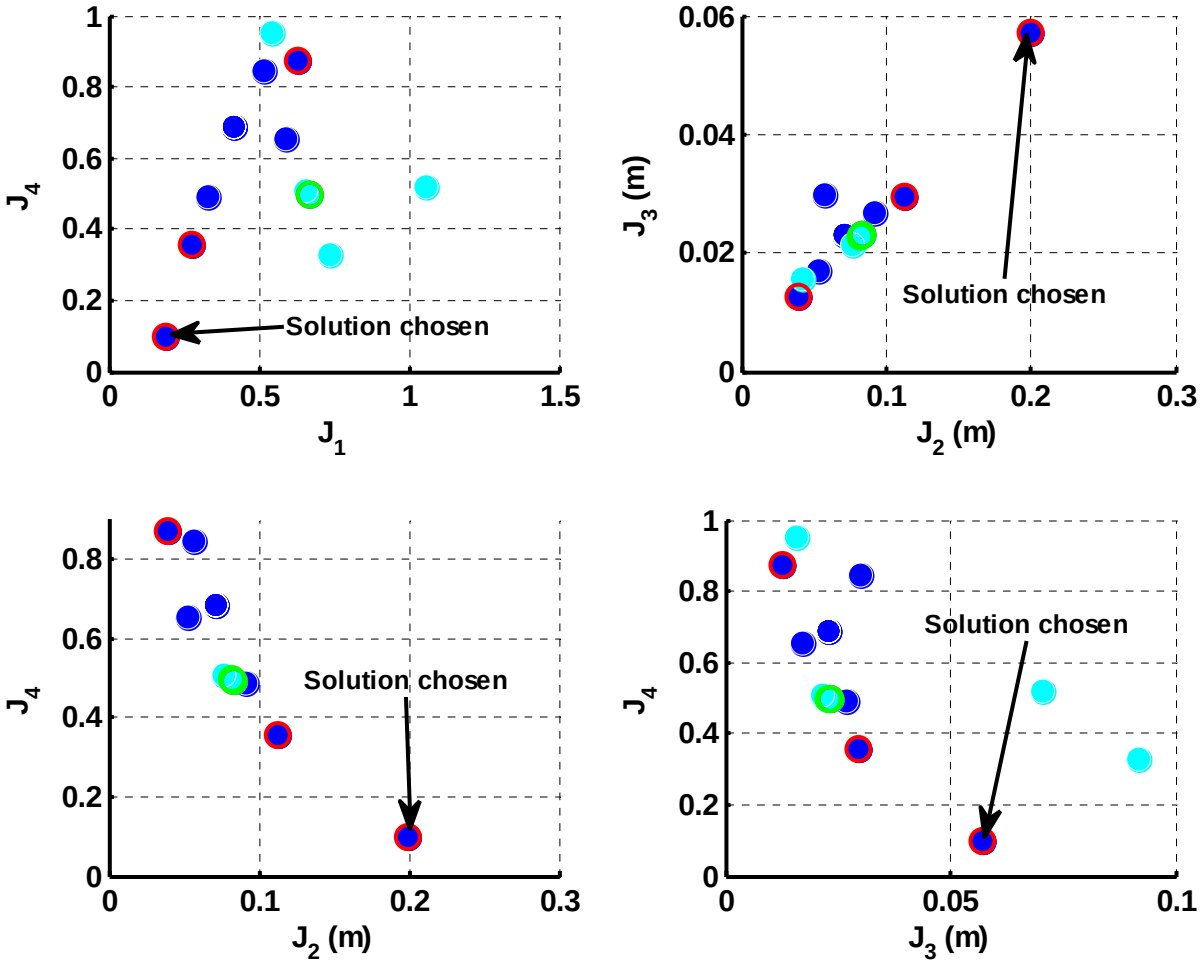

Fig. 84. Continued

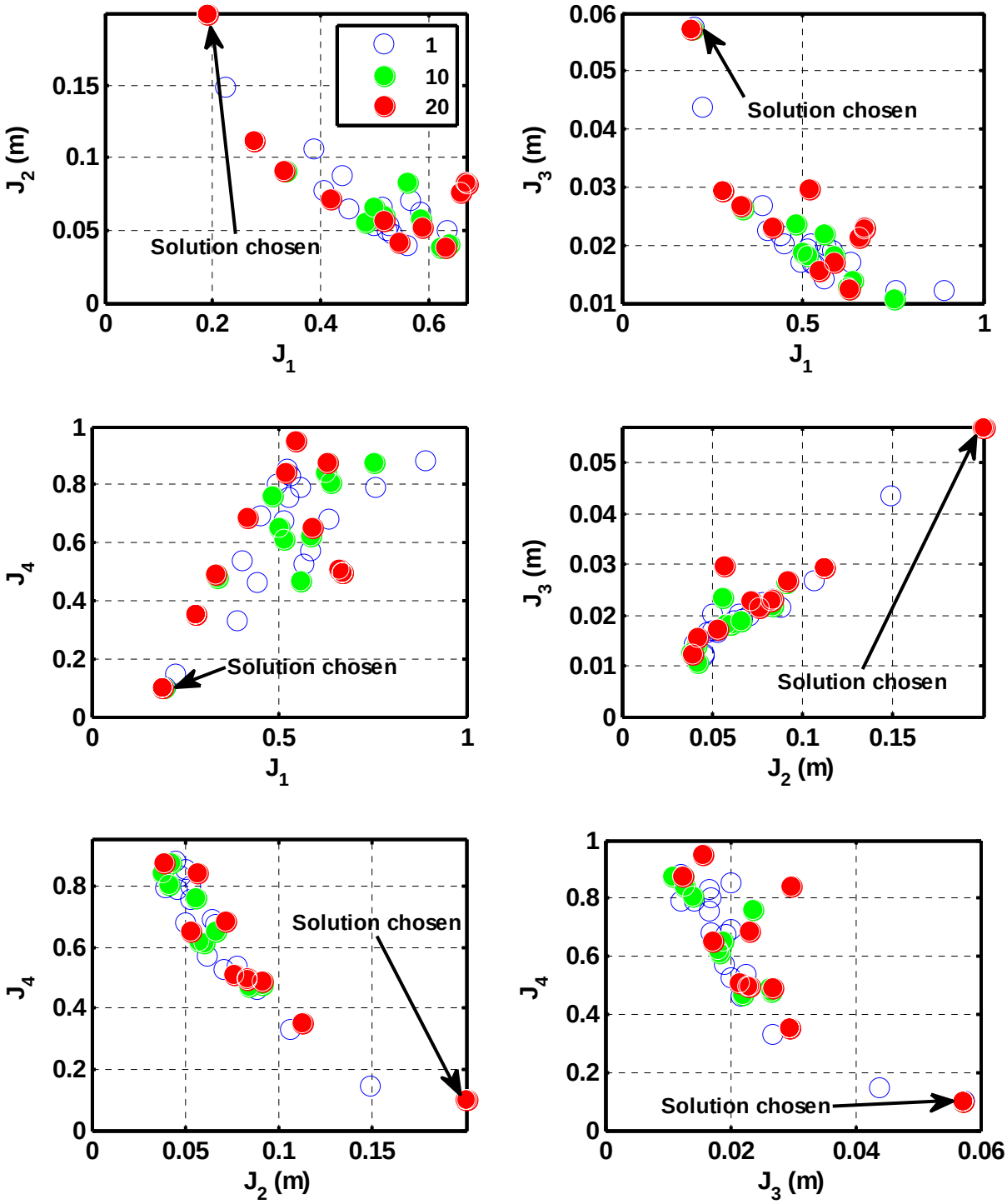

Fig. 85. FPS results after 20 generations

6.5.2. FPS Manual Optimization

After optimization of the FPS parameters is completed using NSGA-II CE, an optimization is performed using a manual method. The same earthquake is used in this analysis as for the GA optimization. Using the manual method, the values for μ range from 0.01 to 0.5 in increments of 0.01 while the values for R range from 0.5 to 25 m in increments of 0.5 m. That is, a total of 2,500 analyses are carried out. The results of these numerical simulations are interpolated by means of surface plots. These surfaces of μ and R plotted against each performance index are shown in Figs. 86-89. It is evident from these figures that base displacement and floor acceleration are competing objectives. It can also be seen that values of μ and R close to zero should be avoided, as a spike occurs in the peak base shear, peak base displacement, RMS base displacement, and RMS floor acceleration. In addition, care should be exercised in choosing the design parameters in order to avoid the elevated region on the RMS base displacement plot (see Fig. 88). It can be concluded that μ should be greater than or equal to approximately 0.03, and R should be greater than 2 m. Using these values prevents a spike in the performances indices and yields an adequate compromise between the competing objectives of displacement and acceleration.

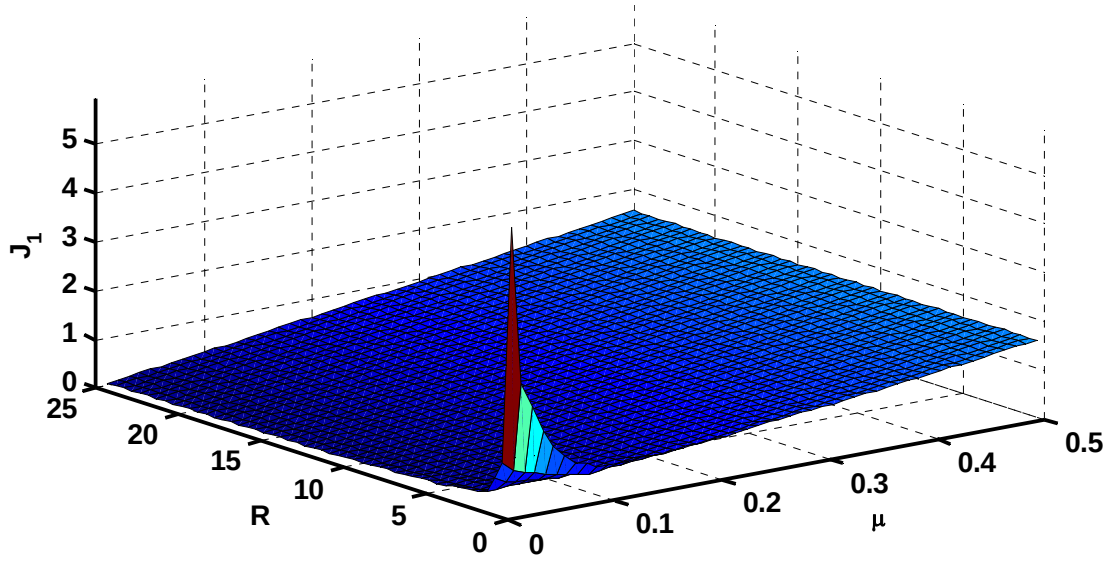

Fig. 86. Peak base shear vs. FPS parameters

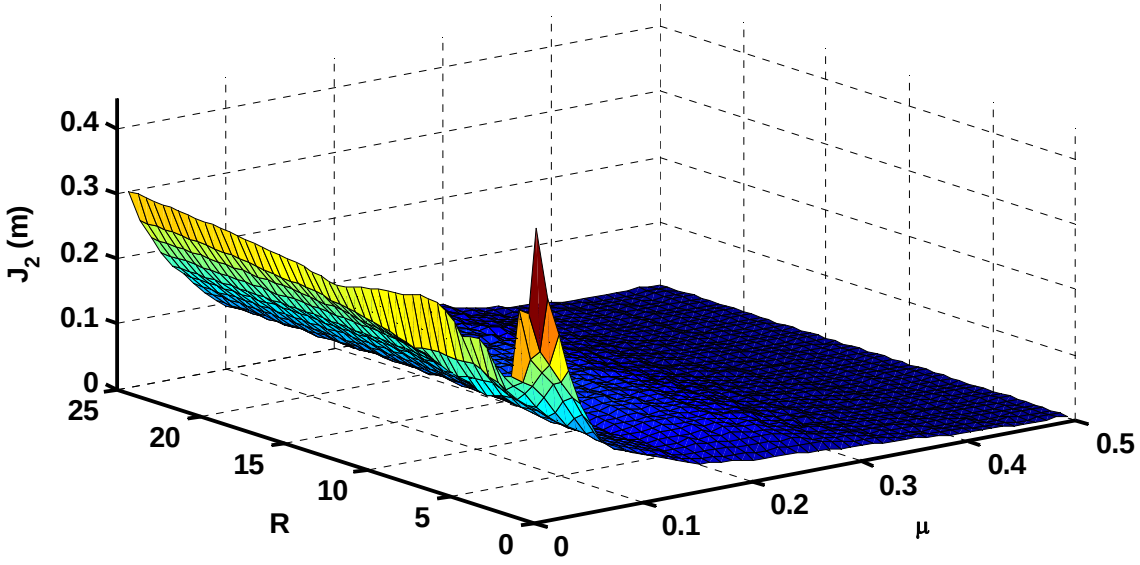

Fig. 87. Peak base displacement vs. FPS parameters

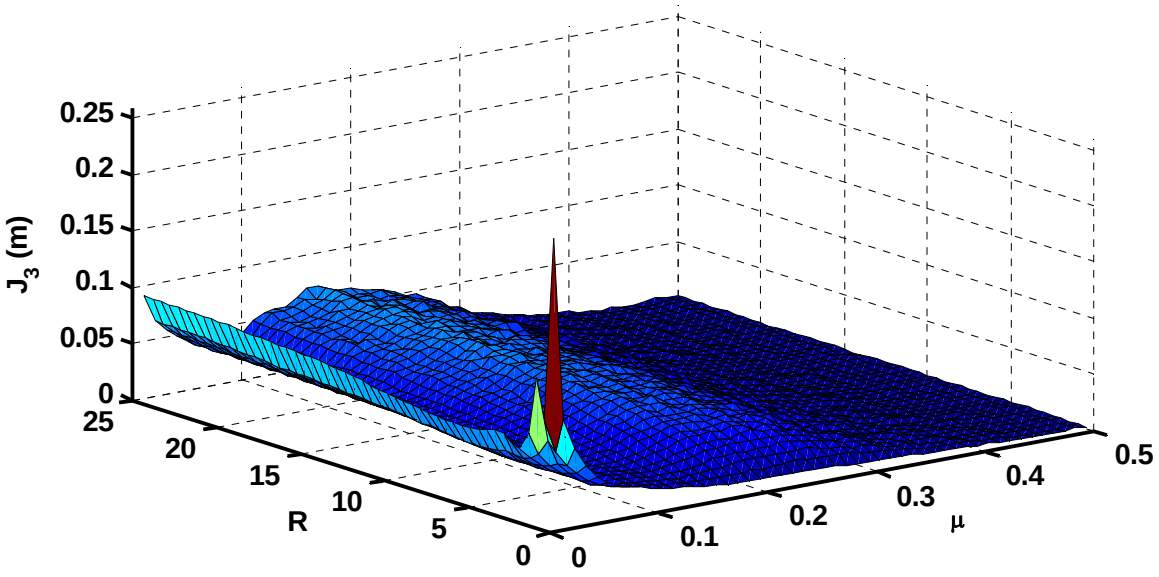

Fig. 88. RMS base displacement vs. FPS parameters

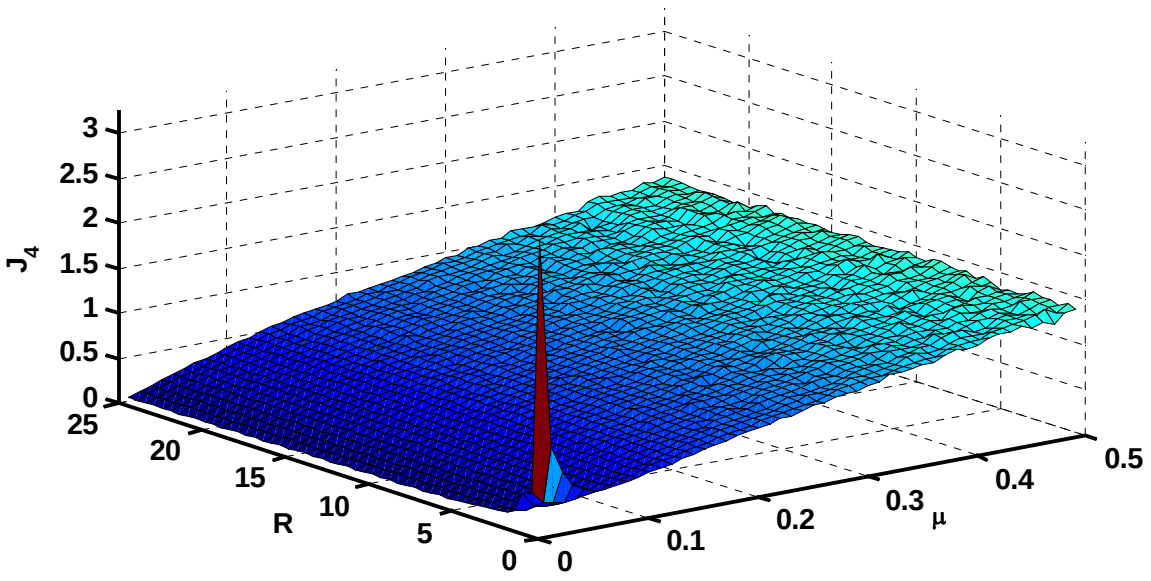

Fig. 89. RMS floor acceleration vs. FPS parameters

6.6. HDRB Optimization

6.6.1. HDRB Parameters

Due to limited accessibility to experimental data, the HDRB optimization involves determination of the most appropriate bearing from the three HDRBs described by Jankowski (2004). Each of the bearings mentioned by Jankowski (2004) is larger than that required for this study. For this reason, each bearing is scaled to the appropriate size by keeping the shear stress-strain relationship and the normal stress on the bearing the same as that tested experimentally. The notion of being able to scale the properties of reduced-scale specimens to represent the behavior of full-scale bearings has been proven through experimental testing (De la Llera et al. 2004). This application uses the reverse approach, namely using existing data from the testing of full-scale bearings to represent the behavior of reduced-scale bearings. The Pan and Yang (1996) model is utilized to simulate the force-displacement behavior of each bearing. For the installation of eight bearings, the axial load on each bearing is 100 kN. As mentioned previously, eight bearings are used in the first comparison made due to the layout of the structure. The second comparison involves some cases in which the number of HDRBs used in the isolation system is more or less than eight. The effect of an axial load on each bearing that is different than 100 kN is addressed in Section 7. The stability of the bearings is checked by verifying that the restoring force that each bearing is able to generate is greater than the base shear force in each bearing due to a given seismic excitation.

The first HDRB considered is a square bearing with dimensions of 89 × 89 × 9.3 cm. It consists of five rubber layers and was tested by a group of Japanese researchers with an axial pressure of 4.95 MPa [Jankowski (2004)]. The parameters for this bearing are included in Table 4. The bearing is scaled to 14 × 14 × 9.3 cm.

Table 4. Constants for 89 × 89 cm HDRB

$b_1 = 7.5509 \times 10^6$ N/m	$b_7 = 7.1213$ s/m

Table 4. Continued

$b_2 = 3.8939\times10^6$ N/m^3	$b_8 = 45.693$ 1/m
$b_3 = 1.3423\times10^8$ N/m^5	$b_9 = 4.9075\times10^5$ N
$b_4 = 3.1749\times10^6$ N/m	$b_{10} = 2.2888\times10^6$ N/m^2
$b_5 = 1.4906$ s/m	$b_{11} = 0.58681$ m/s
$b_6 = 2.8303\times10^7$ N/m	

The second HDRB considered is a round bearing with a 22.3 cm diameter and 18 cm height that was tested by the Denryoku Company of Japan with an axial pressure of 3.14 MPa. The parameters for the bearing to be modeled using the Pan and Yang formulation (1996) are included in Table 5, as reported by Jankowski (2004). The bearing is scaled to a diameter of 20 cm for use in this study.

Table 5. Constants for 22.3 cm Diameter HDRB

$b_1 = 2.0829\times10^5$ N/m	$b_7 = 3.9664$ s/m
$b_2 = 3.3648\times10^6$ N/m^3	$b_8 = 91.482$ 1/m
$b_3 = -8.5978\times10^6$ N/m^5	$b_9 = 1.5080\times10^4$ N
$b_4 = 5.0829\times10^5$ N/m	$b_{10} = 4.0079\times10^5$ N/m^2
$b_5 = 4.3595$ s/m	$b_{11} = 0.13985$ m/s
$b_6 = 5.7544\times10^5$ N/m	

The third HDRB considered is a 33 cm diameter, 17.65 cm tall bearing subject to an axial pressure of 3.9 MPa [Jankowski (2004)]. The bearing tested is classified as a hard Indonesian bearing of type H14. The parameters for the 33 cm diameter bearing for use with the Pan and Yang (1996) model are included in Table 6. The force-

displacement behavior of the bearing is scaled to represent the behavior of an 18 cm diameter, 17.65 cm tall HDRB.

Table 6. Constants for 33 cm Diameter HDRB

b_1 = 4.1051×10^5 N/m	b_7 = 6.9069 s/m
b_2 = -1.7238×10^3 N/m^3	b_8 = 48.371 1/m
b_3 = -98.611 N/m^5	b_9 = 1.0169×10^4 N
b_4 = 1.2261×10^5 N/m	b_{10} = 8.0471×10^4 N/m^2
b_5 = 5.0777 s/m	b_{11} = 0.15621 m/s
b_6 = 3.5740×10^5 N/m	

6.6.2. FIS Training and Validation

A fuzzy surface is created for each bearing, using inputs of displacement and velocity to predict the force exerted by the HDRB on the structure. The velocity is calculated from the displacement by utilizing the fourth-order backward difference formula included as Eq. (34) (Chapra and Canale 1998).

$$\dot{x}(i) = \frac{3x(i-4) - 16x(i-3) + 36x(i-2) - 48x(i-1) + 25x(i)}{12\Delta t} \tag{34}$$

Here, $x(i)$ and $\dot{x}(i)$ are the displacement and velocity at time step i, and Δt is the duration of each time interval. The range of displacement data used to train each fuzzy surface is +/- 30 cm. The displacement data are generated using a random white noise signal, and the corresponding force data are determined using the Pan and Yang (1996) model. The data used to train each of the fuzzy surfaces are shown in Figs. 90 and 97. Different data are used to train the second HDRB FIS than the first and third HDRB FISes because the second HDRB requires the use of more data with higher frequency content to create an appropriate FIS than do the first and third HDRBs. This observation is determined through validation of the HDRB FISes.

The HDRB FIS corresponding to the 14 × 14 × 9.3 cm square bearing is trained using two membership functions of type ‘dsigmf’ for the displacement and velocity inputs. The membership functions for each input variable before and after training are included in Fig. 91. ‘dsigmf’ indicates a membership function that uses the difference between two sigmoidal membership functions. Other training parameters include the use of 100 epochs, a step size of 0.3, and step size increase and decrease rates of 1.2 and 0.8, respectively. A plot of the step size variation throughout the training process is included in Fig. 92. The FIS (shown in Fig. 93) determined by means of the Adaptive Neuro-Fuzzy Inference System (ANFIS) is validated using random white noise data with different frequency content than that used for its training. Fig. 94 shows how the ANFIS prediction of force compares with the data used for training, while Figs. 95 and 96 show how the ANFIS prediction of force compares to the validation data.

The second HDRB FIS, corresponding to a 20 cm diameter HDRB, is trained using the data shown in Fig. 97. Three and two membership functions of type ‘dsigmf’ are utilized for the displacement and velocity inputs, respectively (see Fig. 98). The number of epochs and step size increase and decrease rates are the same as those used for development of the first HDRB FIS. However, in the creation of the second HDRB FIS, a step size of 0.1 is utilized (see Fig. 99). A surface representing the FIS is shown in Fig. 100. It is also validated using random white noise data that are different than those used for training. The other plots related to the FIS training and validation are included in Figs. 101-103.

A third HDRB FIS is created that corresponds to a slightly smaller, 18 cm diameter HDRB. It is trained using the same number of epochs and step size increase and decrease rates as mentioned above, with a step size of 0.05 and two ‘dsigmf’ membership functions for the displacement and velocity inputs. The membership functions before and after training, the variation in step size throughout training, and the FIS are shown in Figs. 104, 105, and 106, respectively. Plots related to the training and validation of the FIS are shown in Figs. 107-109.

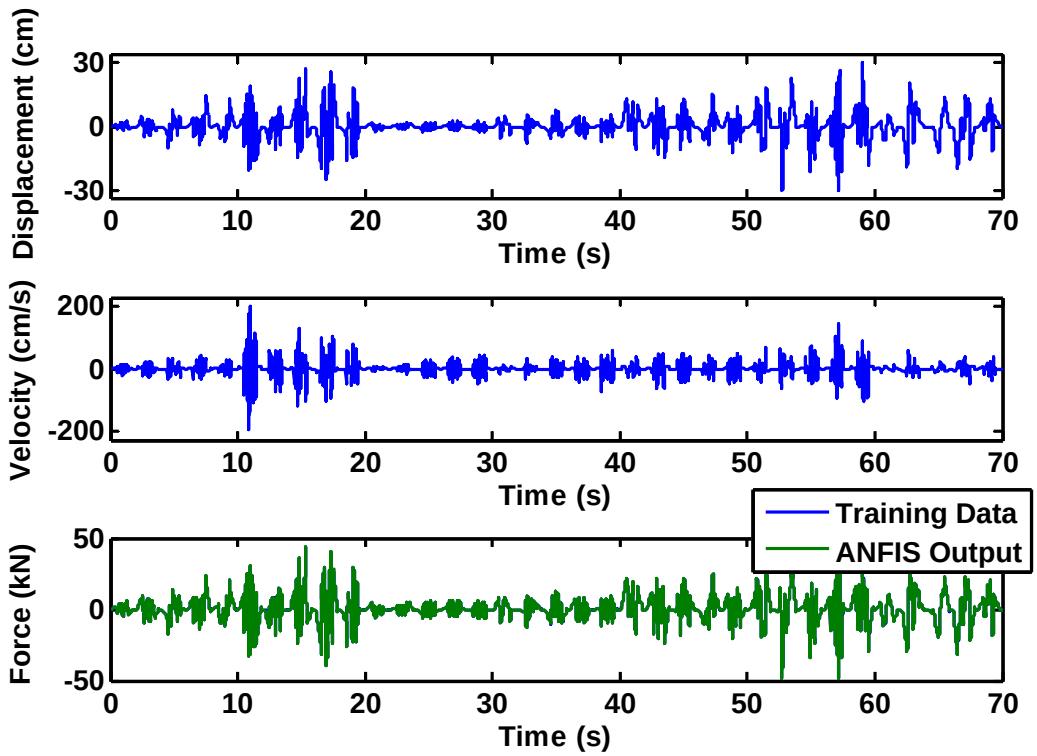

Fig. 90. Training data for 14 × 14 cm HDRB and 18 cm diameter HDRB

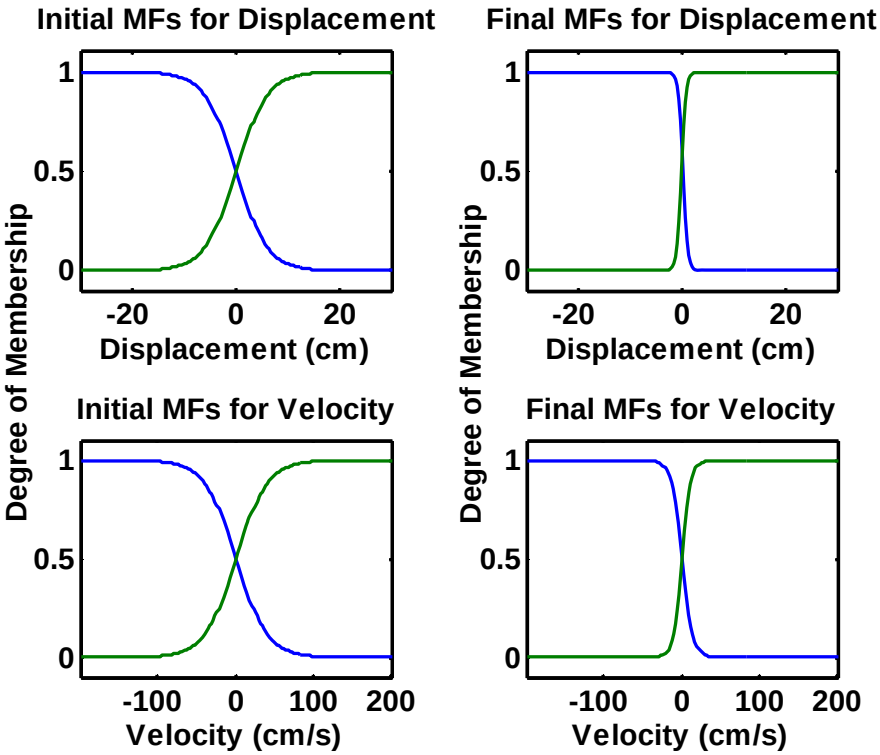

Fig. 91. Membership functions before and after training for 14 × 14 cm HDRB with 100 kN axial load

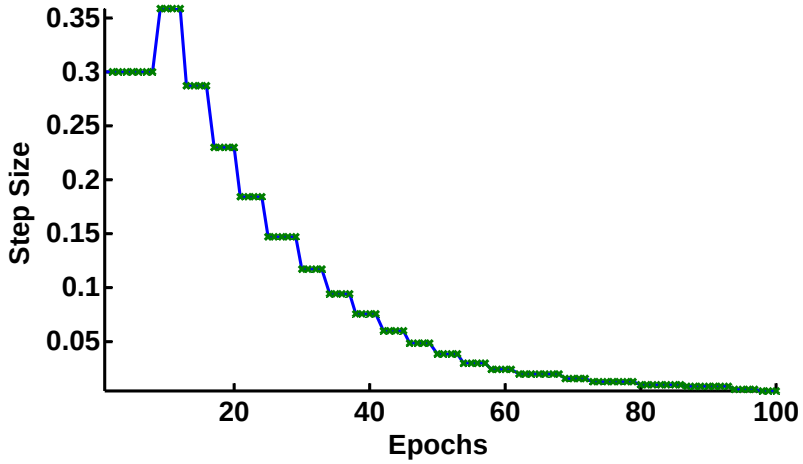

Fig. 92. Variation in step size for 14 × 14 cm HDRB with 100 kN axial load

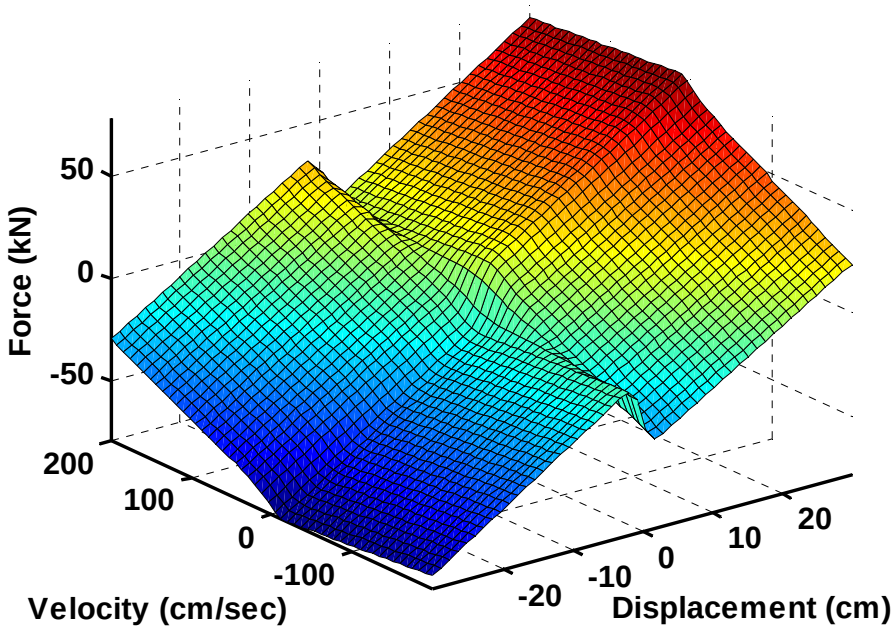

Fig. 93. Fuzzy surface for 14 × 14 cm HDRB with 100 kN axial load

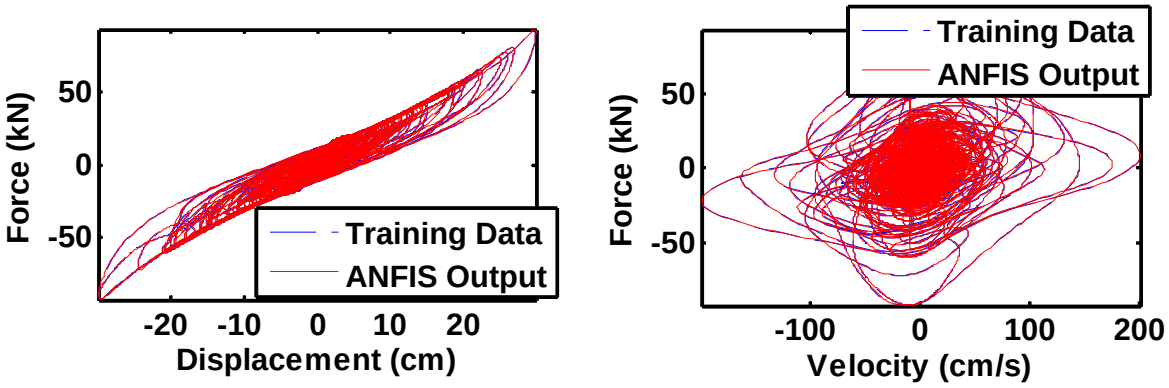

(a) Force versus displacement (b) Force versus velocity

Fig. 94. Training results for 14 × 14 cm HDRB with 100 kN axial load

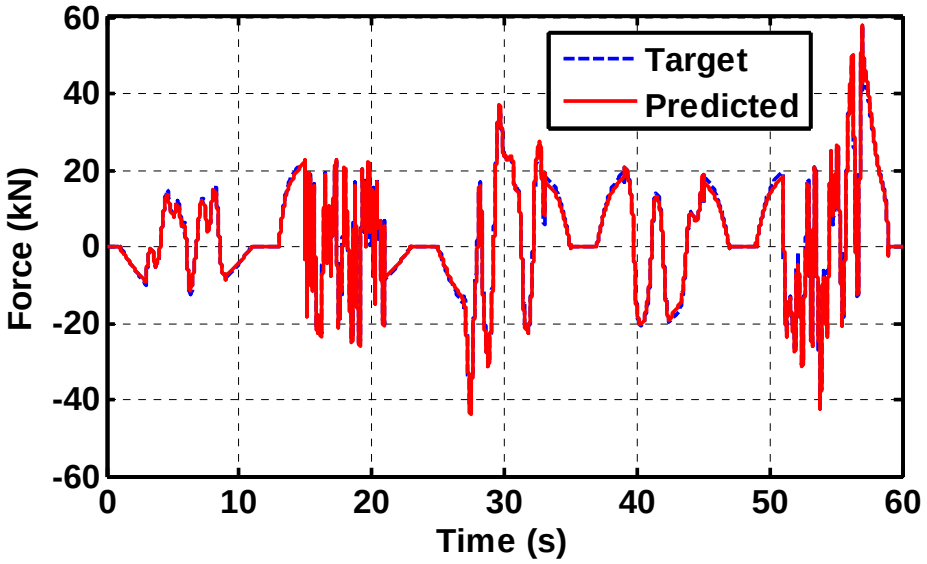

Fig. 95. Validation of force for 14 × 14 cm HDRB with 100 kN axial load

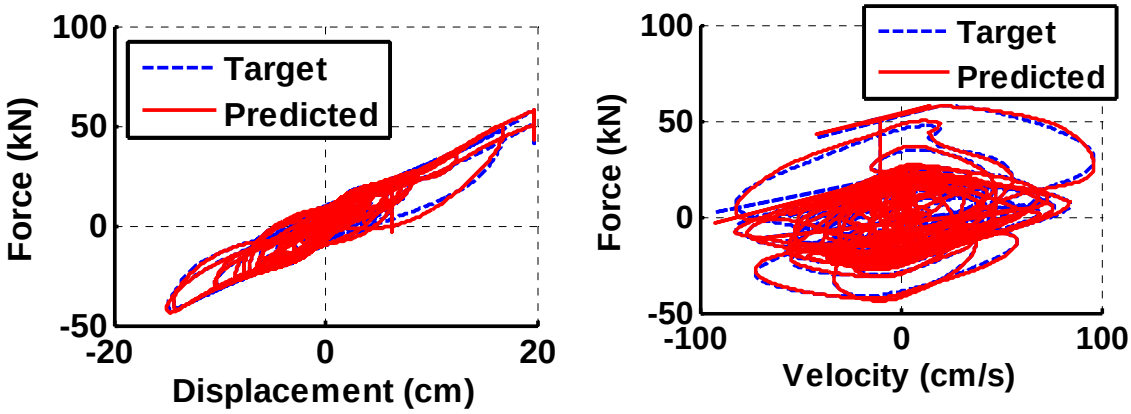

(a) Force versus displacement (b) Force versus velocity

Fig. 96. Validation results for 14 × 14 cm HDRB with 100 kN axial load

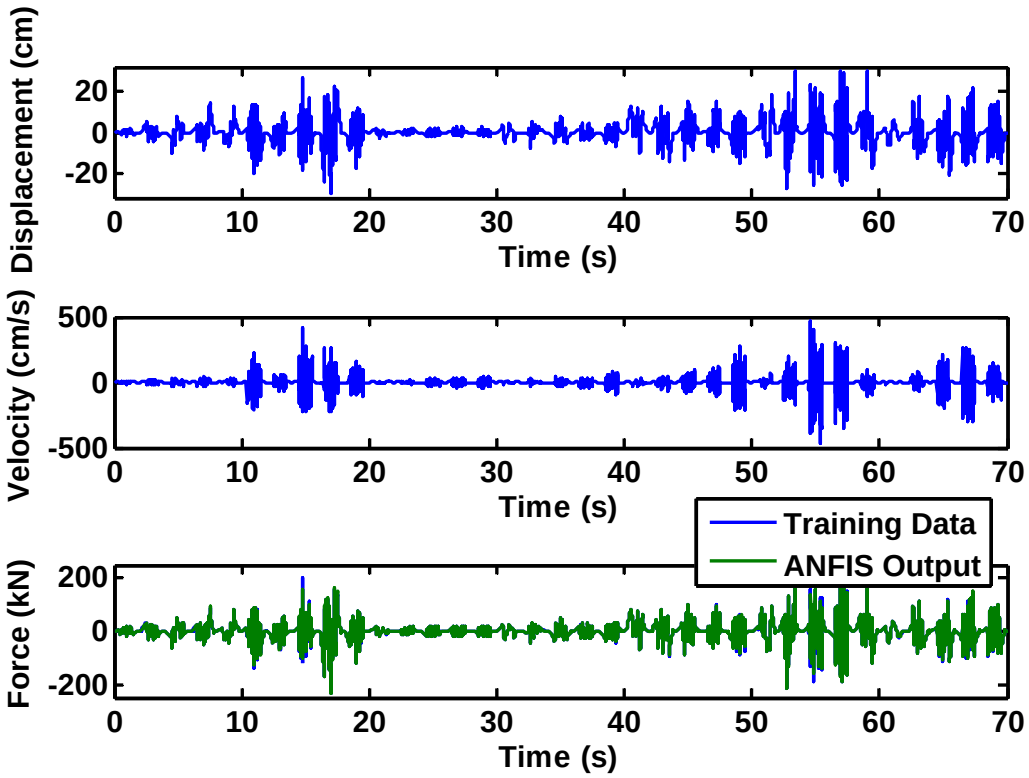

Fig. 97. Training data for 20 cm diameter HDRB

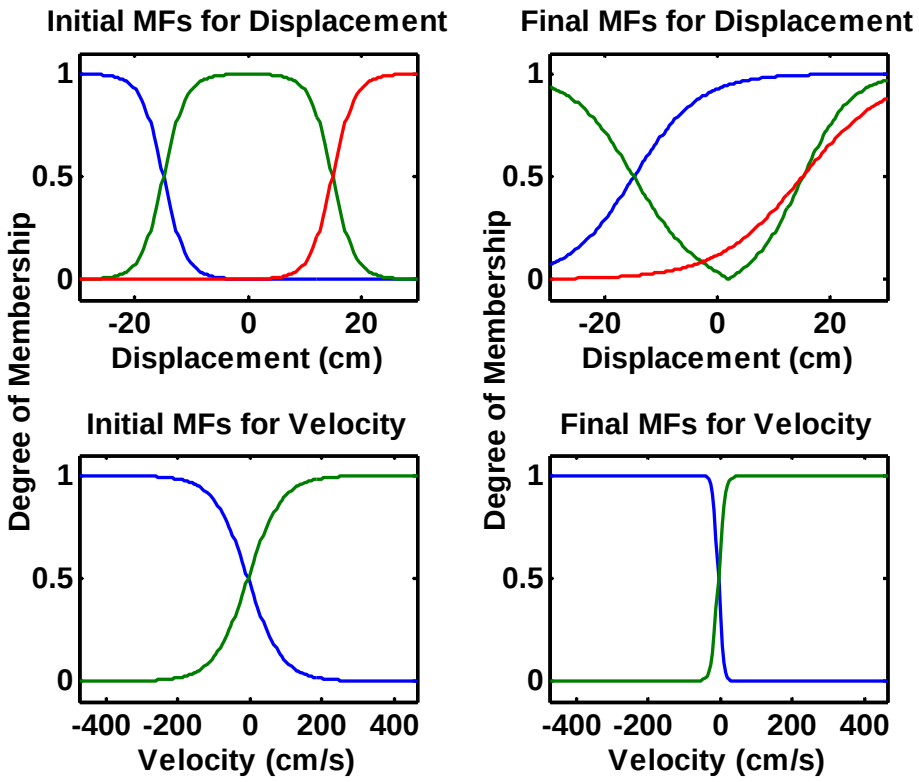

Fig. 98. Membership functions before and after training for 20 cm diameter HDRB with 100 kN axial load

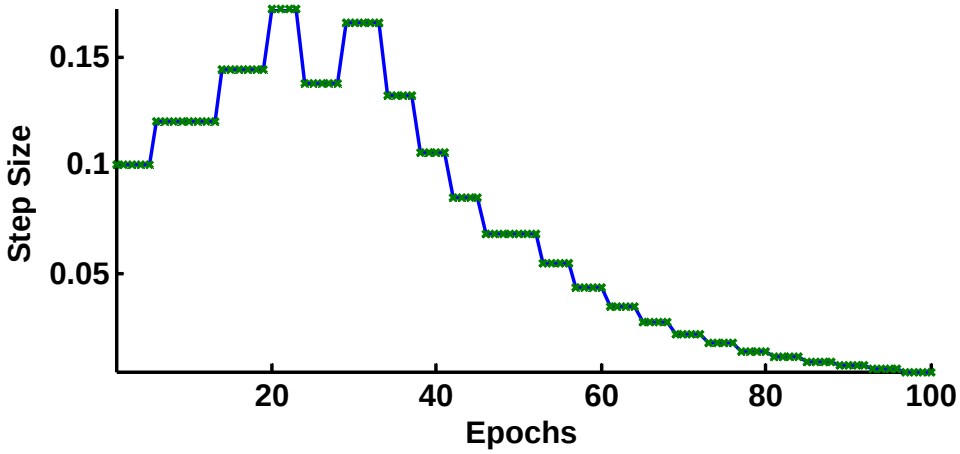

Fig. 99. Variation in step size for 20 cm diameter HDRB with 100 kN axial load

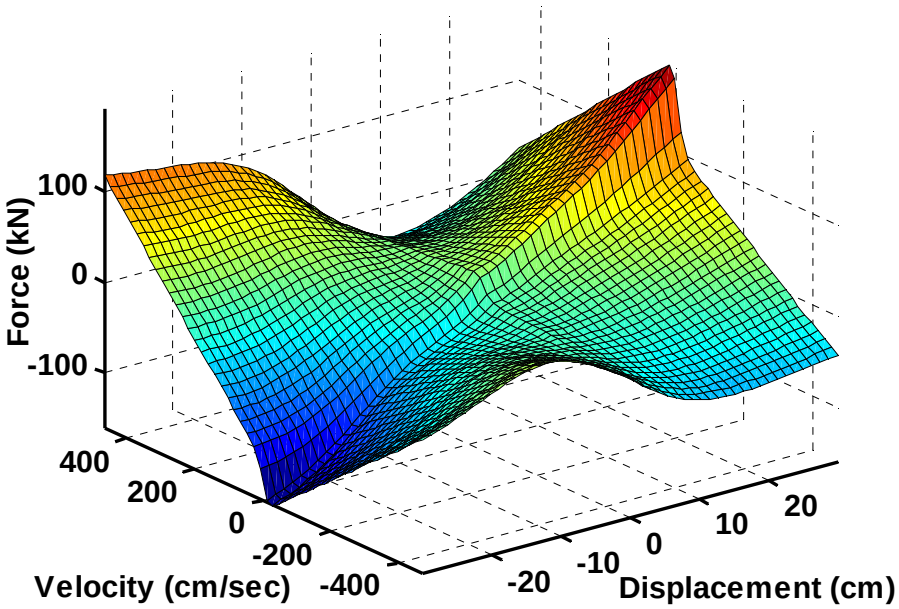

Fig. 100. Fuzzy surface of 20 cm diameter HDRB with 100 kN axial load

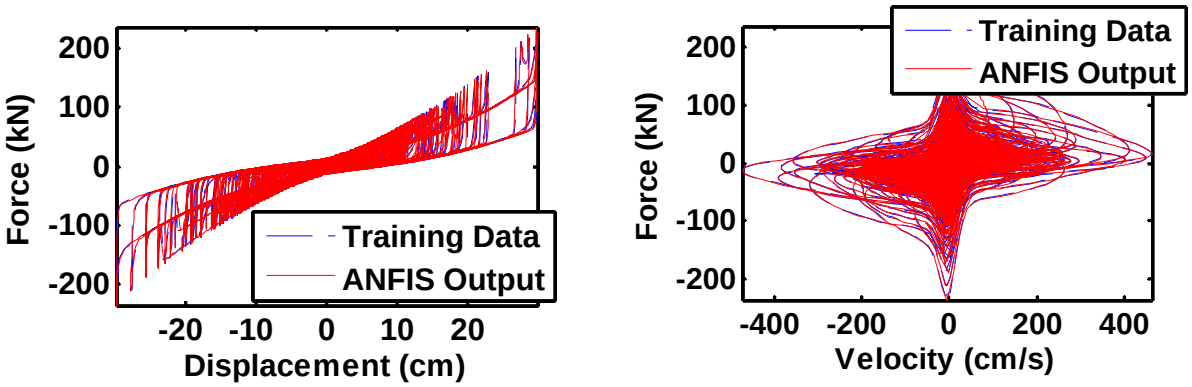

(a) Force versus displacement (b) Force versus velocity

Fig. 101. Training results for 20 cm diameter HDRB with 100 kN axial load

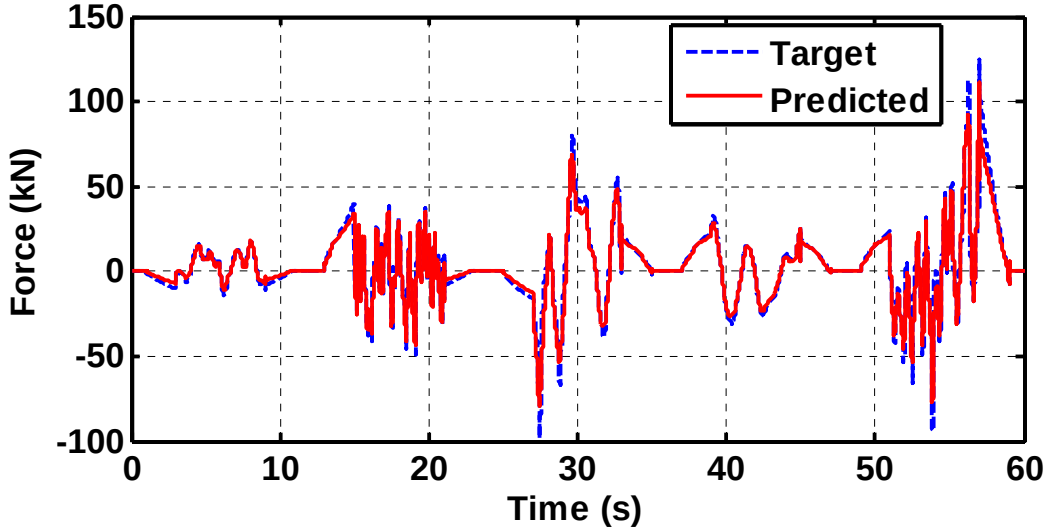

Fig. 102. Validation of force for 20 cm diameter HDRB with 100 kN axial load

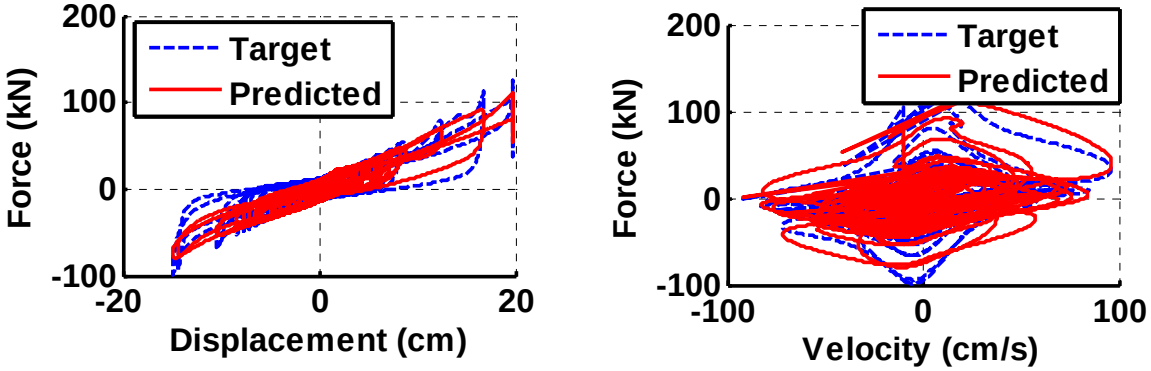

(a) Force versus displacement (b) Force versus velocity

Fig. 103. Validation results for 20 cm diameter HDRB with 100 kN axial load

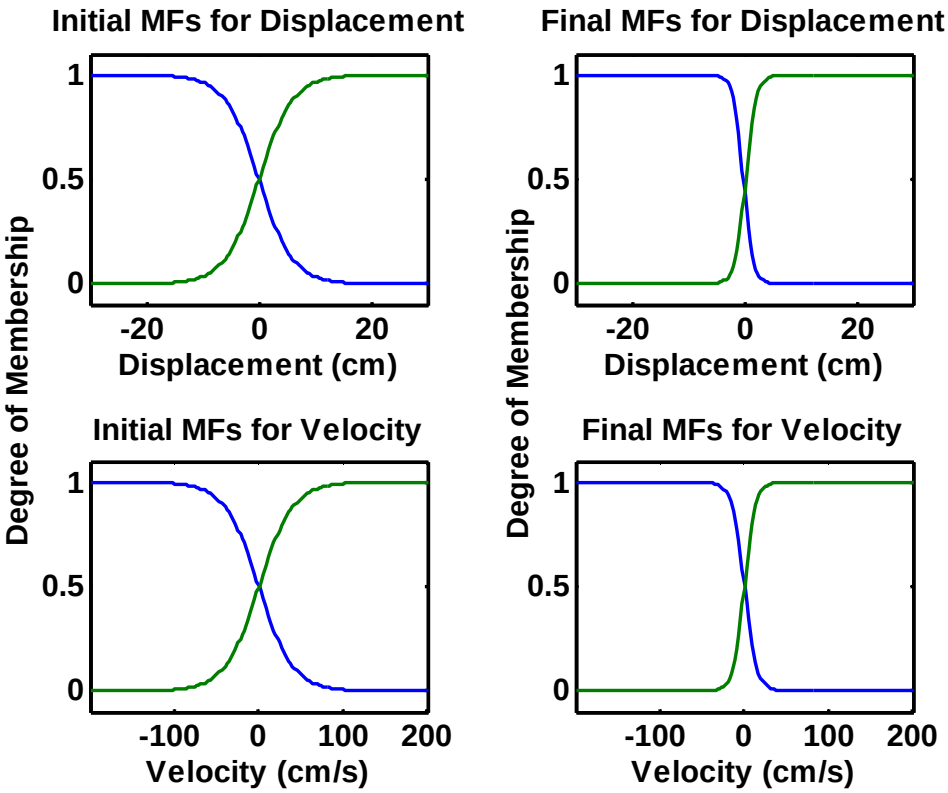

Fig. 104. Membership functions before and after training for 18 cm diameter HDRB with 100 kN axial load

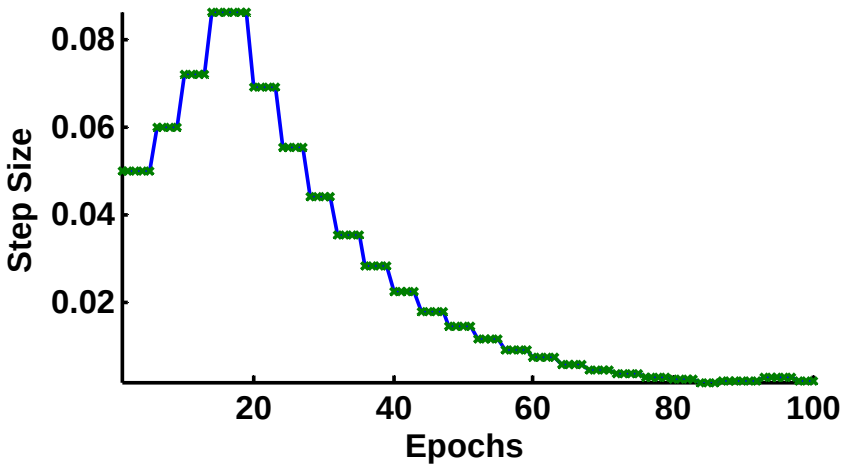

Fig. 105. Variation in step size for 18 cm diameter HDRB with 100 kN axial load

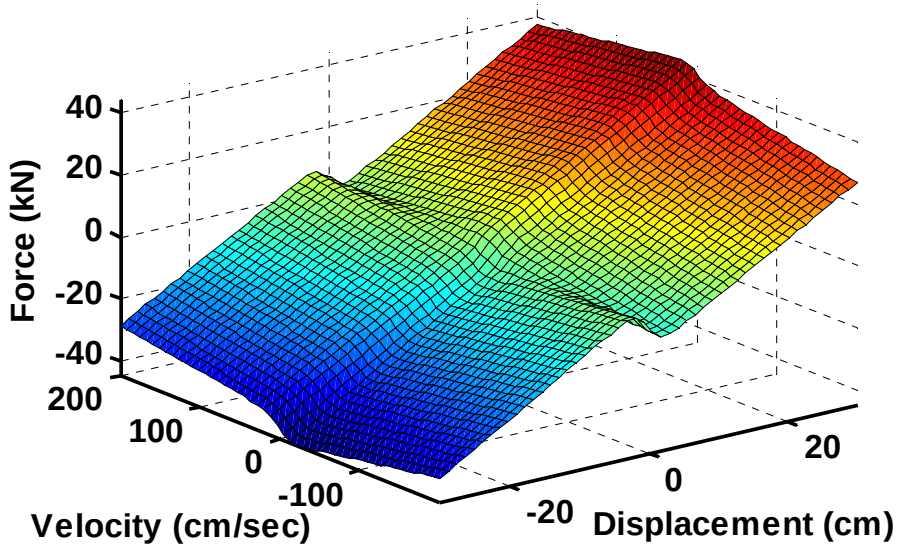

Fig. 106. Fuzzy surface of 18 cm diameter HDRB with 100 kN axial load

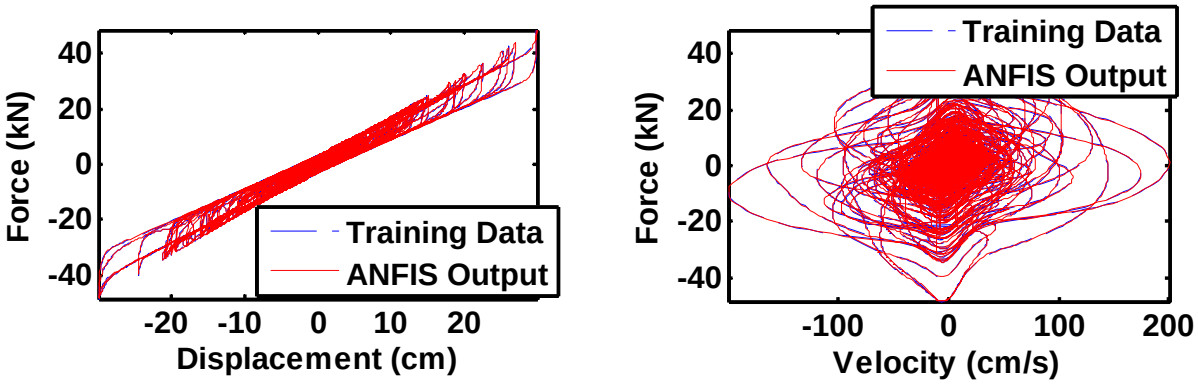

(a) Force versus displacement (b) Force versus velocity

Fig. 107. Training results for 18 cm diameter HDRB with 100 kN axial load

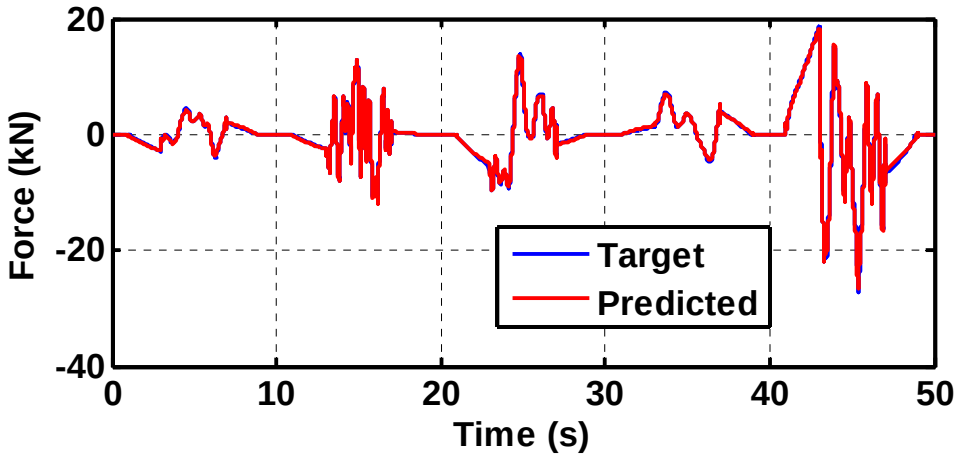

Fig. 108. Validation of force for 18 cm diameter HDRB with 100 kN axial load

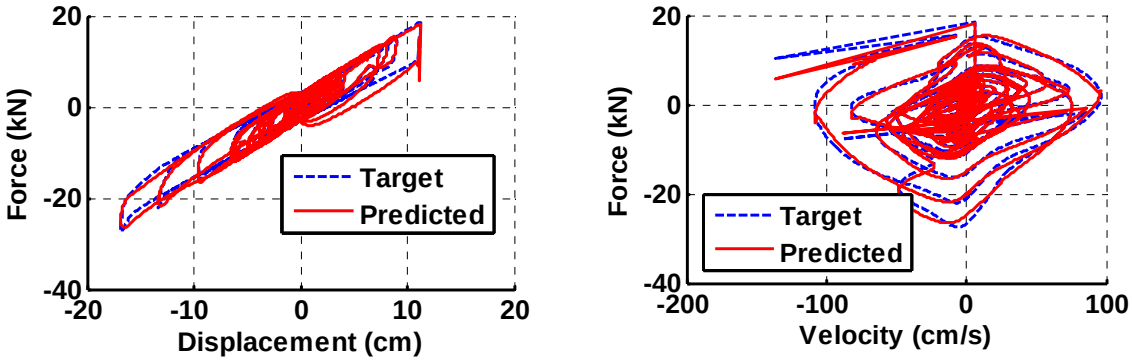

(a) Force versus displacement (b) Force versus velocity

Fig. 109. Validation results for 18 cm diameter HDRB with 100 kN axial load

6.6.3. Determination of Optimal HDRB

To determine which HDRB is optimal for the case study structure, each HDRB FIS is utilized in the MDOF model to isolate the structure. The structures are then subjected to the RSPMatch earthquake for a structure with an isolated period of 2 sec. The results of this analysis, in terms of the performance indices J_1-J_4, are included in Table **7**. It is evident that use of the 18 cm diameter HDRBs results in the most reduction of RMS floor acceleration and the least amplification of base shear. On the

other hand, use of the 18 cm diameter HDRBs also results in the largest peak and RMS base displacement. Due to the 28.2 cm peak base displacement of the 18 cm diameter HDRBs resulting from the RSPMatch earthquake, use of these bearings is not selected for this analysis. Although use of the 14 × 14 cm square HDRBs results in less amplification of base shear than does use of the 20 cm diameter HDRBs, the 20 cm diameter HDRBs are selected for use in this study due to their greater reduction of RMS floor acceleration and smaller peak and RMS base displacement values than the 14 × 14 cm HDRBs. In addition, the 20 cm diameter HDRBs are not significantly scaled from the 22.3 cm diameter HDRB experimentally tested. Fig. 110 shows the force-displacement plot for each of the HDRBs. It is evident that the 20 cm diameter HDRB (HDRB2) is stiffer than the other HDRBs.

Table 7. Comparison of HDRB Devices

	Base Shear J_1	Base Displace-ment J_2 (m)	RMS Base Displace-ment J_3 (m)	RMS Floor Acceler-ation J_4
HDRB 14 × 14 cm (HDRB1)	1.18	0.171	0.024	0.609
HDRB 20 cm diameter (HDRB2)	1.59	0.116	0.013	0.539
HDRB 18 cm diameter (HDRB3)	1.01	0.282	0.039	0.378

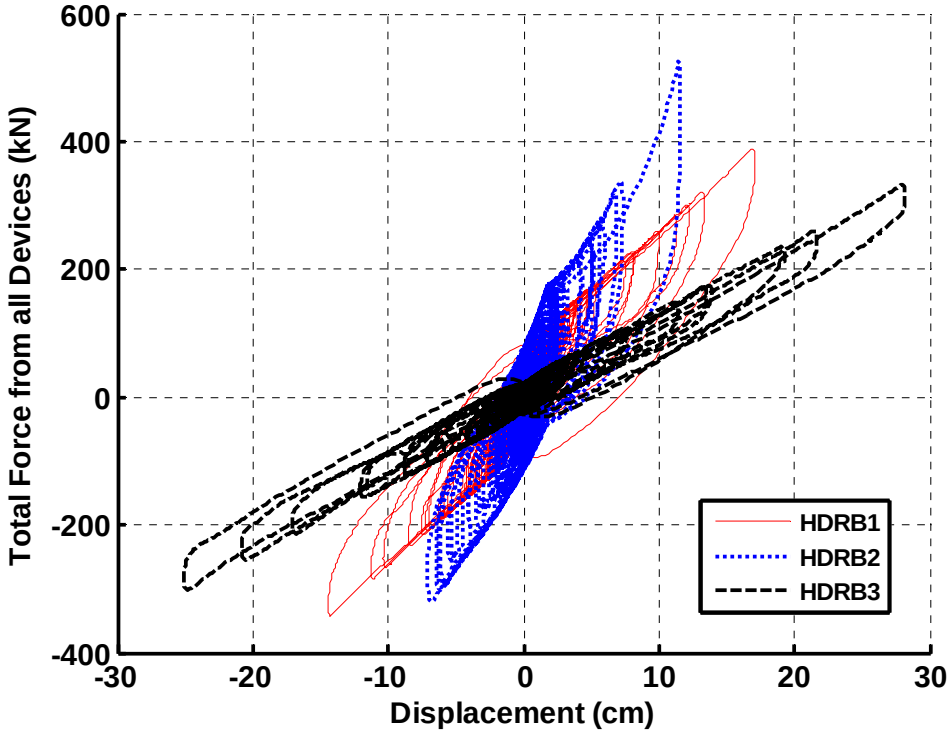

Fig. 110. Force-displacement behavior for each HDRB with 100 kN axial load

6.7. HDRB+SMA1 Optimization

The HDRB+SMA1 isolator involves using 1 mm diameter NiTi SMA wires as diagonal elements within a single HDRB (see Fig. 12). The length of the wires is dictated by the geometry of the bearing. For the 20 cm diameter bearings with height 18 cm that are used in this study, the length of the diagonal wires is approximately 31 cm, assuming 25 cm diameter cover plates are used. The objective in the trial-and-error optimization is to determine the number of wires to be used in each device so that the wires are not overstrained, and yet not to provide so many wires that the device becomes too stiff. In the latter case the horizontal force that the device resists would be transmitted within the SMA wires without taking advantage of the damping characteristics of the HDRBs. The RSPMatch earthquake for a structure with an isolated period of 2 sec is used in the optimization process. After results from a series of numerical solutions are evaluated, the optimal solution selected involves the use of eight

HDRB+SMA1 devices with 60 NiTi SMA wires that are 27 cm long in each of two diagonals.

6.8. HDRB+SMA2 Optimization

The HDRB+SMA2 isolator uses 1 mm diameter NiTi SMA wires to connect adjacent HDRBs (see Figs. 13 and 72). Because the length of the SMA wires does not extend the entire length of the diagonal between adjacent HDRBs, the SMA wires are assumed to be connected to the HDRBs by means of rigid link elements. The same HDRBs are used in the HDRB+SMA2 case as in the HDRB+SMA1 case. Again, eight HDRBs and the RSPMatch earthquake for a structure with an isolated period of 2 sec are used in the optimization process. After results from numerical simulations are compared, 40 wires of 4 m length are used in each diagonal to connect the adjacent HDRBs. There are four braces in the isolation system, one to connect each pair of adjacent HDRBs.

6.9. PPP Optimization

The PPP isolation system (for the first comparison) is optimized using NSGA-II CE. The parameters optimized include the initial prestress in the central cable, the radius of curvature of the spherical top and bottom rolling surfaces, the pile length, the elastic cable stiffness, and the diameter of the ductile rebar at the base of the isolator. The isolation system used in the analysis involves the use of eight PPP isolators. The RSPMatch earthquake for a structure with an isolated period of 2.75 sec is used in the PPP optimization because the isolated period of the structure using PPP isolators tends to be longer than the period of the structure isolated using the other systems. Spherical top and bottom rolling surfaces are selected for the PPP isolators to minimize uplift (Pinochet et al. 2006). Maximum uplift of the PPP isolators in this study is less than 0.5 cm. Additional discussion related to the uplift of the FPS and PPP isolators is included in Section 7.4. It should also be noted that one result of using PPP isolators with

spherical rolling surfaces is the generation of an initial lateral resistance that is relatively small (Besa et al. 2008).

Ranges of appropriate values for the parameters of the PPP isolators are determined based on the experimental testing performed by Pinochet et al. (2006) and by Besa et al. (2008). The ranges are somewhat extended from those used in the testing. The ranges used in this study are 5 to 80 kN for the initial prestress of the central cable, 30 to 150 cm for the radius of curvature of the rolling surfaces, 100 to 250 cm for the length of the pile, 10 to 150 kN/cm for the stiffness of the cable, and 1 to 5 cm for the diameter of the rebar.

Fig. 111 shows the Pareto fronts for the pairs of performance indices after 20 generations of the PPP optimization. Each solution is assigned a rank, ranging from 1 to 4. The lateral and longitudinal diversity of solutions is evident, though some plots show more lateral diversity than longitudinal diversity, while for others the reverse is true. Time to complete the numerical simulation for each generation is 2.5 hours due to the large number of variables per chromosome and the solution of nonlinear equations in the S-function. The population size is 100 for each generation. Fig. 112 shows the solution results from the 1^{st} to the 20^{th} generation. The solution selected as being optimal from the GA optimization is identified in Figs. 111 and 112. Although this solution yields higher values of peak base displacement (J_2) and RMS base displacement (J_3) than many of the other solutions, the values of J_2 and J_3 are acceptable. The main advantage of the solution chosen is that the peak base shear (J_1) and RMS absolute floor acceleration (J_4) are minimized. The solution chosen corresponds to a 73 kN initial prestress in the central cable, a radius of curvature of 50 cm for the spherical top and bottom rolling surfaces, a pile length of 165 cm, an elastic cable stiffness of 104 kN/cm, and the use of four rebars that have a 3.6 cm diameter at the base of the isolator.

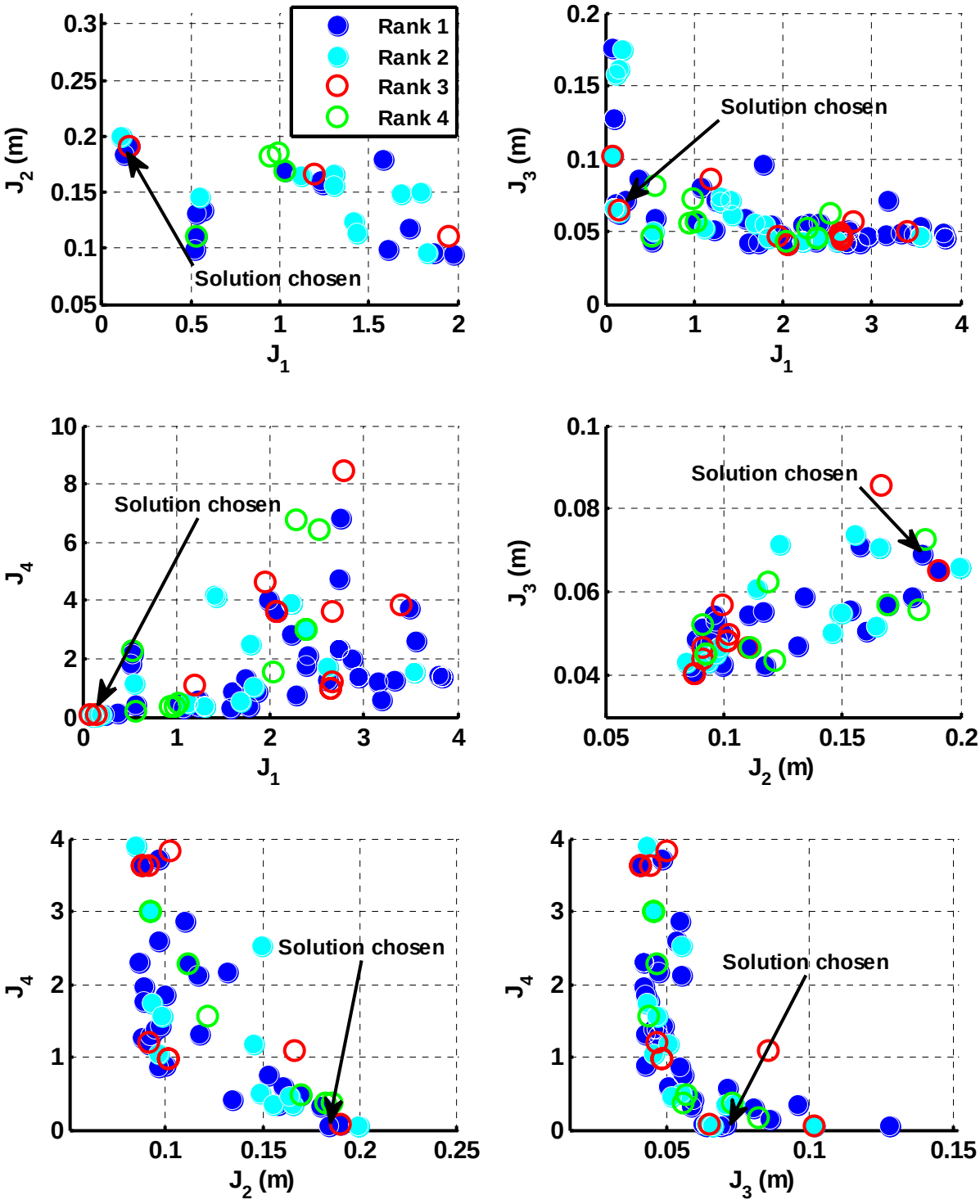

Fig. 111. PPP Pareto fronts after 20 generations

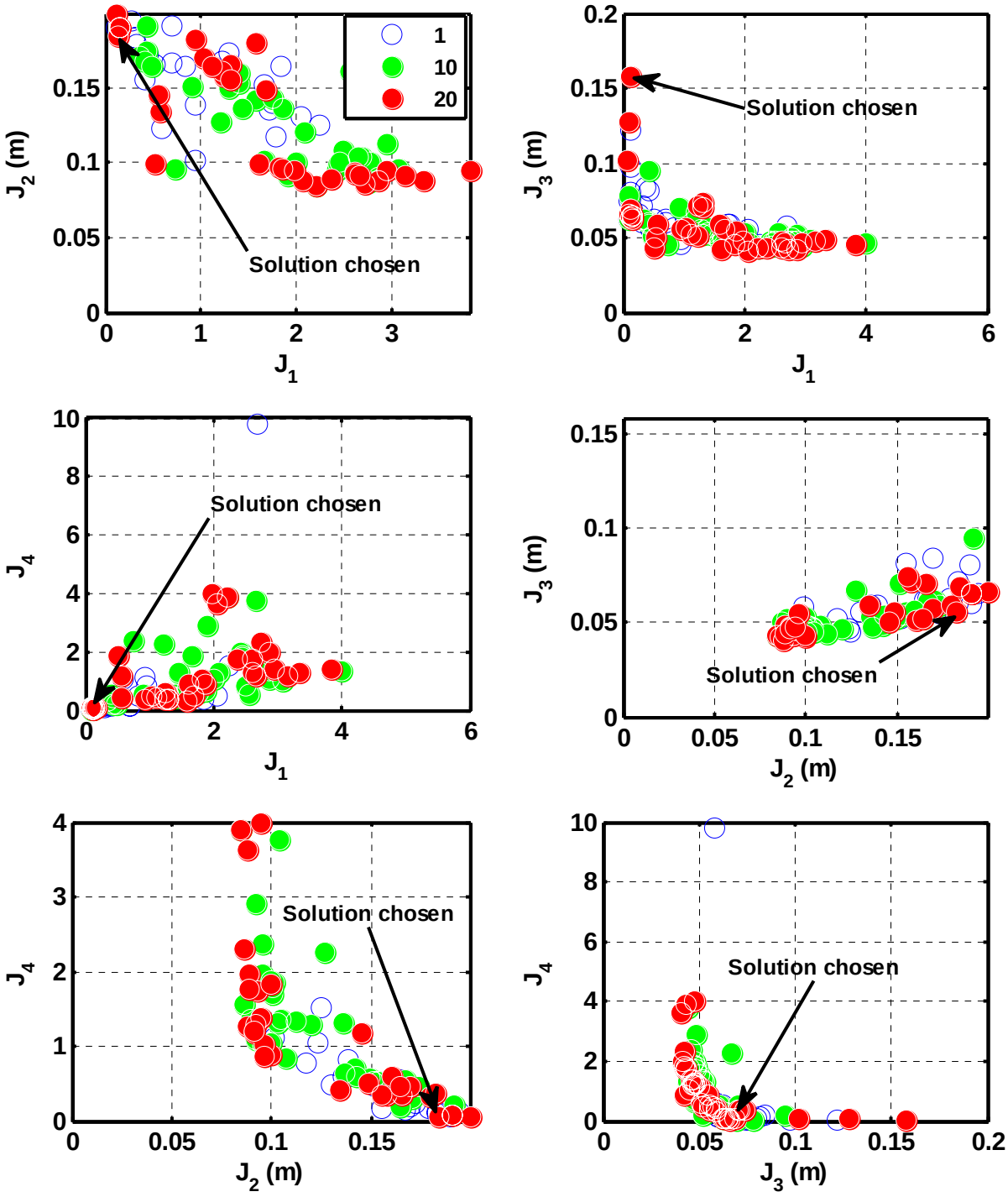

Fig. 112. PPP results after 20 generations

7. COMPARISON OF RESULTS

7.1. General

Two comparisons of the fixed-base and base-isolated structures are made: the first comparison involves the use of the same number of isolation devices that are placed beneath the foundation of the case study structure for each isolation system. In this case the parameters of each type of device are optimized independently of the other systems. As a result the fundamental period of the structure is different for each type of isolator. The process of selecting the parameters of each device used in the first comparison is discussed in Section 6.

The second comparison involves the use of isolation systems with design parameters and the number of isolators selected so that the isolated structure has a fundamental period of 1.0 sec for each configuration. That is, the performance of each isolation system is not necessarily optimized. This period was selected because it is sufficiently long to cause the base-isolated structures to have improved performance over the fixed-base structure (see Section 2.1), and it is a reasonable period for the isolated structure to achieve using each type of isolation system.

The first comparison is more realistic from a practical point of view in the sense that when a given isolation system is to be implemented and the total number of isolators has been determined, the parameters of that system are selected independently of the behavior of other isolation systems. However, the second comparison is performed to enable further study of each isolation system compared to the other isolation systems. In the second comparison, each isolation system has approximately the same stiffness, and therefore the damping ratio of each isolation system is the principal characteristic that distinguishes the behavior of one isolation system from another.

7.2. Comparison 1: Individual Optimizations

7.2.1. Selected Parameters

As mentioned in Section 6, the devices were optimized using the NSGA-II CE optimization algorithm or a trial-and-error approach. Each type of optimized system in

Comparison 1 uses eight isolators. The selected parameters for each FPS bearing are a coefficient of friction μ = 0.03 and a radius of curvature R = 3.5 m. The HDRBs selected correspond to the second HDRB considered (see Table 5 and Figs. 97-103). This bearing is scaled to a diameter of 20 cm and a height of 18 cm from the 22.3 cm diameter bearing of height 18 cm that was experimentally tested. The HDRBs used in the hybrid HDRB+SMA1 and HDRB+SMA2 cases are the same as those used in the HDRB only case. The HDRB+SMA1 isolation case involves the use of 60 wires in each brace diagonal. The 31 cm length of each wire is dictated by the dimensions of the bearing, assuming a cover plate width of 25 cm. If braces are located on two sides of the bearing, 30 wires are placed in each of four brace diagonals, with two diagonals on each side. The HDRB+SMA2 case involves the use of 30 wires that are 4 m long in each diagonal. Again, if braces are on two sides of the HDRBs, 20 wires are placed in each of four diagonals. The optimization of the PPP isolators yielded the choice of a 73 kN initial prestress in the central cable, a radius of curvature of 50 cm for the spherical top and bottom rolling surfaces, a pile length of 165 cm, an elastic cable stiffness of 104 kN/cm, and the use of four rebars that have a 3.6 cm diameter at the base of the isolator.

To determine the fundamental period of each structure that is isolated using the system parameters listed, a Fast Fourier Transform (FFT) is performed on the displacement-time data that result from giving the structure a small initial horizontal displacement at each story, and subsequently allowing the structure to vibrate freely. As can be determined from the FFT plots in Fig. 113, the fundamental period of the isolated structure with eight FPS, HDRB, HDRB+SMA1, HDRB+SMA2, or PPP isolators is 3.8, 1.1, 0.71, 0.96, or 4.1 sec, respectively. It is apparent that the FPS and PPP isolated structures have significantly longer periods than those structures isolated using HDRBs or HDRBs with SMA wires. As expected intuitively, the isolated periods of the HDRB+SMA1 and HDRB+SMA2 structures are lower than those of the HDRB structure because the SMA wires increase the stiffness of the isolation system.

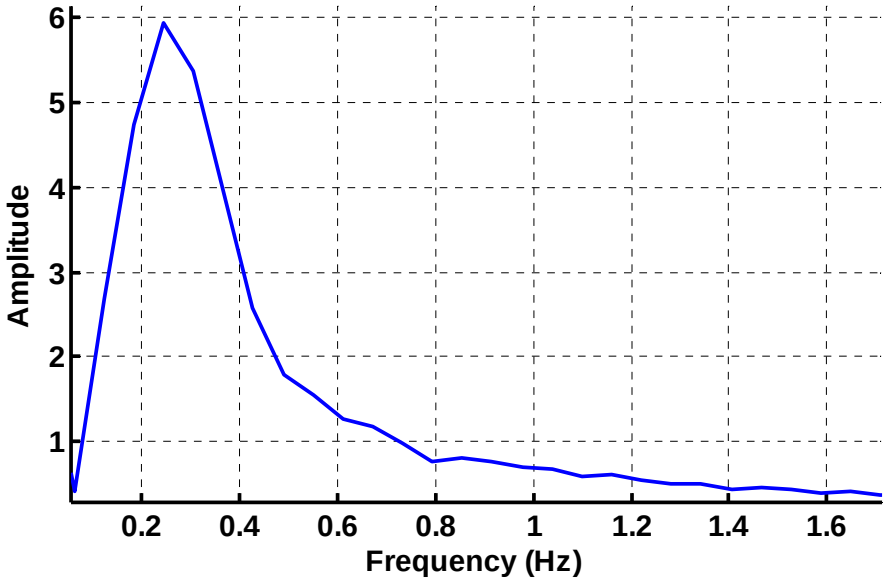

(a)

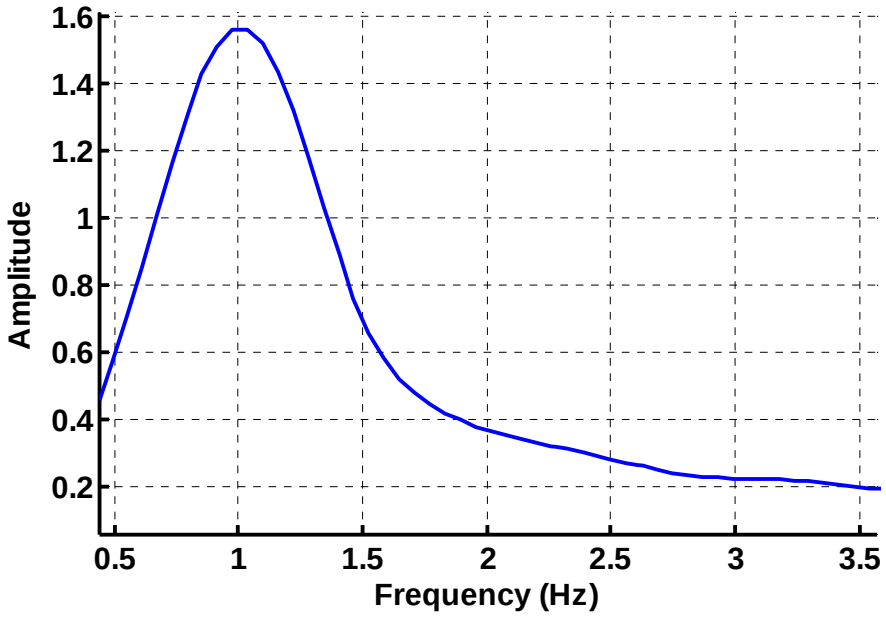

(b)

Fig. 113. Comparison 1: FFT for base-isolated structure (a) FPS, (b) HDRB, (c) HDRB+SMA1, (d) HDRB+SMA2, (e) PPP

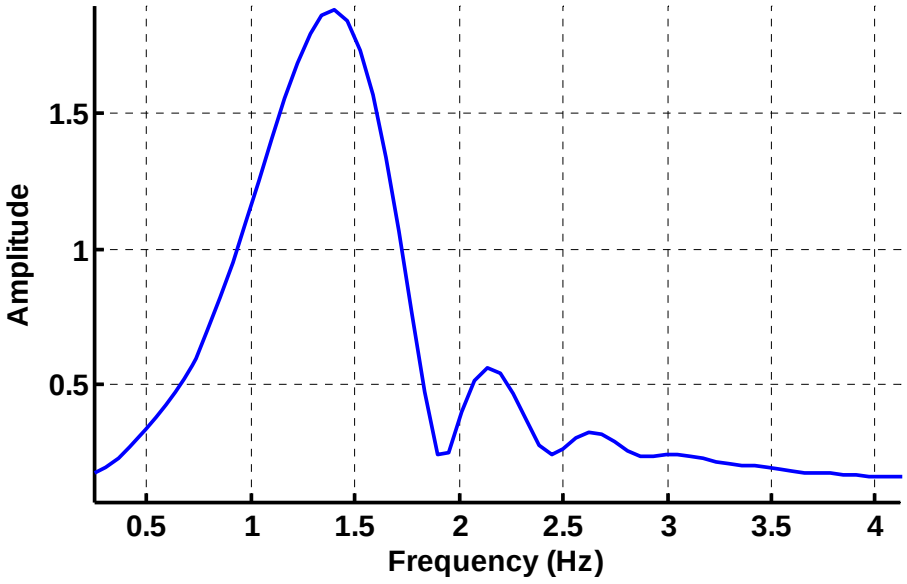

(c)

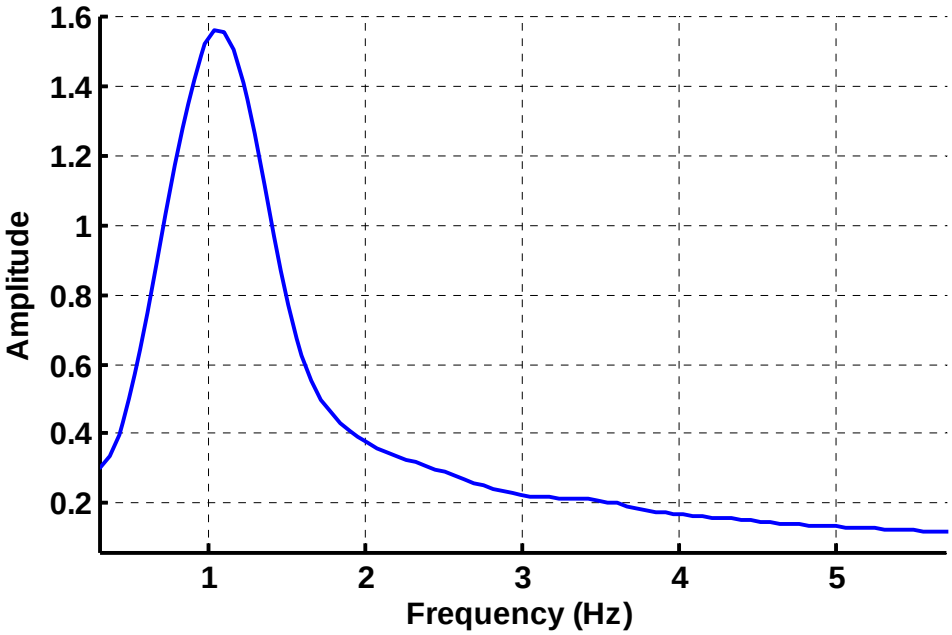

(d)

Fig. 113. Continued

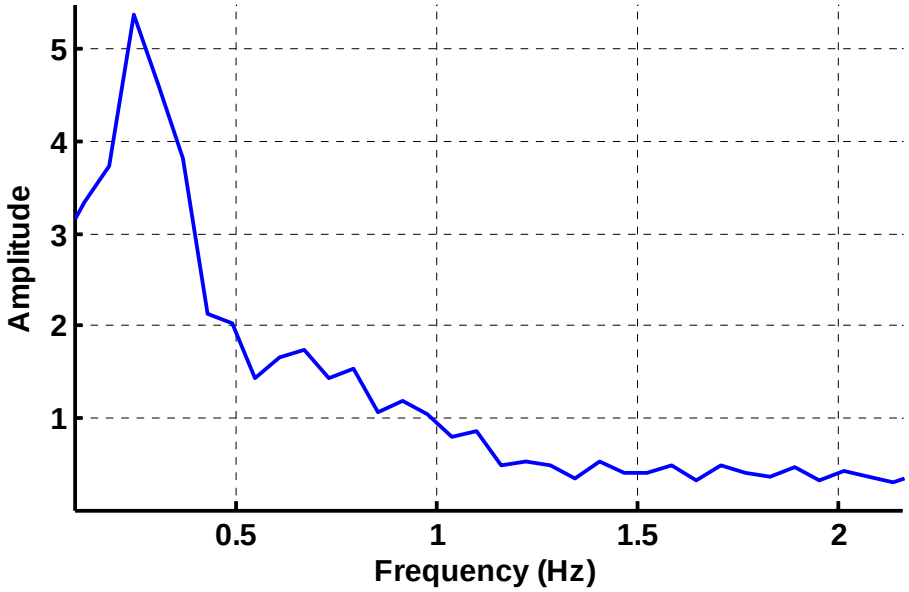

(e)

Fig. 113. Continued

The equivalent viscous damping ratio for each base isolation case is calculated using the logarithmic decrement method. To apply this method, the decay of motion of the structure in free vibration over time that results from the small initial horizontal displacement at each story level is measured. To calculate the damping ratio, the following formula is used (Chopra 2001):

$$\delta = (1/j)\ln(u_1/u_{j+1}) \simeq 2\pi\zeta \tag{35}$$

where δ is the logarithmic decrement, j is the number of cycles of displacement, u_1 is the peak horizontal displacement of the first cycle, u_{j+1} is the peak horizontal displacement of the j+1th cycle, and ζ is the equivalent viscous damping ratio. The damping values for each case, including intrinsic damping from the structure and hysteretic damping from each isolation system, are reported in Table 8.

Table 8. Comparison 1: Equivalent Viscous Damping Values

	Equivalent viscous damping (%)
FPS	9
HDRB	24
HDRB+SMA1	12
HDRB+SMA2	20
PPP	7

7.2.2. Graphical Results from Each Earthquake

Using the optimized isolators, the performance of each isolated structure is assessed through numerical simulation by subjecting the structure to the suite of earthquake records listed in Table 3. Graphical results from each earthquake, including time-histories of base displacement, interstory drift, and absolute floor acceleration, and a graph of the total force exerted by all isolators with the corresponding displacement of the isolators, are presented in Figs. 114-161.

It can be seen from Figs. 114, 120, 126, 138, 150, and 156 that the structure isolated with the eight PPP devices has a small residual displacement, on the order of 2-3 cm, resulting from several of the earthquakes. Another observation is that the interstory drift between the base and 1st floors is generally greater than that between the 1st and 2nd floors for both the fixed-base and base-isolated structures (see Figs. 115 and 116, for example). This is because although the stiffness of the first story is approximately 35% larger than that of the second story, the mass of the first story is approximately 150% greater than that of the second story. However, the interstory drift is very small on an absolute scale and not significant for either the fixed-base or the base-isolated cases due to the high stiffness of the masonry structure. The maximum peak interstory drift resulting from any of the earthquakes is 0.18 cm, which corresponds to a 0.07% drift (see Fig. 127). This interstory drift occurs for the fixed-base structure during the

Tarapacá earthquake. The reduction in interstory drift of the base-isolated structure from that of the fixed-base structure is evident in all of the earthquakes, except for the scaled Kobe earthquake. The maximum reduction of interstory drift (a reduction of 98%) occurs for the PPP isolation system during the 1981 Chile earthquake.

There is a type of "hanging" in the base displacement response of the FPS isolated structure due to the El Centro and scaled Mexico City earthquakes (see Figs. 132 and 144). A study is performed using FPS isolators with various friction coefficients and a radius of curvature of 3.5 m. The "hanging" effect in the base displacement is not evident for friction coefficients less than 0.01, while it is evident for friction coefficients in the range of 0.01 – 0.05. Thus, the "hanging" effect in the base displacement for the El Centro and scaled Mexico City earthquakes can be attributed to the friction of the FPS isolators.

For all of the earthquakes the acceleration of the second floor of the fixed-base structure is greater than that of the first floor (see Figs. 117 and 118, for example). The fixed-base structure also often experiences an amplification of floor acceleration from that of the ground motion. These results have also been observed by other researchers (Dolce et al. 2007). They can be attributed to the stiffness and mass characteristics of the structure, and the fact that the fixed-base structure does not behave as a rigid body. However, the accelerations of the first and second floors of the base-isolated structure are approximately equal for a given isolation system because the isolation systems cause the structure to move almost as a rigid body (see Figs. 117 and 118, for example). In response to certain earthquakes, there is a significant amount of oscillation in the FPS acceleration response (see Figs. 135, 136, 147, and 148).

Upon examination of the device force-displacement plots resulting from each earthquake for each of the isolation systems (see Figs. 119, 125, 131, 137, 143, 149, 155, and 161), the greater stiffness of the HDRB, HDRB+SMA1, and HDRB+SMA2 isolation systems compared to the FPS and PPP isolated systems is apparent. Although lower stiffness is generally desirable for the isolation systems in terms of acceleration and shear quantities, it also results in higher base displacements. The isolation systems

involving the use of HDRBs are relatively stiff compared to the FPS and PPP isolation systems; this increased stiffness serves to maintain reasonable displacements of the HDRBs and prevent the SMA wires from being overstrained.

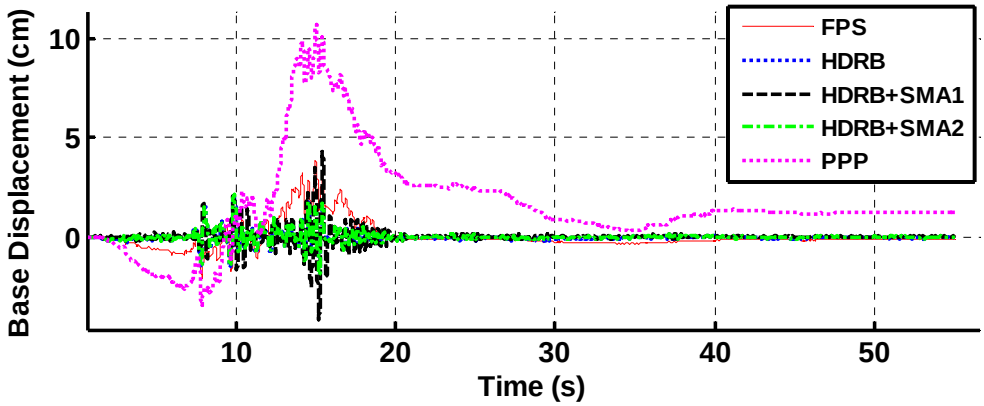

Fig. 114. Comparison 1: Base displacement from 1981 Chile earthquake

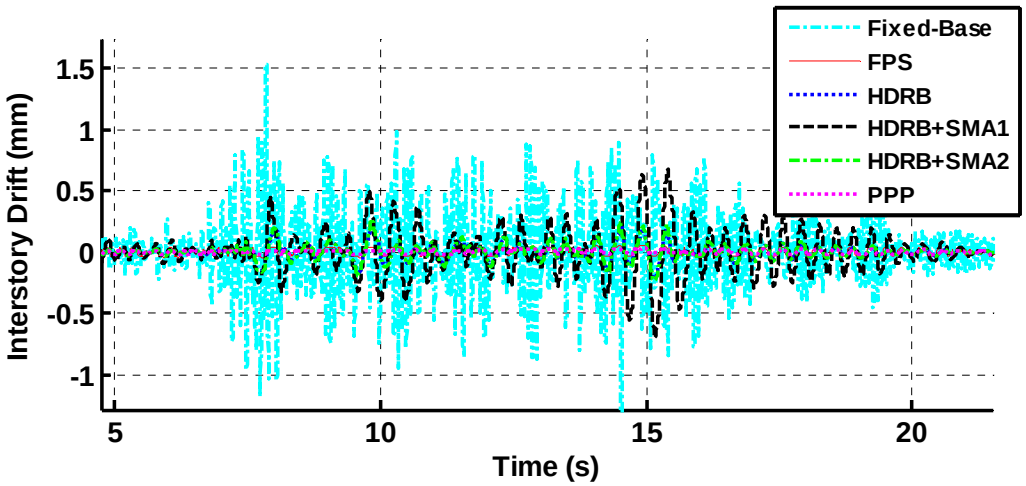

Fig. 115. Comparison 1: Interstory drift between base and 1st floor from 1981 Chile earthquake

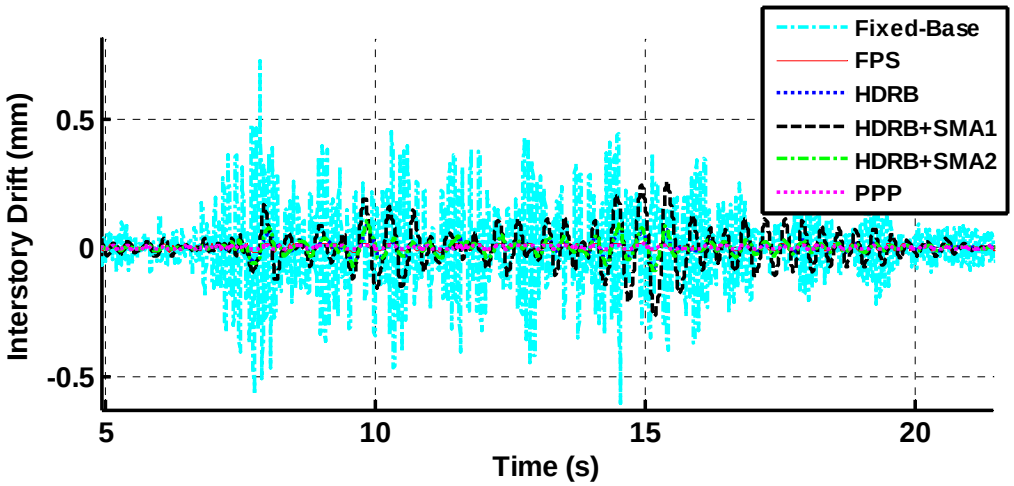

Fig. 116. Comparison 1: Interstory drift between 1st and 2nd floors from 1981 Chile earthquake

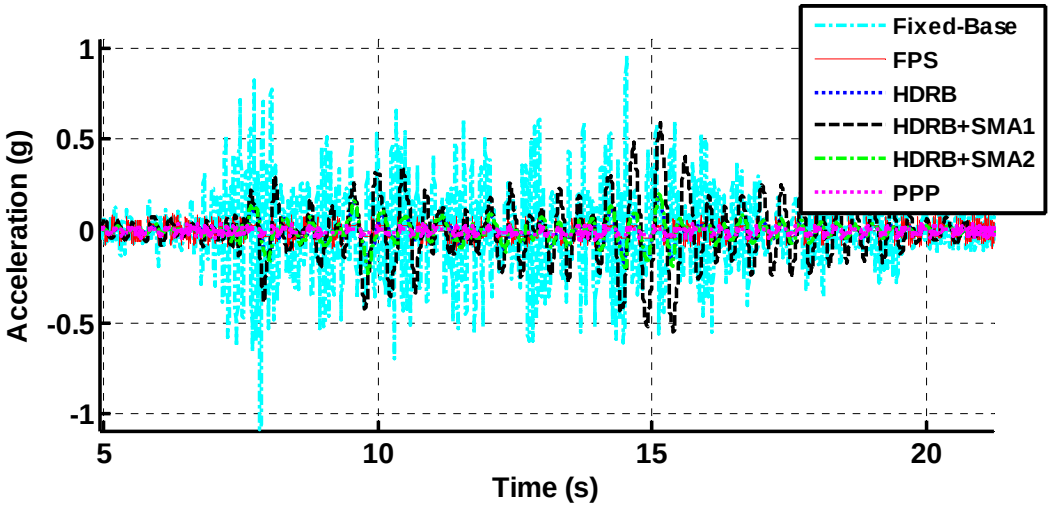

Fig. 117. Comparison 1: Absolute acceleration of 1st floor from 1981 Chile earthquake

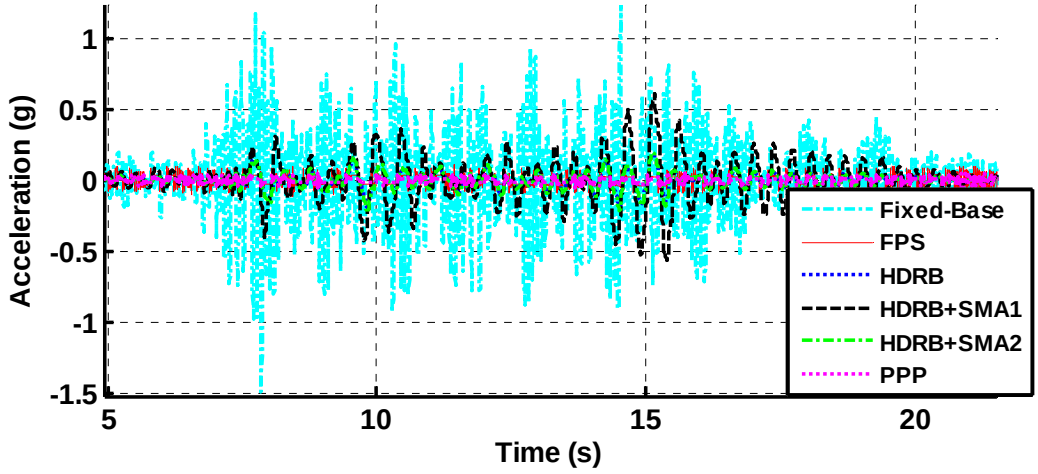

Fig. 118. Comparison 1: Absolute acceleration of 2nd floor from 1981 Chile earthquake

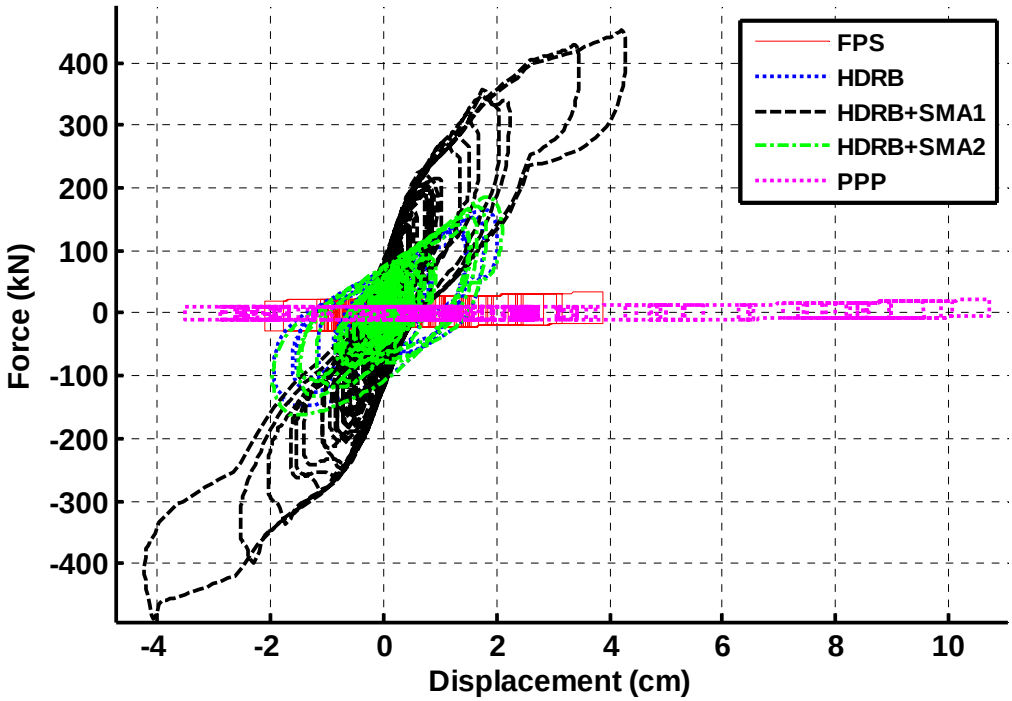

Fig. 119. Comparison 1: Total force from all isolation devices from 1981 Chile earthquake

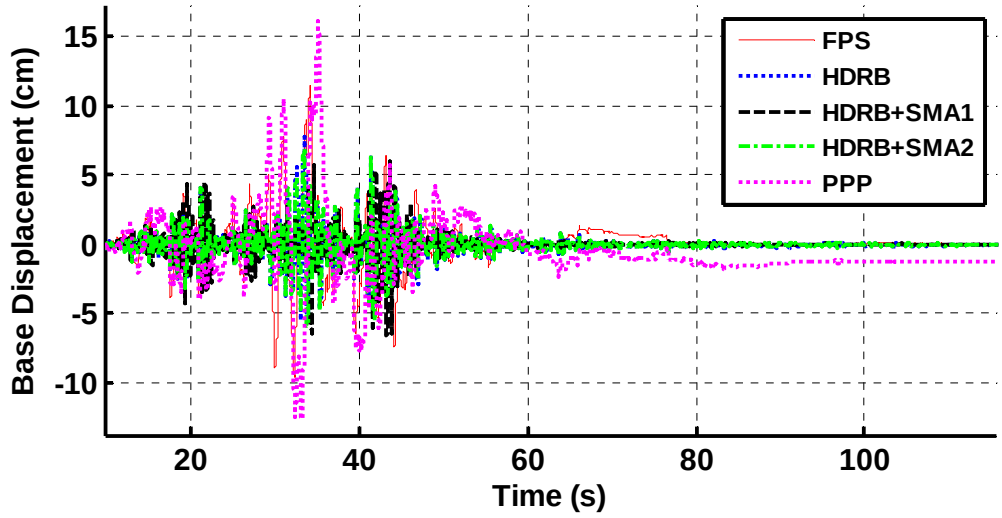

Fig. 120. Comparison 1: Base displacement from 1985 Llolleo, Chile, earthquake

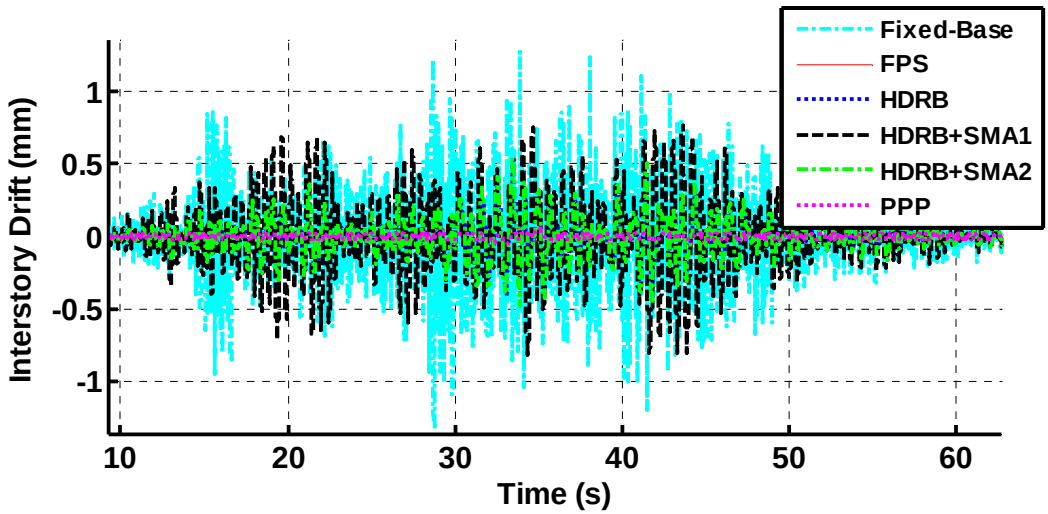

Fig. 121. Comparison 1: Interstory drift between base and 1st floor from 1985 Llolleo, Chile, earthquake

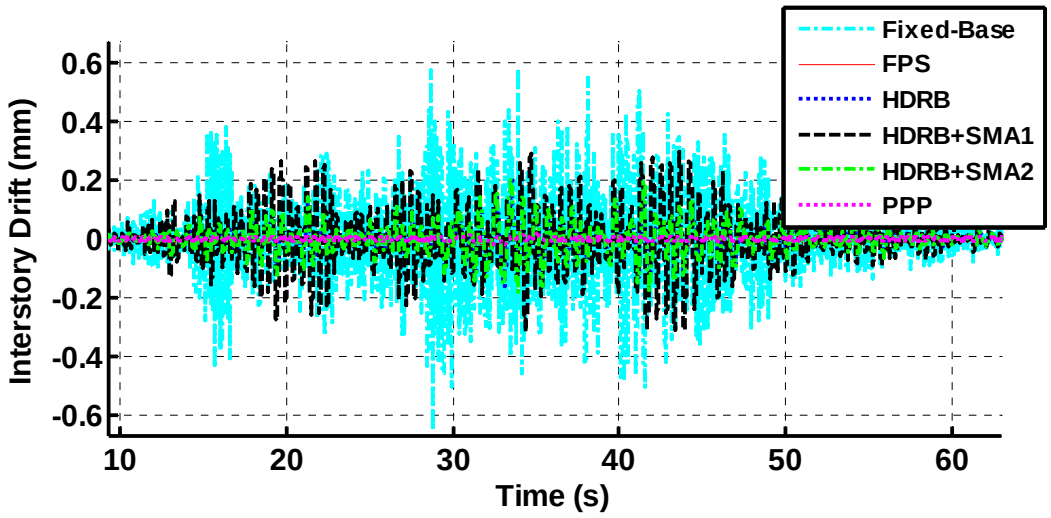

Fig. 122. Comparison 1: Interstory drift between 1st and 2nd floors from 1985 Llolleo, Chile, earthquake

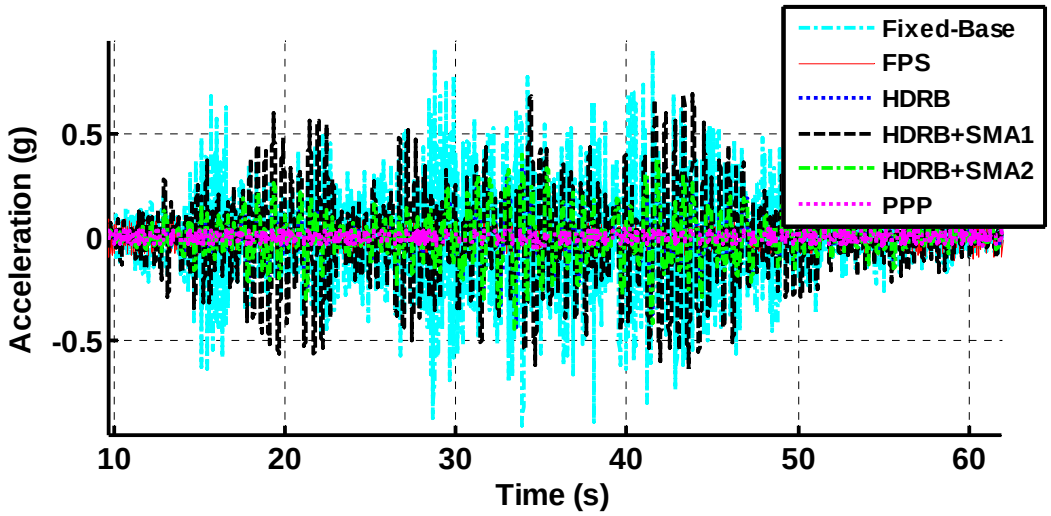

Fig. 123. Comparison 1: Absolute acceleration of 1st floor from 1985 Llolleo, Chile, earthquake

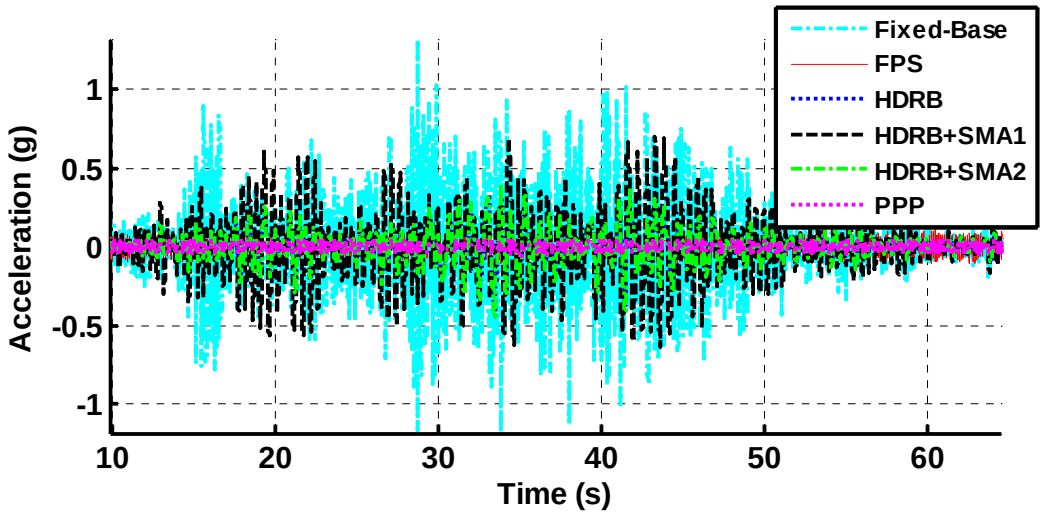

Fig. 124. Comparison 1: Absolute acceleration of 2nd floor from 1985 Llolleo, Chile, earthquake

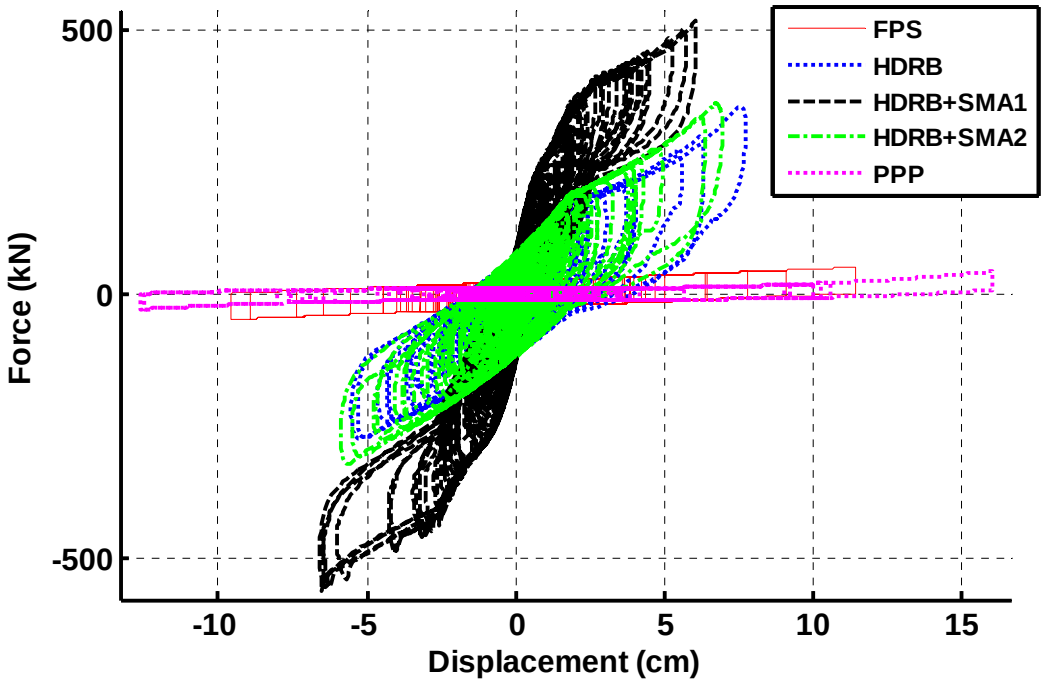

Fig. 125. Comparison 1: Total force from all isolation devices from 1985 Llolleo, Chile, earthquake

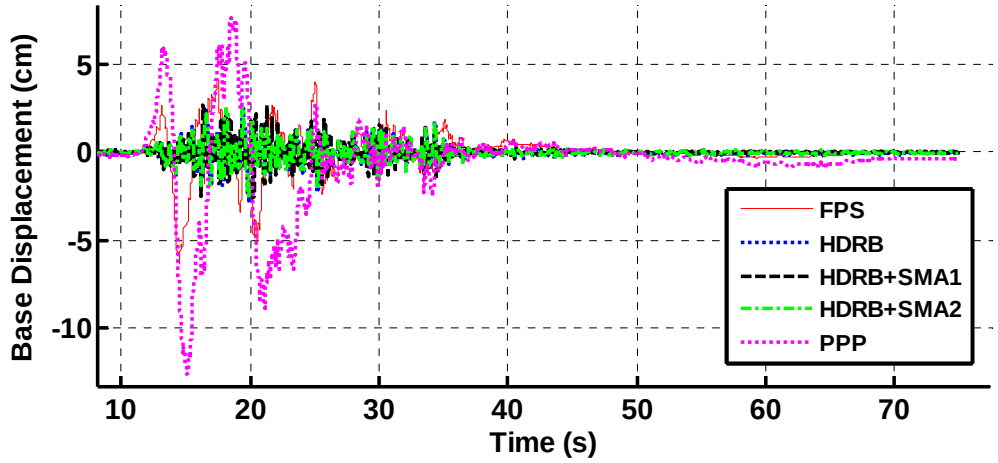

Fig. 126. Comparison 1: Base displacement from 2005 Tarapacá, Chile, earthquake

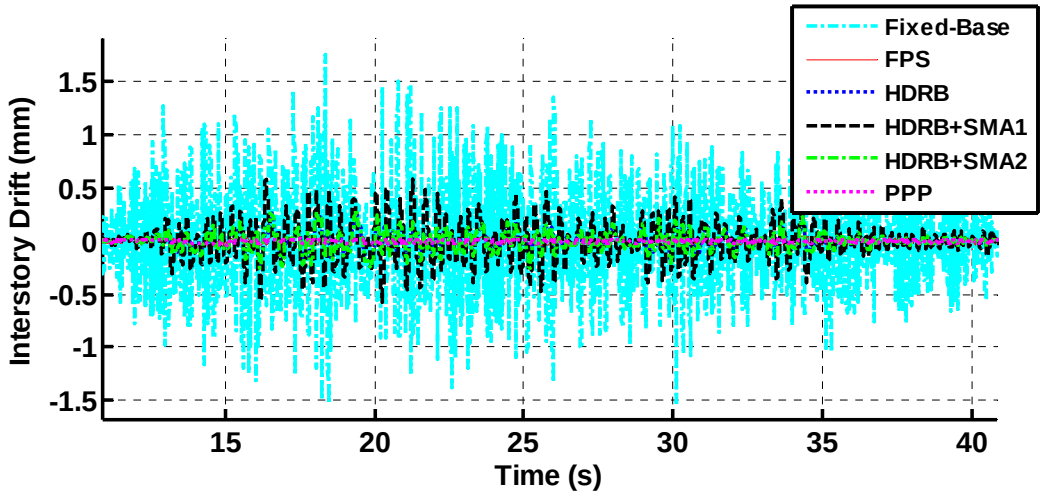

Fig. 127. Comparison 1: Interstory drift between base and 1st floor from 2005 Tarapacá, Chile, earthquake

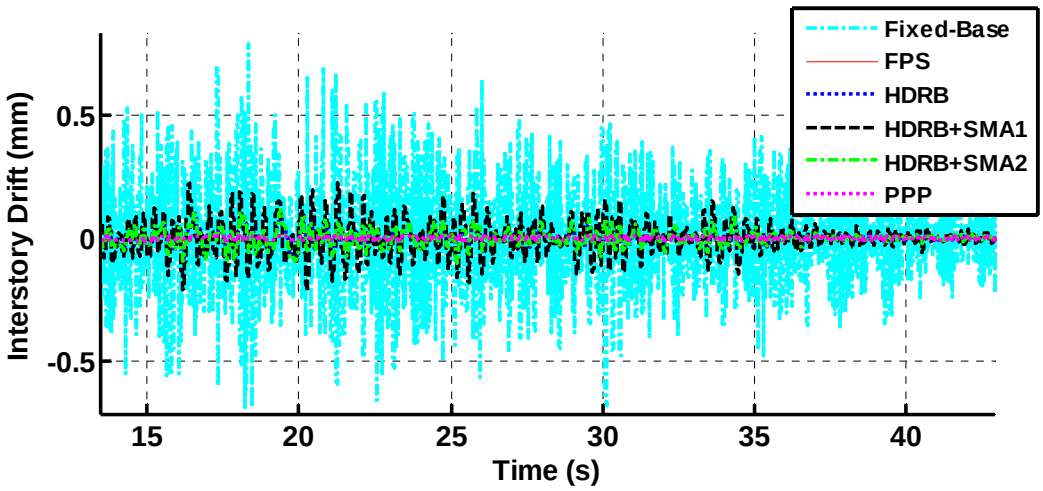

Fig. 128. Comparison 1: Interstory drift between 1st and 2nd floors from 2005 Tarapacá, Chile, earthquake

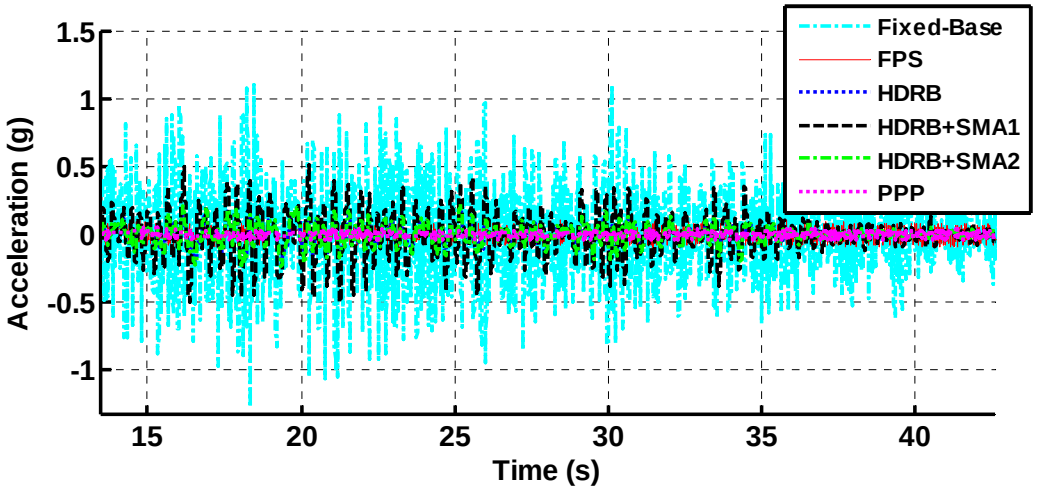

Fig. 129. Comparison 1: Absolute acceleration of 1st floor from 2005 Tarapacá, Chile, earthquake

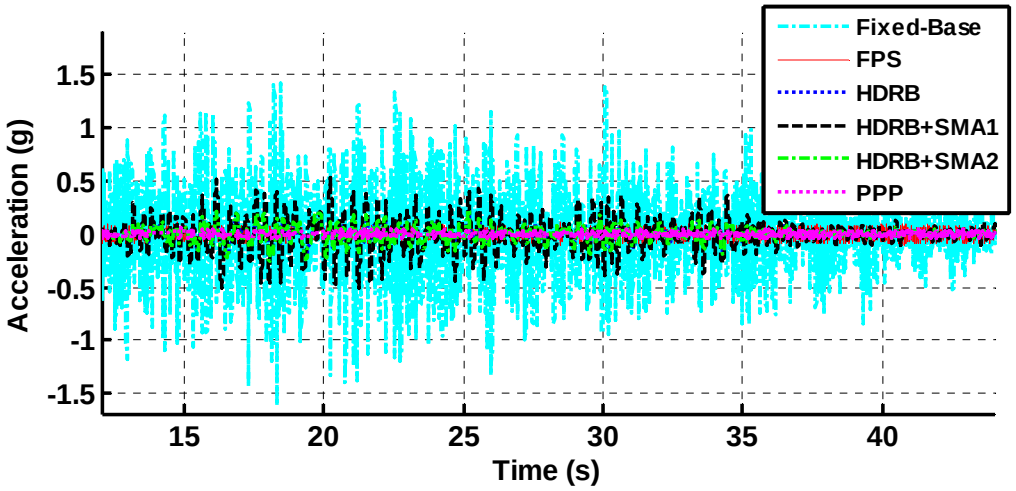

Fig. 130. Comparison 1: Absolute acceleration of 2nd floor from 2005 Tarapacá, Chile, earthquake

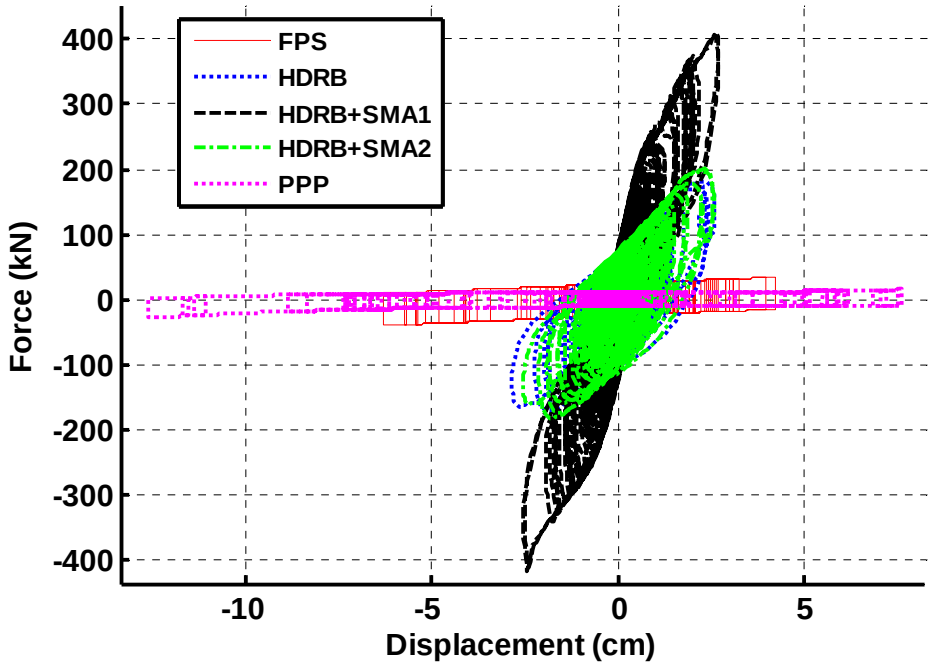

Fig. 131. Comparison 1: Total force from all isolation devices from 2005 Tarapacá, Chile, earthquake

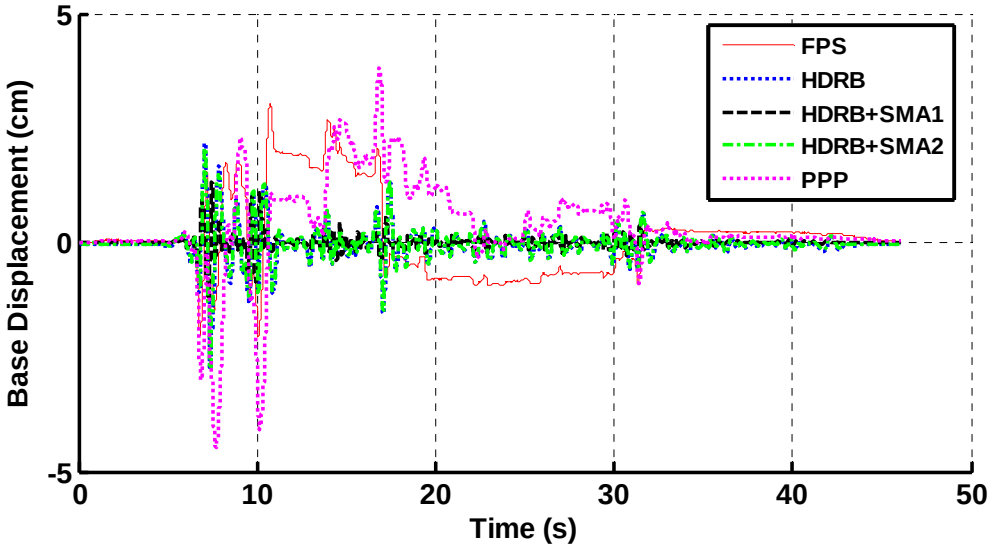

Fig. 132. Comparison 1: Base displacement from El Centro earthquake

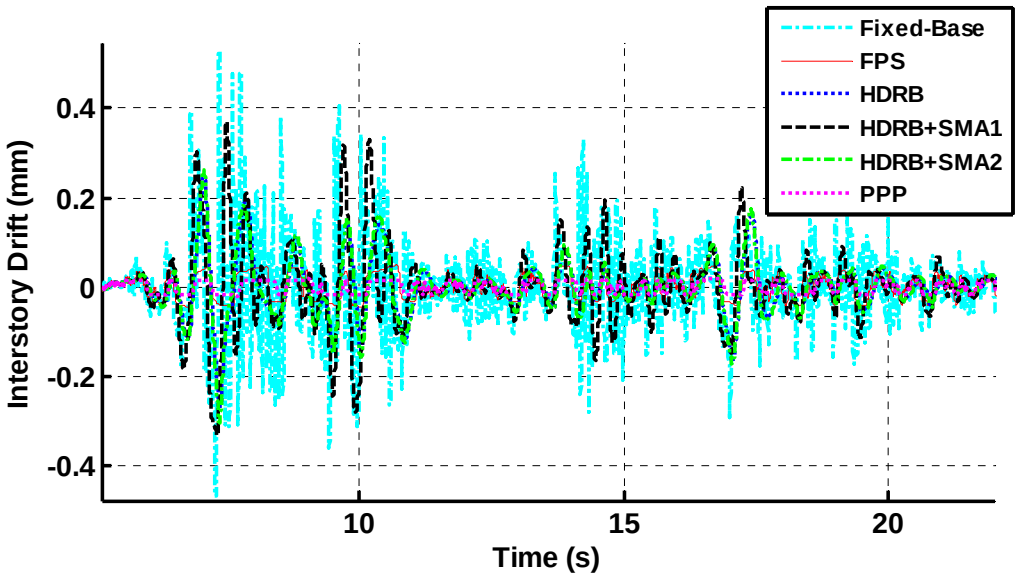

Fig. 133. Comparison 1: Interstory drift between base and 1st floor from El Centro earthquake

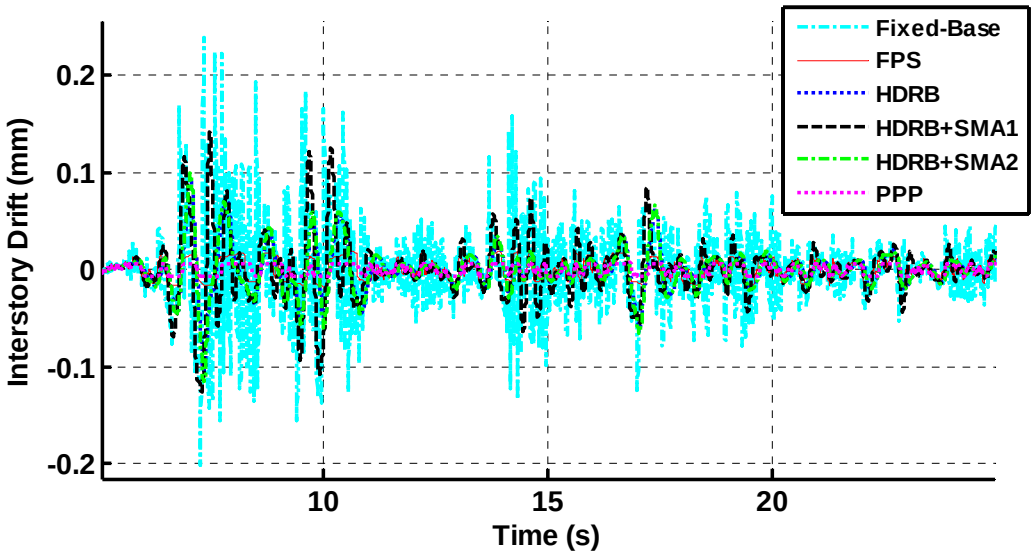

Fig. 134. Comparison 1: Interstory drift between 1st and 2nd floors from El Centro earthquake

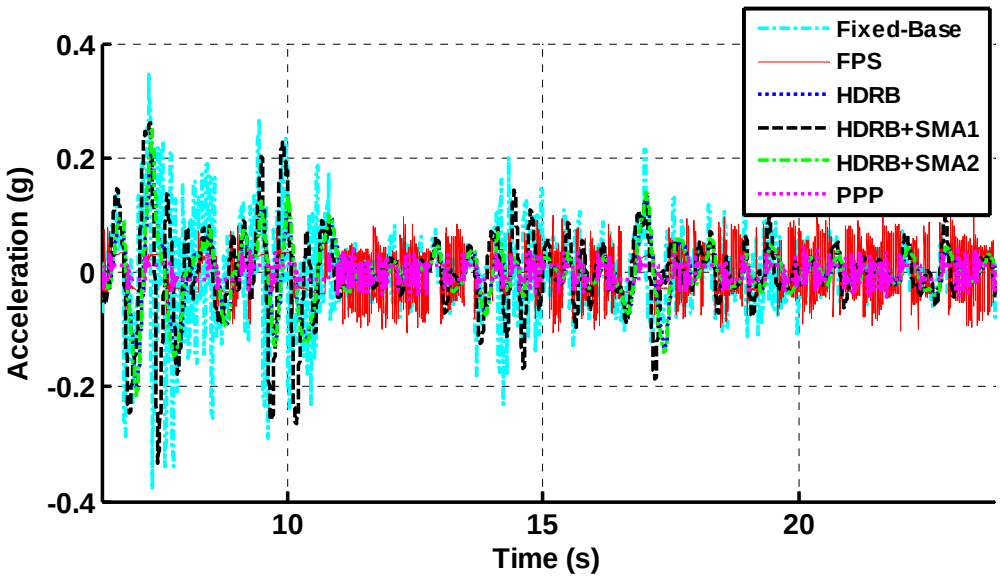

Fig. 135. Comparison 1: Absolute acceleration of 1st floor from El Centro earthquake

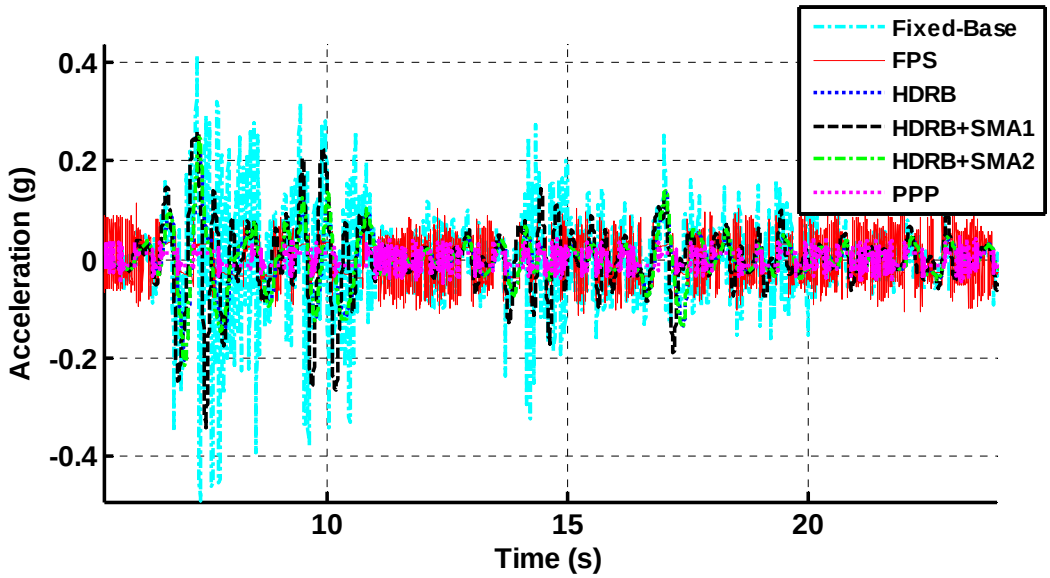

Fig. 136. Comparison 1: Absolute acceleration of 2nd floor from El Centro earthquake

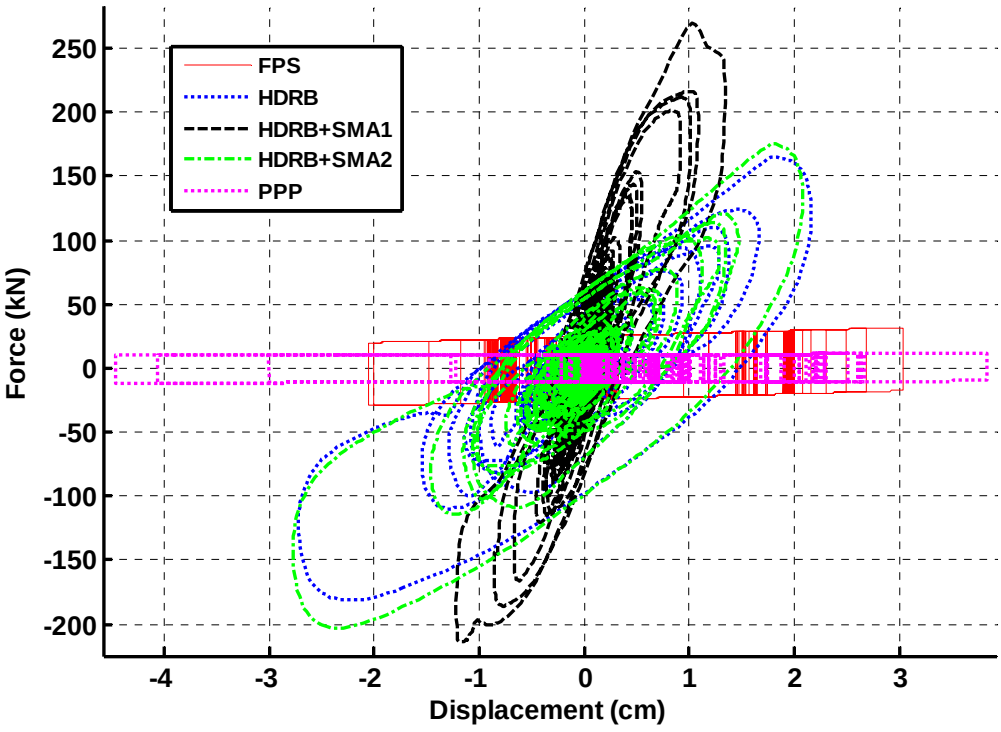

Fig. 137. Comparison 1: Total force from all isolation devices from El Centro earthquake

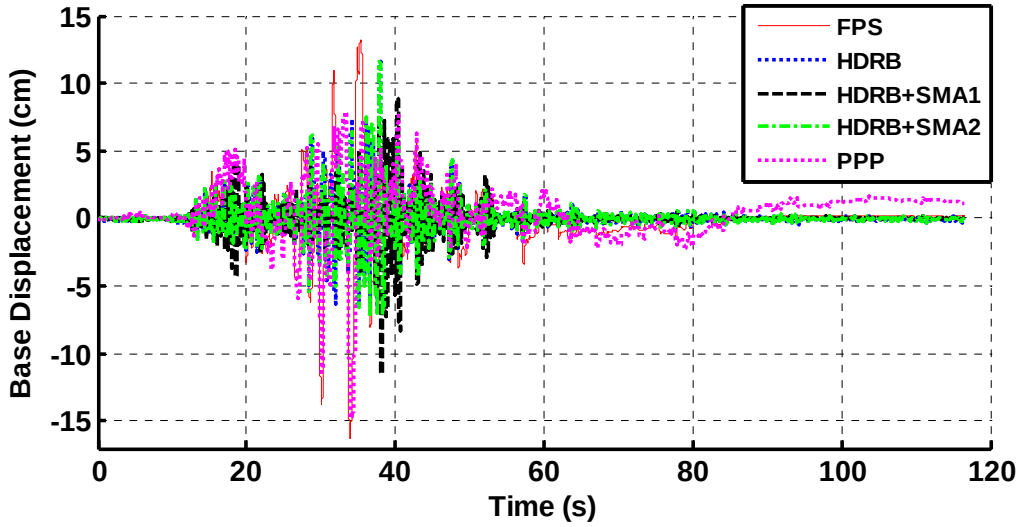

Fig. 138. Comparison 1: Base displacement from RSPMatch earthquake

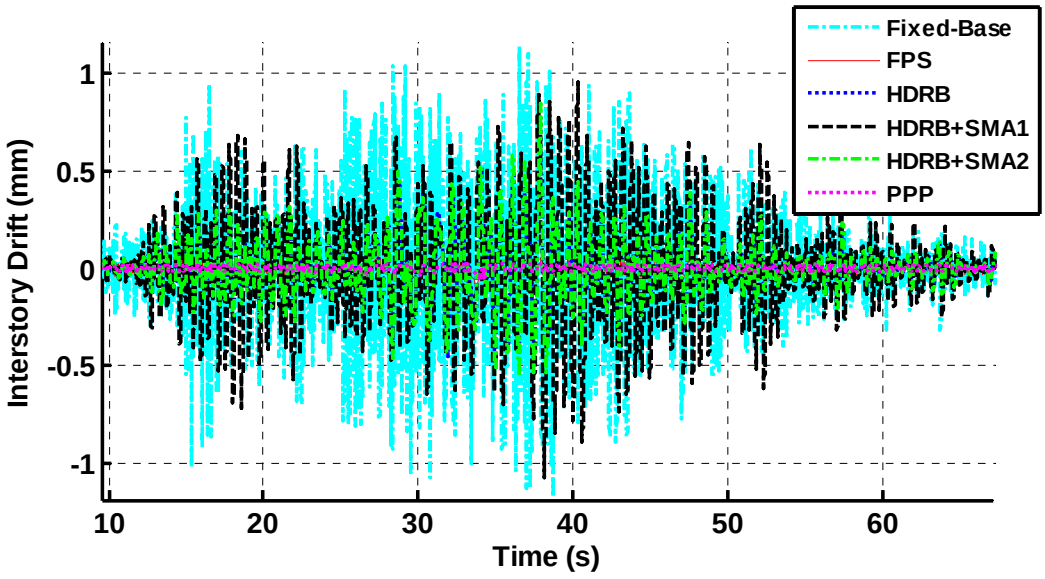

Fig. 139. Comparison 1: Interstory drift between base and 1st floor from RSPMatch earthquake

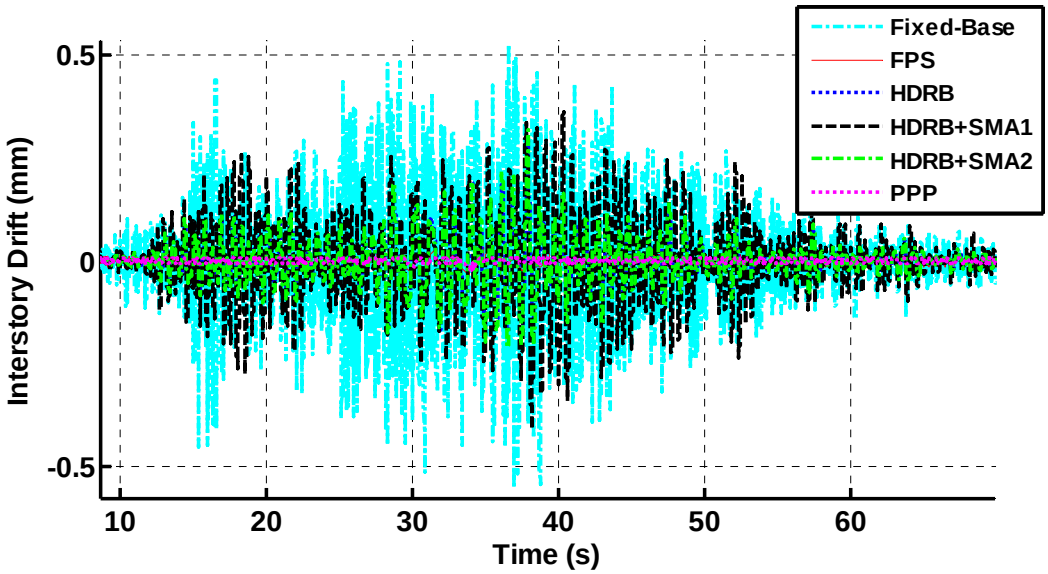

Fig. 140. Comparison 1: Interstory drift between 1st and 2nd floors from RSPMatch earthquake

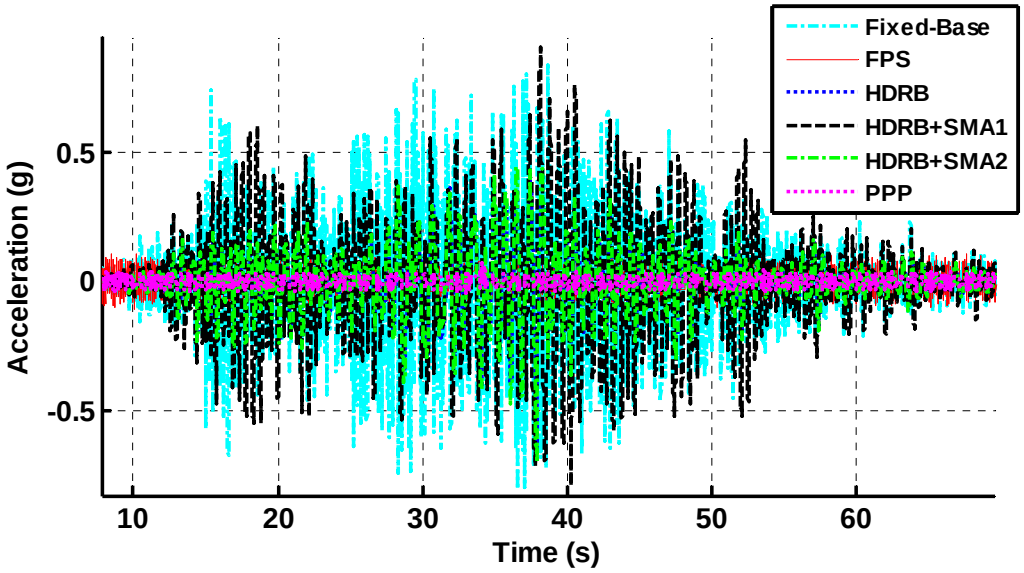

Fig. 141. Comparison 1: Absolute acceleration of 1st floor from RSPMatch earthquake

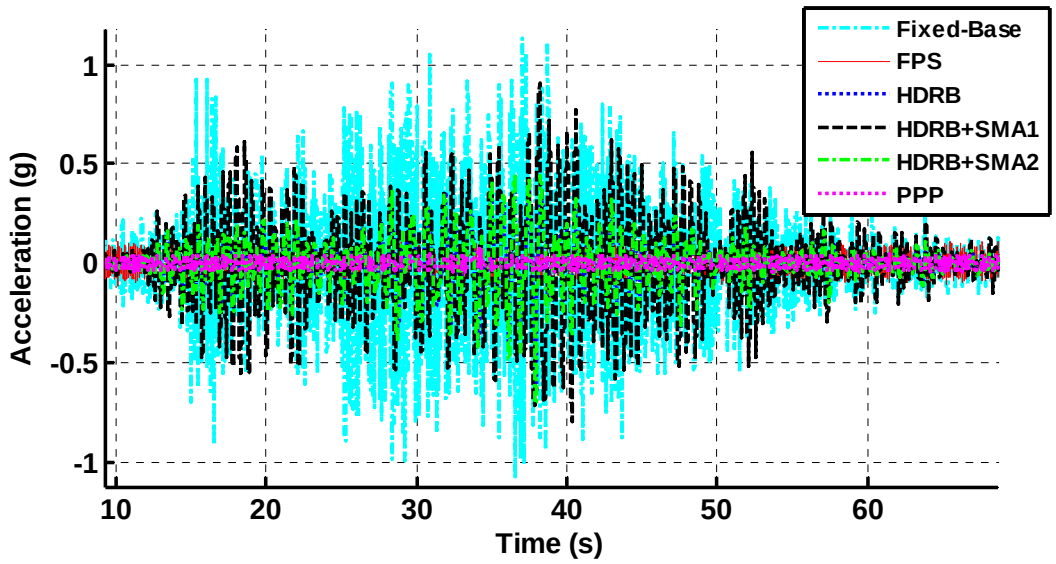

Fig. 142. Comparison 1: Absolute acceleration of 2nd floor from RSPMatch earthquake

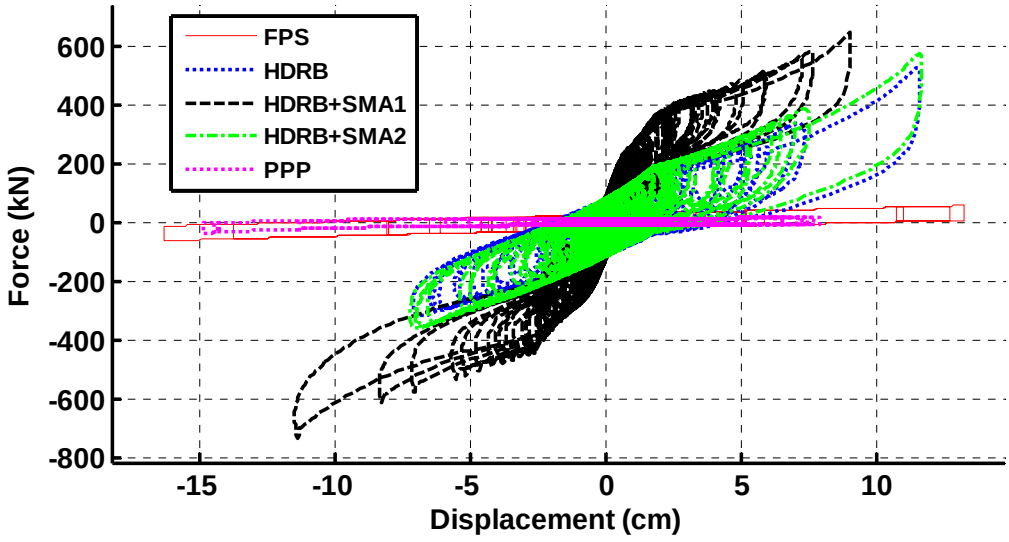

Fig. 143. Comparison 1: Total force from all isolation devices from RSPMatch earthquake

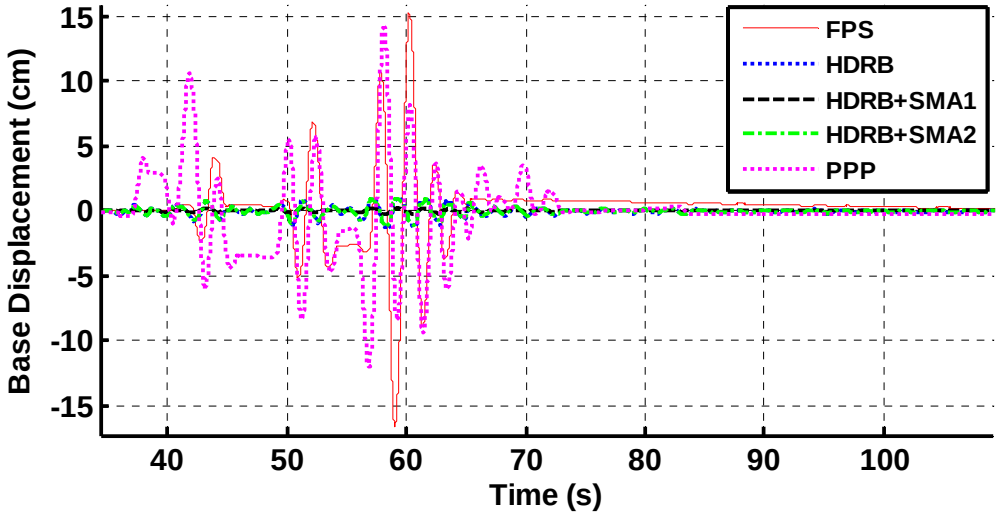

Fig. 144. Comparison 1: Base displacement from 1985 Mexico City earthquake

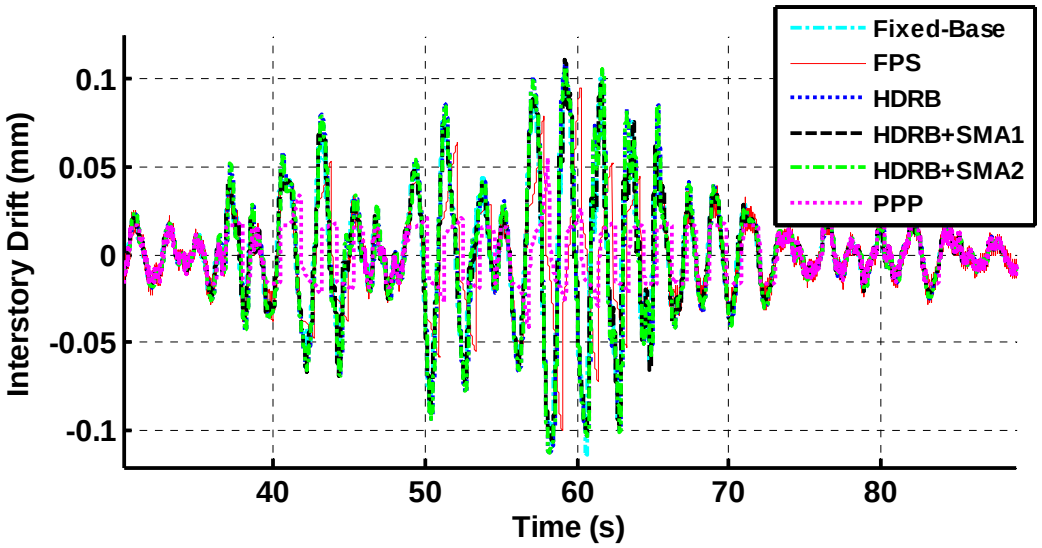

Fig. 145. Comparison 1: Interstory drift between base and 1st floor from 1985 Mexico City earthquake

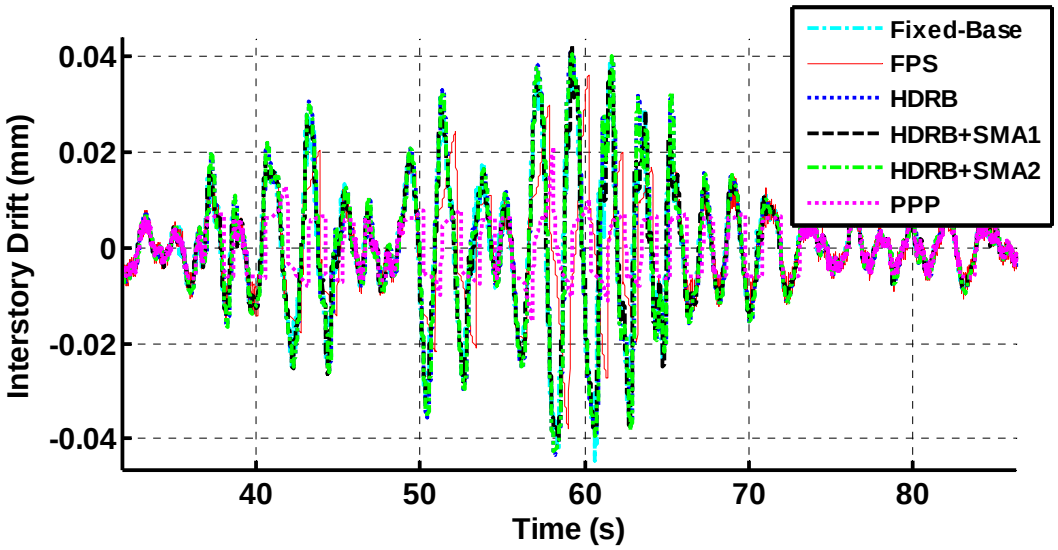

Fig. 146. Comparison 1: Interstory drift between 1st and 2nd floors from 1985 Mexico City earthquake

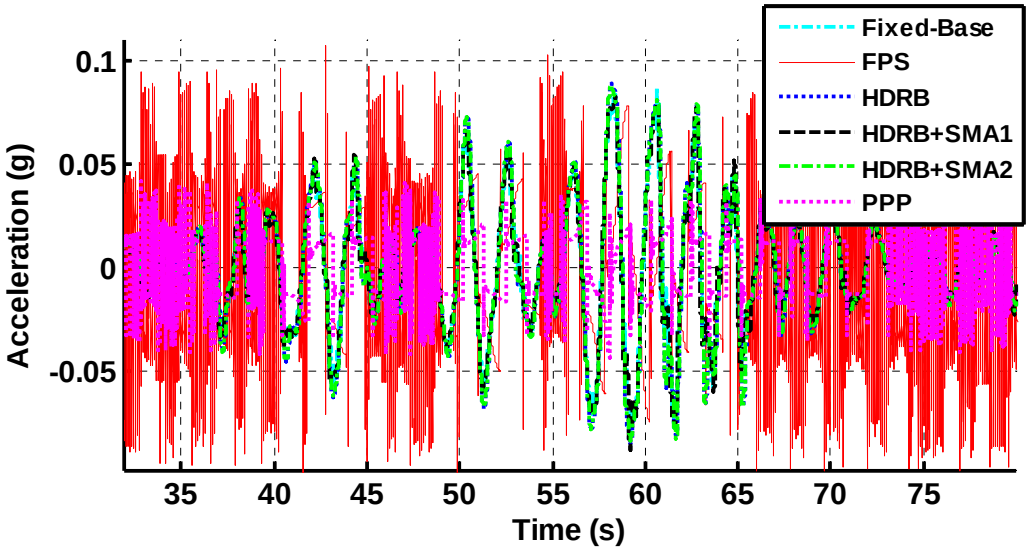

Fig. 147. Comparison 1: Absolute acceleration of 1st floor from 1985 Mexico City earthquake

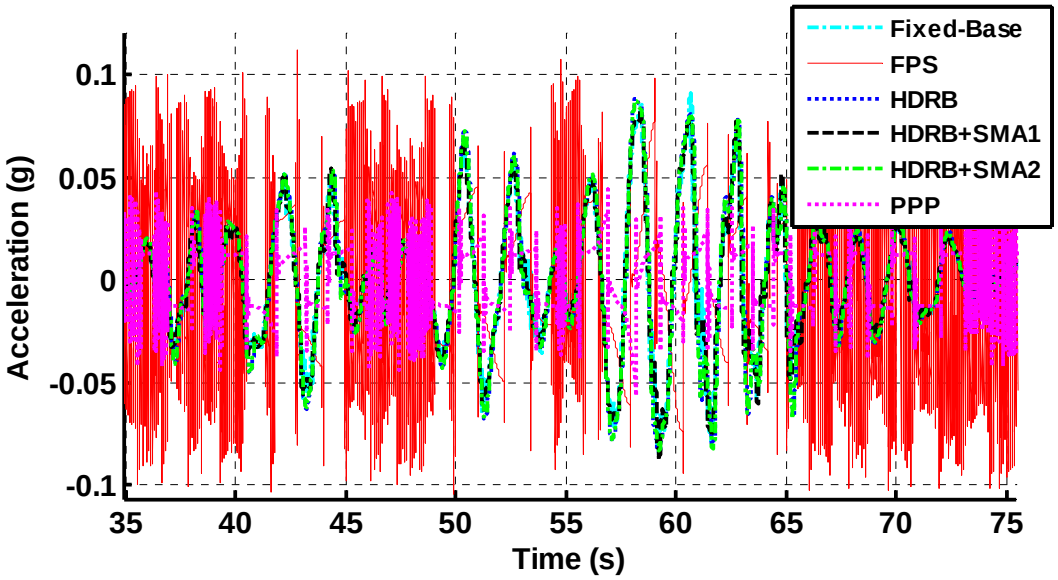

Fig. 148. Comparison 1: Absolute acceleration of 2nd floor from 1985 Mexico City earthquake

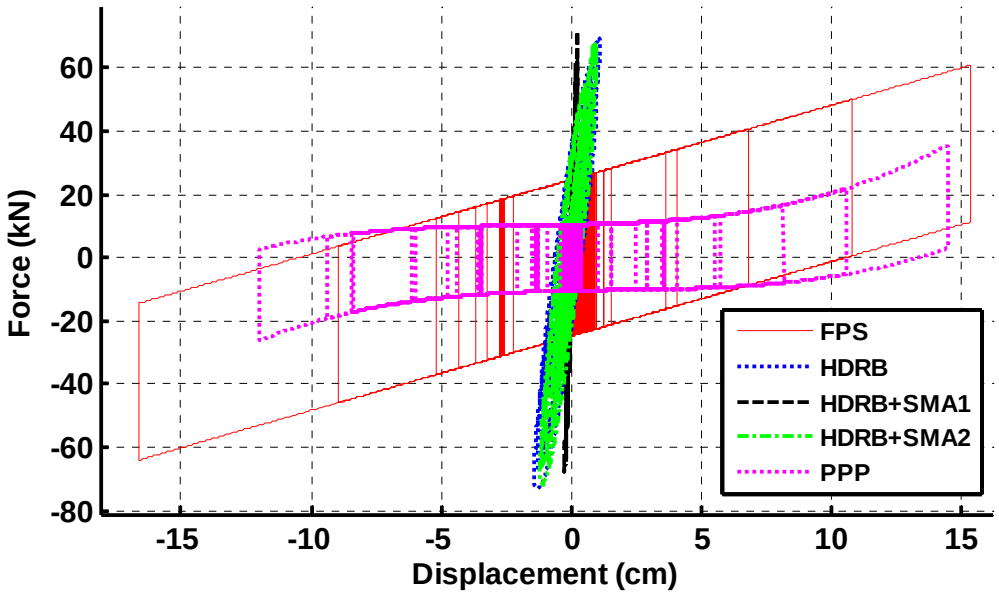

Fig. 149. Comparison 1: Total force from all isolation devices from 1985 Mexico City earthquake

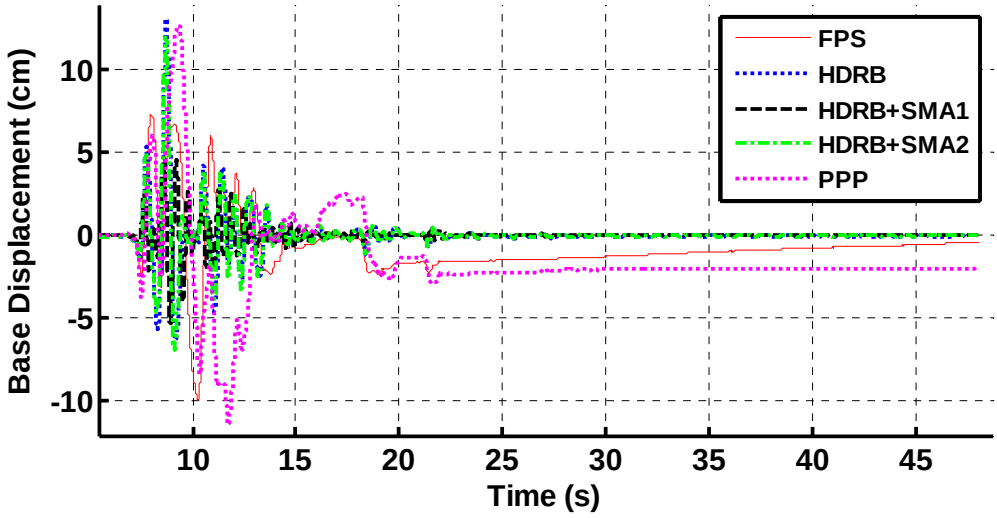

Fig. 150. Comparison 1: Base displacement from Kobe earthquake

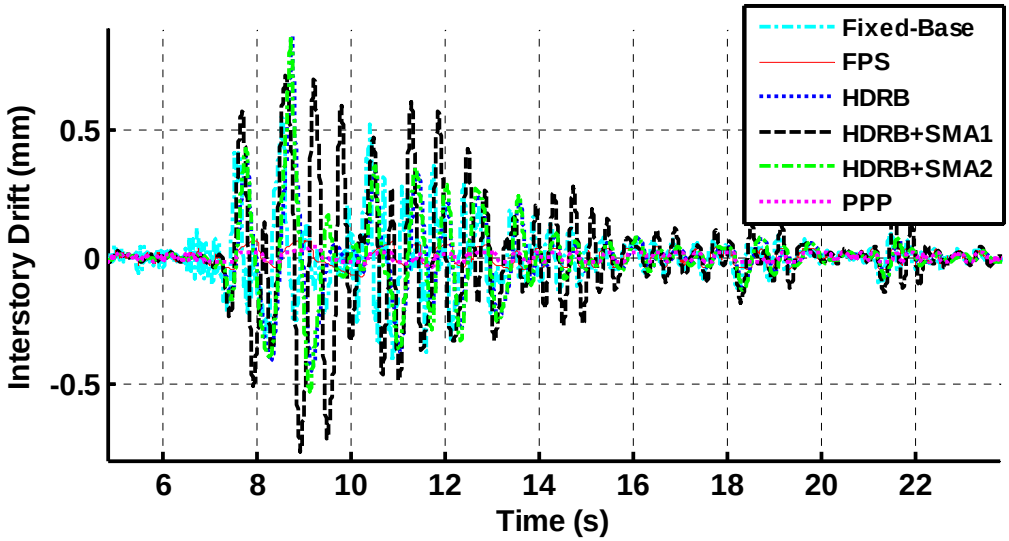

Fig. 151. Comparison 1: Interstory drift between base and 1st floor from Kobe earthquake

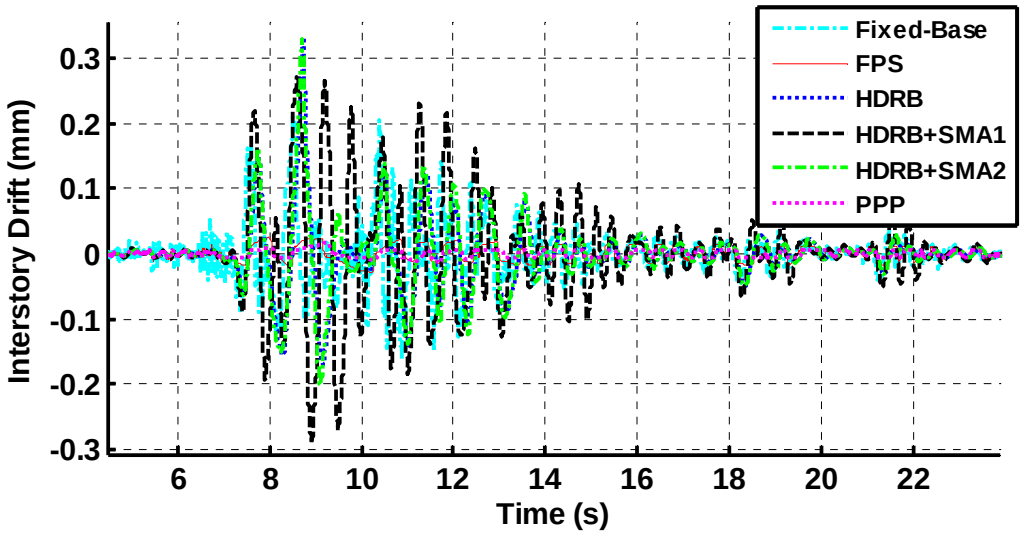

Fig. 152. Comparison 1: Interstory drift between 1st and 2nd floors from Kobe earthquake

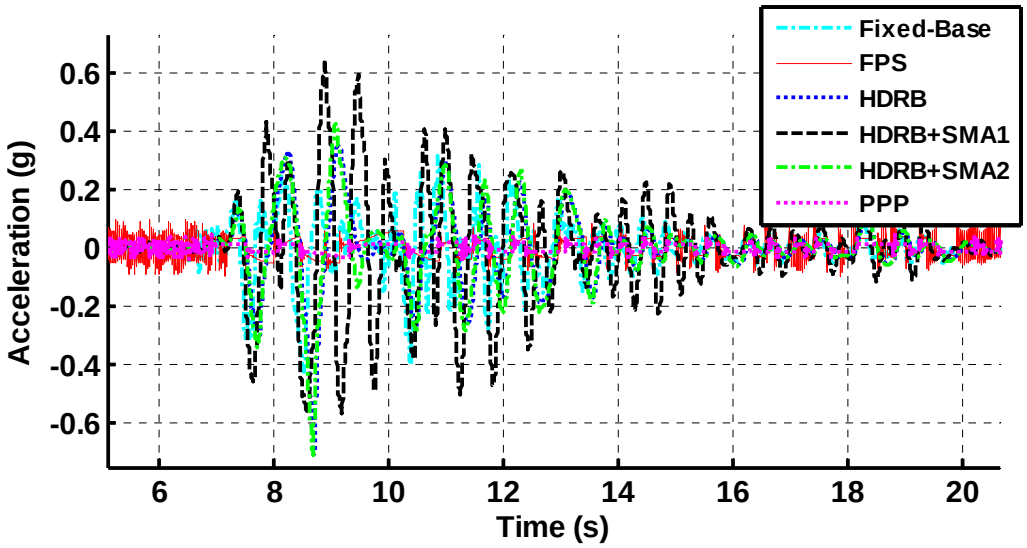

Fig. 153. Comparison 1: Absolute acceleration of 1st floor from Kobe earthquake

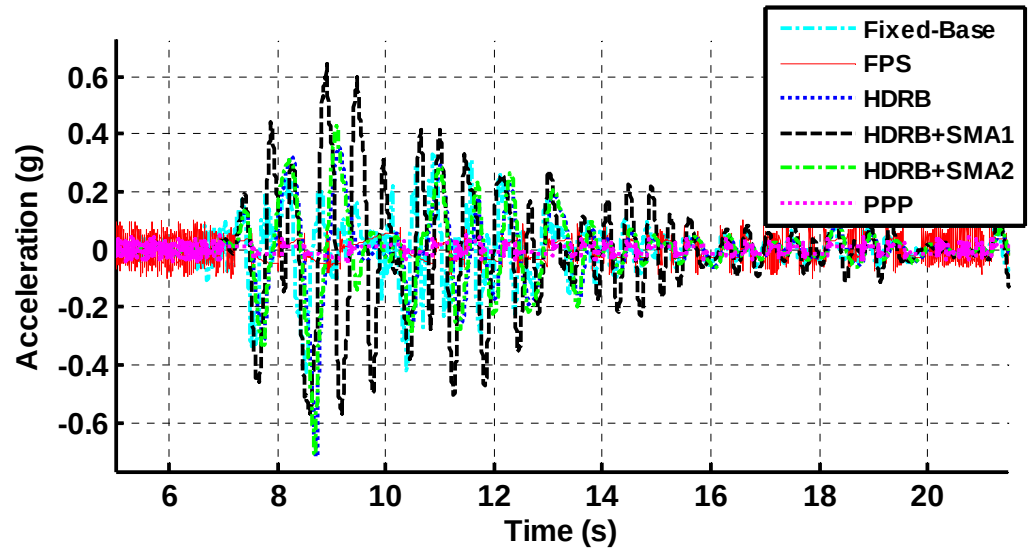

Fig. 154. Comparison 1: Absolute acceleration of 2nd floor from Kobe earthquake

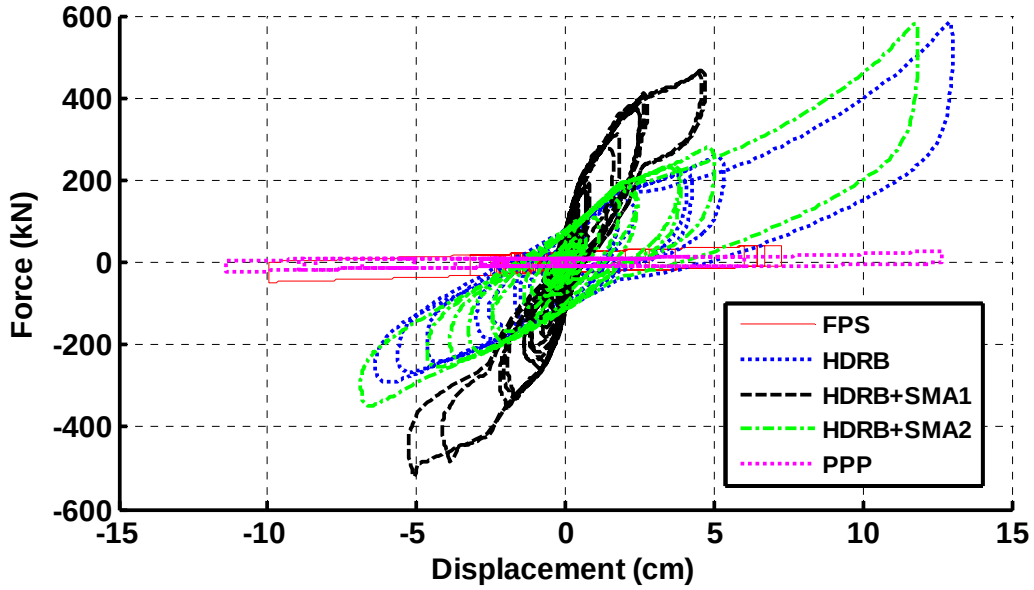

Fig. 155. Comparison 1: Total force from all isolation devices from Kobe earthquake

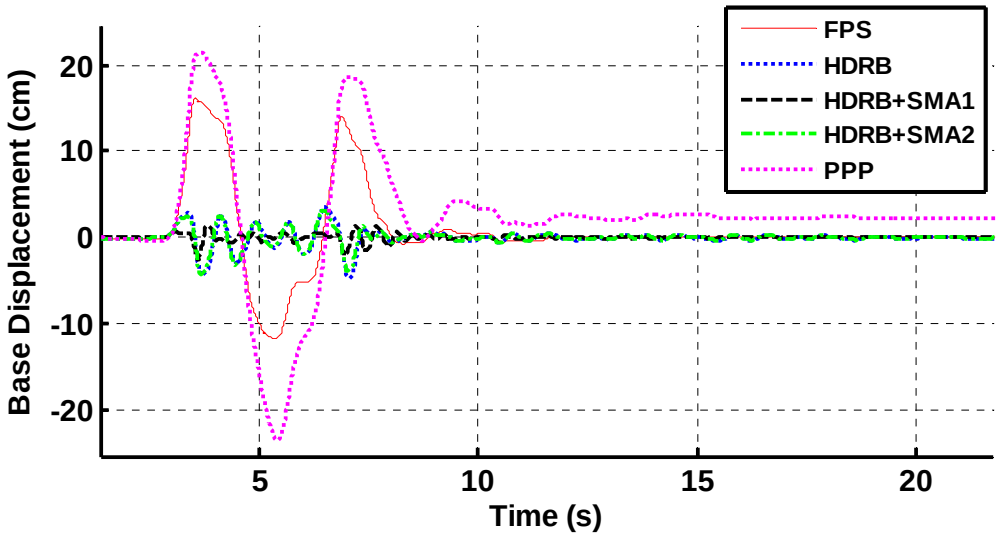

Fig. 156. Comparison 1: Base displacement from Northridge earthquake

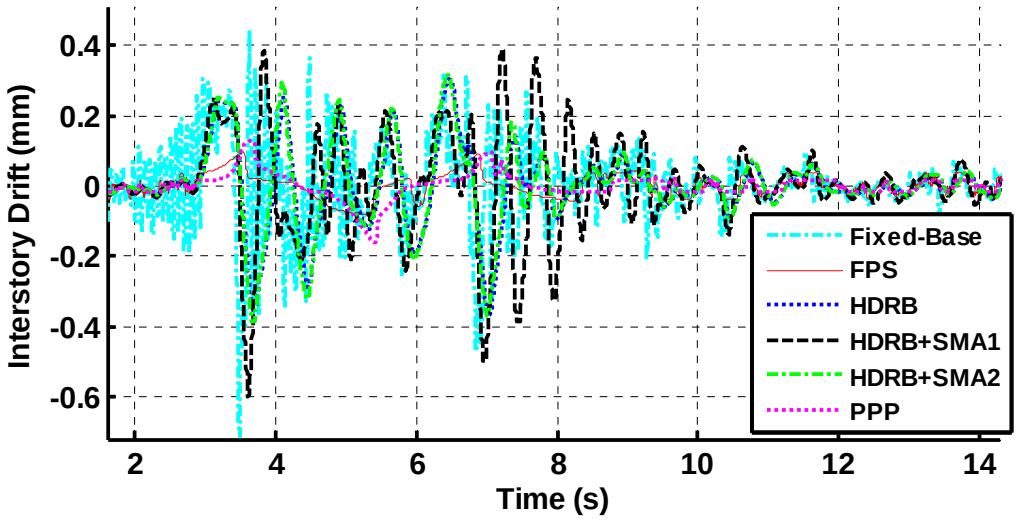

Fig. 157. Comparison 1: Interstory drift between base and 1st floor from Northridge earthquake

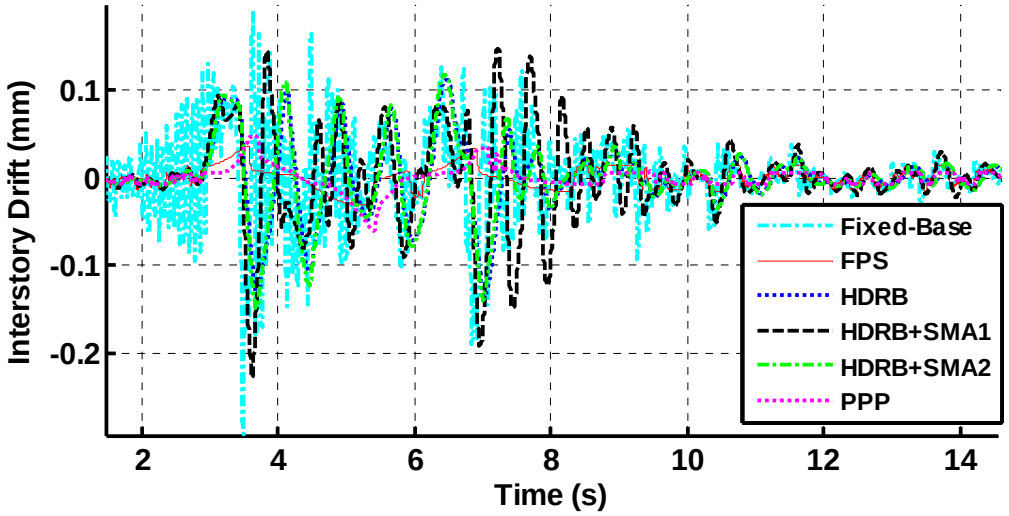

Fig. 158. Comparison 1: Interstory drift between 1st and 2nd floors from Northridge earthquake

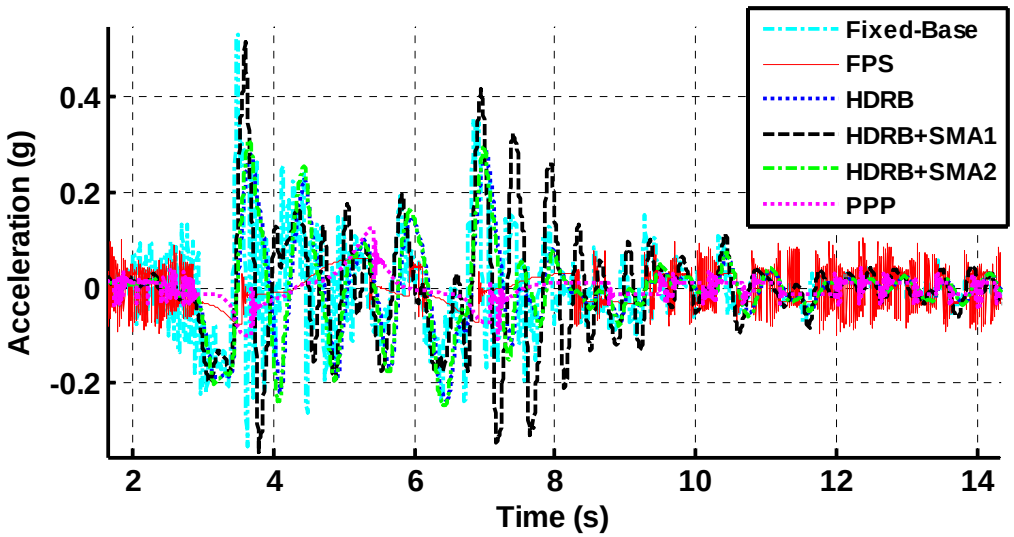

Fig. 159. Comparison 1: Absolute acceleration of 1st floor from Northridge earthquake

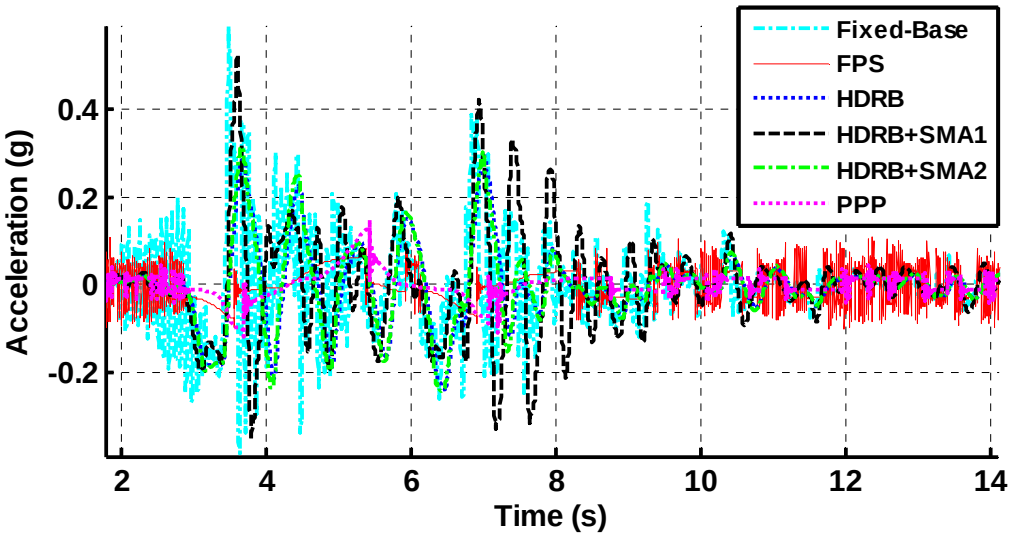

Fig. 160. Comparison 1: Absolute acceleration of 2nd floor from Northridge earthquake

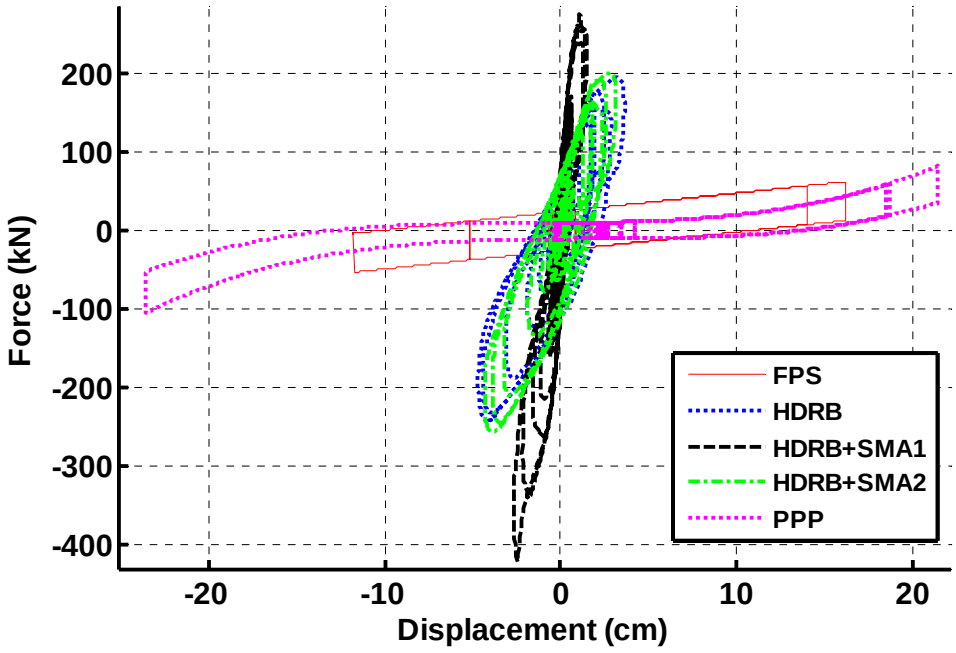

Fig. 161. Comparison 1: Total force from all isolation devices from Northridge earthquake

7.2.3. Performance Indices Explanation

Seven performance indices (PIs) are used to characterize the seismic performance of each isolated structure. As mentioned in Section 6.3, values of the normalized PIs that are less than unity indicate a reduction in response of the isolated structure from that of the fixed-base structure. The PIs J_1 through J_4 are as defined in Section 6.3, while J_5 through J_7 are as defined in what follows (Narasimhan et al. 2006). J_5 quantifies peak structural shear at the first story level, J_6 quantifies peak interstory drift for both floors, and J_7 quantifies peak absolute acceleration for both floors.

$$J_5 = \frac{\max_t \left| V_{1,isolated} \right|}{\max_t \left| V_{1,fixed} \right|} \tag{36}$$

$$J_6 = \frac{\max_f \left| d_{f,isolated}(t) \right|}{\max_f \left| d_{f,fixed}(t) \right|} \tag{37}$$

$$J_7 = \frac{\max_f \left| a_{f,isolated}(t) \right|}{\max_f \left| a_{f,fixed}(t) \right|} \tag{38}$$

where V_1 is structural shear at the first story level, d_f is the peak interstory drift between two floors, and a_f is the peak acceleration of any floor. The subscripts *t* and *f* refer to all time and all floors, respectively.

7.2.4. Performance Indices for Each Earthquake

A summary of the results for each earthquake, in terms of the PIs, are included in Tables 9-16.

Table 9. Comparison 1: Results from 1981 Chile Earthquake

	Base Shear	Base Displace-ment	RMS Base Displace-ment	RMS Floor Acceleration	Structural Shear	Interstory Drift	Floor Accel-eration
	J_1	J_2 (m)	J_3 (m)	J_4	J_5	J_6	J_7
FPS	0.118	0.039	0.007	0.320	0.034	0.034	0.109
HDRB	0.581	0.020	0.003	0.226	0.156	0.156	0.189
HDRB+SMA1	1.70	0.043	0.005	0.712	0.439	0.457	0.549
HDRB+SMA2	0.630	0.021	0.003	0.241	0.169	0.169	0.205
PPP	0.077	0.107	0.029	0.130	0.022	0.022	0.048

Table 10. Comparison 1: Results from 1985 Llolleo, Chile, Earthquake

	Base Shear	Base Displace-ment	RMS Base Displace-ment	RMS Floor Acceleration	Structural Shear	Interstory Drift	Floor Accel-eration
	J_1	J_2 (m)	J_3 (m)	J_4	J_5	J_6	J_7
FPS	0.142	0.114	0.017	0.279	0.063	0.061	0.125
HDRB	0.978	0.077	0.010	0.470	0.419	0.402	0.478
HDRB+SMA1	1.54	0.066	0.009	1.07	0.608	0.620	0.757
HDRB+SMA2	1.00	0.072	0.010	0.503	0.430	0.412	0.489
PPP	0.119	0.161	0.025	0.113	0.053	0.051	0.058

Table 11. Comparison 1: Results from 2005 Tarapacá, Chile, Earthquake

	Base Shear	Base Displace-ment	RMS Base Displace-ment	RMS Floor Acceleration	Structural Shear	Interstory Drift	Floor Accel-eration
	J_1	J_2 (m)	J_3 (m)	J_4	J_5	J_6	J_7
FPS	0.099	0.063	0.011	0.177	0.031	0.035	0.087
HDRB	0.448	0.029	0.005	0.195	0.154	0.154	0.173
HDRB+SMA1	1.04	0.027	0.004	0.447	0.333	0.333	0.403

Table 11. Continued

	Base Shear J_1	Base Displacement J_2 (m)	RMS Base Displacement J_3 (m)	RMS Floor Acceleration J_4	Structural Shear J_5	Interstory Drift J_6	Floor Acceleration J_7
HDRB+SMA2	0.485	0.026	0.004	0.204	0.164	0.164	0.188
PPP	0.070	0.126	0.024	0.074	0.014	0.025	0.045

Table 12. Comparison 1: Results from El Centro Earthquake

	Base Shear J_1	Base Displacement J_2 (m)	RMS Base Displacement J_3 (m)	RMS Floor Acceleration J_4	Structural Shear J_5	Interstory Drift J_6	Floor Acceleration J_7
FPS	0.183	0.030	0.009	0.809	0.094	0.094	0.293
HDRB	1.04	0.027	0.004	0.657	0.466	0.515	0.586
HDRB+SMA1	1.55	0.013	0.002	1.01	0.702	0.702	0.883
HDRB+SMA2	1.14	0.028	0.004	0.684	0.488	0.560	0.639
PPP	0.070	0.045	0.011	0.324	0.035	0.036	0.123

Table 13. Comparison 1: Results from RSPMatch Earthquake

	Base Shear J_1	Base Displacement J_2 (m)	RMS Base Displacement J_3 (m)	RMS Floor Acceleration J_4	Structural Shear J_5	Interstory Drift J_6	Floor Acceleration J_7
FPS	0.192	0.163	0.023	0.258	0.077	0.085	0.133
HDRB	1.59	0.116	0.013	0.541	0.679	0.661	0.769
HDRB+SMA1	2.23	0.115	0.012	1.16	0.838	0.918	1.08
HDRB+SMA2	1.73	0.117	0.013	0.599	0.739	0.719	0.836
PPP	0.114	0.149	0.023	0.103	0.022	0.049	0.087

Table 14. Comparison 1: Results from 1985 Mexico City Earthquake

	Base Shear	Base Displace-ment	RMS Base Displace-ment	RMS Floor Acceleration	Structural Shear	Interstory Drift	Floor Accel-eration
	J_1	J_2 (m)	J_3 (m)	J_4	J_5	J_6	J_7
FPS	1.39	0.166	0.018	3.24	0.897	0.881	1.23
HDRB	1.59	0.015	0.002	1.15	1.03	1.01	1.02
HDRB+SMA1	1.56	0.003	0.001	1.04	1.05	0.980	1.01
HDRB+SMA2	1.57	0.013	0.002	1.14	1.01	0.996	1.01
PPP	0.773	0.144	0.020	1.31	0.521	0.488	0.623

Table 15. Comparison 1: Results from Kobe Earthquake

	Base Shear	Base Displace-ment	RMS Base Displace-ment	RMS Floor Acceleration	Structural Shear	Interstory Drift	Floor Accel-eration
	J_1	J_2 (m)	J_3 (m)	J_4	J_5	J_6	J_7
FPS	0.211	0.100	0.019	0.773	0.120	0.138	0.260
HDRB	2.55	0.130	0.013	1.20	1.59	1.59	1.68
HDRB+SMA1	2.27	0.053	0.007	1.91	1.31	1.40	1.52
HDRB+SMA2	2.54	0.122	0.012	1.26	1.59	1.59	1.68
PPP	0.124	0.127	0.029	0.322	0.081	0.081	0.119

Table 16. Comparison 1: Results from Northridge Earthquake

	Base Shear	Base Displace-ment	RMS Base Displace-ment	RMS Floor Acceleration	Structural Shear	Interstory Drift	Floor Accel-eration
	J_1	J_2 (m)	J_3 (m)	J_4	J_5	J_6	J_7
FPS	0.273	0.162	0.033	0.789	0.219	0.138	0.201
HDRB	1.05	0.047	0.007	0.954	0.681	0.519	0.555
HDRB+SMA1	1.83	0.027	0.003	1.27	0.878	0.844	0.969
HDRB+SMA2	1.08	0.044	0.007	0.988	0.699	0.539	0.572

Table 16. Continued

	Base Shear J_1	Base Displace-ment J_2 (m)	RMS Base Displace-ment J_3 (m)	RMS Floor Acceleration J_4	Structural Shear J_5	Interstory Drift J_6	Floor Accel-eration J_7
PPP	0.451	0.236	0.057	0.427	0.289	0.228	0.247

From the tabulated results, it can be concluded that the PPP isolation system yields the most favorable PIs for the structure when it is subjected to the 1981 Chile, 1985 Llolleo, Chile, 2005 Tarapacá, Chile, 1940 El Centro, RSPMatch, and the scaled 1985 Mexico City and 1995 Kobe earthquakes. Although individual PIs resulting from other isolation systems are sometimes less than those resulting from the PPP isolation system for a given earthquake, the PPP isolation system yields the best overall performance during each of these earthquakes when compared to the other isolation systems. Emphasis is placed on reducing the base shear, structure shear, and peak and RMS floor accelerations while maintaining reasonable values of base displacement, RMS base displacement, and interstory drift. Generally, the PPP isolation system minimizes all of the PIs except those related to base displacement (J_2 and J_3) when compared to the other isolation systems.

The only earthquake in which the PPP isolation system is outperformed in terms of the PIs for the structure is for the scaled 1994 Northridge earthquake. For this earthquake, the FPS case results in lower peak base shear, base displacement, structural shear, interstory drift, and floor acceleration than that of the PPP case, although the values of these PIs for the PPP isolated structure are acceptable. The reason for the better performance of the FPS isolated structure than the PPP isolated structure can be attributed to the unique characteristics of the ground motion from the Northridge earthquake. The Northridge earthquake has long duration pulses, typical of near-fault ground motions (Jangid and Kelly 2001).

The HDRB+SMA1 and HDRB+SMA2 cases generally result in higher peak base shear, RMS floor acceleration, peak structural shear, and peak floor acceleration than the HDRB only case due to increased stiffness of the isolation system that the SMA wires provide. However, the use of SMA wires in the hybrid HDRB+SMA systems often reduces base displacement and RMS base displacement from that of the HDRB only case. Wilde et al. (2000) formed a similar conclusion through study of a bridge isolation system incorporating the use of elastomeric bearings and SMA bars. They concluded that use of SMA bars in the isolation system served to control displacements and energy dissipation capacity while providing a recentering ability. On the other hand, use of SMA bars increased the stiffness of the isolation system and thereby resulted in a larger shear force transmitted to the pier and an increase in the acceleration response from that of other isolation systems (Wilde et al. 2000).

With the exception of the HDRB+SMA1 system, each of the isolation systems considered reduces the response of the isolated structure from that of the fixed-base structure with respect to all PIs for the three Chilean earthquakes studied. However, note that the HDRB+SMA1 isolation system amplifies the base shear from that of the fixed-base case for the Chilean earthquakes. Also, in the El Centro and RSPMatch earthquakes, the HDRB, HDRB+SMA1, and HDRB+SMA2 isolation systems amplify the base shear of the isolated structure from that of the fixed-base structure. The HDRB+SMA1 system also somewhat amplifies the PIs related to acceleration.

For the scaled Mexico City, Kobe, and Northridge earthquakes, more of the PIs are amplified from that of the fixed-base case due to the extremely high energy in the Mexico City earthquake and the near-fault characteristics of the Kobe and Northridge earthquakes. Because the PPP isolation system does not amplify the PIs from that of the fixed-base case (with the exception of J_4 in the Mexico City earthquake), and it in fact reduces the response of the isolated structure from that of the fixed-base structure, it is chosen as the most appropriate isolation system for the case study structure based on the results of Comparison 1.

7.3. Comparison 2: Fundamental Period of 1.0 sec

7.3.1. Selected Parameters

For the second comparison, the number of devices and the design parameters of each device are selected such that the fundamental period of the isolated structure is close to 1.0 sec. This period of 1.0 sec was selected because it is sufficiently long for the base isolation systems to be effective for most of the historical earthquakes that are being studied, and it is a reasonable period for all of the isolation systems to achieve. A trial-and-error procedure is employed to determine how many devices of each type are to be used as well as the design parameters for each device.

The selected number of devices and device design parameters are as follows. The FPS isolation system includes the use of eight bearings with coefficient of friction μ = 0.05 and a radius of curvature R = 0.25 m. Note that this coefficient of friction is greater than that used in the first comparison, while the radius of curvature is less than that used in the first comparison.

The same HDRBs used in the first comparison are used here, although a total of nine HDRBs are utilized in this comparison to yield an isolated period of 1.0 sec. The HDRB FIS trained for a 20 cm diameter HDRB with a 100 kN axial load is sufficient for use in this case because the axial load is not significantly reduced when using nine bearings instead of the eight bearings previously used.

The HDRB+SMA1 case involves the use of four HDRBs, with 70 wires in each of two diagonals for each bearing. Because the use of four HDRBs in the isolation system results in two times the axial load on each bearing when compared to the isolation system with eight HDRBs, a new HDRB FIS is created by employing the same procedure as described in Section 6. This HDRB FIS models the behavior of a 20 cm diameter HDRB with an axial load of 200 kN, using the test data from the 22.3 cm diameter HDRB (see Table 5).

The HDRB+SMA2 case is the same as that used in Comparison 1. It involves the use of eight HDRBs with braces connecting adjacent HDRBs (see Figs. 13 and 72).

The HDRBs have a diameter of 20 cm with a 100 kN axial load on each bearing. The braces have 30 SMA wires that are 4 m long in each of two diagonal elements.

The use of 18 PPP isolators with a 118 kN initial prestress in the central cable, a radius of curvature of 50 cm for the spherical top and bottom rolling surfaces, a pile length of 100 cm, an elastic cable stiffness of 128 kN/cm, and four rebars that have a diameter of 1.6 cm at the base of the isolator is required to yield an isolated period of 1.0 sec.

As in Comparison 1, an FFT is performed on the free vibration displacement data resulting from numerical simulation in which the structure is given a small initial horizontal displacement at each story and allowed to freely vibrate. The FFT plots of the structural response that are shown in Fig. 162 confirm that the fundamental period of the structure using each of the isolation systems is approximately 1.0 sec.

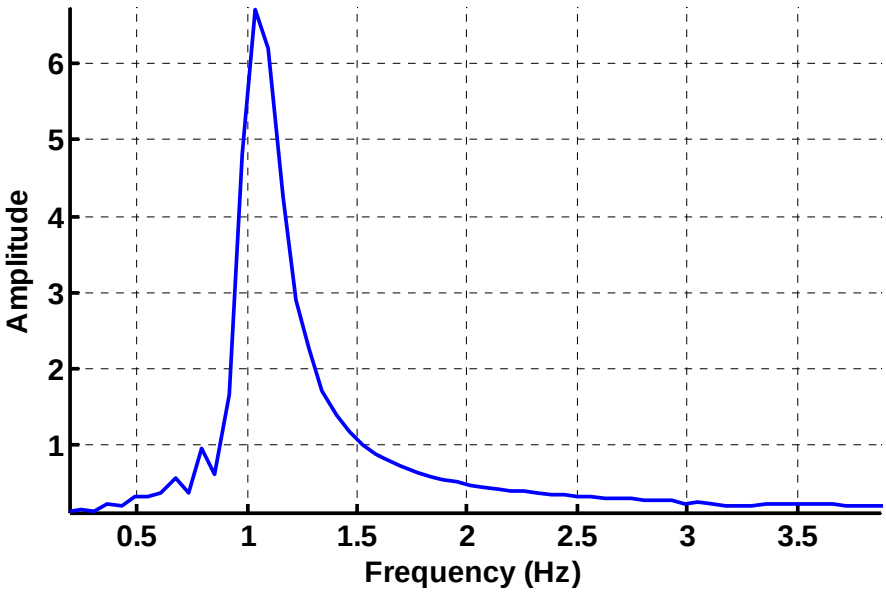

(a)

Fig. 162. Comparison 2: FFT for base-isolated structure (a) FPS, (b) HDRB, (c) HDRB+SMA1, (d) HDRB+SMA2, (e) PPP

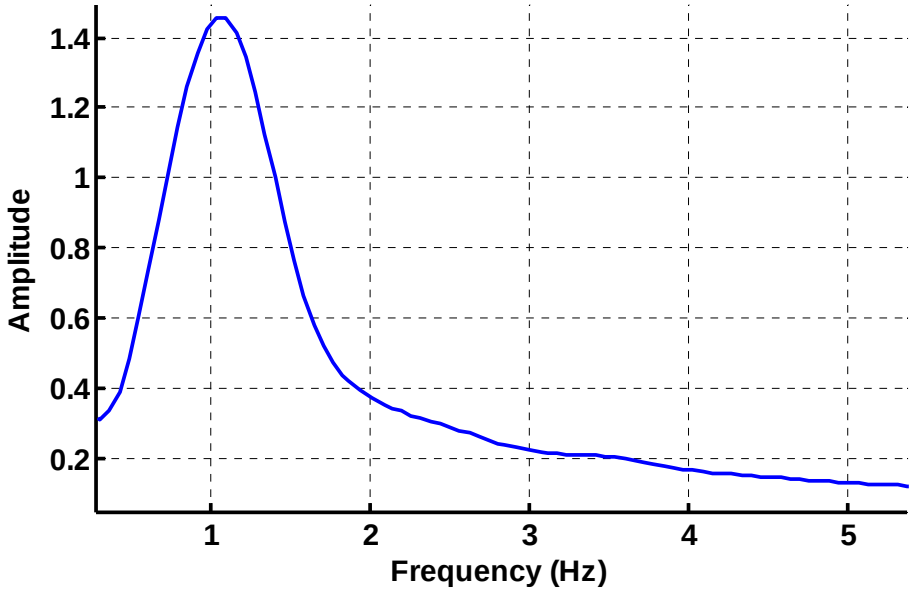

(b)

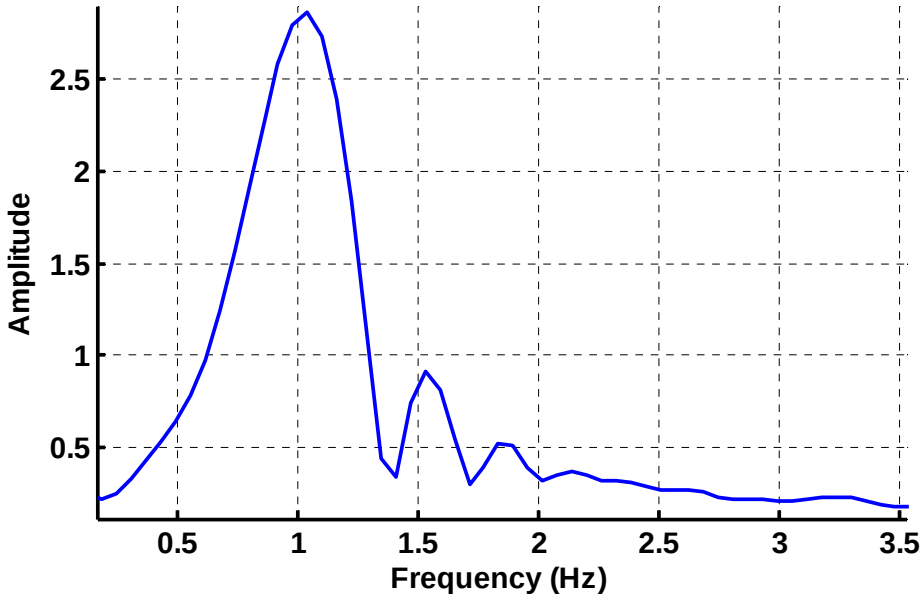

(c)

Fig. 162. Continued

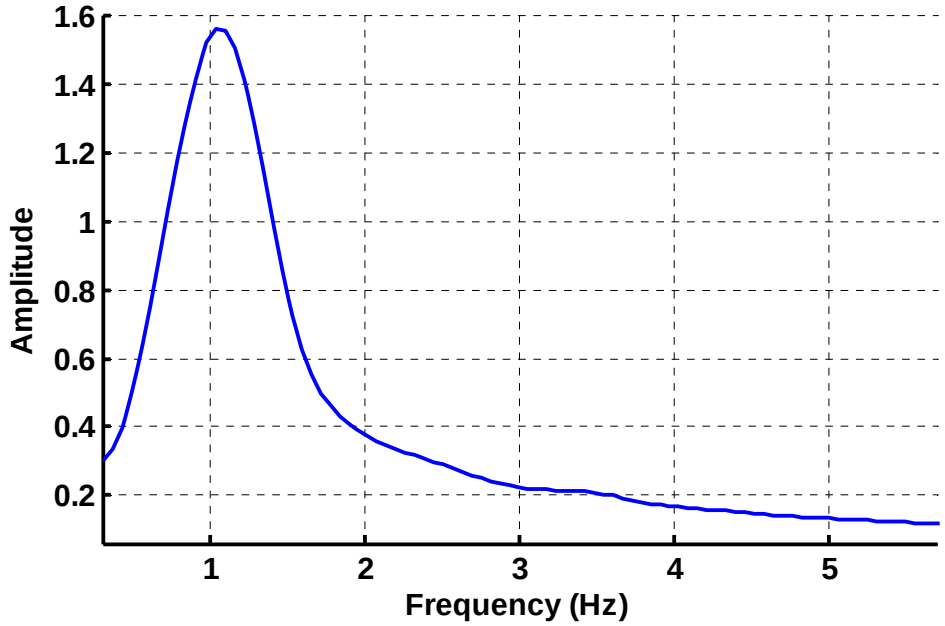

(d)

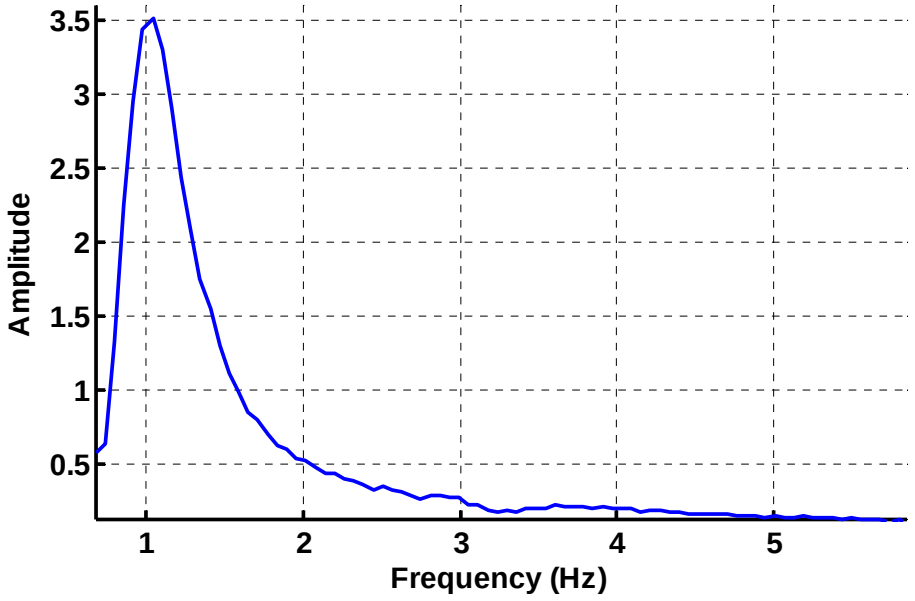

(e)

Fig. 162. Continued

As in Comparison 1, the equivalent viscous damping ratio for each base isolation case is calculated using the logarithmic decrement method. The damping values for each case, including intrinsic damping from the structure and hysteretic damping from each isolation system, are reported in Table 17.

Table 17. Comparison 2: Equivalent Viscous Damping Values

	Equivalent viscous damping (%)
FPS	6
HDRB	24
HDRB+SMA1	13
HDRB+SMA2	20
PPP	5

7.3.2. Graphical Results from Each Earthquake

Graphical results from the numerical simulation of each earthquake are included in Figs. 163-210. Contrary to the findings from Comparison 1, the PPP isolated structure does not experience residual displacement resulting from the earthquakes in Comparison 2 (see Fig. 163, for example). This result can be attributed to the increased self-centering capacity of the PPP isolation system in Comparison 2 due to the larger initial prestress in the central cable and the larger elastic cable stiffness than in Comparison 1. As in Comparison 1, the interstory drift between the base and 1st floors is greater than the interstory drift between the 1st and 2nd floors for both the fixed-base and base-isolated cases (see Figs. 164 and 165, for example). Again, the interstory drift of the 1st and 2nd floors is not significant for either the fixed-base or the base-isolated cases. The maximum peak interstory drift from any of the earthquakes occurs for the fixed-base structure during the 2005 Tarapacá, Chile, earthquake. The maximum peak interstory

drift is 0.18 cm, which corresponds to a 0.07% drift. The "hanging" of the FPS and PPP isolators with respect to base displacement occurs in response to the El Centro earthquake (see Fig. 181).

The same conclusions with respect to acceleration can be drawn in Comparison 2 as in Comparison 1. Specifically, the absolute acceleration of the 2nd floor is greater than that of the 1st floor for the fixed-base case (see Figs. 166 and 167, for example), and the absolute acceleration of the 1st and 2nd floors are approximately equal for a given one of the base-isolated cases (see Figs. 166 and 167, for example). Again, an amplification of the horizontal ground acceleration occurs for the fixed-base case. As in Comparison 1, significant oscillation in the acceleration response of the FPS isolated structure occurs for certain earthquakes (see Figs. 184 and 185, for example). However, this effect is also evident for the PPP isolated structure in Comparison 2 (see Figs. 184 and 185, for example). Contrary to Comparison 1, the stiffness of each isolation system is approximately the same in Comparison 2 (see Fig. 168).

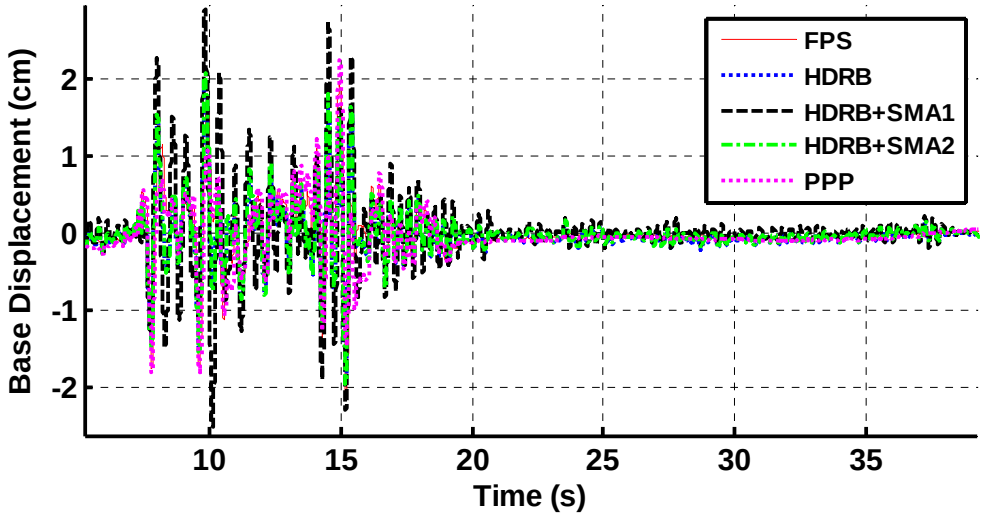

Fig. 163. Comparison 2: Base displacement from 1981 Chile earthquake

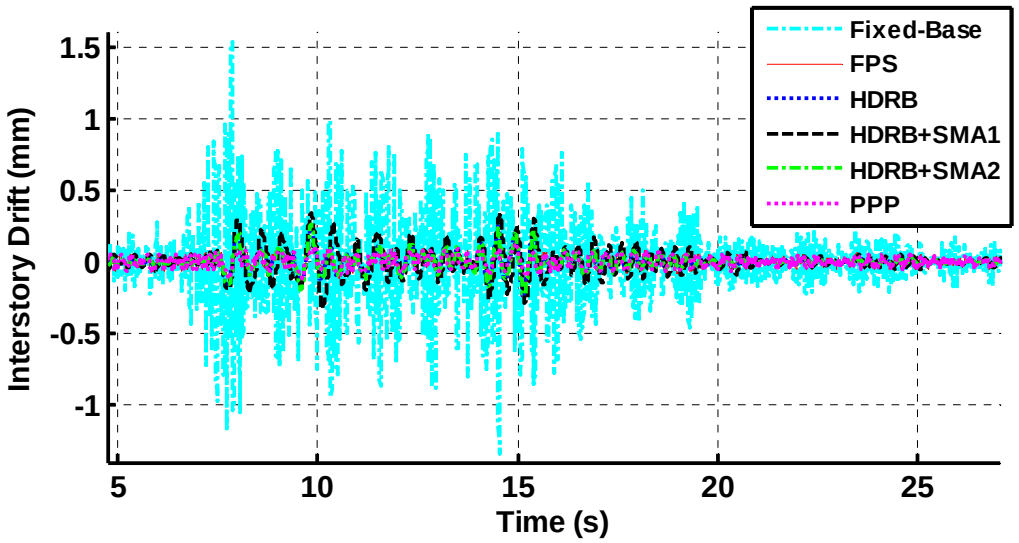

Fig. 164. Comparison 2: Interstory drift between base and 1st floor from 1981 Chile earthquake

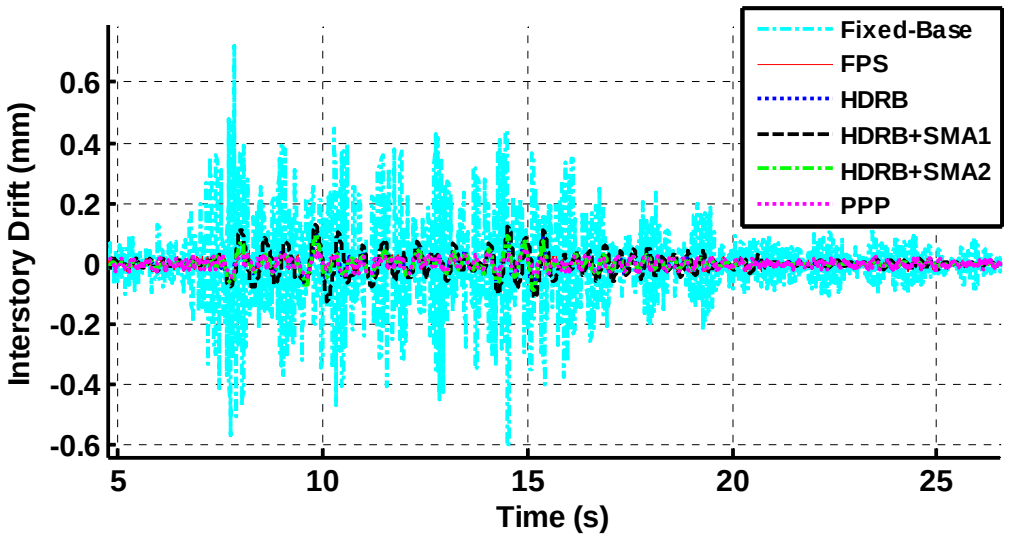

Fig. 165. Comparison 2: Interstory drift between 1st and 2nd floors from 1981 Chile earthquake

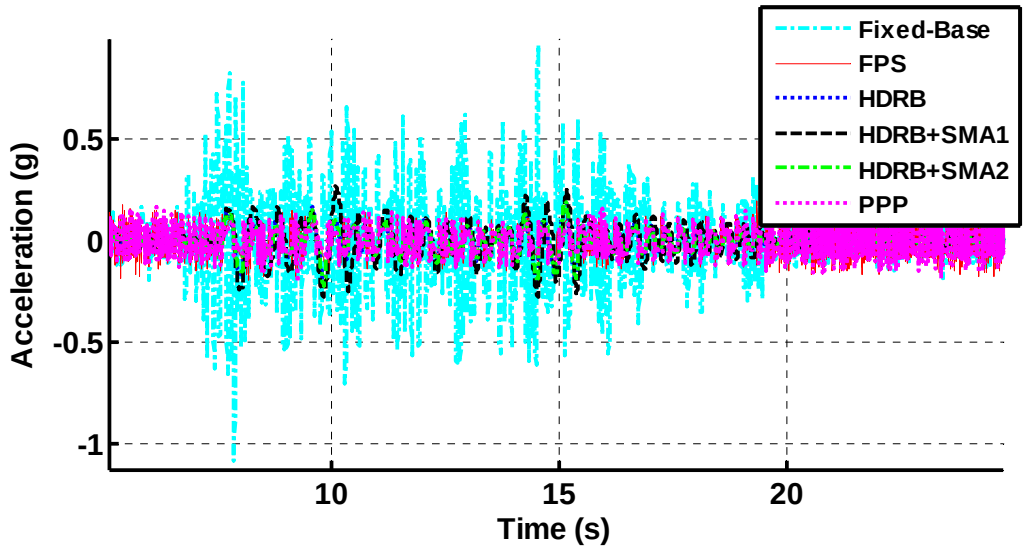

Fig. 166. Comparison 2: Absolute acceleration of 1st floor from 1981 Chile earthquake

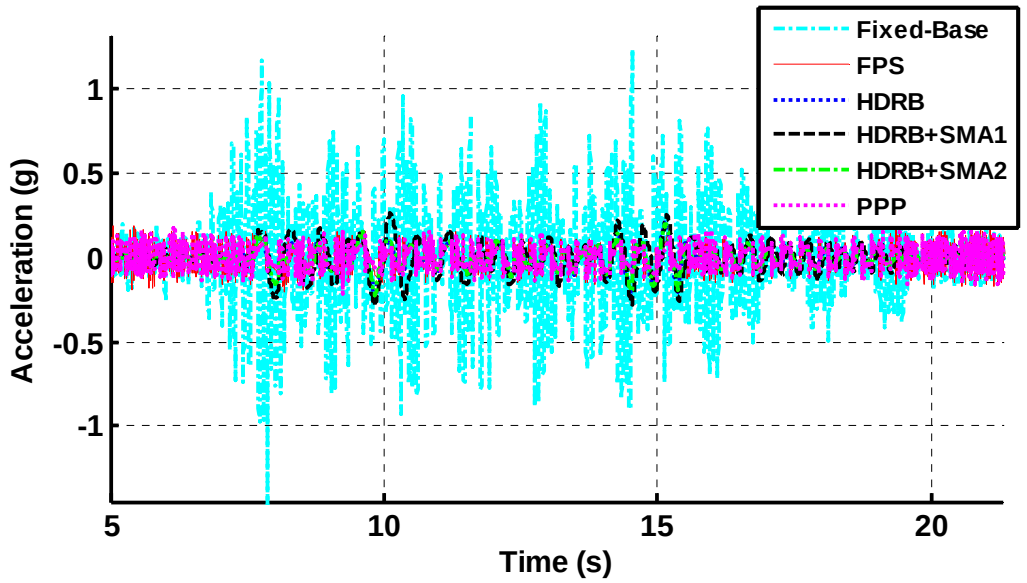

Fig. 167. Comparison 2: Absolute acceleration of 2nd floor from 1981 Chile earthquake

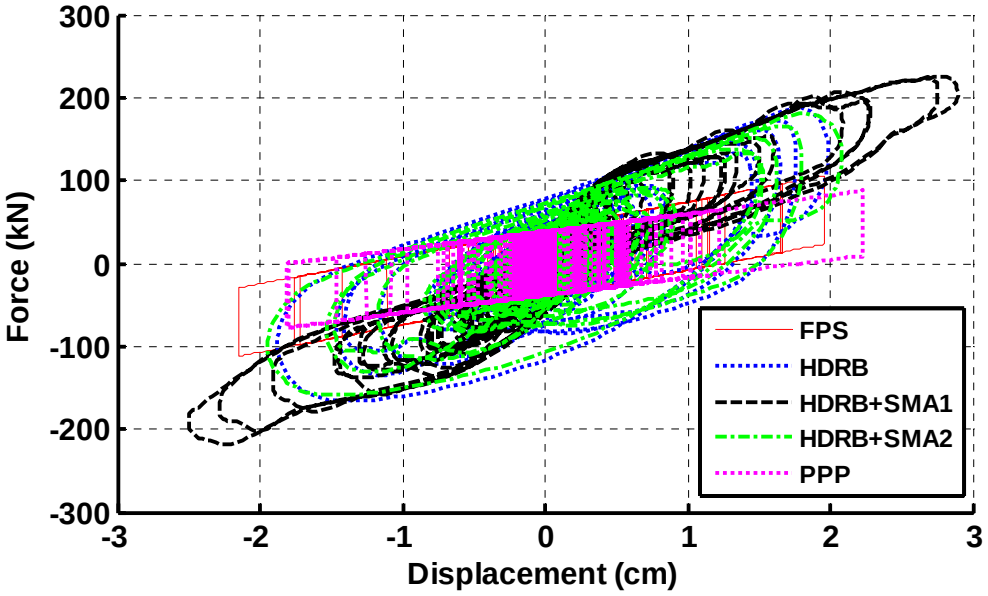

Fig. 168. Comparison 2: Total force from all isolation devices from 1981 Chile earthquake

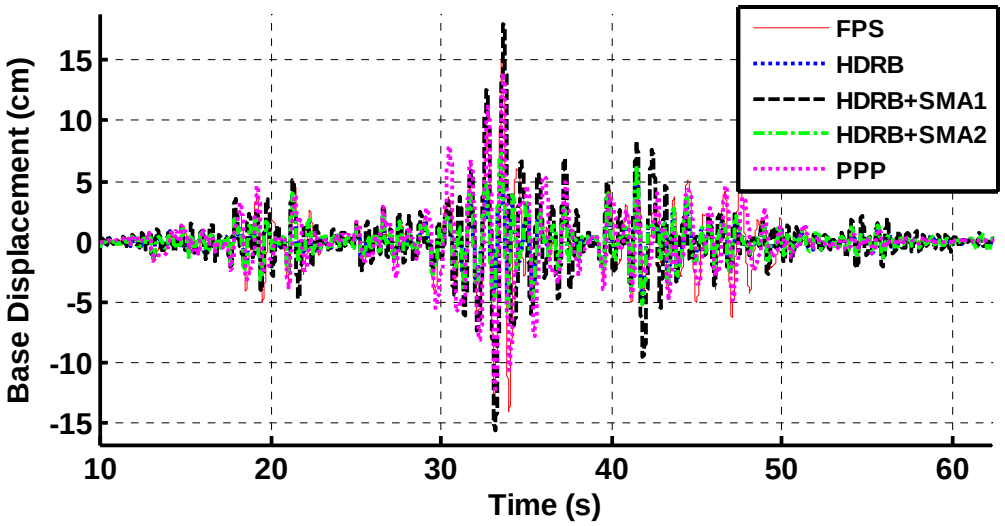

Fig. 169. Comparison 2: Base displacement from 1985 Llolleo, Chile, earthquake

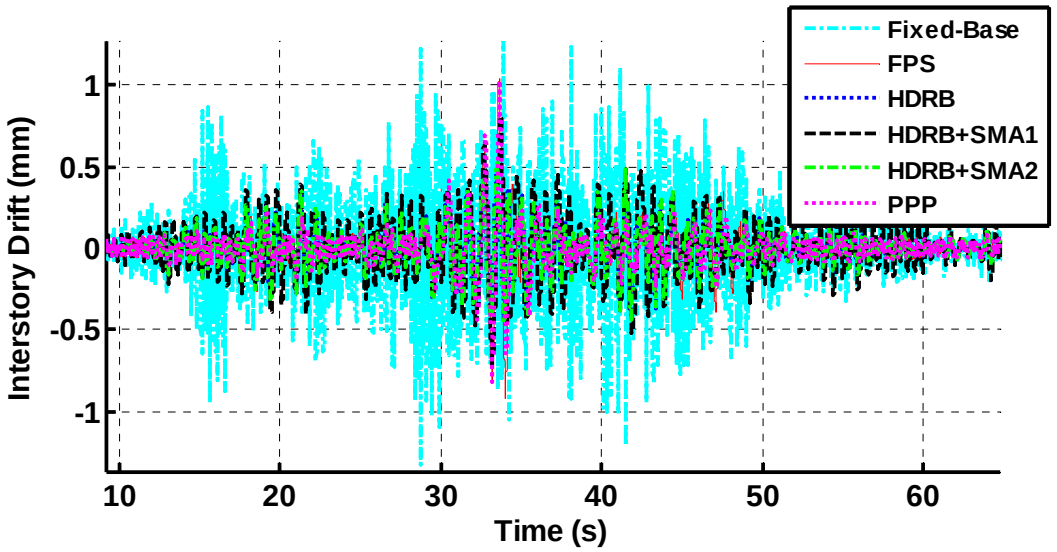

Fig. 170. Comparison 2: Interstory drift between base and 1st floor from 1985 Llolleo, Chile, earthquake

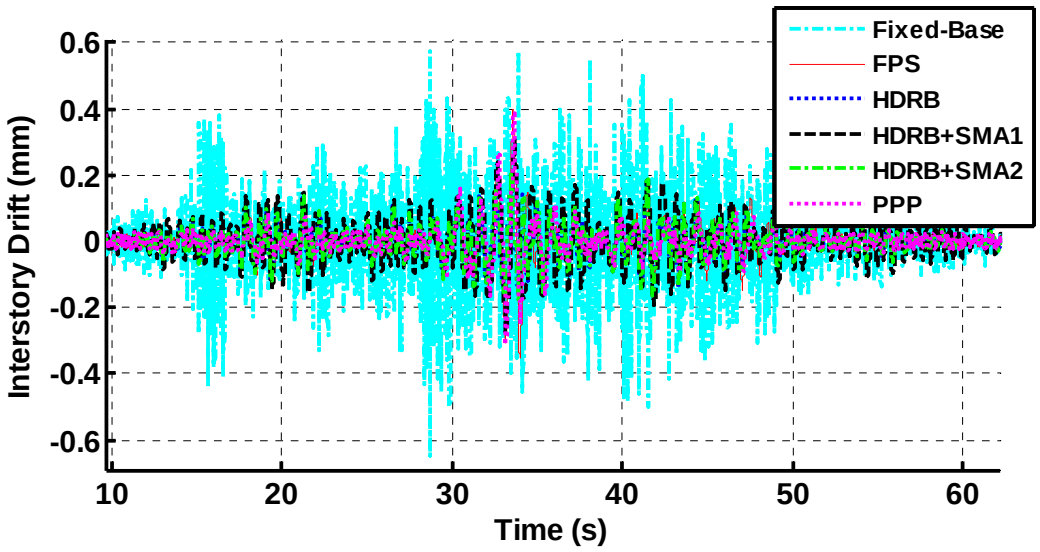

Fig. 171. Comparison 2: Interstory drift between 1st and 2nd floors from 1985 Llolleo, Chile, earthquake

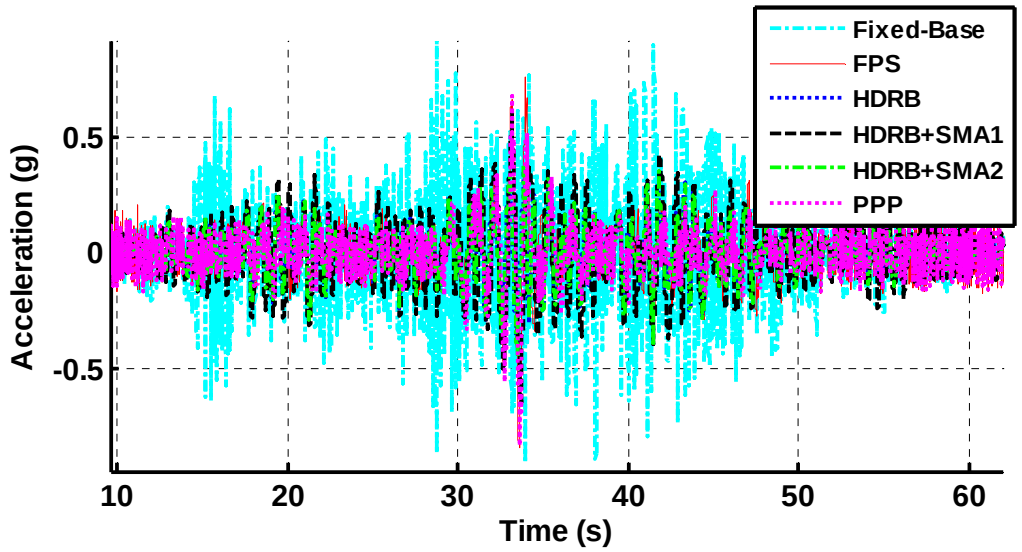

Fig. 172. Comparison 2: Absolute acceleration of 1st floor from 1985 Llolleo, Chile, earthquake

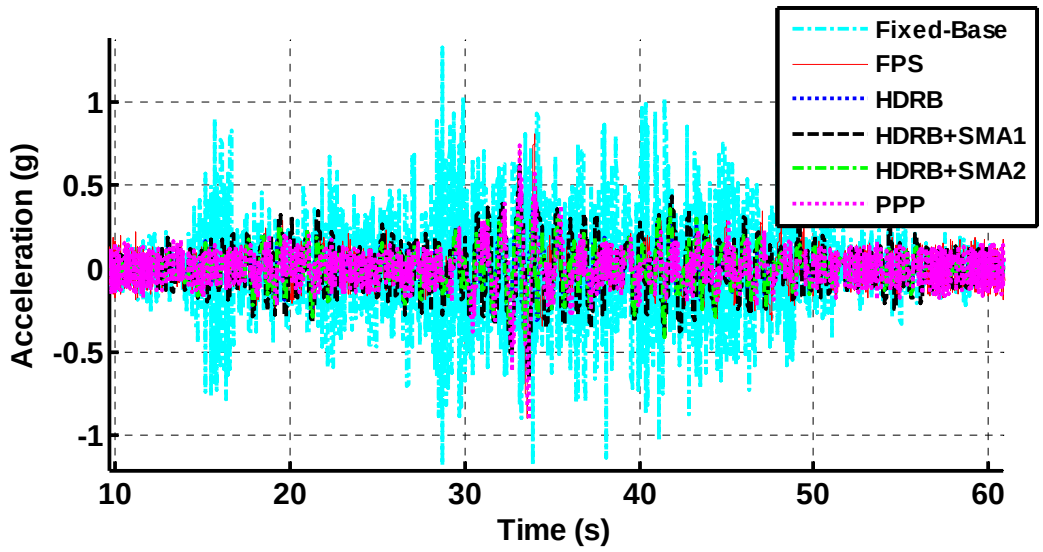

Fig. 173. Comparison 2: Absolute acceleration of 2nd floor from 1985 Llolleo, Chile, earthquake

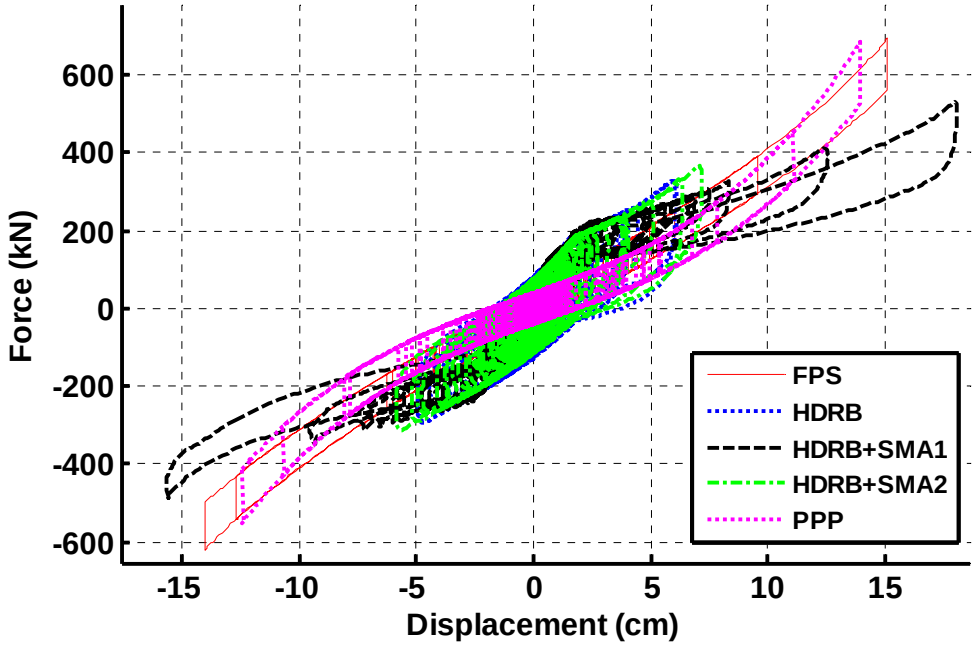

Fig. 174. Comparison 2: Total force from all isolation devices from 1985 Llolleo, Chile, earthquake

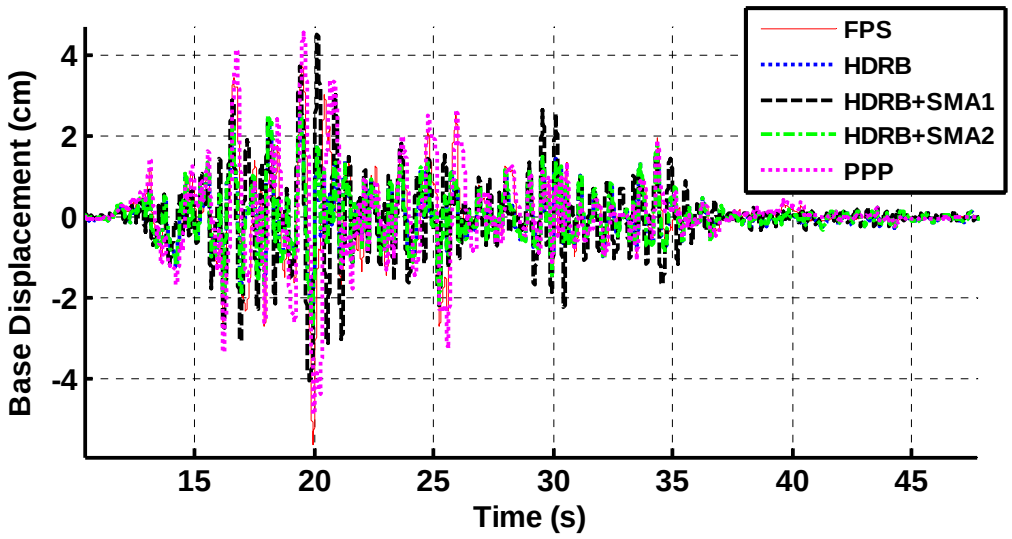

Fig. 175. Comparison 2: Base displacement from 2005 Tarapacá, Chile, earthquake

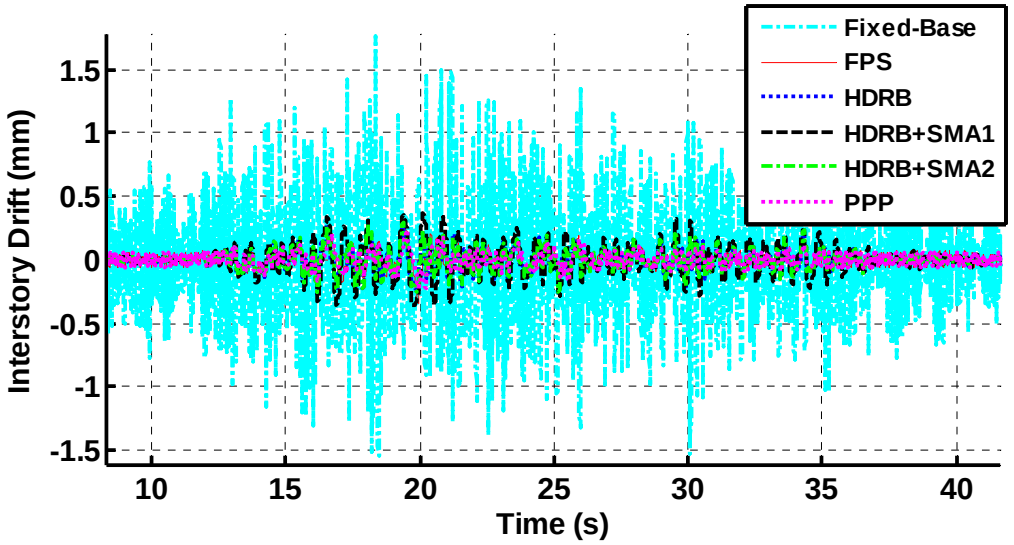

Fig. 176. Comparison 2: Interstory drift between base and 1st floor from 2005 Tarapacá, Chile, earthquake

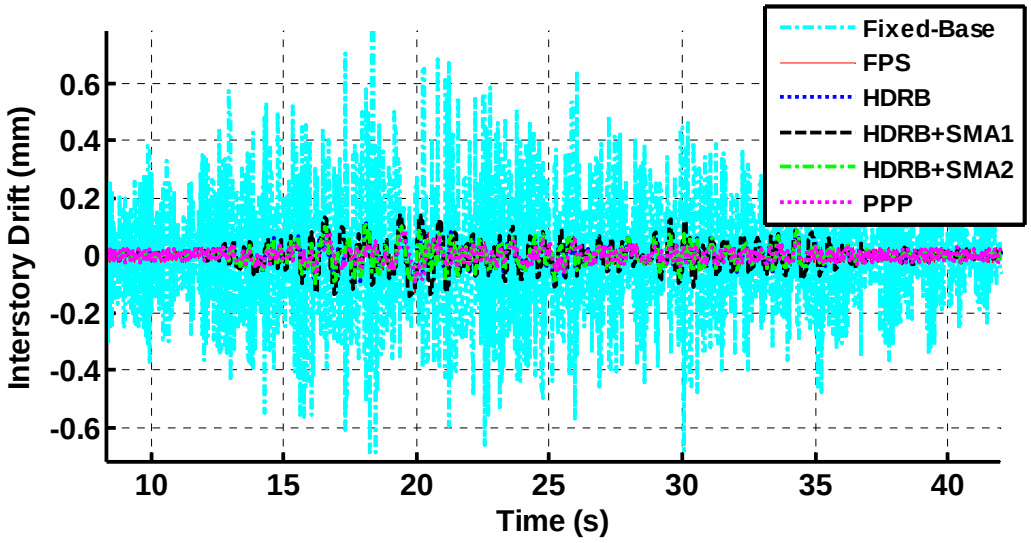

Fig. 177. Comparison 2: Interstory drift between 1st and 2nd floors from 2005 Tarapacá, Chile, earthquake

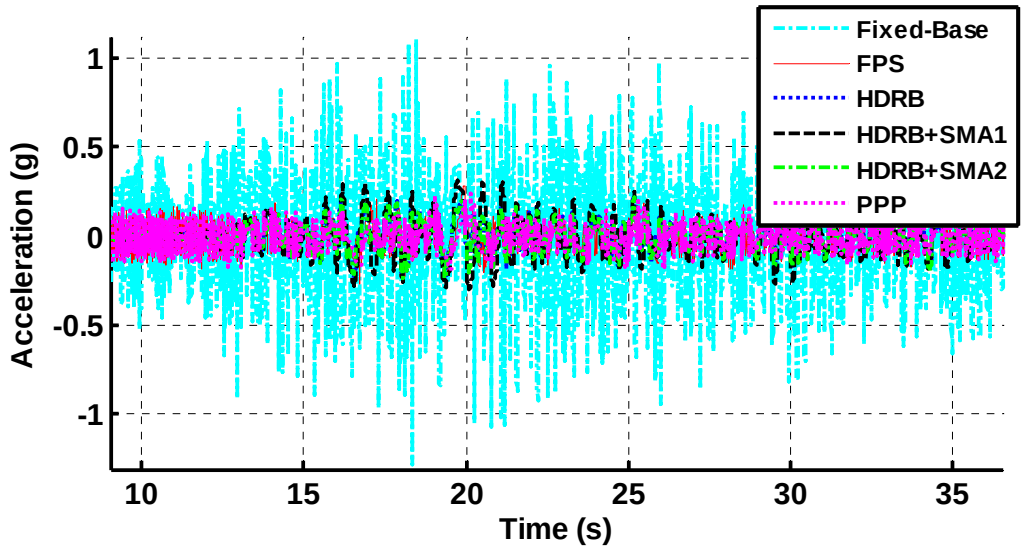

Fig. 178. Comparison 2: Absolute acceleration of 1st floor from 2005 Tarapacá, Chile, earthquake

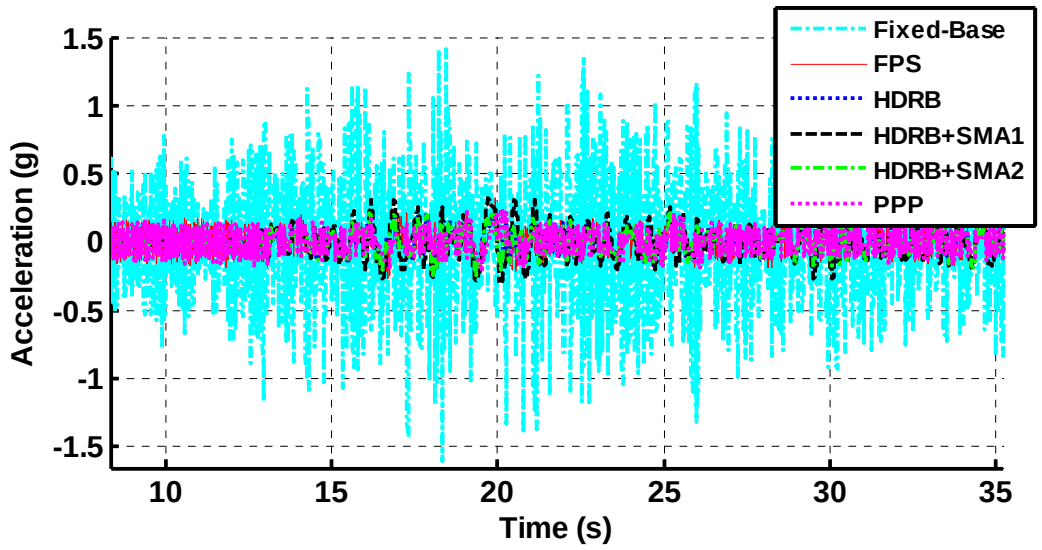

Fig. 179. Comparison 2: Absolute acceleration of 2nd floor from 2005 Tarapacá, Chile, earthquake

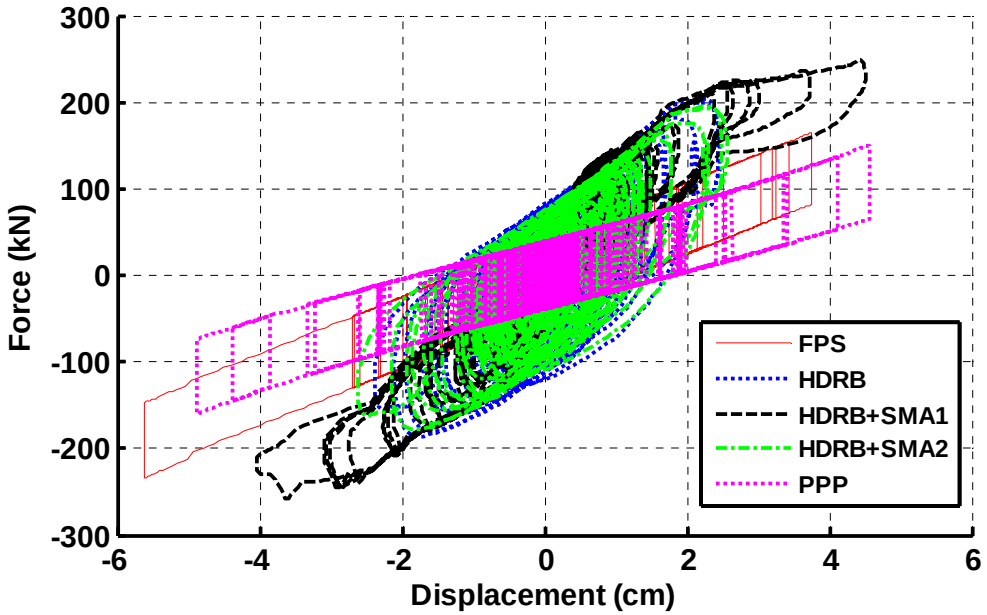

Fig. 180. Comparison 2: Total force from all isolation devices from 2005 Tarapacá, Chile, earthquake

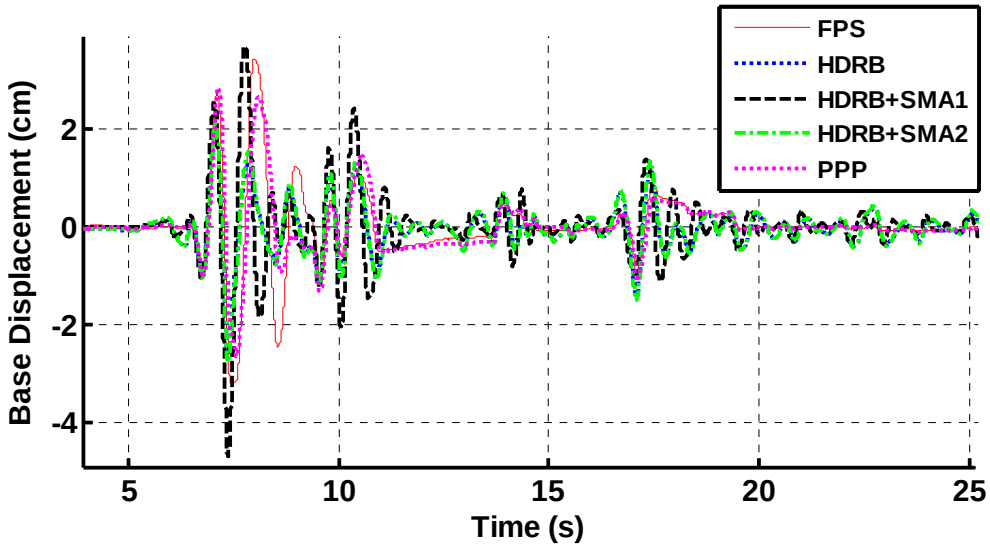

Fig. 181. Comparison 2: Base displacement from El Centro earthquake

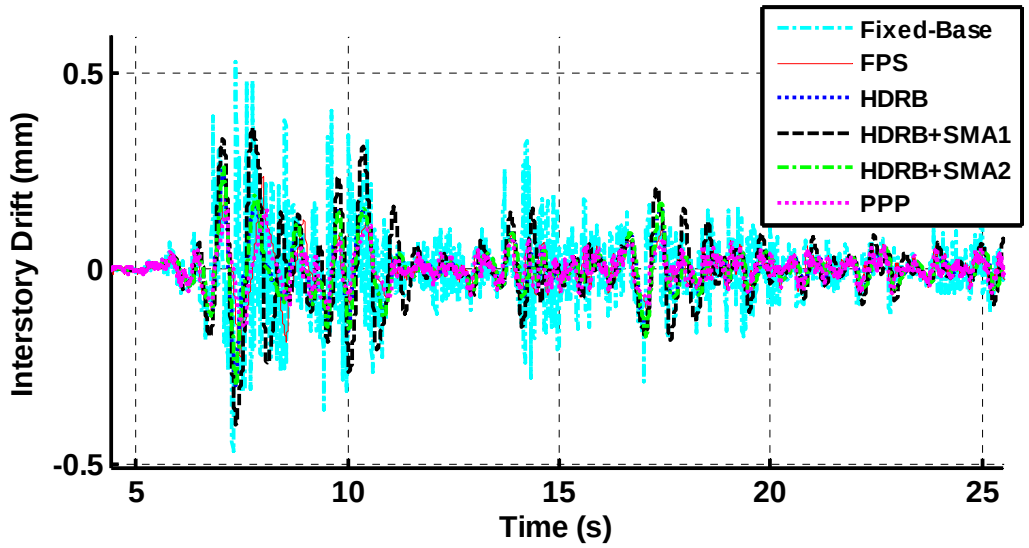

Fig. 182. Comparison 2: Interstory drift between base and 1st floor from El Centro earthquake

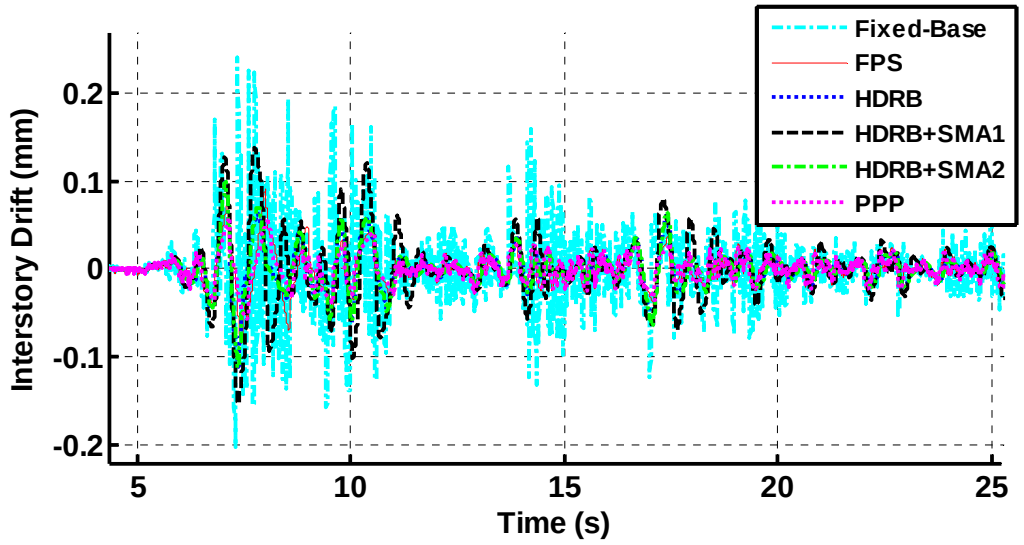

Fig. 183. Comparison 2: Interstory drift between 1st and 2nd floors from El Centro earthquake

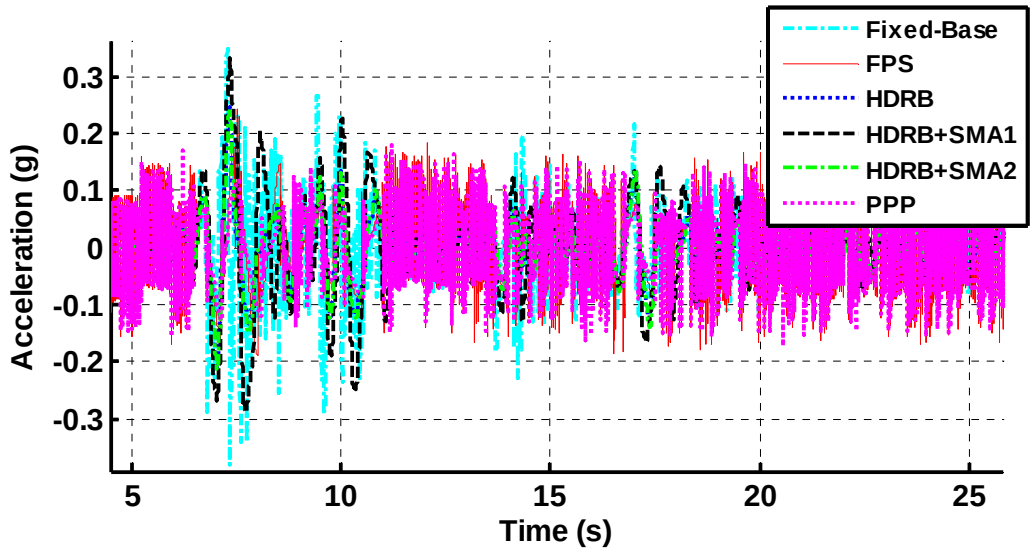

Fig. 184. Comparison 2: Absolute acceleration of 1st floor from El Centro earthquake

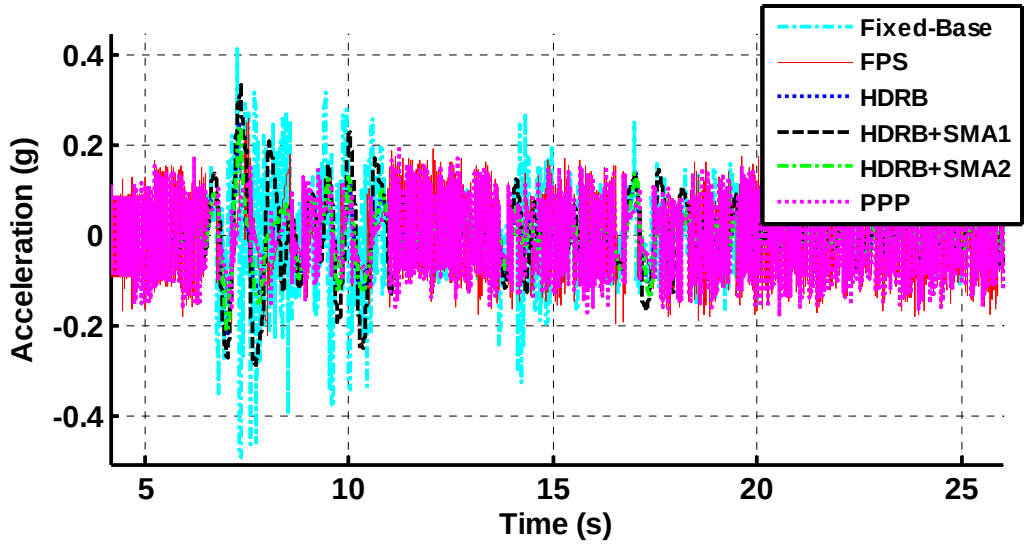

Fig. 185. Comparison 2: Absolute acceleration of 2nd floor from El Centro earthquake

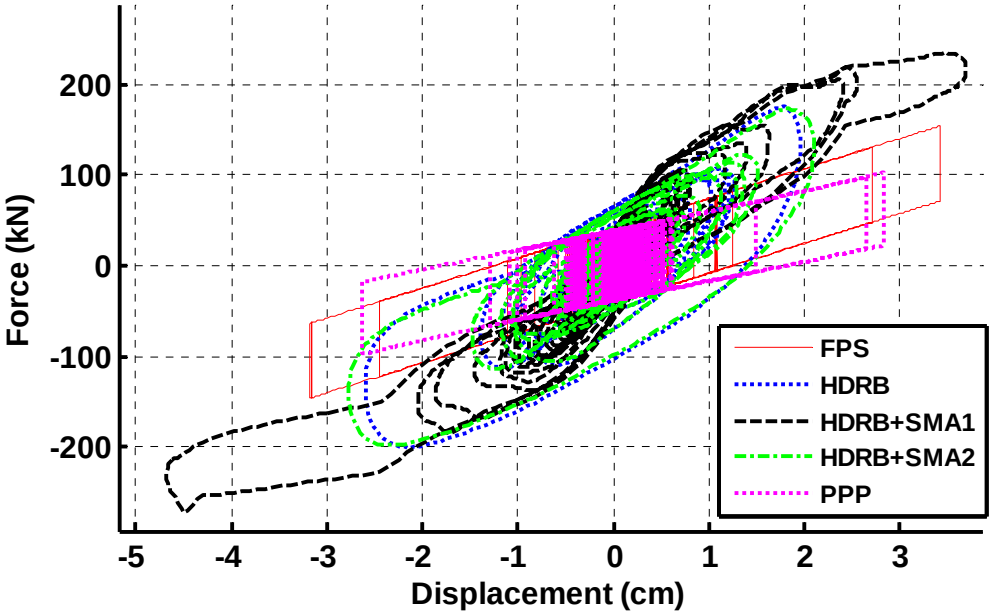

Fig. 186. Comparison 2: Total force from all isolation devices from El Centro earthquake

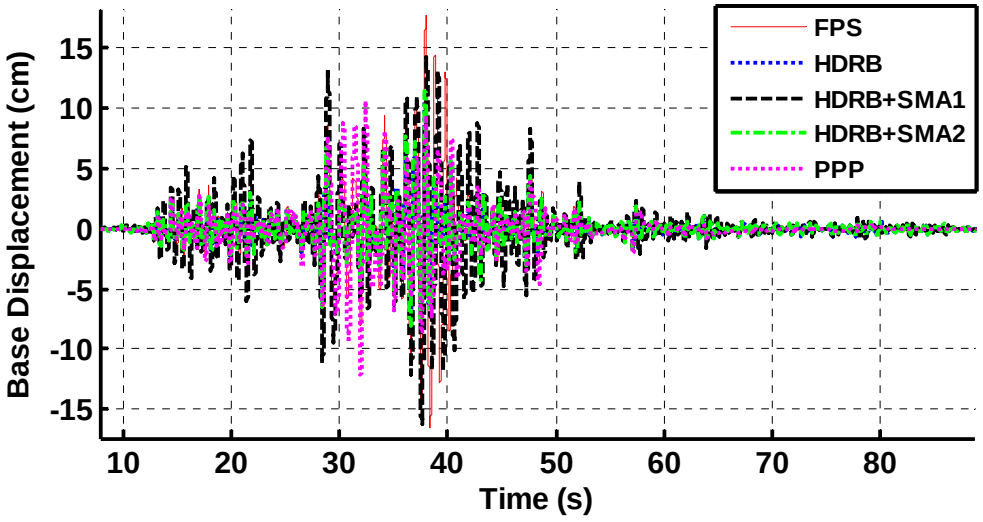

Fig. 187. Comparison 2: Base displacement from RSPMatch earthquake

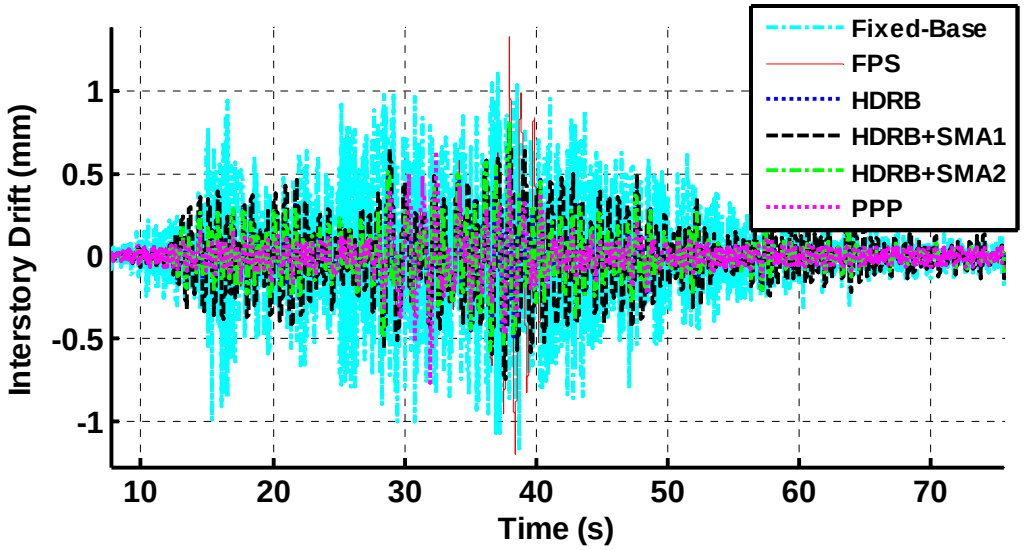

Fig. 188. Comparison 2: Interstory drift between base and 1st floor from RSPMatch earthquake

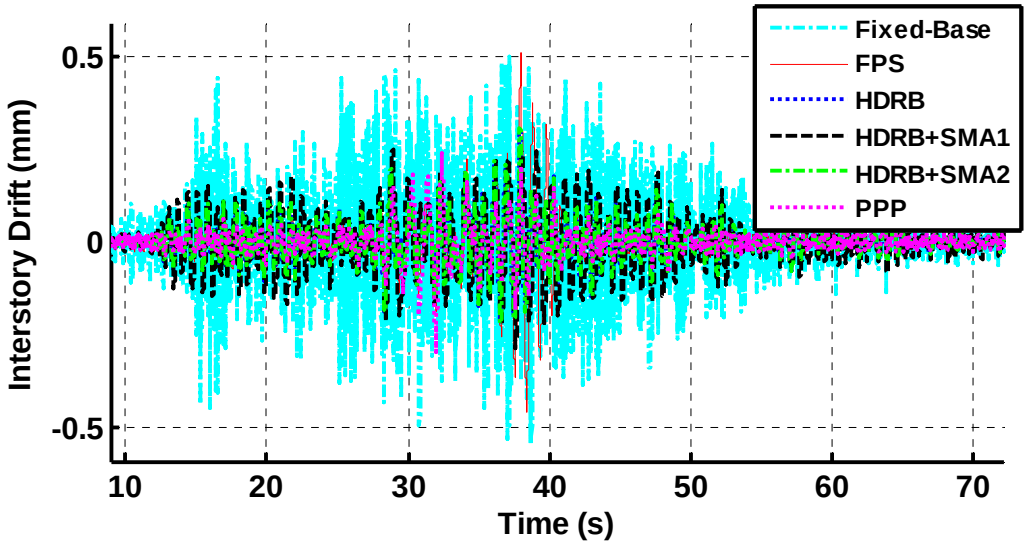

Fig. 189. Comparison 2: Interstory drift between 1st and 2nd floors from RSPMatch earthquake

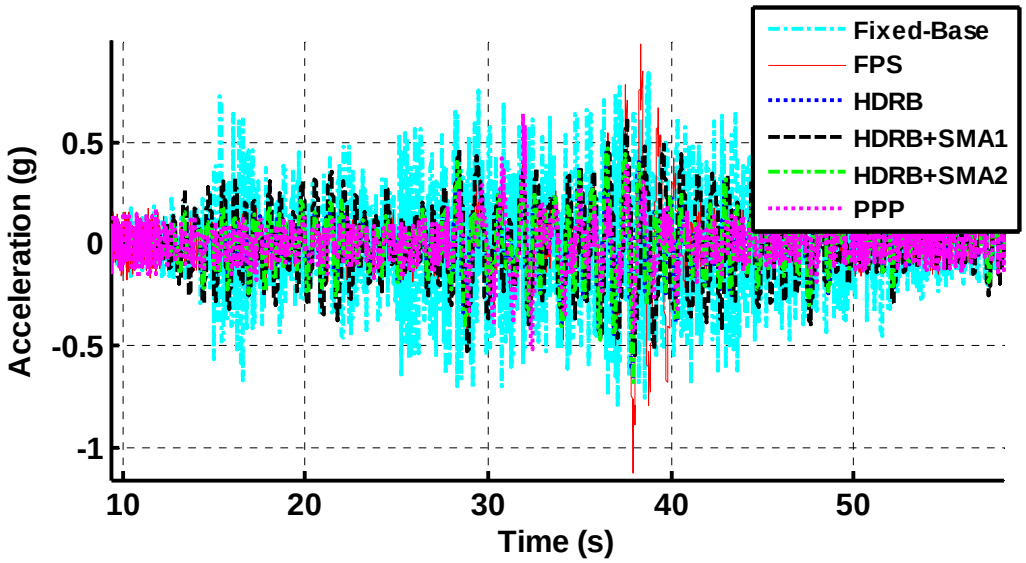

Fig. 190. Comparison 2: Absolute acceleration of 1st floor from RSPMatch earthquake

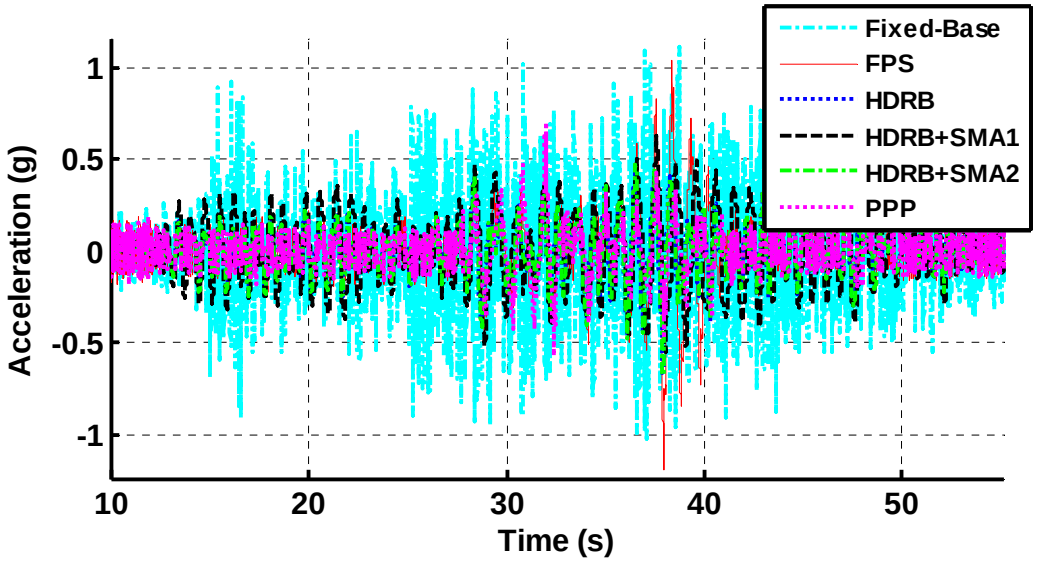

Fig. 191. Comparison 2: Absolute acceleration of 2nd floor from RSPMatch earthquake

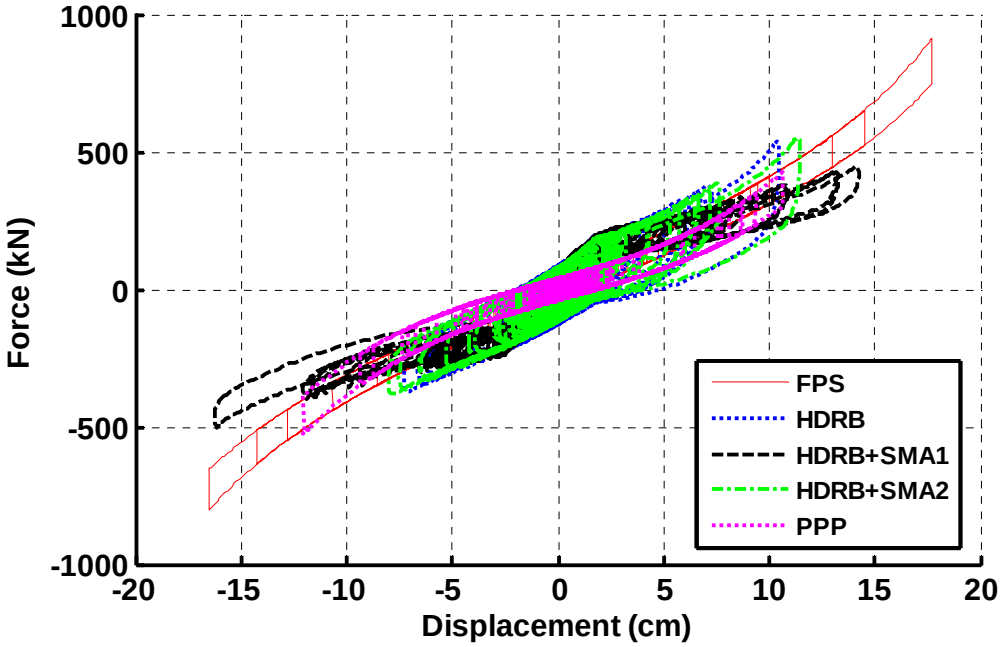

Fig. 192. Comparison 2: Total force from all isolation devices from RSPMatch earthquake

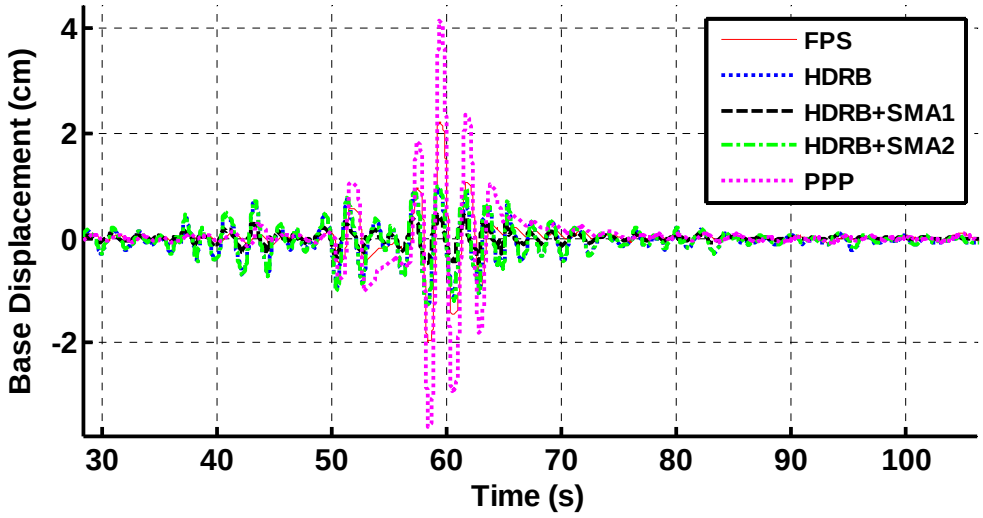

Fig. 193. Comparison 2: Base displacement from 1985 Mexico City earthquake

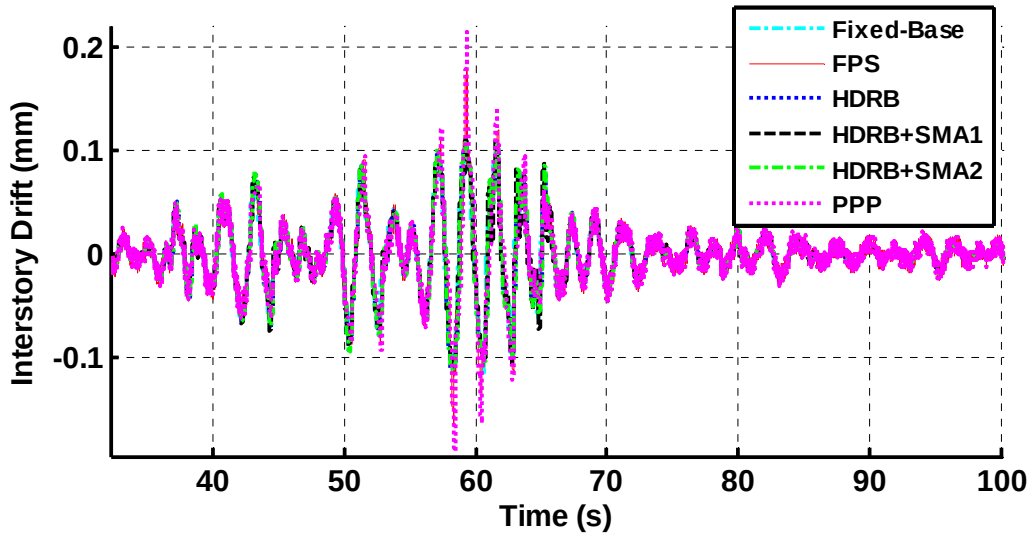

Fig. 194. Comparison 2: Interstory drift between base and 1st floor from 1985 Mexico City earthquake

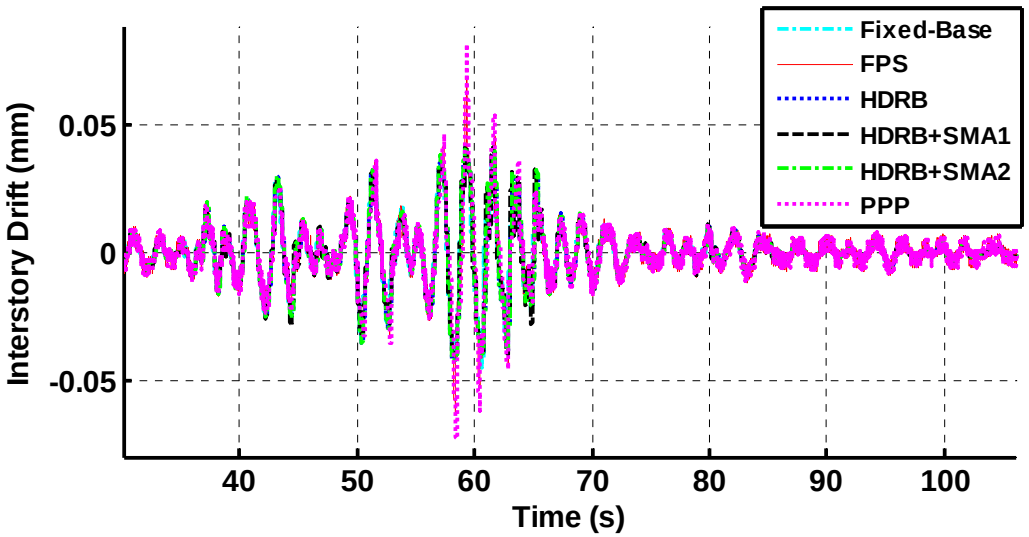

Fig. 195. Comparison 2: Interstory drift between 1st and 2nd floors from 1985 Mexico City earthquake

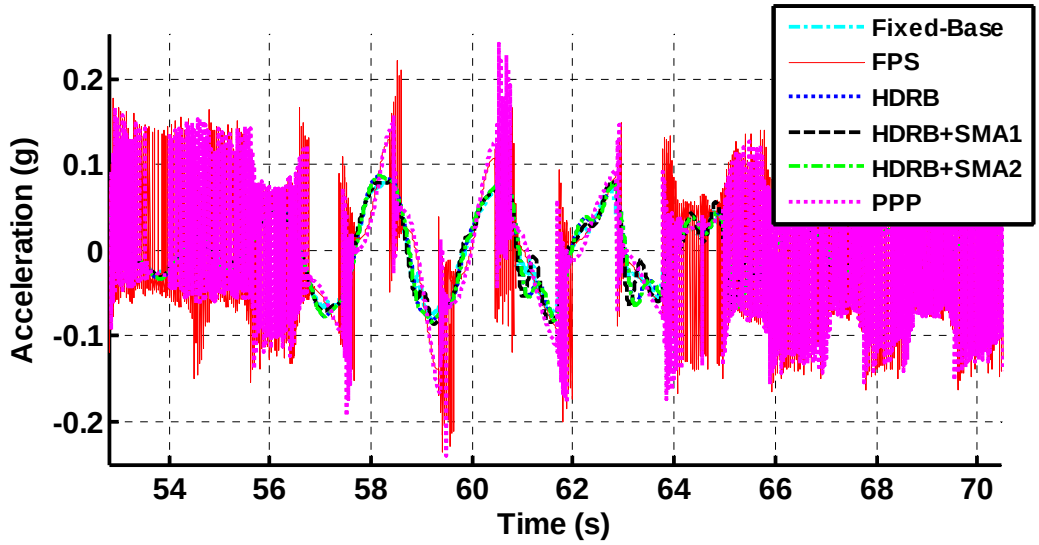

Fig. 196. Comparison 2: Absolute acceleration of 1st floor from 1985 Mexico City earthquake

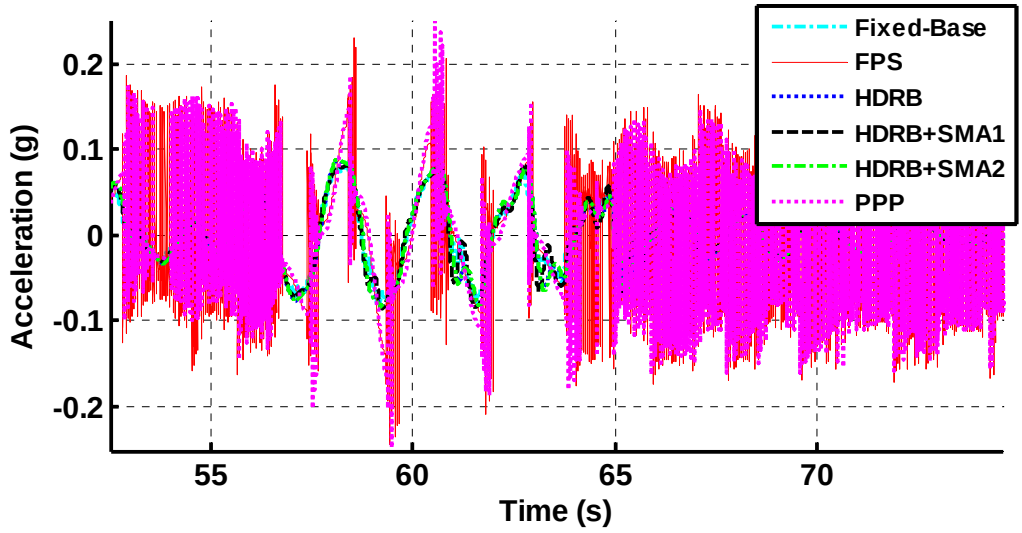

Fig. 197. Comparison 2: Absolute acceleration of 2nd floor from 1985 Mexico City earthquake

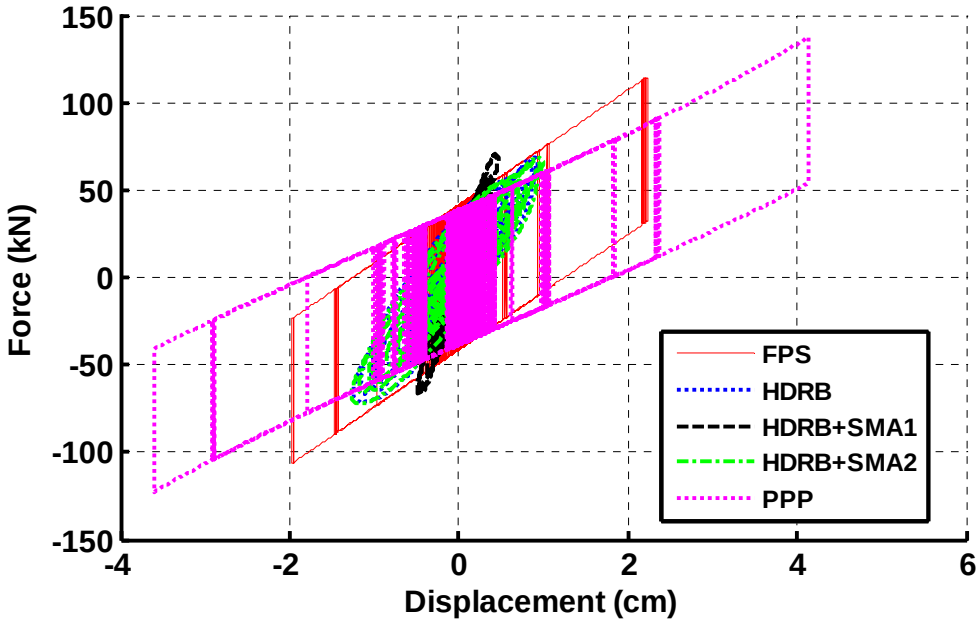

Fig. 198. Comparison 2: Total force from all isolation devices from 1985 Mexico City earthquake

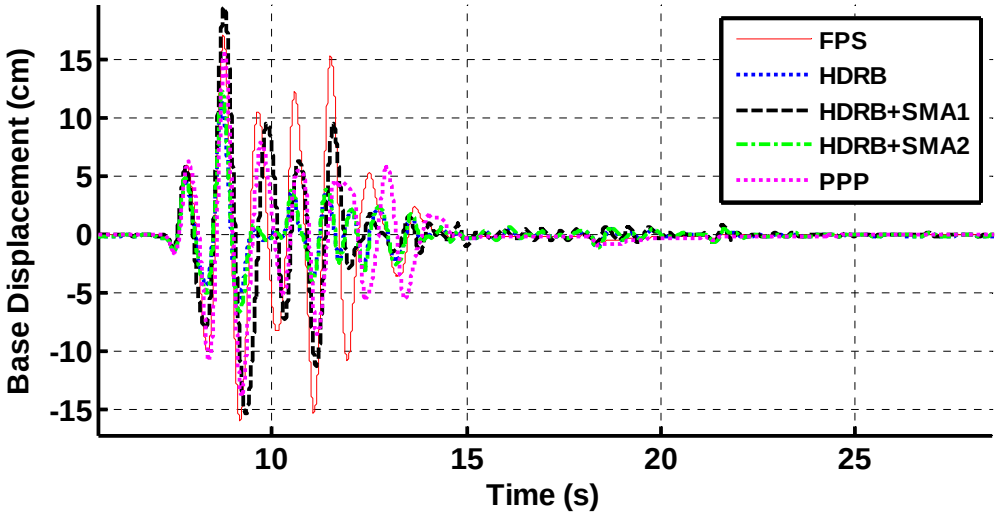

Fig. 199. Comparison 2: Base displacement from Kobe earthquake

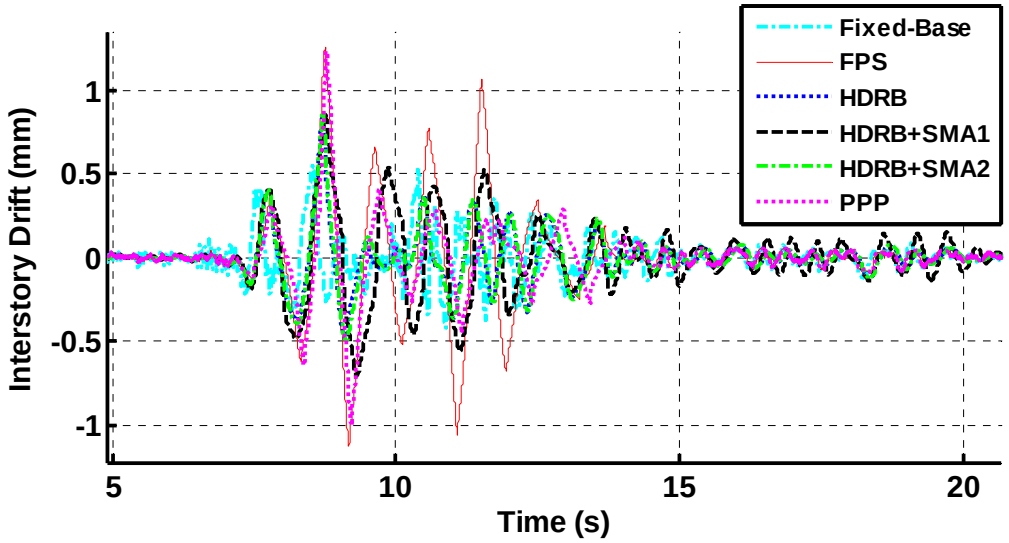

Fig. 200. Comparison 2: Interstory drift between base and 1st floor from Kobe earthquake

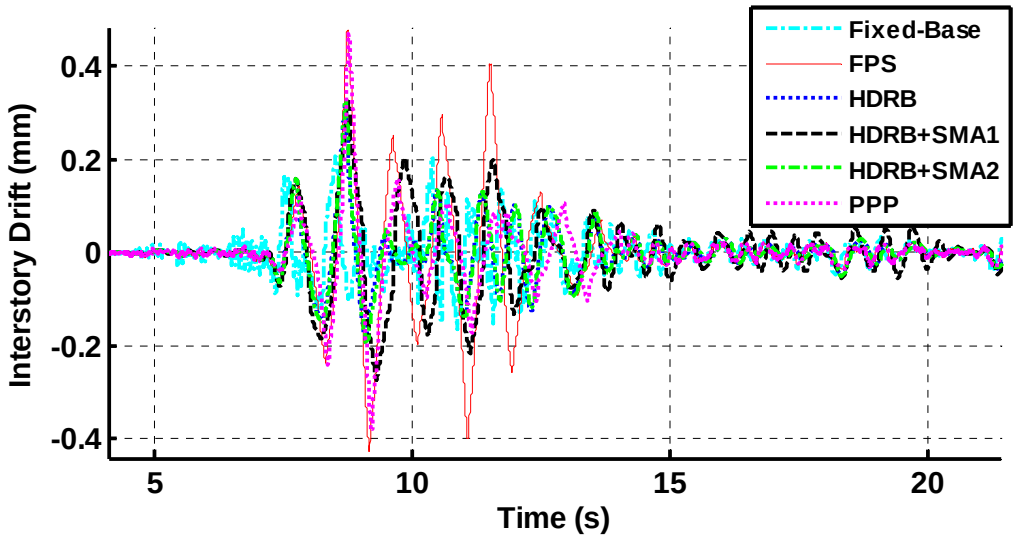

Fig. 201. Comparison 2: Interstory drift between 1st and 2nd floors from Kobe earthquake

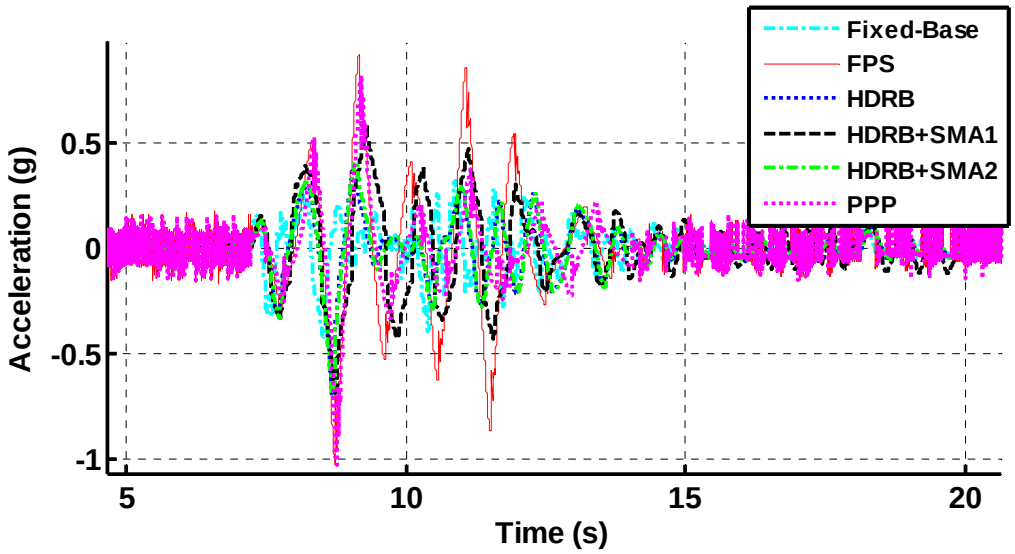

Fig. 202. Comparison 2: Absolute acceleration of 1st floor from Kobe earthquake

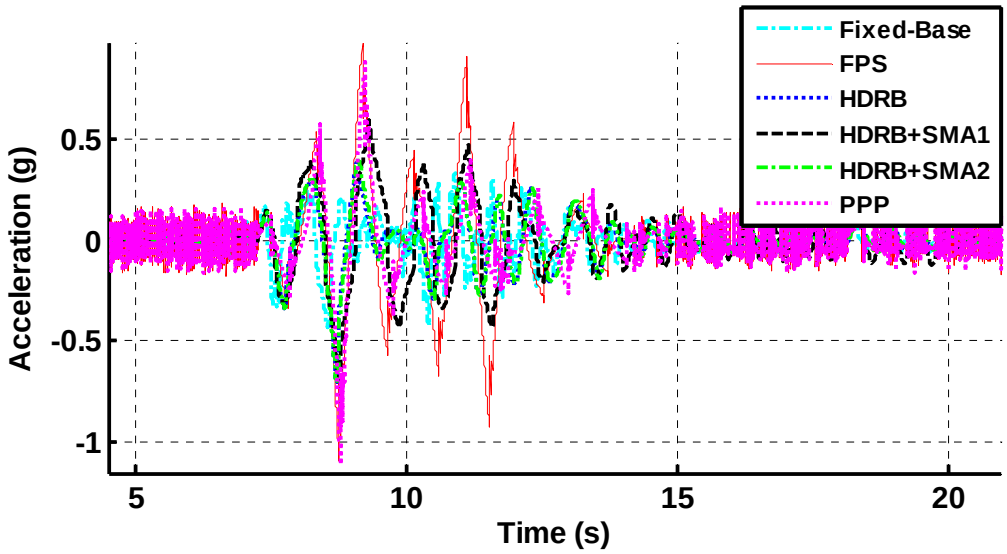

Fig. 203. Comparison 2: Absolute acceleration of 2nd floor from Kobe earthquake

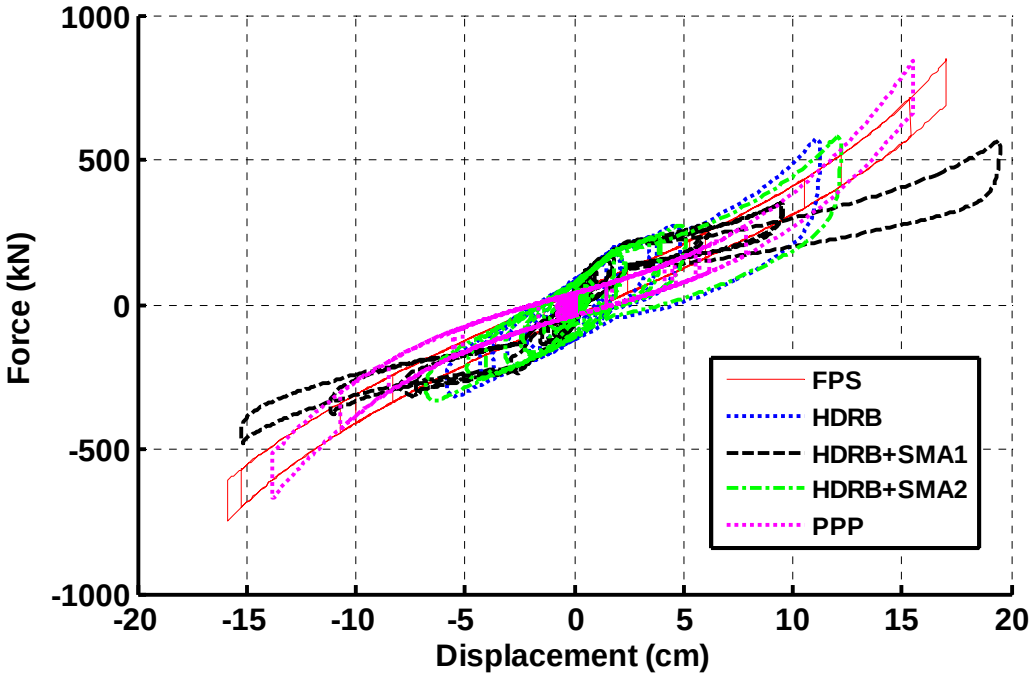

Fig. 204. Comparison 2: Total force from all isolation devices from Kobe earthquake

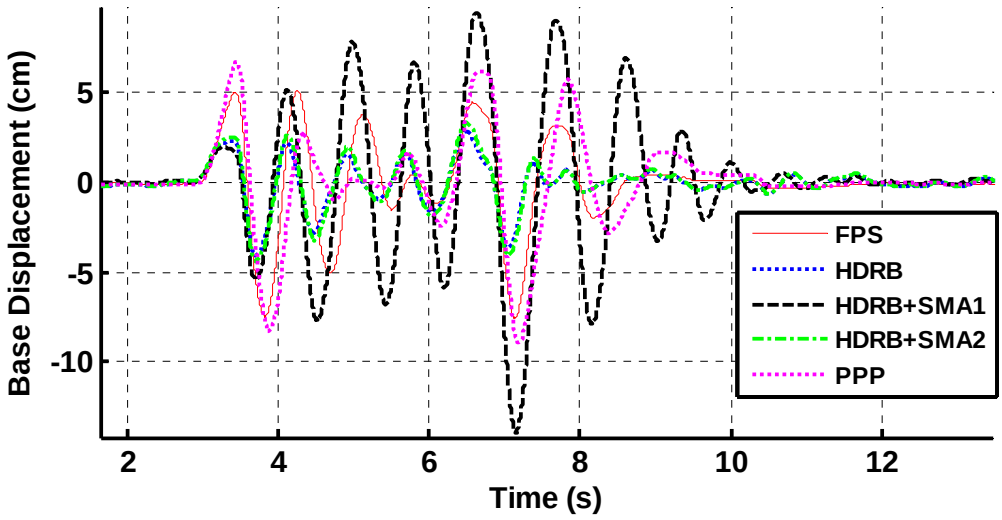

Fig. 205. Comparison 2: Base displacement from Northridge earthquake

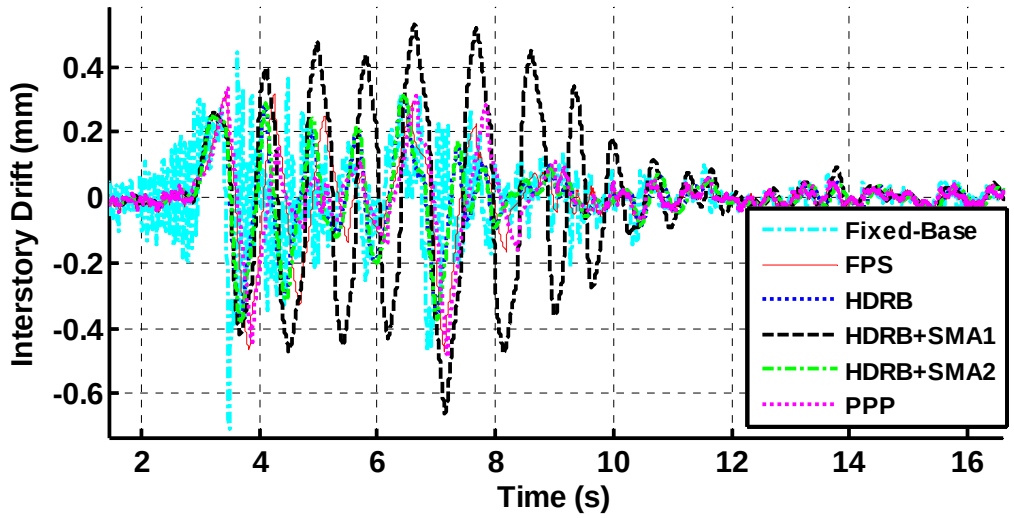

Fig. 206. Comparison 2: Interstory drift between base and 1st floor from Northridge earthquake

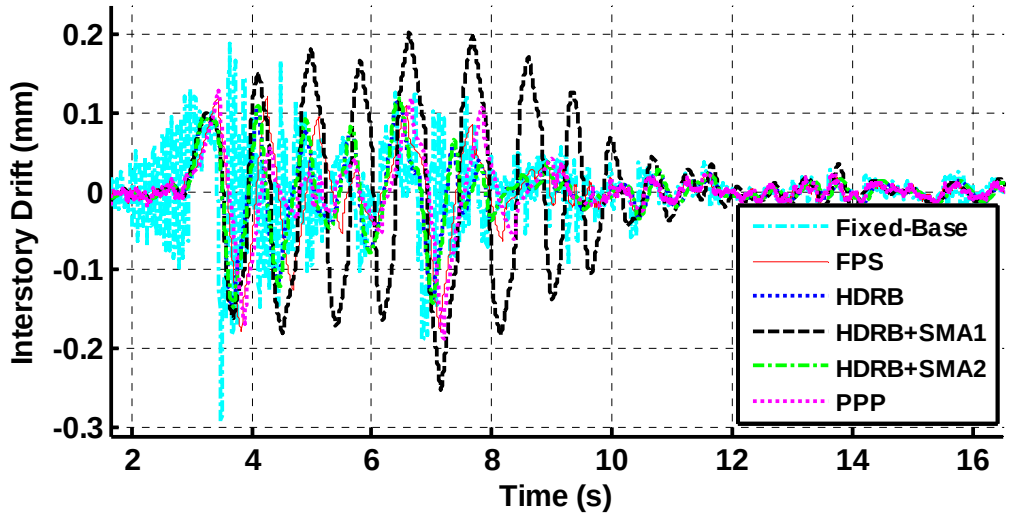

Fig. 207. Comparison 2: Interstory drift between 1st and 2nd floors from Northridge earthquake

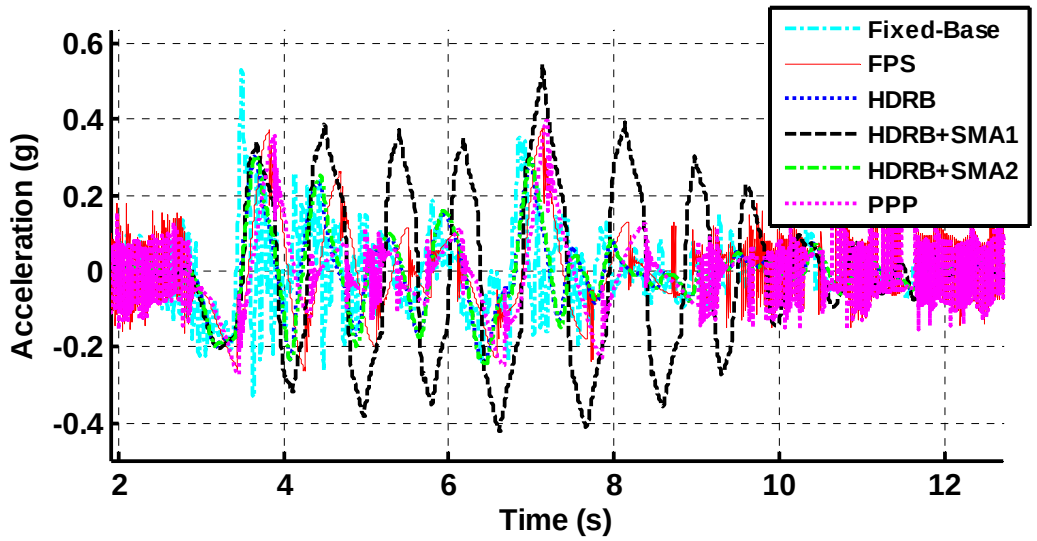

Fig. 208. Comparison 2: Absolute acceleration of 1st floor from Northridge earthquake

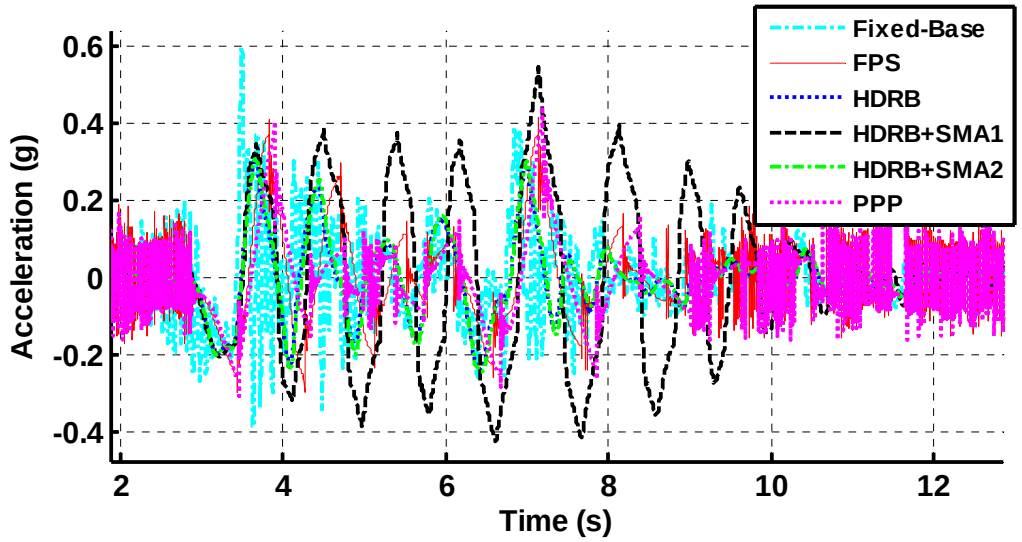

Fig. 209. Comparison 2: Absolute acceleration of 2nd floor from Northridge earthquake

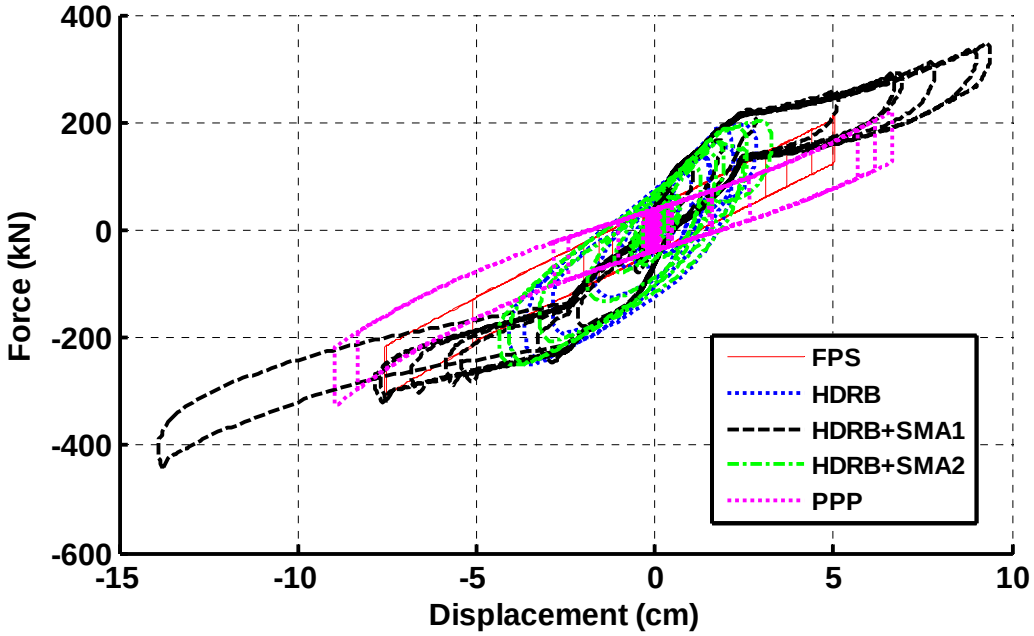

Fig. 210. Comparison 2: Total force from all isolation devices from Northridge earthquake

7.3.3. Performance Indices for Each Earthquake

The same set of PIs used to evaluate the performance of the base-isolated structure in Comparison 1 is utilized in Comparison 2. The suite of earthquakes applied to the base-isolated structure is also the same in Comparison 2 as in Comparison 1, except that the RSPMatch earthquake used here is created for a structure with an isolated period of 1.0 sec (see Fig. 50), instead of 2.0 sec. The PIs for each earthquake that result from numerical simulation are listed in Tables 18-25.

Determination of the optimal isolation system based on the PIs is more difficult for Comparison 2 than Comparison 1. For many of the earthquakes (such as the 1981 Chile, 2005 Tarapacá, Chile, El Centro, and RSPMatch earthquakes), one isolation system minimizes two or three PIs, while other isolation systems minimize the remaining PIs. However, for the 1985 Llolleo, Chile, and the scaled Mexico City, Kobe, and Northridge earthquakes, one isolation system minimizes the response of almost all

of the PIs. For the 1985 Llolleo, Chile, Kobe, and Northridge earthquakes, the HDRB isolation system minimizes generally all of the PIs over the other isolation systems. For the Mexico City earthquake, this is true for the HDRB+SMA1 isolation system. Although different isolation systems minimize the PIs for various earthquakes, the structure isolated using each of the isolation systems generally reduces the corresponding response from that of the fixed-base structure, except when subjected to the scaled Mexico City, Kobe, and Northridge earthquakes. In response to the three Chilean earthquakes (see Tables 18-20), every isolation system reduces all of the PIs from that of the fixed-base structure, except for the peak base shear resulting from the 1985 Llolleo, Chile, earthquake.

In contrast to Comparison 1, the HDRB+SMA1 and HDRB+SMA2 isolated structures do not consistently have higher peak base shear, RMS floor acceleration, peak structural shear, and peak floor acceleration than the HDRB isolated structure. This result and the relatively small differences in PIs resulting from many of the earthquakes for each isolation system are due to the fact that each isolation system is designed to result in the same fundamental period of vibration. Therefore, on a plot of spectral acceleration versus the period of the structure, each isolation system would result in designing the structure for the same spectral acceleration.

Because the HDRB isolated structure generally performs well in all of the earthquakes, including those with high spectral accelerations at long periods, this is the optimal isolation system for the case study structure based on a specified isolated period of 1.0 sec. A discussion of the results from Comparisons 1 and 2 is presented at the end of this section.

Table 18. Comparison 2: Results from 1981 Chile Earthquake

	Base Shear	Base Displace-ment	RMS Base Displace-ment	RMS Floor Acceleration	Structural Shear	Interstory Drift	Floor Accel-eration
	J_1	J_2 (m)	J_3 (m)	J_4	J_5	J_6	J_7
FPS	0.389	0.021	0.003	0.550	0.104	0.108	0.183
HDRB	0.652	0.020	0.003	0.251	0.175	0.175	0.212
HDRB+SMA1	0.785	0.029	0.004	0.406	0.221	0.221	0.254
HDRB+SMA2	0.630	0.021	0.003	0.241	0.169	0.169	0.205
PPP	0.305	0.022	0.003	0.506	0.087	0.087	0.186

Table 19. Comparison 2: Results from 1985 Llolleo, Chile, Earthquake

	Base Shear	Base Displace-ment	RMS Base Displace-ment	RMS Floor Acceleration	Structural Shear	Interstory Drift	Floor Accel-eration
	J_1	J_2 (m)	J_3 (m)	J_4	J_5	J_6	J_7
FPS	1.90	0.151	0.016	0.694	0.818	0.785	0.926
HDRB	0.901	0.061	0.009	0.500	0.389	0.373	0.440
HDRB+SMA1	1.45	0.180	0.019	0.802	0.630	0.605	0.708
HDRB+SMA2	1.00	0.072	0.010	0.503	0.430	0.412	0.489
PPP	1.88	0.139	0.017	0.617	0.804	0.772	0.916

Table 20. Comparison 2: Results from 2005 Tarapacá, Chile, Earthquake

	Base Shear	Base Displace-ment	RMS Base Displace-ment	RMS Floor Acceleration	Structural Shear	Interstory Drift	Floor Accel-eration
	J_1	J_2 (m)	J_3 (m)	J_4	J_5	J_6	J_7
FPS	0.580	0.056	0.006	0.321	0.144	0.198	0.223
HDRB	0.505	0.025	0.004	0.211	0.170	0.170	0.196
HDRB+SMA1	0.639	0.045	0.006	0.306	0.212	0.215	0.246
HDRB+SMA2	0.485	0.026	0.004	0.204	0.164	0.164	0.188

Table 20. Continued

	Base Shear J_1	Base Displacement J_2 (m)	RMS Base Displacement J_3 (m)	RMS Floor Acceleration J_4	Structural Shear J_5	Interstory Drift J_6	Floor Acceleration J_7
PPP	0.397	0.049	0.008	0.293	0.130	0.134	0.184

Table 21. Comparison 2: Results from El Centro Earthquake

	Base Shear J_1	Base Displacement J_2 (m)	RMS Base Displacement J_3 (m)	RMS Floor Acceleration J_4	Structural Shear J_5	Interstory Drift J_6	Floor Acceleration J_7
FPS	0.883	0.034	0.005	1.42	0.447	0.447	0.643
HDRB	1.15	0.026	0.003	0.673	0.495	0.566	0.647
HDRB+SMA1	1.56	0.047	0.005	1.20	0.684	0.758	0.876
HDRB+SMA2	1.14	0.028	0.004	0.684	0.488	0.560	0.639
PPP	0.587	0.028	0.004	1.29	0.295	0.295	0.480

Table 22. Comparison 2: Results from RSPMatch Earthquake

	Base Shear J_1	Base Displacement J_2 (m)	RMS Base Displacement J_3 (m)	RMS Floor Acceleration J_4	Structural Shear J_5	Interstory Drift J_6	Floor Acceleration J_7
FPS	2.96	0.177	0.022	0.812	1.21	1.14	1.33
HDRB	1.74	0.105	0.012	0.571	0.710	0.670	0.785
HDRB+SMA1	1.63	0.163	0.025	0.920	0.605	0.638	0.738
HDRB+SMA2	1.79	0.115	0.013	0.577	0.731	0.689	0.805
PPP	1.69	0.121	0.018	0.566	0.573	0.658	0.762

Table 23. Comparison 2: Results from 1985 Mexico City Earthquake

	Base Shear	Base Displace-ment	RMS Base Displace-ment	RMS Floor Acceleration	Structural Shear	Interstory Drift	Floor Accel-eration
	J_1	J_2 (m)	J_3 (m)	J_4	J_5	J_6	J_7
FPS	2.49	0.022	0.002	5.48	1.67	1.57	2.71
HDRB	1.56	0.013	0.002	1.13	1.01	0.986	1.00
HDRB+SMA1	1.55	0.005	0.001	1.08	1.04	0.973	0.997
HDRB+SMA2	1.57	0.013	0.002	1.14	1.01	0.996	1.01
PPP	2.99	0.041	0.005	5.08	2.01	1.88	2.78

Table 24. Comparison 2: Results from Kobe Earthquake

	Base Shear	Base Displace-ment	RMS Base Displace-ment	RMS Floor Acceleration	Structural Shear	Interstory Drift	Floor Accel-eration
	J_1	J_2 (m)	J_3 (m)	J_4	J_5	J_6	J_7
FPS	3.69	0.170	0.028	2.60	2.30	2.30	2.57
HDRB	2.50	0.112	0.011	1.22	1.56	1.56	1.66
HDRB+SMA1	2.46	0.195	0.025	1.84	1.56	1.56	1.63
HDRB+SMA2	2.54	0.122	0.012	1.26	1.59	1.59	1.68
PPP	3.69	0.155	0.021	1.90	2.25	2.25	2.59

Table 25. Comparison 2: Results from Northridge Earthquake

	Base Shear	Base Displace-ment	RMS Base Displace-ment	RMS Floor Acceleration	Structural Shear	Interstory Drift	Floor Accel-eration
	J_1	J_2 (m)	J_3 (m)	J_4	J_5	J_6	J_7
FPS	1.33	0.076	0.012	1.63	0.716	0.661	0.703
HDRB	1.08	0.041	0.006	0.949	0.679	0.534	0.571
HDRB+SMA1	1.92	0.139	0.022	2.12	1.19	0.929	1.02
HDRB+SMA2	1.08	0.044	0.007	0.988	0.699	0.539	0.572

Table 25. Continued

	Base Shear J_1	Base Displace-ment J_2 (m)	RMS Base Displace-ment J_3 (m)	RMS Floor Acceleration J_4	Structural Shear J_5	Interstory Drift J_6	Floor Accel-eration J_7
PPP	1.41	0.089	0.014	1.48	0.757	0.692	0.745

7.4. Evaluation of Comparisons 1 and 2

Overall, the FPS and PPP isolated structures perform significantly better in Comparison 1 than in Comparison 2 in terms of the PIs, except for the PIs related to base displacement. However, the peak and RMS base displacement values for the FPS and PPP isolation systems are acceptable in both Comparisons 1 and 2. The HDRB isolated structure has comparable results in Comparisons 1 and 2 due to the eight - 20 cm diameter HDRBs used in Comparison 1 and the nine - 20 cm diameter HDRBs used in Comparison 2. The HDRB+SMA1 isolated structure performs somewhat better in Comparison 2 than in Comparison 1 in response to the 1981 Chile, 1985 Llolleo, Chile, 2005 Tarapaca, Chile, El Centro, and RSPMatch earthquakes. The results for the HDRB+SMA1 isolated structure are comparable in Comparisons 1 and 2 for the scaled Mexico City earthquake, while the results are better in Comparison 1 for the scaled Kobe and Northridge earthquakes. This difference in performance of the HDRB+SMA1 system resulting from different earthquakes can be attributed to the near-fault characteristics of the scaled Kobe and Northridge ground motions. The HDRB+SMA2 isolated structure yields the same PIs in both Comparisons 1 and 2, except for those resulting from the RSPMatch earthquakes, because the selected design parameters and number of devices are the same for both comparisons. The PIs resulting from the RSPMatch earthquakes are somewhat better in Comparison 2 for the HDRB+SMA2 case than in Comparison 1 because the RSPMatch earthquake used in Comparison 1 was based on a 2.0 sec period of the isolated structure, while the RSPMatch earthquake used in Comparison 2 was based on a 1.0 sec period of the isolated structure. As discussed in

Section 4.2, a shorter isolated period of the structure results in a response spectrum with lower spectral acceleration values at long periods than that of a structure with a longer isolated period (see Fig. 33).

Comparison 1 is considered more practical than Comparison 2 because in the design process, the isolation system would be optimized based on characteristics of the structure (Comparison 1) rather than forcing the isolated structure to have a specific fundamental period of vibration (Comparison 2). In addition, Comparison 2 forced the FPS and PPP base-isolated structures to each have a significantly shorter period than the periods resulting from the optimizations in Comparison 1. Parameters for the FPS and PPP base-isolated structures were selected in Comparison 2 to result in a fundamental period of 1.0 sec, which is approximately the period of the optimized HDRB, HDRB+SMA1, and HDRB+SMA2 base-isolated structures in Comparison 1.

The uplift of the FPS and PPP isolation systems can also be compared for each of the analyses. Eq. (16) is utilized to calculate the vertical displacement, or uplift, of the FPS bearings. In Comparison 1, the maximum uplift of the FPS bearings for any of the earthquakes is 0.39 cm, while the maximum uplift of the FPS bearings in Comparison 2 is 7.7 cm. The maximum horizontal displacement in Comparison 1 is approximately 17 cm, which occurs during the Mexico City earthquake. For Comparison 2, the maximum horizontal displacement is approximately 18 cm, which occurs during the RSPMatch earthquake. The significant difference in vertical displacement between the two comparisons is due to the large difference in the radius of curvature of the FPS bearings. Because an uplift of 7.7 cm is considered to be unacceptable for the structure, the FPS bearings used in Comparison 2, with $R = 0.25$ m and $\mu = 0.05$ are determined to be unacceptable for application in the structure. The maximum uplift for the PPP system is calculated from the difference between the y-coordinate of the top capital and the length of the pile. The PPP system has less than 0.5 cm uplift for every earthquake in both Comparisons 1 and 2.

Table 26 shows the minimum reduction in response of the base-isolated structure from that of the fixed-base structure for each of the Chilean earthquakes considered,

namely the 1981 Chile, 1985 Llolleo, Chile, and 2005 Tarapacá, Chile, earthquakes. The quantities in parentheses indicate amplification occurs in the response of the base-isolated structure compared to that of the fixed-base case. The tabulated values are based on the device parameters included in Comparison 1, in which eight devices were used in each isolation system. It can be concluded that the PPP isolation system in Comparison 1 results in the greatest reduction in response of the fixed-base structure, though it often results in a residual displacement of 2-3 cm after the cessation of earthquake motion (see Fig. 114, for example). The PPP isolated structure (in Comparison 1) also generally reduces the response of the fixed-base structure more than the other isolation systems in response to the El Centro, RSPMatch, Mexico City, and Kobe earthquakes. In addition, the PPP isolation system is manufactured from readily available construction materials, including concrete, reinforcing steel, prestressing steel, and steel plates. For these reasons, the PPP isolation system utilized in Comparison 1 is the most optimal system considered for the case study structure, assuming a residual displacement of the structure on the order of 2-3 cm is tolerable. If this residual displacement is not tolerable, the FPS isolation system in Comparison 1 is the most optimal of the isolation systems studied. It should be noted that the isolation systems involving the use of HDRBs would likely be more effective if they resulted in a longer fundamental period of vibration of the base-isolated structure.

Table 26. Minimum Reduction in Response to Chilean Earthquakes (in %)

Isolation System	Base Shear	RMS Floor Acceleration	Structural Shear	Interstory Drift	Floor Acceleration
FPS	86	68	94	94	87
HDRB	2	53	58	60	52
HDRB+SMA1	(70)	(7)	39	38	24
HDRB+SMA2	0	50	57	59	51
PPP	88	87	95	95	94

8. CONCLUSIONS

The aim of this research has been to assess how implementing various base isolation systems would impact the seismic performance of a typical Chilean masonry house. Towards this end, several topics of study are included, as listed below:

- Ambient vibration testing of a case study structure
- Dynamic analysis of the structure as a MDOF model using state-space formulation
- Generation of an earthquake to match the design response spectrum using RSPMatch2005b for use in optimization of the base isolation systems
- Selection of earthquakes with various intensities and frequency content for use in dynamic analysis
- Numerical modeling of several base isolation devices using analytical formulations and experimental data through means of fuzzy logic and S-functions
- Optimization of each device using NSGA-II CE or a trial-and-error approach
- Two part comparison of five isolation systems subjected to a suite of earthquakes

Discussion of each of the topics mentioned above is included in eight corresponding sections.

Section 1 gives an introduction to the need for seismic mitigation measures in Chile due to its strong seismicity, evident through historic earthquakes in the region. An overview of confined masonry construction, the building method employed in the case study structure and in many structures in South and Central America, is also presented. Finally, an overview of base isolation applications in Chile is included.

Section 2 provides a review of literature and background information for the topics involved in the study. This is included to give the reader knowledge of the current and historical research efforts carried out in topics applicable to this study.

Section 3 discusses the case study structure and the ambient vibration testing performed on it to determine its stiffness and damping characteristics. This section also includes mass calculations used together with the stiffness and damping properties to create a MDOF model of the structure.

Section 4 includes a description of the generation of the design response spectra utilized to create corresponding earthquake acceleration-time histories used to optimize the base isolation devices. The process of creating the earthquake acceleration-time histories using RSPMatch2005b is also described. In addition, the other ground motions used in the suite of earthquakes and their characteristics are explained.

Section 5 presents an explanation of the analytical models and experimental data used to model each of the isolation devices, including the FPS, HDRB, HDRB+SMA1, HDRB+SMA2, and PPP isolators. It also explains how a FIS was created to model the NiTi SMA wires based on experimental testing.

Section 6 explains the NSGA-II CE algorithm, and how it was used to optimize the parameters of the FPS and PPP isolators based on several objective functions. Pareto fronts and results of the GA optimization are presented. A manual optimization of the FPS parameters is included for comparison with the GA results. The trial-and-error optimization of the HDRB, HDRB+SMA1, and HDRB+SMA2 isolators using the same objective functions is also discussed.

Section 7 presents a two part comparison of the response of the base-isolated structures to a suite of earthquake motions. The first comparison uses base isolation systems with optimized device parameters from the NSGA-II CE and trial-and-error procedures, while the second comparison uses the quantity of isolators and isolator parameters to yield an isolated period of 1.0 sec for the structure. The effectiveness of each isolation system is measured in terms of seven PIs, which quantify peak base and structural shear, peak and RMS base displacement, peak interstory drift, and peak and RMS absolute floor acceleration.

8.1. Overall Effectiveness of Base Isolation Systems

The FPS and PPP isolation systems utilizing eight devices with optimized parameters (Comparison 1) significantly reduce the peak base and structural shear, peak interstory drift, and peak and RMS absolute floor acceleration from that of the fixed-base case for all of the earthquakes considered, except for the scaled 1985 Mexico City earthquake. For this earthquake, the PPP isolated structure outperforms the FPS isolated structure because the only quantity it amplifies is the RMS floor acceleration of the fixed-base structure (by 31%). Acceptable magnitudes of base displacement are maintained for both the FPS and PPP isolation systems with optimized parameters. The isolation systems involving the use of optimized HDRBs (the HDRB, HDRB+SMA1, and HDRB+SMA2 cases in Comparison 1) are generally effective in reducing the response of the fixed-base structure to the Chilean earthquakes considered (the 1981 Chile, 1985 Llolleo, Chile, and 2005 Tarapacá, Chile, earthquakes), but they often result in amplification of the shear and acceleration quantities from the El Centro, RSPMatch, and scaled Mexico City, Kobe, and Northridge earthquakes.

For the comparison in which the parameters of each isolation system were selected to result in a fundamental period of vibration of 1.0 sec for the structure (Comparison 2), all of the isolation systems generally reduce the response of the base-isolated structure from that of the fixed-base structure for the Chilean earthquakes considered. However, significant amplifications in the response of the base-isolated structure from that of the fixed-base structure occur for the other (non-Chilean) earthquakes considered.

Overall, the FPS and PPP isolation systems using eight devices with optimized parameters (Comparison 1) result in the most significant reductions in the response of the base-isolated structure from that of the fixed-base structure. The FPS isolation system with optimized parameters reduces the response of the base-isolated structure from that of the fixed-base structure by a minimum of 86% for peak base shear, 68% for RMS floor acceleration, 94% for structural shear, 94% for interstory drift, and 87% for floor acceleration for the Chilean earthquakes considered. Similarly, the PPP isolation

system with optimized parameters reduces the response of the base-isolated structure from that of the fixed-base structure by a minimum of 88% for peak base shear, 87% for RMS floor acceleration, 95% for structural shear, 95% for interstory drift, and 94% for floor acceleration for the Chilean earthquakes considered, though it results in residual displacement on the order of 2-3 cm after the occurrence of each earthquake.

8.2. Future Work

With a comprehensive study of the seismic performance of the case study structure base-isolated using the FPS, HDRB, HDRB+SMA1, HDRB+SMA2, and PPP isolation systems having been conducted, several possibilities for extension of the study exist. One area for extension of the study is related to the devices studied. It would be beneficial to have access to more experimental testing data of HDRBs subjected to cyclic loading to improve optimization of the isolation systems that use HDRBs. Another possibility for future work would be to model the behavior of FRBs, should experimental results become available. A third aspect for future consideration would be to study the behavior of PPP isolators with various rolling surfaces. Lastly, additional devices could be considered.

Another logical extension of the present study would be to analyze the performance of the case study structure in two or three directions. Torsion of the monosymmetric case study structure could also be studied by modeling the structure using groups of eccentric masses. The overhang of the second floor of the case study structure could cause torsion of the structure to be an important consideration.

REFERENCES

Abrahamson, N. A. (1992). "Non-stationary spectral matching." *Seismological Research Letters*, 63(1), 30.

Almazan, J. L., and De la Llera, J. C. (2003). "Physical model for dynamic analysis of structures with FPS isolators." *Earthquake Eng. Struct. Dyn.*, 32, 1157-1184.

Andrawes, B., and DesRoches, R. (2007). "Effect of ambient temperature on the hinge opening in bridges with shape memory alloy seismic restrainers." *Eng. Struct.*, 29, 2294-2301.

Arias, A. (1970). "A measure of earthquake intensity." *Seismic design for nuclear power plants*, R. J. Hansen, ed., The MIT Press, Cambridge, Mass., 438-483.

Astroza, M., Moroni, M. O., Muñoz, M., and Perez, F. (2005a). "Estudio de la vulnerabilidad sísmica de edificios de vivienda social." *Proc., IX Jornadas*, Concepción, Chile.

Astroza, M., Moroni, M. O., Norambuena, A., and Astroza, R. (2005b). "Intensities and damage distribution in the June 2005 Tarapacá, Chile, earthquake." *Earthquake Engineering Research Institute Special Earthquake Report*, EERI, Oakland, Calif., 1-8.

Besa, J., de la Llera, J. C., Jünemann, R., and Luders, C. (2008). "Experimental behavior and design of the PPP isolator." *Earthquake Eng. Struct. Dyn.*, In Review.

Boroschek, R. L., Moroni, M. O., and Sarrazin, M. (2003). "Dynamic characteristics of a long span seismic isolated bridge." *Eng. Struct.*, 25, 1479-1490.

Boroschek, R. L., and Yañez, F. V. (2000). "Experimental verification of basic analytical assumptions used in the analysis of structural wall buildings." *Eng. Struct.*, 22, 657-669.

Bruno, S., and Valente, C. (2002). "Comparative response analysis of conventional and innovative seismic protection strategies." *Earthquake Eng. Struct. Dyn.*, 31, 1067-1092.

Chapra, S., and Canale, R. (1998). *Numerical methods for engineers: With programming and software applications*, McGraw-Hill, Blacklick, Ohio.

Chopra, A. K. (2001). *Dynamics of structures: Theory and applications to earthquake engineering*, Prentice Hall, Upper Saddle River, N.J.

Chopra, A. K., and Chintanapakdee, C. (2001). "Comparing response of SDF systems to near-fault and far-fault earthquake motions in the context of spectral regions." *Earthquake Eng. Struct. Dyn.*, 30, 1769-1789.

CIA. (2008). "The world factbook: Chile." <https://www.cia.gov/library/publications/the-world-factbook/geos/ci.html#Econ> (Jan. 15, 2008).

De la Llera, J. C., Luders, C., Leigh, P., and Sady, H. (2004). "Analysis, testing, and implementation of seismic isolation of buildings in Chile." *Earthquake Eng. Struct. Dyn.*, 33, 543-574.

Deb, K. (2001). *Multiobjective optimization using evolutionary algorithms*, John Wiley and Sons, Ltd., West Sussex, England.

Deb, K., and Goel, T. (2001). "Controlled-elitist non-dominated sorting genetic algorithms for better convergence." *Proc., First Internat. Conf. on Evolutionary Multi-Criterion Optimization*, Zurich, Switzerland, 67-81.

Deb, K., Pratap, A., Agarwal, S., and Meyarivan, T. (2002). "A fast and elitist multiobjective genetic algorithm: NSGA-II." *IEEE Trans. on Evolutionary Computation*, 6(2), 182-197.

Dolce, M., Cardone, D., and Ponzo, F. (2007). "Shaking-table tests on reinforced concrete frames with different isolation systems." *Earthquake Eng. Struct. Dyn.*, 36, 573-596.

Hancock, J., Watson-Lamprey, J., Abrahamson, N. A., Bommer, J. J., Markatis, A., McCoy, E., and Mendis, R. (2006). "An improved method of matching response spectra of recorded earthquake ground motion using wavelets." *J. Earthquake Eng.*, 10(1), 67-89.

Hart, G. C., and Wong, K. (2000). *Structural dynamics for structural engineers*, John Wiley & Sons, Inc., New York.

Holland, J. (1975). *Adaptation in natural and artificial systems*, The University of Michigan Press, Ann Arbor, Mich.

Hwang, J. S., and Ku, S. W. (1997). "Analytical modeling of high damping rubber bearings." *J. of Struct. Eng.*, 123(8), 1029-1036.

Hwang, J. S., Wu, J. D., Pan, T.-C., and Yang, G. (2002). "A mathematical hysteretic model for elastomeric isolation bearings." *Earthquake Eng. Struct. Dyn.*, 31, 771-789.

Instituto Nacional de Normalización. (1996). “Earthquake resistant design of buildings.” *NCh433.Of96*, Santiago.

Instituto Nacional de Normalización. (2003a). “Earthquake-resistant design of industrial structures and facilities.” *NCh2369.Of2003*, Santiago.

Instituto Nacional de Normalización. (2003b). “Earthquake-resistant design of base-isolated buildings.” *NCh2745.Of2003*, Santiago.

Jangid, R. S. (2000). "Optimum frictional elements in sliding isolation systems." *Comput. Struct.*, 76, 651-661.

Jangid, R. S. (2005). "Optimum friction pendulum system for near-fault motions." *Eng. Struct.*, 27, 349-359.

Jangid, R. S., and Kelly, J. M. (2001). "Base isolation for near-fault motions." *Earthquake Eng. Struct. Dyn.*, 30, 691-707.

Jankowski, R. (2004). "Nonlinear rate dependent model of high damping rubber bearing." *Bulletin of Earthquake Eng.*, 1, 397-403.

Jankowski, R., Wilde, K., and Fujino, Y. (1998). "Pounding of superstructure segments in isolated elevated bridge during earthquakes." *Earthquake Eng. Struct. Dyn.*, 27, 487-502.

Jünemann, R., de la Llera, J. C., Besa, J., and Almazán, J. L. (2008). "Three-dimensional behavior of a self-centering, spherical precast prestressed pile isolator." *Earthquake Eng. Struct. Dyn.*, In Review.

Kelly, J. M. (2002). "EERI Distinguished Lecture 2001: Seismic isolation systems for developing countries." *Earthquake Spectra*, 18(3), 385-406.

Kikuchi, M., and Aiken, I. D. (1997). "An analytical hysteresis model for elastomeric seismic isolation bearings." *Earthquake Eng. Struct. Dyn.*, 26, 215-231.

Kim, H.-S., and Roschke, P. N. (2006). "Fuzzy control of base-isolation system using multiobjective genetic algorithm." *Comput.-Aided Civil Infrastruct. Eng.*, 21, 436-449.

Kim, H.-S., Roschke, P. N., Lin, P.-Y., and Loh, C.-H. (2006). "Neuro-fuzzy model of hybrid semi-active base isolation system with FPS bearings and an MR damper." *Eng. Struct.*, 28, 947-958.

Lilhanand, K., and Tseng, W. S. (1987). "Generation of synthetic time histories compatible with multiple design response spectra." *Proc., 9th Internat. Conf. on Struct. Mechanics in Reactor Tech.*, Lausanne, Switzerland, K2/10.

Lilhanand, K., and Tseng, W. S. (1988). "Development and application of realistic earthquake time histories compatible with multiple-damping design spectra." *Proc., 9th World Conf. on Earthquake Eng.*, Vol. II, Tokyo, Japan, 819-824.

Lin, P.-Y., Roschke, P. N., and Loh, C.-H. (2007). "Hybrid base-isolation with magnetorheological damper and fuzzy control." *Struct. Control and Health Monitoring*, 14, 384-405.

MATLAB/Simulink, The MathWorks, Inc., Natick, Mass., 2007.

McCormick, J., DesRoches, R., Fugazza, D., Auricchio, F. (2007). "Seismic assessment of concentrically braced steel frames with shape memory alloy braces." *J. Struct. Eng.*, 133(6), 862-870.

Mikhail, P. (2000). "World earthquake timeline." *CNT Group*, <http://www.mapreport.com/subtopics/d/e.html> (Dec. 18, 2007).

Moroni, M. O., Astroza, M., and Acevedo, C. (2004). "Performance and seismic vulnerability of masonry housing types used in Chile." *J. Perform. Constructed Facilities*, 18(3), 173-179.

Moroni, M. O., Astroza, M., Gomez, J., and Guzman, R. (1996). "Establishing R_w and C_d factors for confined masonry buildings." *J. Struct. Eng.*, 122(10), 1208-1215.

Moroni, M. O., Sarrazin, M., and Boroschek, R. (1998). "Experiments on a base-isolated building in Santiago, Chile." *Eng. Struct.*, 20(8), 720-725.

Mosqueda, G., Whittaker, A. S., and Fenves, G. L. (2004). "Characterization and modeling of friction pendulum bearings subjected to multiple components of excitation." *J. Struct. Eng.*, 130(3), 433-442.

Mullins, L. (1987). "Engineering with rubber." *CHEMTECH*, 17(12), 720-727.

Murty, C. V. R., Brzev, S., Faidon, H., Comartin, C. D., and Irfanoglu, A. (2006). "At risk: The seismic performance of reinforced concrete frame buildings with masonry infill walls." *Pub. No. WHE-2006-03*, EERI, Oakland.

Naeim, F., and Kelly, J. M. (1999). *Design of seismic isolated structures: From theory to practice*, John Wiley & Sons, Inc., New York.

Narasimhan. S., Nagarajaiah, S., Johnson, E. A., and Gavin, H. P. (2006). "Smart base-isolated benchmark building. Part I: problem definition." *Struct. Cont. and Health Mon.*, 13, 573-588.

Narayanan, S., and Azarm, S. (1999). "On improving multiobjective genetic algorithms for design optimization." *Struct. Opt.*, 18, 146-155.

Ozbulut, O. E., Moroni, M. O., Sarrazin, M., and Roschke, P. N. (2006). "Fuzzy model of pseudoelastic CuAlBe behavior for seismic loads." *Proc., 4th World Conf. Struct. Cont. and Mon.*, San Diego, 176-183.

Pan, T.-C., and Yang, G. (1996). "Nonlinear analysis of base-isolated MDOF structures." *Proc., 11th World Conf. Earthquake Eng.*, Mexico, Paper No. 1534.

Pinochet, J., de la Llera, J. C., and Luders, C. (2006). "Analysis of a kinematic self-centering seismic isolator." *Earthquake Eng. Struct. Dyn.*, 35, 1533-1561.

Roussis, P., and Constantinou, M. C. (2006). "Uplift-restraining friction pendulum seismic isolation system." *Earthquake Eng. Struct. Dyn.*, 35, 577-593.

Saez, P. (2007). "Thousands of Chileans homeless after quake, mayor says." *CNN*, < http://www.cnn.com/2007/WORLD/americas/11/14/earthquake.chile> (Dec. 20, 2007).

SeismoSoft. (2006). "SeismoSignal v.3.2.0." <http://www.seismosoft.com/> (June 10, 2007).

Servicio Sismológico (2007). "Terremotos en Chile.", <http://ssn.dgf.uchile.cl/home/terrem.html> (Dec. 20, 2007).

Shook, D. (2006). "Control of a benchmark structure using GA-optimized fuzzy logic control." MS Thesis, Texas A&M University, College Station, Tex.

Shook, D., Roschke, P., Lin, P.-Y., and Loh, C.-H. (2008). "Experimental investigation of super-elastic semi-active damping for seismically excited structures." *Smart Structures and Systems*, In-Press.

Song, G., Ma, N., Li, H.-N. (2006). "Applications of shape memory alloys in civil structures." *Eng. Struct.*, 28, 1266-1274.

Stroker, K. (2008). "Great Chile earthquake of May 22, 1960 – Anniversary edition." *National Geophysical Data Center*, <http://www.ngdc.noaa.gov/> (Jan. 2, 2008).

Symans, M. D., Chamey, F. A., Whittaker, A. S., Constantinou, M. C., Kircher, C. A., Johnson, M. W., and McNamara, R. J. (2008). "Energy dissipation systems for seismic applications: Current practice and recent developments." *J. Struct. Eng.*, 134(1), 3-21.

Torra, V., Isalgue, A., Martorell, F., Terriault, P., and Lovey, F. C. (2007). "Built in dampers for family homes via SMA: An ANSYS computation scheme based on mesoscopic and microscopic experimental analyses." *Eng. Struct.*, 29, 1889-1902.

Tsopelas, P., Constantinou, M. C., Kim, Y. S., and Okamoto, S. (1996). "Experimental study of FPS system in bridge seismic isolation." *Earthquake Eng. Struct. Dyn.*, 25, 65-78.

Watson-Lamprey, J. A., and Abrahamson, N. A. (2006). "Bias caused by use of spectrum compatible motions." *100th Ann. Earthquake Conf. Commemorating the 1906 San Francisco Earthquake*, San Francisco, Paper No. 0909.

Wenzel, H., and Pichler, D. (2005). *Ambient vibration monitoring*, John Wiley & Sons, Inc., Hoboken, N.J.

Wilde, K., Gardoni, P., Fujino, Y. (2000). "Base isolation system with shape memory alloy device for elevated highway bridges." *Eng. Struct.*, 22, 222-229.

Yen, J., and Langari, R. (1999). *Fuzzy logic: Intelligence, control, and information*, Prentice-Hall, New York.

Zayas, V., and Low, S. (2000). "Seismic isolation for strong, near-field earthquake motions." *Proc., 12th World Conf. Earthquake Eng.*, Auckland, New Zealand.

APPENDIX A

STRUCTURAL PLANS AND SPECIFICATIONS

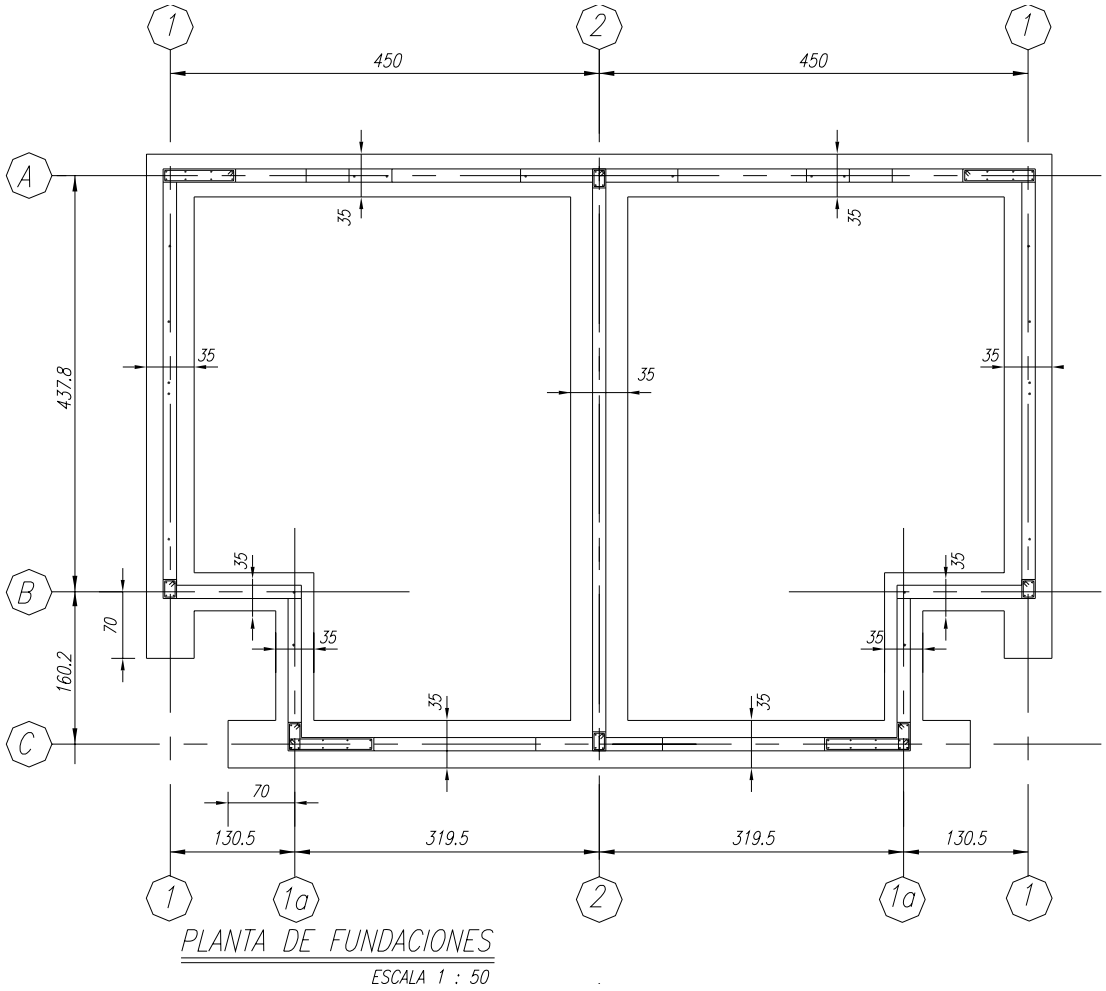

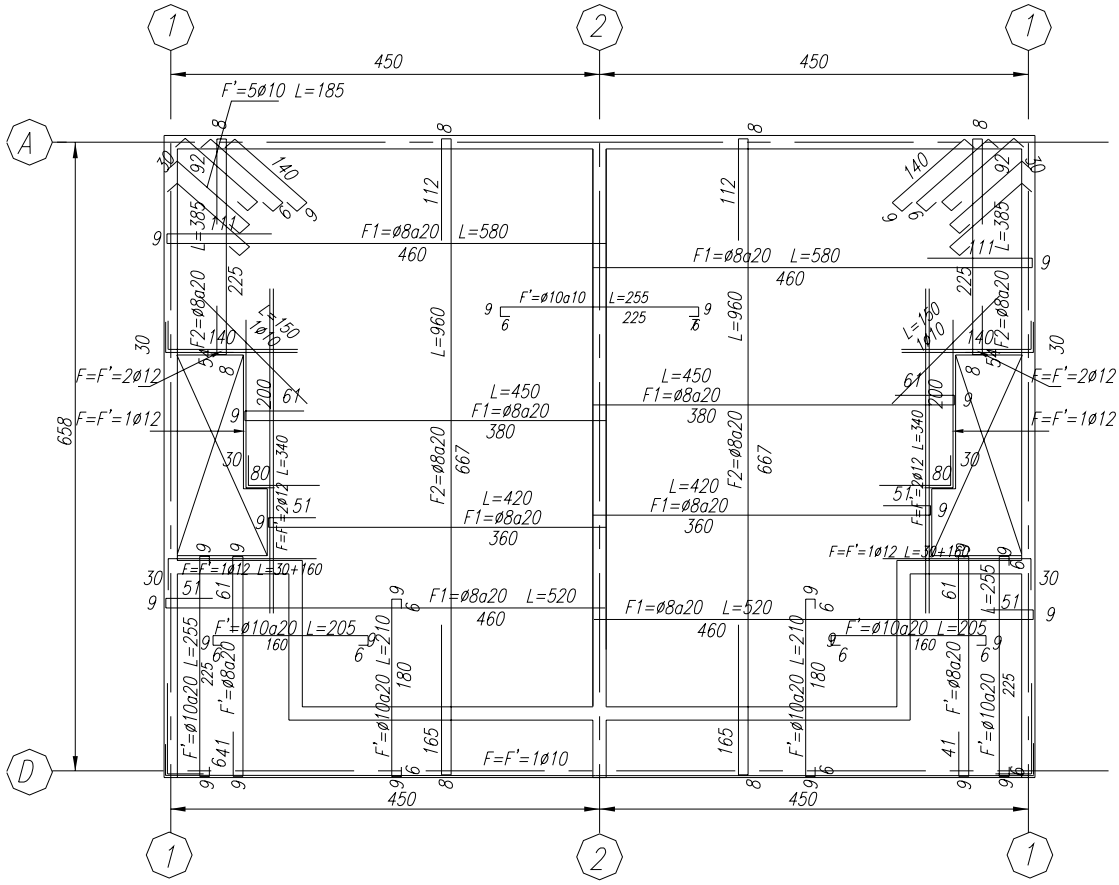

PLANTA DE LOSAS

ESCALA 1 : 50

NOTA: FE REPARTICION ARMADURA SUPERIOR EN LOSAS ø8A25

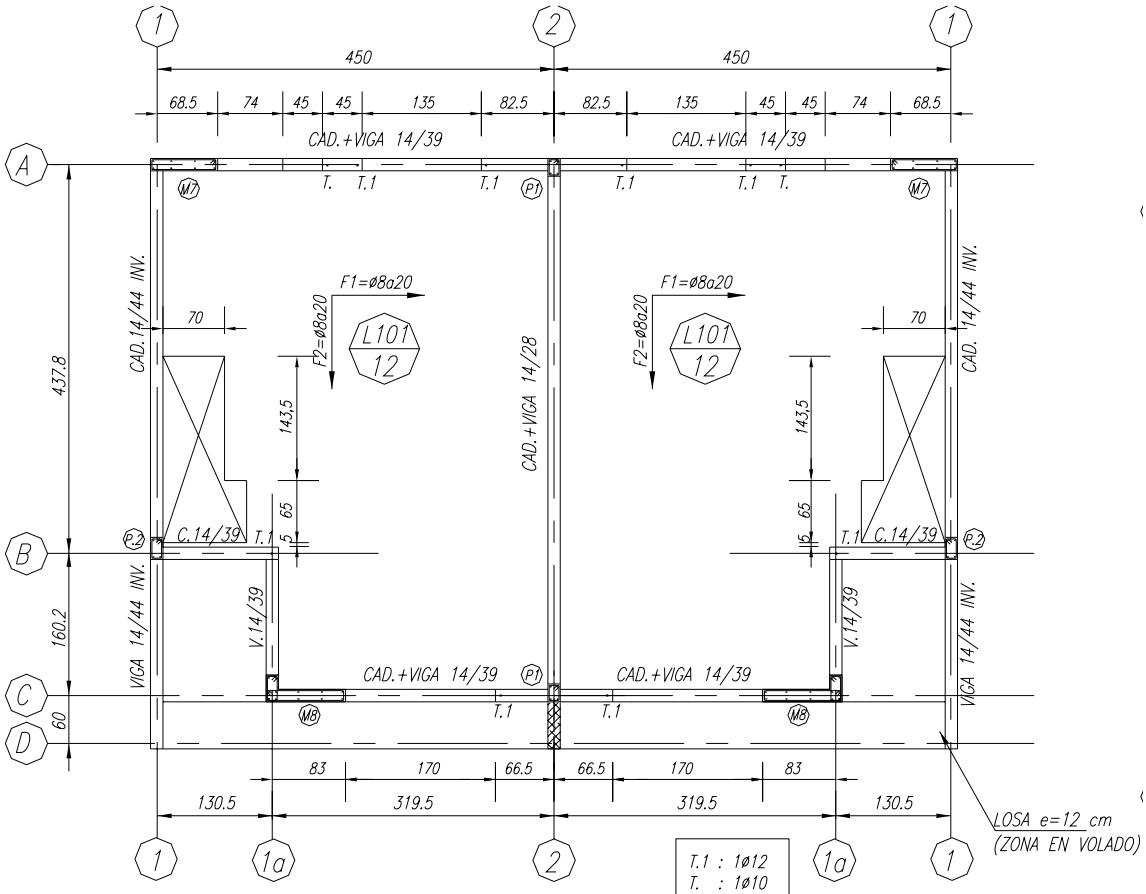

PLANTA DE ESTRUCTURA CIELO 1° PISO

ESCALA 1 : 50

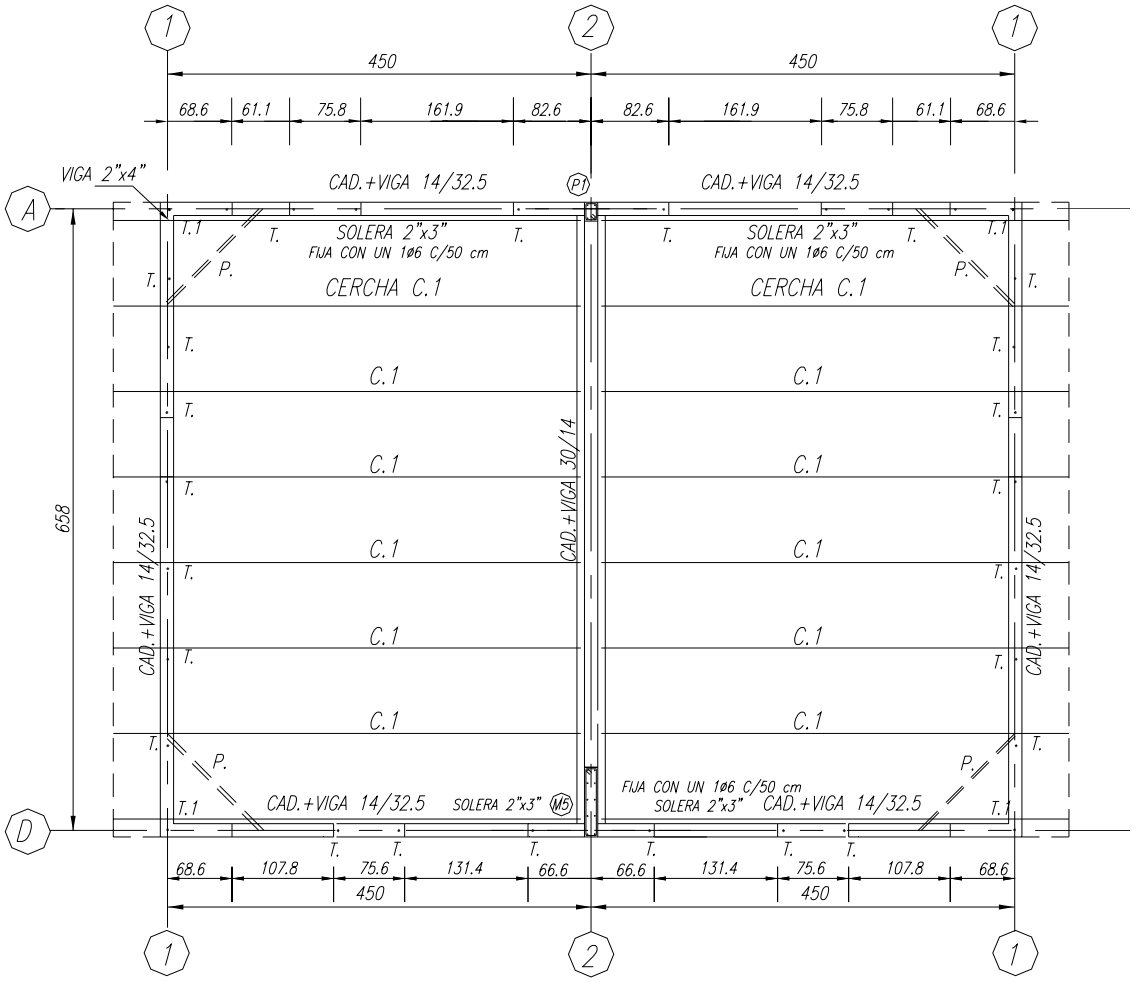

PLANTA DE ESTRUCTURA CIELO 2° PISO Y TECHUMBRE

ESCALA 1 : 50

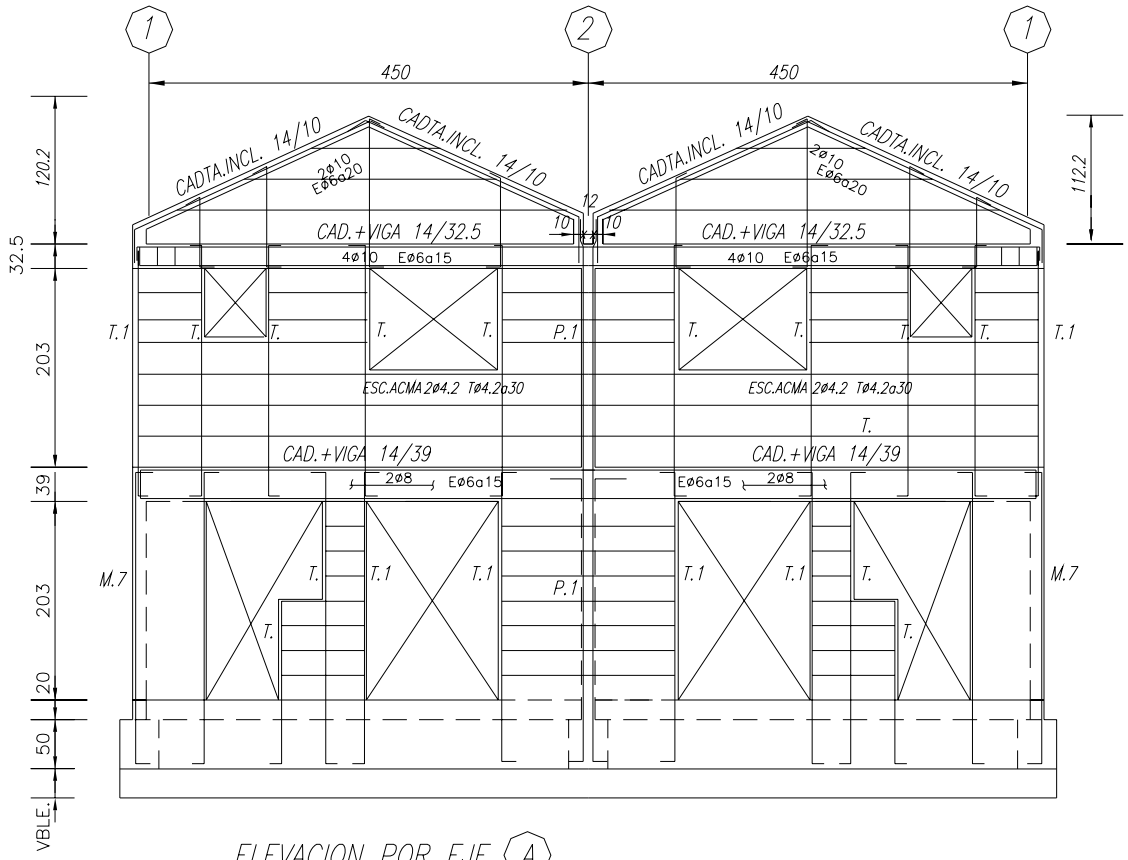

ELEVACION POR EJE (A)

ESCALA 1 : 50

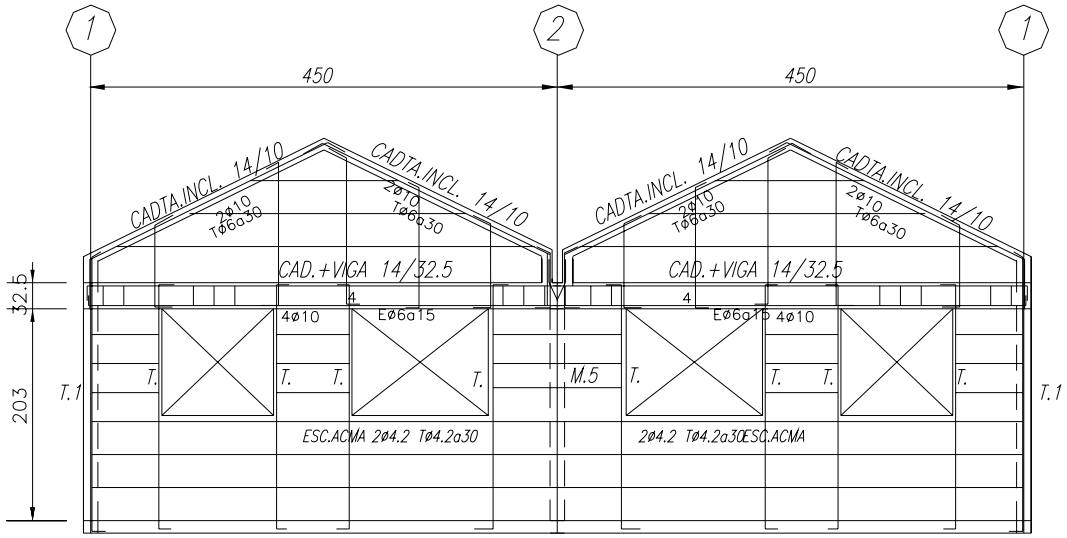

ELEVACION POR EJE (D)

ESCALA 1 : 50

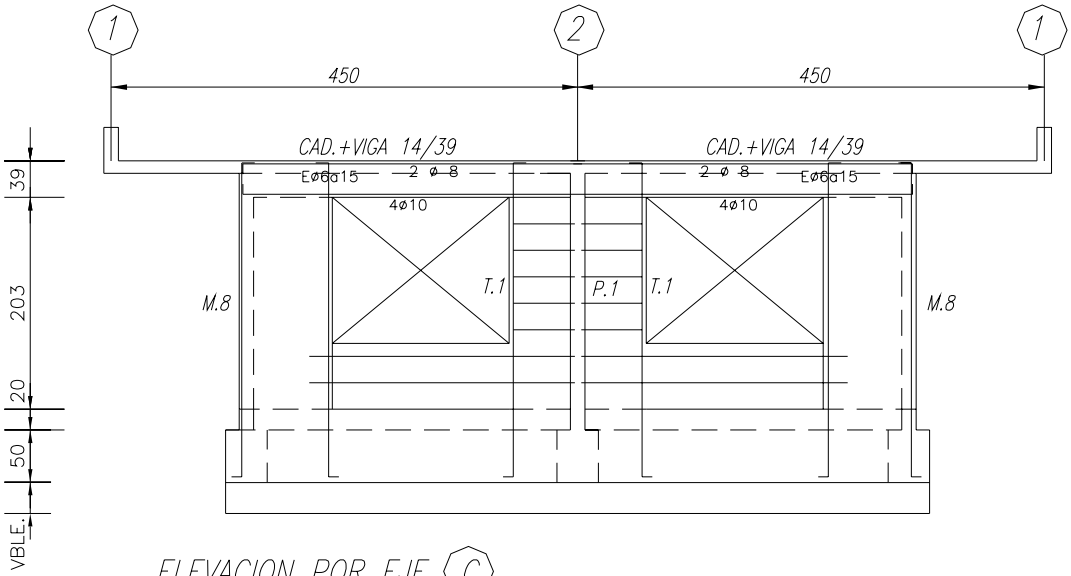

ELEVACION POR EJE (C)

ESCALA 1 : 50

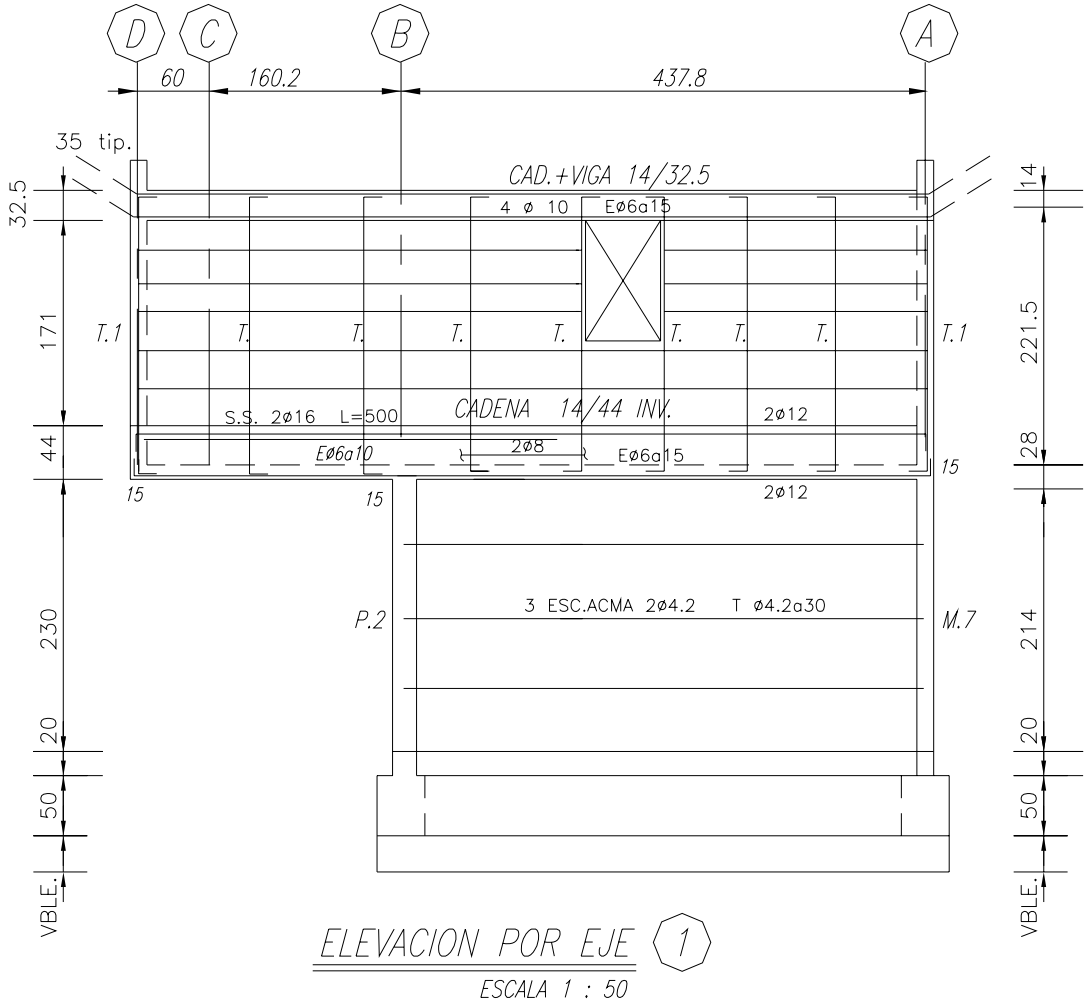

ELEVACION POR EJE (1)

ESCALA 1 : 50

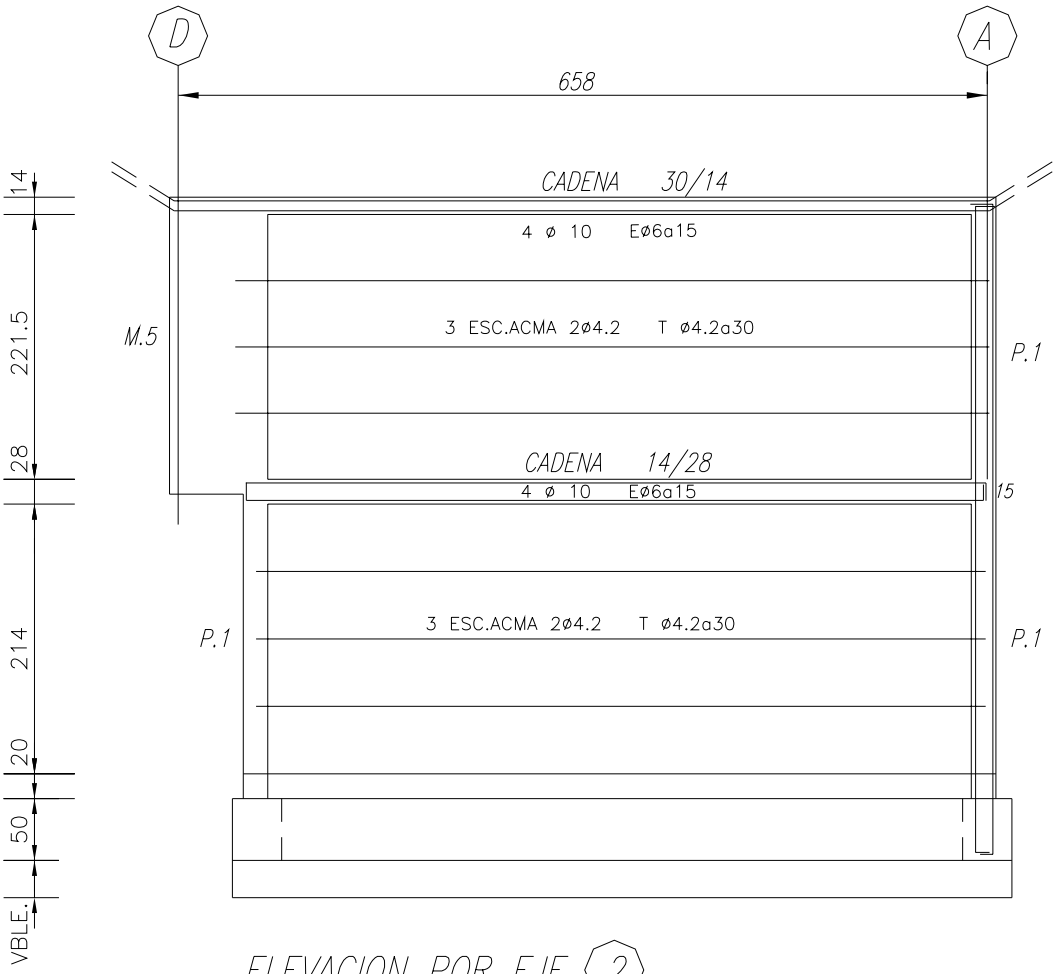

ELEVACION POR EJE (2)

ESCALA 1 : 50

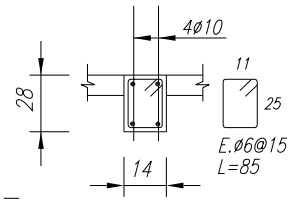

CADENA 14/28

ESC. 1 : 20

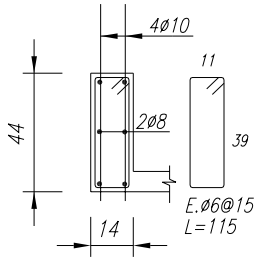

CADENA 14/44 INV.

ESC. 1 : 20

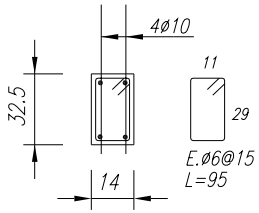

CADENA 14/32.5

ESC. 1 : 20

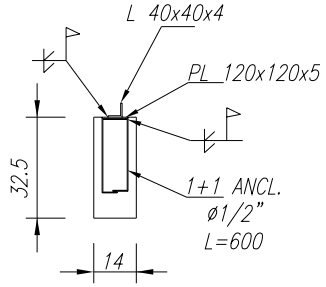

DETALLE PUNTAL – P

ESC. 1 : 20

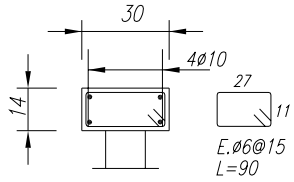

CADENA 30/14

ESC. 1 : 20

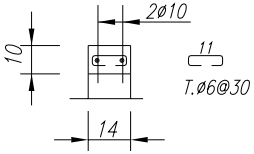

CADENETA 14/10

ESC. 1 : 20

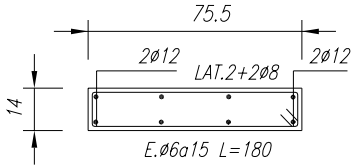

MACHON M7 14/75.5

ESC. 1 : 20

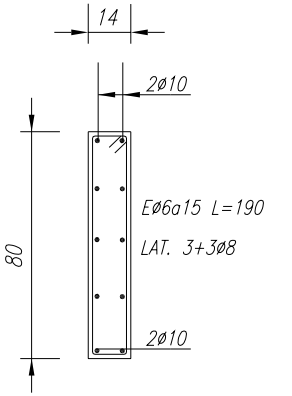

MACHON M5 14/80

ESC. 1 : 20

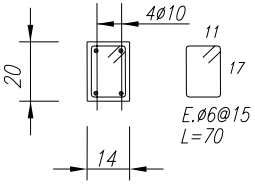

PILAR P.1 14/20

ESC. 1 : 20

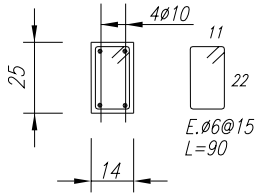

PILAR P.2 14/25

ESC. 1 : 20

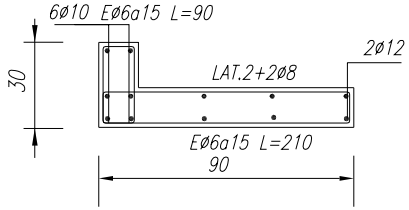

MACHON M8

ESC. 1 : 20

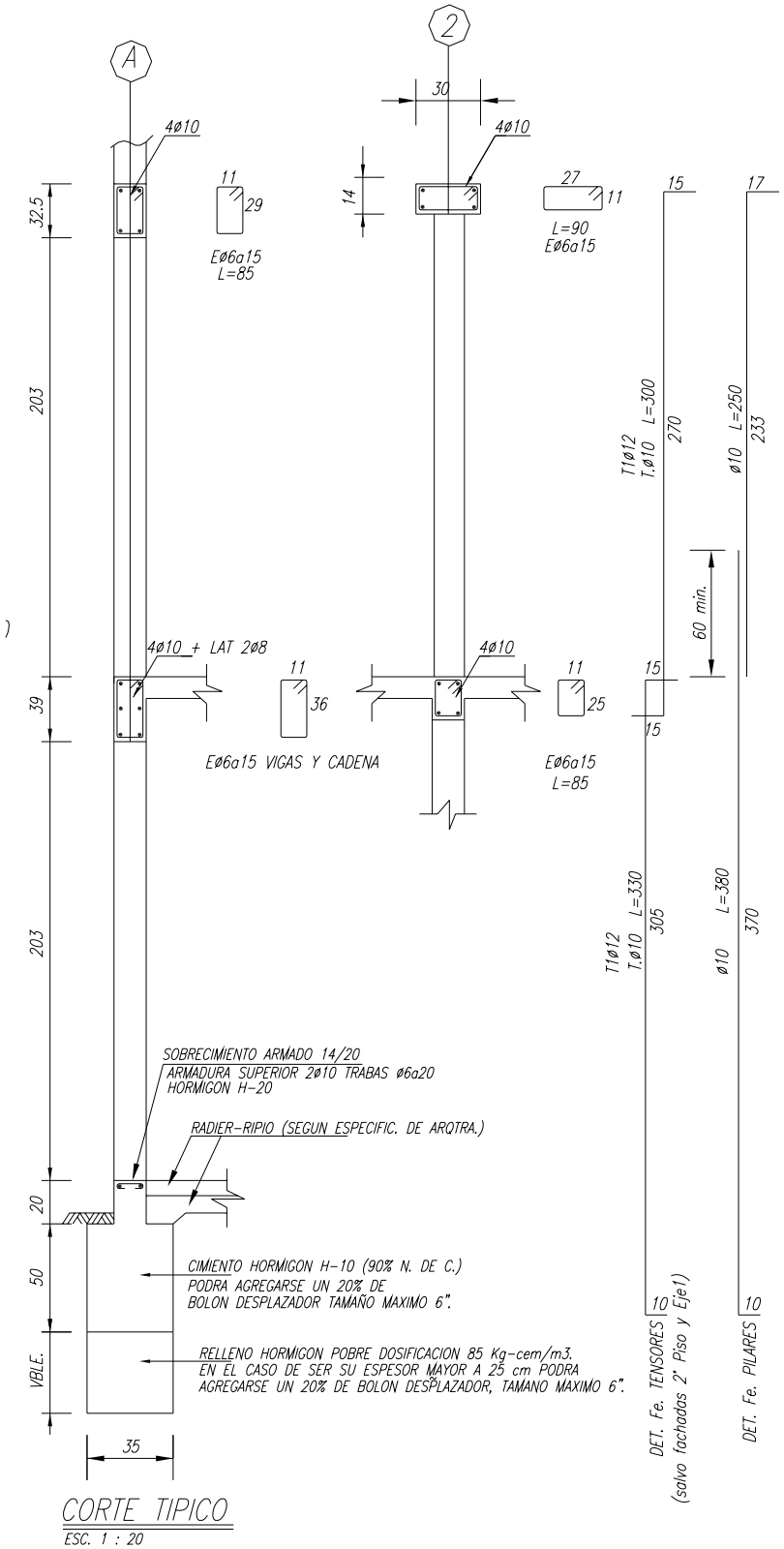

CORTE TIPICO

ESC. 1 : 20

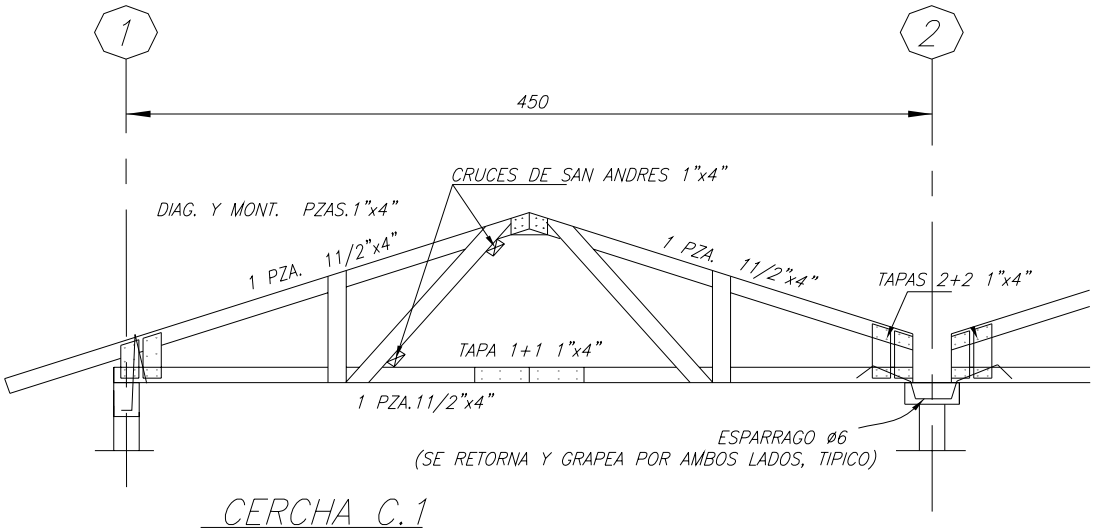

CERCHA C.1

ESCALA 1 : 33

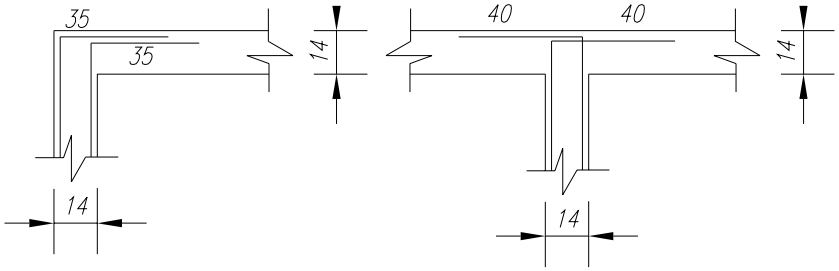

CRUCE EN L CRUCE EN T

DETALLE CRUCE Fe. CAD.VIGA CIELO 2°PISO

ESC. 1 : 20

ESPECIFICACIONES TECNICAS

1.- HORMIGON ARMADO CALIDAD H-20 CON UN NIVEL DE CONFIANZA DE 90%.

2.- ACERO HORMIGON A63-42H CON RESALTES EXCEPTO ø6.
TRASLAPOS ANCLAJES Y EMPALMES NO INDICADOS 50ø+10cm.
SE PODRA USAR ALTERNATIVAMENTE ACERO CALIDAD AT 56-50H
ACERO TENSORES A44 - 28H (NO SE PERMITE TRASLAPOS)

"x4"

3.- ALBAÑILERIA LADRILLO HECHO A MAQUINA DE 14x29x9.4cm MqP Grado 2
MORTERO RELACION CEMENTO ARENA 1:4 REVUELTO MECANICAMENTE
R_{28} ⩾100 Kg/cm2 ALBAÑILERIA f'm ⩾ 60 Kg/cm2.

4.- ENMADERACION PINO DE OPTIMA CALIDAD, GRADO G1
HUMEDAD MAXIMA 18%

NOTAS:
-DIMENSIONES EN CEMTIMETROS.
-LAS COTAS PREVALECEN SOBRE EL TRAZADO

C O N A V I C O O P		
UBICACION PROGRAMA HERNAN DIAZ ARRIETA COMUNA DE MAIPU	MATERIA VIVIENDA C50-2VTF	PLANO N° 7 DE 9
CONTENIDO PLANTA FUNDACIONES, ESTRUCTURA CIELO 1° PISO Y DETALLES VARIOS	INGENIERO ERNESTO HERBACH ALVAREZ INGENIERO CIVIL UNIVERSIDAD DE CHILE	ESCALA INDICADAS FECHA JULIO 2006 DIBUJO M.G.L

MEMORIA DE CALCULO

VIVIENDA TIPO C50

CONAVICOOP

1.- *DESCRIPCION DE LA ESTRUCTURA*

La construcción comprende dos viviendas pareadas, de dos pisos. La vivienda tiene una superficie en planta de 4,50 m de frente por 5,98 m de fondo en el primer piso y 4,50 m de frente por 6,58 m de fondo en segundo piso.

La estructura en el primer piso está conformada por muros de albañilería armada con refuerzos de machones de hormigón armado en el sentido de las fachadas principales, y por muros de albañilería confinada en el muro medianero y en los laterales. En el segundo piso está conformada por muros de albañilería armada y por un muro de albañilería confinada en el muro medianero. Los muros señalados son los elementos resistentes frente a las solicitaciones horizontales de sismo y verticales de carga estática. La estructura de cielo del primer piso de la vivienda está conformada por una losa de hormigón armado, hecha in situ, de 12 cm de espesor.

Los muros de fachada del segundo piso se prolongan a nivel de techumbre conformando tímpanos frontales.

La techumbre está conformada por un sistema de cerchas de pino, sobre las que se apoyan costaneras de 2" por 2".

Las fundaciones son del tipo continuas bajo los muros de albañilería y descargan directamente en el terreno de fundación.

La disposición de los elementos descritos se indican en los planos de cálculo respectivos.

2.- *BASES DE CALCULO Y MATERIALES*

2.1 Solicitaciones

2.1.1 Cargas de peso propio

Pesos específicos considerados

Hormigón armado	2.500 kg/m^3	NCH 1537

Hormigón simple		2.400 kg/m^3	NCH 1537
	Albañilería	1.600 kg/m^3	NCH 1537
2.1.2	Sobrecarga de losa	200 kg/m^2	NCH 1537
2.1.3	Sobrecarga útil de techumbre	30 kg/m^2	NCH 1537

2.1.4 Viento

Presión básica considerada 65 kg/m^2 NCH 432

Factor de forma s/tablas.

2.1.5 Sismo

Coeficiente sísmico considerado según NCH 433of96 "Cálculo Antisísmico de Edificios".

2.2 Materiales

2.2.1 Hormigón Armado H 20, con un nivel de confianza de 90%.

2.2.2 Acero A63-42H con resaltes para ϕ <= 8 mm

2.2.3 Albañilería de ladrillo hecho a maquina de 14*29*9,4 cm MqP Grado 2.

2.2.4 Enmaderación: Pino Grado G1, humedad máxima 18%.

2.3 Tensiones admisibles

2.3.1 Hormigón H 20, f'_c=160 kg/cm^2

2.3.2 Acero A63-42H, f_y=4.200 kg/cm^2

2.3.3 Albañilería, f'_m >= 60 kg/cm^2

Mortero revuelto mecánicamente, R_{28} >= 100 kg/cm^2

Deformación máxima de cadenas del segundo piso: 1/500 altura del piso.

2.3.4 Enmaderación de Pino

Flexión	65 kg/cm^2
Cizalle	8 kg/cm^2
Compresión Paralela	60 kg/cm^2
Tracción	70 kg/cm^2
Módulo de Elasticidad	80.000 kg/cm^2

3.- ***FUNDACIONES***

Las condiciones del terreno de apoyo se verificarán por un ingeniero mecánico de suelos durante la ejecución de las excavaciones para las fundaciones.

Ernesto Herbach Alvarez
Ingeniero Civil

APPENDIX B

STRUCTURAL MASS AND STIFFNESS CALCULATIONS

Mass of Structure

Reinforced Concrete:

Unit weight 2500 kg/m^3

	Area (m^3)	Weight (kg)
Slab-on-grade	6.60	16,508
1st floor slab	6.76	16,888
1st floor concrete columns		
M7	0.47	1,179
P1	0.12	312
P2	0.16	390
M8	0.66	1,655
2nd floor concrete columns		
P1	0.06	156
M5	0.25	624
Roof concrete beams		
Inclined beams	0.29	714
1st floor concrete beams		
14/39	1.16	2,894
14/44	0.81	2,027
14/28	0.23	586
2nd floor concrete beams		
14/32.5	1.42	3,544
Total	18.99	47,477

Masonry:

Unit weight 1600 kg/m^3

	Area (m^3)	Weight (kg)
1st floor walls	7.49	11,982
2nd floor walls		
Main	9.19	14,705
Roof peaks	1.81	2,894
Total	18.49	29,582

Roof:

Pine trusses	383	kg
Tin (estimate)	385	kg
Total	768	kg

Total Mass of Structure (not including LL):

77,827 kg

Mass of Structure with Live Load Included (Per NCh433 5.5.1)

Live Load:

Slab	200	kg/m^2
Roof	30	kg/m^2

Area by floor:

	Area (m^2)
Ground slab	55
1st floor slab	56
Entire roof	65

Mass by floor:

	Mass (kg)
Base	
Slab-on-grade	16,508
Columns	1,768
Walls	5,991
25% live load	2,752
Total	**27,018**
1st floor	
1st floor slab	16,888
Columns	2,158
Beams	5,506
Walls	13,344
25% live load	2,815
Total	**40,711**
2nd floor	
Columns	390
Beams	4,258
Walls	10,247
Roof	768
25% live load	485
Total	**16,148**

Stiffness Calculations

G_m = 0.3E	1,260	MPa
G_c = 0.3E	6,000	MPa
G_c/G_m	4.762	

		Normalize masonry WRT G_c (Multiply mass of masonry by G_c/G_m)
	Mass (kg)	**Mass WRT concrete (kg)**
1st floor		
Masonry walls	13,344	63,542
Concrete columns	2,158	2,158
Total		65,700
2nd floor		
Masonry walls	10,247	48,794
Concrete columns	390	390
Total		49,184
Total mass		114,885

	Proportion
1st floor contribution to stiffness	0.572
2nd floor contribution to stiffness	0.428
Total	1.000

from solve_stiffnesses_new_damping.m

k1 =	**4.33E+08**	**N/m**
k2 =	**3.24E+08**	**N/m**

solve_stiffnesses_new_damping.m

```
%Created by Rachel Husfeld on 9/26/2007
%Revised on 11/7/07

%This program solves for the stiffness values of the case study %structure using two methods: one neglects damping of the structure and %the other does not, both solutions yield the same result

%References are made to Hart, G. C., and Wong, K. (2000). Structural
%dynamics for structural engineers, John Wiley & Sons, Inc., New York.

clear all
```

```
syms k2

%USING HART AND WONG FORMULATION PG 103-104
%Calculated mass values
m1 = 40711; %kg, including 25% LL
m2 = 16148; %kg, including 25% LL

%Assumed ratio between stiffness values
k1 = (0.572/0.428)*k2;

%Measured natural frequency
w1 = 81.68; %rad/sec

%Mass and stiffness matrices
m = [m1 0; 0 m2];
k = [k1+k2 -k2; -k2 k2];

%See pg 89 Hart and Wong
r1 = k2/(-m2*w1^2 + k2);

%See pg 90 Hart and Wong
phi1 = [1; r1];

%See pg 97 Hart and Wong
m1star = phi1'*m*phi1;
k1star = phi1'*k*phi1;
w1eq = sqrt(k1star/m1star)

%Pause program here

%To solve w1eq = 81.68 for k2,
%Paste below the resulting equation from above

k2sol = solve('((250/107*k2-conj(k2/(-903732913107475/8388608+k2))…
*k2+(-k2+conj(k2/(-903732913107475/8388608+k2))*k2)*k2/…
(-903732913107475/8388608+k2))/(40711+16148*conj(k2/…
(-903732913107475/8388608+k2))*k2/(-903732913107475/8388608+k2)))…
^(1/2)=81.68',k2);

%Solve for k1
k1 = (0.572/0.428)*k2sol

k2 = k2sol %N/m

%Plug in k1 and k2
r1 = k2/(-m2*w1^2 + k2);

phi1 = [1; r1];

m1star = phi1'*m*phi1;

k = [k1+k2 -k2; -k2 k2];

k1star = phi1'*k*phi1;

w2 = 150.8; %rad/sec

zeta1 = 0.0382; %percent damping from structure for mode 1 - calc using %bandwidth method - using microvibration data
zeta2 = 0.0382; %percent damping from structure for mode 2 - assume %same as mode 1

k = [k1+k2 -k2; -k2 k2];

%Compare to a0 for Rayleigh damping
alpha = (2*w1*w2*(zeta1*w2 - zeta2*w1))/(w2^2 - w1^2);
```

```
%Compare to a1 for Rayleigh damping
beta = (2*(zeta2*w2 - zeta1*w1))/(w2^2 - w1^2);

r2 = k2/(-m2*w2^2 + k2);

phi2 = [1; r2];

m2star = phi2'*m*phi2;

k2star = phi2'*k*phi2;

c1star = alpha*m1star + beta*k1star;

c2star = alpha*m2star + beta*k2star;

%Formulation 2 - Hart and Wong pg 88
syms k2a

%Assumed ratio between stiffness values
k1a = (0.572/0.428)*k2a;

%Measured natural frequency
w1a = 81.68; %rad/sec

w1eq2 = sqrt((((k1a+k2a)*m2+k2a*m1)-sqrt(((k1a+k2a)*m2+k2a*m1)^2…
-4*m1*m2*k1a*k2a))/(2*m1*m2))

k2sola = simplify(solve('1/1957920148228*(24875616405310979455 4*k2a…
-978960074114*23459569254061433^(1/2)*(k2a^2)^(1/2))^(1/2)=81.68',k2a))

k2a = k2sola

k1a = (0.638/0.362)*k2a
```

APPENDIX C

RSPMATCH SAMPLE FILES

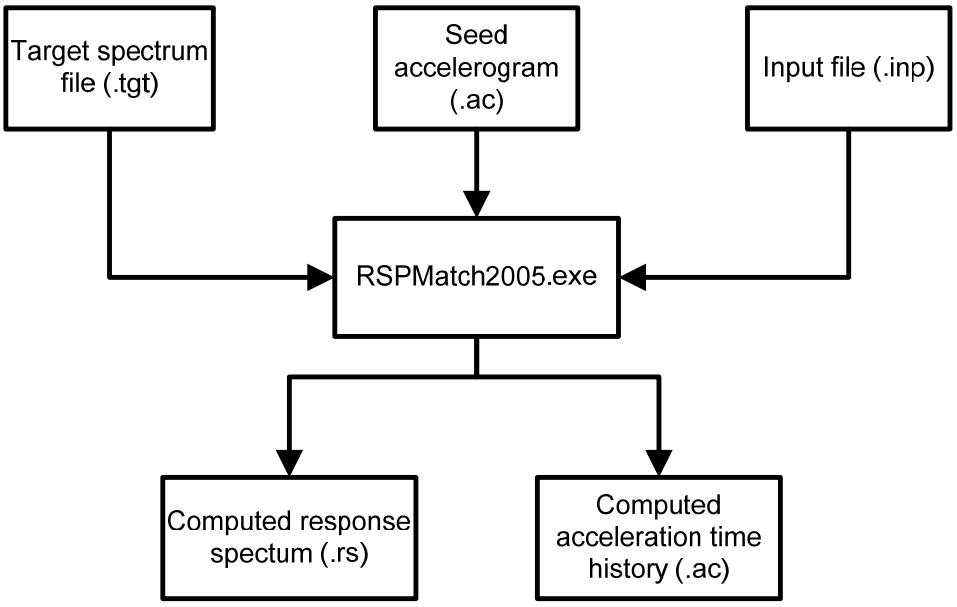

Example .tgt file:
Maipu_NCh2745_10percent_Tiso_2sec.tgt

Maipu Design Response Spectrum - 10% damping, Tiso = 2 sec
84 1
0.1
33.333333 0 1000.000000 0.407872
31.108477 0 1000.000000 0.416881
29.032120 0 1000.000000 0.426533
27.094351 0 1000.000000 0.436877
25.285919 0 1000.000000 0.447960
23.598193 0 1000.000000 0.459835
22.023115 0 1000.000000 0.472560
20.553167 0 1000.000000 0.486195
19.181331 0 1000.000000 0.500806
17.901060 0 1000.000000 0.516461
16.706241 0 1000.000000 0.533236
15.591171 0 1000.000000 0.551210
14.550528 0 1000.000000 0.570470
13.579343 0 1000.000000 0.591108
12.672980 0 1000.000000 0.613221
11.827113 0 1000.000000 0.636916
11.037704 0 1000.000000 0.662306
10.300985 0 1000.000000 0.689512
9.613438 0 1000.000000 0.718663
8.971783 0 1000.000000 0.749899

8.372955	0	1000.000000	0.783369
7.814096	0	1000.000000	0.819233
7.292539	0	1000.000000	0.857662
6.805793	0	1000.000000	0.898839
6.351536	0	1000.000000	0.942961
5.927598	0	1000.000000	0.990239
5.531956	0	1000.000000	1.040898
5.162722	0	1000.000000	1.095180
4.818133	0	1000.000000	1.121648
4.496543	0	1000.000000	1.121648
4.196418	0	1000.000000	1.121648
3.916325	0	1000.000000	1.121648
3.654927	0	1000.000000	1.121648
3.410977	0	1000.000000	1.121648
3.183309	0	1000.000000	1.121648
2.970836	0	1000.000000	1.121648
2.772546	0	1000.000000	1.121648
2.587490	0	1000.000000	1.121648
2.414787	0	1000.000000	1.121648
2.253610	0	1000.000000	1.121648
2.103191	0	1000.000000	1.121648
1.962812	0	1000.000000	1.121648
1.831803	0	1000.000000	1.103190
1.709538	0	1000.000000	1.029557
1.595434	0	1000.000000	0.960838
1.488945	0	1000.000000	0.896706
1.389565	0	1000.000000	0.836855
1.296817	0	1000.000000	0.780999
1.210260	0	1000.000000	0.728870
1.129481	0	1000.000000	0.680221
1.054093	0	1000.000000	0.634820
0.983736	0	1000.000000	0.592448
0.918076	0	1000.000000	0.552905
0.856799	0	1000.000000	0.516001
0.799611	0	1000.000000	0.481560
0.746240	0	1000.000000	0.449418
0.696432	0	1000.000000	0.419421
0.649948	0	1000.000000	0.391427
0.606567	0	1000.000000	0.365301
0.566081	0	1000.000000	0.340918
0.528298	0	1000.000000	0.318163
0.493036	0	1000.000000	0.214280
0.460128	0	1000.000000	0.186630
0.429417	0	1000.000000	0.162548
0.400755	0	1000.000000	0.141573
0.374006	0	1000.000000	0.123305
0.349043	0	1000.000000	0.107394
0.325746	0	1000.000000	0.093537
0.304004	0	1000.000000	0.081467
0.283713	0	1000.000000	0.070955
0.264776	0	1000.000000	0.061799
0.247103	0	1000.000000	0.053825
0.230610	0	1000.000000	0.046879
0.215218	0	1000.000000	0.040830
0.200853	0	1000.000000	0.035562
0.187447	0	1000.000000	0.030973
0.174936	0	1000.000000	0.026976
0.163260	0	1000.000000	0.023495
0.152363	0	1000.000000	0.020464
0.142193	0	1000.000000	0.017823
0.132702	0	1000.000000	0.015523
0.123845	0	1000.000000	0.013520
0.115579	0	1000.000000	0.011776
0.107865	0	1000.000000	0.010256

Example .acc file:
Maipu_design_eq_llolleo_S80E_1p5.acc
(Only part of this file is shown due to the long earthquake record)

```
Llolleo 1985 equake x1p5
23286        5.000000e-003
0.001305
-0.015225
-0.013290
-0.011355
-0.009420
-0.007470
-0.005550
-0.003600
-0.000120
0.004440
0.008985
0.013545
0.018090
0.022635
0.027180
0.028425
0.028830
0.029250
0.029640
0.030075
0.030465
0.030870
0.027645
0.021930
0.016230
0.010515
0.004035
-0.002445
-0.008955
-0.013425
-0.014850
-0.016320
-0.017760
-0.019215
-0.020655
-0.022095
-0.023835
-0.026685
-0.029535
-0.032385
-0.035235
-0.038085
```

Example .inp file:
Design_Maipu_llolleo_S80E.inp

```
Maipu_design_eq_llolleo_S80E_1p5.acc
3            0                          \ Number of Passes and pass to re-start from

Maipu_NCh2745_10percent_Tiso_2sec.tgt
20                  \maximum no. of iterations
0.05                \tolerance for maximum mismatch (in fraction of target)
1.0                 \convergence damping (recommended default value of 1.0)
14                  \model (1 or 6. 6=tapered cosine wave, 10=numerical evaluation of model1, 11= new
                    \displacement compatible wavelet, 12=as 11 but will automatically reduce wavelet to
                    \ensure displacement compatible, 13=same as 12 but using sinusoidal correction, 14=as 13
```

```
                \but implicit integration)
1.25 0.25 1.0 4.0       \alpha model, a1, a2, f1, f2 (recommended values)
10              \Max number of waves for model 11,12 or 13 (Must be integer. Higher numbers more
                \stable in frequency domain, lower numbers more stable in time domain, recommended
                \value 10)
25              \Max number of "additional wavelet" iterations - sub iterations used to prevent
                \divergence by adding wavelets or reducing correction amplitude (suggest 20)
0.7             \Off diagonal reduction, should be between 0.0 and 1.0, value of 1.0 recommended for
                  \wavelet model 1, 0.7 recommended for wavelet model 11, as improves stability.
2               \Spectral acceleration switch (1=absolute, 2=pseudo) use 1 for spectral acceleration
                  \matching, 2 for matching spectral displacement.
0  0.           \scale flag(=0 no, =1 yes, =2 yes but once before adjustment) scale period, note that
                \scaling for nearest target period with lowest damping level
1               \interpolate to 1/dtFlag of the input time step
1.0e-04         \minimum eigenvalue (control on convergence, recommended 1.0e-04)
350             \group size (control on convergence, recommended 25 if subgroups used else make larger
                  \than number of points to match if using full C matrix and off-diagonal reduction)
0               \PGA correction 0=none, 1= harmonic three cycle displacement compatible PGA
                  \adjustment (just enter amplitude and frequency on next line, 2= model 13 wavelet enter all
                  \parameters on next line
0.133   25.0  0.1  6    \PGA wavelet options: Target PGA, Frequency of adjustment (in Hz - suggest record
                        \high pass filter frequency or 50Hz if no HP filter), damping and num cycles of PGA
                        \correction
0  0.0          \randomize target? (iSeed, ranFactor)
1.0  100.0      \freqMatch
1.0             \scale factor

Maipu_NCh2745_10percent_Tiso_2sec.tgt
20              \maximum no. of iterations
0.05            \tolerance for maximum mismatch (in fraction of target)
1.0             \convergence damping (recommended default value of 1.0)
14              \model (1 or 6. 6=tapered cosine wave, 10=numerical evaluation of model1, 11= new
                   \displacement compatible wavelet, 12=as 11 but will automatically reduce wavelet to
                     \ensure displacement compatible, 13=same as 12 but using sinusoidal correction, 14=as \13 but implicit
                     integration)
1.25 0.25 1.0 4.0       \alpha model, a1, a2, f1, f2 (recommended values)
10              \Max number of waves for model 11,12 or 13 (Must be integer. Higher numbers more
                  \stable in frequency domain, lower numbers more stable in time domain, recommended
                  \value 10)
25              \Max number of "additional wavelet" iterations - sub iterations used to prevent
                  \divergence by adding wavelets or reducing correction amplitude (suggest 20)
0.7             \Off diagonal reduction, should be between 0.0 and 1.0, value of 1.0 recommended for
                  \wavelet model 1, 0.7 recommended for wavelet model 11, as improves stability.
2               \Spectral acceleration switch (1=absolute, 2=pseudo) use 1 for spectral acceleration
                  \matching, 2 for matching spectral displacement.
0  0.           \scale flag(=0 no, =1 yes, =2 yes but once before adjustment) scale period, note that
                  \scaling for nearest target period with lowest damping level
1               \interpolate to 1/dtFlag of the input time step
1.0e-04         \minimum eigenvalue (control on convergence, recommended 1.0e-04)
350             \group size (control on convergence, recommended 25 if subgroups used else make larger
                  \than number of points to match if using full C matrix and off-diagonal reduction)
0               \PGA correction 0=none, 1= harmonic three cycle displacement compatible PGA
                     \adjustment (just enter amplitude and frequency on next line, 2= model 13 wavelet enter  \all parameters on next
                     line
0.133   25.0  0.1  6    \PGA wavelet options: Target PGA, Frequency of adjustment (in Hz - suggest record
                           \high pass filter frequency or 50Hz if no HP filter), damping and num cycles of PGA \correction
0  0.0          \randomize target? (iSeed, ranFactor)
0.2  100.0      \freqMatch
1.0             \scale factor

Maipu_NCh2745_10percent_Tiso_2sec.tgt
20              \maximum no. of iterations
0.05            \tolerance for maximum mismatch (in fraction of target)
1.0             \convergence damping (recommended default value of 1.0)
14              \model (1 or 6. 6=tapered cosine wave, 10=numerical evaluation of model1, 11= new
```

```
                    \displacement compatible wavelet, 12=as 11 but will automatically reduce wavelet to \ensure displacement
                    compatible, 13=same as 12 but using sinusoidal correction, 14=as 13 \but implicit integration)
1.25 0.25 1.0 4.0   \alpha model, a1, a2, f1, f2 (recommended values)
10                  \Max number of waves for model 11,12 or 13 (Must be integer. Higher numbers more
                    \stable in frequency domain, lower numbers more stable in time domain, recommended \value 10)
25                  \Max number of "additional wavelet" iterations - sub iterations used to prevent divergence
                    \by adding wavelets or reducing correction amplitude (suggest 20)
0.7                 \Off diagonal reduction, should be between 0.0 and 1.0, value of 1.0 recommended for
                    \wavelet model 1, 0.7 recommended for wavelet model 11, as improves stability.
2                   \Spectral acceleration switch (1=absolute, 2=pseudo) use 1 for spectral acceleration
                    \matching, 2 for matching spectral displacement.
0  0.               \scale flag(=0 no, =1 yes, =2 yes but once before adjustment) scale period, note that
                    \scaling for nearest target period with lowest damping level
1                   \interpolate to 1/dtFlag of the input time step
1.0e-04             \minimum eigenvalue (control on convergence, recommended 1.0e-04)
350                 \group size (control on convergence, recommended 25 if subgroups used else make larger
                    \than number of points to match if using full C matrix and off-diagonal reduction)
0                   \PGA correction 0=none, 1= harmonic three cycle displacement compatible PGA
                    \adjustment (just enter amplitude and frequency on next line, 2= model 13 wavelet enter \all parameters on next
                    line
0.133   25.0  0.1  6    \PGA wavelet options: Target PGA, Frequency of adjustment (in Hz - suggest record
                         \high pass filter frequency or 50Hz if no HP filter), damping and num cycles of PGA \correction
0  0.0              \randomize target? (iSeed, ranFactor)
0.1  100.0          \freqMatch
1.0                 \scale factor
```

Example .rs output file: Maipu_design_eq_llolleo_S80E_1p5.rs3

```
 Program Version: 5.0b
 Solution did not achieve full converge in maximum number of iterations
 Maximum misfit =   43.98 percent

 Run Parameters:
 Input time history:              Maipu_design_eq_llolleo_S80E_1p5.ac2
 Output time history:              Maipu_design_eq_llolleo_S80E_1p5.ac3
 Target spectrum:                 Maipu_NCh2745_10percent_Tiso_2sec.tgt
 Maximum number of iterations =   20
 Convergence tolerance =    0.0500
 Convergence Damping factor =    1.0000
 Adjustment time history model =   14
 Adjustment TH tapers (a1,a2,f1.f2) =    1.2500    0.2500    1.0000    4.0000
 Interpolate TH Flag =    1
 Scale TH Flag =    0
 minimum eigenvalue =  0.1000E-03
 Group Size =  350
 PGA =    0.5923

 Matched spectrum:
  84 = Number of spectral frequencies
   1  = Number of Damping Values
    0.100
 Random flags    0    0.0000

    Freq     Damping   Target   Computed   Initial Randomized tPeak
  33.3333    0.1000    0.4079    0.5873    0.5985    0.4079   33.5950
  31.1085    0.1000    0.4169    0.5880    0.6014    0.4169   40.3550
  29.0321    0.1000    0.4265    0.5902    0.6100    0.4265   34.0000
  27.0944    0.1000    0.4369    0.5919    0.6121    0.4369   33.6000
  25.2859    0.1000    0.4480    0.6112    0.6128    0.4480   40.3500
  23.5982    0.1000    0.4598    0.6158    0.6002    0.4598   40.3500
  22.0231    0.1000    0.4726    0.6265    0.6119    0.4726   40.3550
  20.5532    0.1000    0.4862    0.6305    0.6334    0.4862   40.3550
```

19.1813	0.1000	0.5008	0.6553	0.6438	0.5008	40.3550
17.9011	0.1000	0.5165	0.6905	0.6462	0.5165	40.3550
16.7062	0.1000	0.5332	0.6924	0.6511	0.5332	40.3600
15.5912	0.1000	0.5512	0.6754	0.6524	0.5512	40.3650
14.5505	0.1000	0.5705	0.6551	0.6761	0.5705	33.3950
13.5793	0.1000	0.5911	0.6629	0.6834	0.5911	33.4000
12.6730	0.1000	0.6132	0.6434	0.6675	0.6132	33.4050
11.8271	0.1000	0.6369	0.6691	0.7092	0.6369	43.5250
11.0377	0.1000	0.6623	0.7211	0.7726	0.6623	34.0100
10.3010	0.1000	0.6895	0.7234	0.7758	0.6895	34.8450
9.6134	0.1000	0.7187	0.7450	0.8011	0.7187	40.5850
8.9718	0.1000	0.7499	0.7603	0.8136	0.7499	40.3700
8.3730	0.1000	0.7834	0.7898	0.8248	0.7834	40.3800
7.8141	0.1000	0.8192	0.8305	0.8781	0.8192	37.7750
7.2925	0.1000	0.8577	0.8976	0.9168	0.8577	37.7850
6.8058	0.1000	0.8988	0.9031	0.9283	0.8988	40.8250
6.3515	0.1000	0.9430	0.9438	0.9518	0.9430	43.5500
5.9276	0.1000	0.9902	0.9946	1.0034	0.9902	36.3150
5.5320	0.1000	1.0409	1.0348	1.0272	1.0409	36.3300
5.1627	0.1000	1.0952	1.0873	1.0846	1.0952	43.5750
4.8181	0.1000	1.1216	1.1368	1.1416	1.1216	43.5900
4.4965	0.1000	1.1216	1.1149	1.1156	1.1216	43.6000
4.1964	0.1000	1.1216	1.1123	1.0941	1.1216	15.4250
3.9163	0.1000	1.1216	1.1285	1.1425	1.1216	15.4350
3.6549	0.1000	1.1216	1.1287	1.1451	1.1216	15.4450
3.4110	0.1000	1.1216	1.1147	1.0995	1.1216	15.4600
3.1833	0.1000	1.1216	1.1289	1.1345	1.1216	38.0000
2.9708	0.1000	1.1216	1.1133	1.1083	1.1216	38.0300
2.7725	0.1000	1.1216	1.1214	1.1179	1.1216	38.9650
2.5875	0.1000	1.1216	1.1143	1.1057	1.1216	43.1000
2.4148	0.1000	1.1216	1.1295	1.1377	1.1216	43.1300
2.2536	0.1000	1.1216	1.1085	1.1110	1.1216	40.4500
2.1032	0.1000	1.1216	1.1499	1.1529	1.1216	40.4650
1.9628	0.1000	1.1216	1.1041	1.0908	1.1216	40.4850
1.8318	0.1000	1.1032	1.0879	1.0998	1.1032	38.0750
1.7095	0.1000	1.0296	1.0465	1.0490	1.0296	38.1050
1.5954	0.1000	0.9608	0.9607	0.9611	0.9608	34.9650
1.4889	0.1000	0.8967	0.8770	0.8929	0.8967	36.4000
1.3896	0.1000	0.8369	0.8749	0.8769	0.8369	36.8100
1.2968	0.1000	0.7810	0.7591	0.7699	0.7810	36.8650
1.2103	0.1000	0.7289	0.7233	0.7232	0.7289	38.2250
1.1295	0.1000	0.6802	0.7028	0.7050	0.6802	37.9050
1.0541	0.1000	0.6348	0.6197	0.6205	0.6348	37.9450
0.9837	0.1000	0.5924	0.5787	0.5642	0.5924	31.9550
0.9181	0.1000	0.5529	0.5718	0.5860	0.5529	32.0000
0.8568	0.1000	0.5160	0.5075	0.5136	0.5160	31.5650
0.7996	0.1000	0.4816	0.4911	0.4934	0.4816	31.6400
0.7462	0.1000	0.4494	0.4447	0.4480	0.4494	35.0800
0.6964	0.1000	0.4194	0.4244	0.3866	0.4194	30.4950
0.6499	0.1000	0.3914	0.4025	0.3224	0.3914	30.5400
0.6066	0.1000	0.3653	0.3526	0.2397	0.3653	30.6300
0.5661	0.1000	0.3409	0.3035	0.1926	0.3409	29.9950
0.5283	0.1000	0.3182	0.2812	0.1760	0.3182	34.7700
0.4930	0.1000	0.2143	0.2233	0.1488	0.2143	34.8100
0.4601	0.1000	0.1866	0.1776	0.1231	0.1866	34.8150
0.4294	0.1000	0.1625	0.1595	0.1025	0.1625	35.9250
0.4008	0.1000	0.1416	0.1411	0.0867	0.1416	34.8350
0.3740	0.1000	0.1233	0.1249	0.0823	0.1233	34.8450
0.3490	0.1000	0.1074	0.1085	0.0766	0.1074	34.8550
0.3257	0.1000	0.0935	0.0943	0.0691	0.0935	34.8650
0.3040	0.1000	0.0815	0.0807	0.0619	0.0815	34.8750
0.2837	0.1000	0.0710	0.0710	0.0527	0.0710	35.2950
0.2648	0.1000	0.0618	0.0622	0.0502	0.0618	33.9700
0.2471	0.1000	0.0538	0.0540	0.0496	0.0538	33.9850
0.2306	0.1000	0.0469	0.0469	0.0451	0.0469	33.9950
0.2152	0.1000	0.0408	0.0405	0.0375	0.0408	34.0000

0.2009	0.1000	0.0356	0.0358	0.0320	0.0356	34.0050
0.1874	0.1000	0.0310	0.0315	0.0265	0.0310	34.0100
0.1749	0.1000	0.0270	0.0269	0.0210	0.0270	34.0200
0.1633	0.1000	0.0235	0.0236	0.0171	0.0235	34.3250
0.1524	0.1000	0.0205	0.0211	0.0144	0.0205	34.3400
0.1422	0.1000	0.0178	0.0180	0.0113	0.0178	34.3500
0.1327	0.1000	0.0155	0.0151	0.0085	0.0155	34.3600
0.1238	0.1000	0.0135	0.0129	0.0067	0.0135	34.3650
0.1156	0.1000	0.0118	0.0110	0.0056	0.0118	34.3700
0.1079	0.1000	0.0103	0.0091	0.0048	0.0103	34.3750

Example .ac output file:
Maipu_design_eq_llolleo_S80E_1p5.ac3
(Only part of this file is shown due to the long earthquake record)

```
Time history matched to spectrum:Maipu_NCh2745_10percent_Tiso_2sec.tgt
23286    0.0050
  0.13050E-02
 -0.15225E-01
 -0.13290E-01
 -0.11355E-01
 -0.94200E-02
 -0.74700E-02
 -0.55500E-02
 -0.36000E-02
 -0.12000E-03
  0.44400E-02
  0.89850E-02
  0.13545E-01
  0.18090E-01
  0.22635E-01
  0.27180E-01
  0.28425E-01
  0.28830E-01
  0.29250E-01
  0.29640E-01
  0.30075E-01
  0.30465E-01
  0.30870E-01
  0.27645E-01
  0.21930E-01
  0.16230E-01
  0.10515E-01
  0.40350E-02
 -0.24450E-02
 -0.89550E-02
 -0.13425E-01
 -0.14850E-01
 -0.16320E-01
 -0.17760E-01
 -0.19215E-01
 -0.20655E-01
 -0.22095E-01
 -0.23835E-01
 -0.26685E-01
 -0.29535E-01
 -0.32385E-01
 -0.35235E-01
 -0.38085E-01
 -0.40920E-01
 -0.40800E-01
 -0.36225E-01
```

APPENDIX D

MATLAB CODE FOR NSGA-II CE OPTIMIZATION

Note: See Shook (2006) for flow chart of file relationships and MATLAB code for files not included here.

runopt_PPP.m

```
%runopt_PPP.m
%This file prepares the NSGA-II CE optimization of the parameters for
%the PPP isolators
%The optimization is performed on five variables

  clc;clear;
% Created by : Hyun-Su Kim
%              09-06-2004
% Modified by: PR    18 December 2004
% Modified by: DS    8  August 2005
%              RH   20  November 2007
% Load Global Variables
glbvar;
% Units are m, N unless noted otherwise

% Input Parameters
% Set the total population size
popSize = 100 ;
%Number of generations for GA optimization
genNum = 200;
%Number of mutation generations for GA optimization
mutGenNum = genNum; % Generally same as genNum

% Initialize Variables
nIter = 0; % Set iteration counter to zero
nDOF = 3 ; % Define the degrees of freedom of the structure
fitnessFunc = 'fitfunc1_PPP'; % Fitness Function to be used
% Determine Number of Variables to be optimized
numVar = 5; % T0, R, Lp, ke, drebar that yields

% Define Training Excitation
load RSP_llolleo_S80E_1p5_2p75sec_10per_eq_mat_file %acceleration in g
eq = [eq_mat_file(1,:);eq_mat_file(2,:)*9.80665];
%convert accel from g to m/s2

% Extract the time vector from the input file.
dt = eq(1,2) - eq(1,1) ;

eq = eq(:,30/dt:1:53/dt);
t = eq(1,:);

save eq eq

% Prepare time increment and total simulation time for Simulink
dt = 0.0029;
tbegin = min(t(:));
tend = max(t(:));

% Command Window Prompt
% Enter the number of the run from the keyboard.  There are only two
% possibilities:  1 = first time run, 2 = any restart run.
numRun = input('Input number of run [Default = 1]: ');
```

```
if isempty(numRun)
  numRun = 1;
end
if numRun ~= 1
    disp('If you loaded previous results, strike any key to continue. Otherwise, press [Ctrl+C], load previous results and try again!');
  pause
  initPop = endPop;
  bResume = 1;
else
  initPop = [];
  bResume = 0;
end

% Define range of parameters to be optimized
To_range = [0.5 8]; %initial prestress of cable (tonf)
R_range = [30 150]; %radius (cm)
Lp_range = [100 250]; %length of pile (cm)
ke_range = [1 15]; %stiffness of cable (tonf/cm)
drebar_range = [1 5]; %diameter of rebar (cm)

initRange = [To_range; R_range; Lp_range; ke_range; drebar_range] ;

% Check to see that the number of variables matches the initRange
if numVar ~= size(initRange,1)
    disp ('Check the size of the initRange and the number of rules, etc.');
    stop
end

% Set the mutation rate for child individuals that are created by the
% mutation operator.
mutRate = 0.2;
% Compute the number of population members in the next generation that % are obtained from mutation.
mutNum =  mutRate*popSize;

% Set the rate of child individuals that are created by the crossover operator.
xoverRate = 0.8;
% Calculate the number of population members for the next generation
% that are obtained from
% rounding down the crossover rate times the total population and
% dividing by 2.  Division by 2 is done because the population is not
% large enough to handle a large crossover rate.
xoverNum =  floor(xoverRate*popSize/2.);
% Set a tolerance rate.
tolerance = 1e-6;
% Set a switch for displaying values to the screen during calculations.
dispOnOff = 1;

% Define the number of multiobjective functions
numObj = 4;

% The objectives to be minimized are:
%    1. Peak base shear normalized by fixed-base case
%    2. Peak base displacement
%    3. RMS base displacement
%    4. RMS absolute floor acceleration normalized by uncontrolled case

% === Start GA function ================================================
[x,endPop,bPop,traceInfo] = NSGA2(initRange, fitnessFunc,[],initPop,...
    [popSize tolerance dispOnOff numObj bResume],'maxGenTerm',genNum,...
  'tournSelectNSGA2',[2],['simpleXoverNSGA2'],[xoverNum 0],'nonUnifMutateNSGA2',[mutNum mutGenNum 3]);
```

fitfunc1_PPP.m

```
function [chrom fitness] = fitfunc1_PPP (chrom, param)
```

```
%% fitfunc1_PPP.m
% Inputs for this function are
%    1. The chromosome chrom whose fitness is to be evaluated
%    2. A vector of parameters related to the chrom
% Outputs for this function are:
%    1. The chromosome string
%    2. The fitness of the chromosome
% There is a total 'x' rules and only one direction of motion.

% Declare global variables so that they are available.
glbvar;

To1 = chrom(1);
R = chrom(2);
Lp1 = chrom(3);
ke1 = chrom(4);
drebar = chrom(5);

% Compute the vertical force of the mass acting on the PPP system:
% (divide by 8 to obtain the mass per PPP).  Mass units are given in tons
% force here.
mass = -84/8; %tonf : vertical applied load

%% Run simulation file runsim_PPP.m for structure to be analyzed.
runsim_PPP;

%% Declare Fitness
fitness(1) = J1;
fitness(2) = J2;
fitness(3) = J3;
fitness(4) = J4;

%% Increment the counter for the number of simulations that have been run.
nIter = nIter + 1
```

APPENDIX E

MATLAB CODE FOR NEURO-FUZZY TRAINING

Note: The sample files included here are related to creation of an ANFIS model for the HDRB. The training and validation of the SMA FIS are performed using a similar procedure.

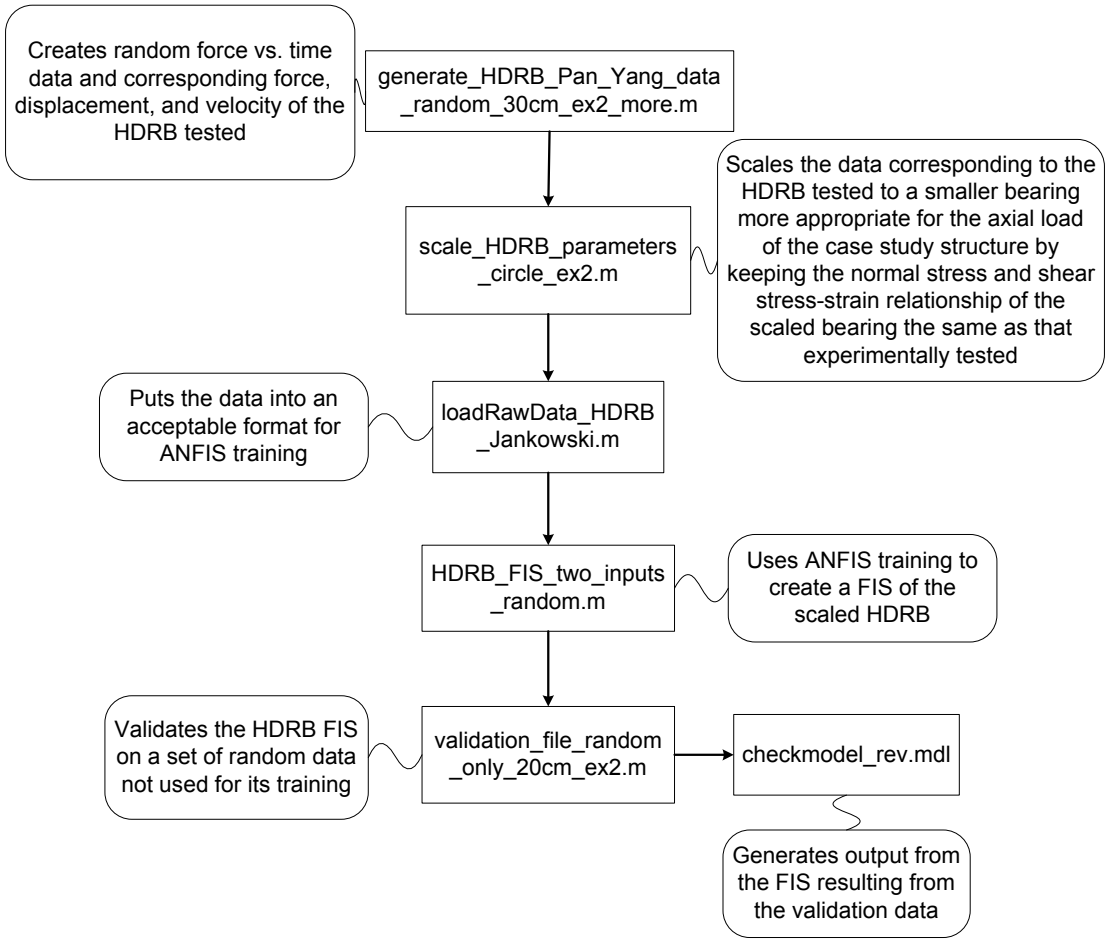

generate_HDRB_Pan_Yang_data_random_30cm_ex2_more.m

```
%Written by Rachel Husfeld
%July 2007
%Rev. Jan. 2008
```

```
%Model of HDRB or LRB using equations developed by Pan and Yang (1996)
%see Hwang et al. 2002 paper

%This file creates random, white noise excitation force vs. time data %and corresponding force, displacement, and velocity of the
HDRB tested

clear all
close all

% Generate displacement and velocity data using different loading
% frequencies and ranges of displacement.

%%%%%%%%%%%%%%%%%%%%%%%%%%%%%%%%%%%%%%%%%%%%%%%%%%%%%%%%%%%%%%%%
%%%%%
% The following is inserted from:
% RandDisp.m
% M-file creating Random White Noise Displacement for HD Rubber
% Bearings
%
% Modified by : Visit Likhitrunagsilp
%               Department of Civil Engineering
%               Texas A&M University
%
% Last modification: May 15, 2001
% Modified  3 August 2001   Prof. Roschke

clc;

duration = input('Duration of each subset of data (sec) : ');
dt       = input('Time step (sec) : ');
disp(' ');
zerotime = input('Enter time for zero data (sec) : ');
ramptime = input('Enter time for ramp (sec)      : ');
disp(' ');

%%%%%%%%%%%%%%%%%%%%%%%
% Generate Random Data %
%%%%%%%%%%%%%%%%%%%%%%%

% Generate variables with random white noise signal
% Note that the prefix 'wn' of variables implies 'random white noise'.
% 5 levels of maximum stroke are considered

% Generate random data
% Note that each random data must be created separately to prevent
% repetition
tout  = duration + 3.0;      % extend 3 seconds longer (will be %truncated later to prevent noise)
tout1 = [0:dt:tout];
rand('state',0);
wnDisp1 = rand(size(tout1));
wnDisp2 = rand(size(tout1));
wnDisp3 = rand(size(tout1));
wnDisp4 = rand(size(tout1));
wnDisp5 = rand(size(tout1));
wnDisp6 = rand(size(tout1));
wnDisp7 = rand(size(tout1));
wnDisp8 = rand(size(tout1));
wnDisp9 = rand(size(tout1));
wnDisp10 = rand(size(tout1));
wnDisp11 = rand(size(tout1));
wnDisp12 = rand(size(tout1));
wnDisp13 = rand(size(tout1));
wnDisp14 = rand(size(tout1));
wnDisp15 = rand(size(tout1));
wnDisp16 = rand(size(tout1));
wnDisp17 = rand(size(tout1));
```

```
wnDisp18 = rand(size(tout1));
wnDisp19 = rand(size(tout1));
wnDisp20 = rand(size(tout1));
wnDisp21 = rand(size(tout1));
wnDisp22 = rand(size(tout1));
wnDisp23 = rand(size(tout1));
wnDisp24 = rand(size(tout1));
wnDisp25 = rand(size(tout1));
wnDisp26 = rand(size(tout1));
wnDisp27 = rand(size(tout1));
wnDisp28 = rand(size(tout1));
wnDisp29 = rand(size(tout1));
wnDisp30 = rand(size(tout1));
wnDisp31 = rand(size(tout1));
wnDisp32 = rand(size(tout1));
wnDisp33 = rand(size(tout1));
wnDisp34 = rand(size(tout1));
wnDisp35 = rand(size(tout1));

clear tout tout1;

% Override Matlab defaults for plotting
% Prepare to set different line weights and fonts from the defaults.
set (0, 'DefaultAxesFontSize', 12)
set (0, 'DefaultAxesFontWeight', 'bold')
set (0, 'DefaultAxesLineWidth', 2)
set (0, 'DefaultLineLineWidth', 2)

%%%%%%%%%%%%%%%%%%%%%%%%%%%%
% Generate random data files %
%%%%%%%%%%%%%%%%%%%%%%%%%%%%

% --> Here 7 different sets of displacement data are generated

%%%%%%%%%%%%%%%%%%%%%%%%%%%%%%%%%%%%%%%%%%%%%%%%%%%%%%%%%%%%%%
%%%%%
% --> 1st data set
disp('1st data set');
disp(' ');

Disp = 25;        Freq = 2.0;
RDisp_all1_1 = RandDispGen(duration, dt, zerotime, ramptime, wnDisp1, Disp, Freq, 1, 'RDisp_all1_1', 1);

Disp = 50;        Freq = 1.5;
RDisp_all1_2 = RandDispGen(duration, dt, zerotime, ramptime, wnDisp2, Disp, Freq, 0, 'RDisp_all1_2', 1);

Disp = 100;        Freq = 1.2;
RDisp_all1_3 = RandDispGen(duration, dt, zerotime, ramptime, wnDisp3, Disp, Freq, 0, 'RDisp_all1_3', 1);

Disp = 150;        Freq = 1.0;
RDisp_all1_4 = RandDispGen(duration, dt, zerotime, ramptime, wnDisp4, Disp, Freq, 0, 'RDisp_all1_4', 1);

Disp = 125;        Freq = 0.9;
RDisp_all1_5 = RandDispGen(duration, dt, zerotime, ramptime, wnDisp5, Disp, Freq, 0, 'RDisp_all1_5', 1);

Disp = 200;        Freq = 3.0;
RDisp_all1_6 = RandDispGen(duration, dt, zerotime, ramptime, wnDisp6, Disp, Freq, 0, 'RDisp_all1_6', 1);

Disp = 110;        Freq = 1.5;
RDisp_all1_7 = RandDispGen(duration, dt, zerotime, ramptime, wnDisp7, Disp, Freq, 0, 'RDisp_all1_7', 1);

Disp = 270;        Freq = 3.5;
RDisp_all1_8 = RandDispGen(duration, dt, zerotime, ramptime, wnDisp8, Disp, Freq, 0, 'RDisp_all1_8', 1);

Disp = 300;        Freq = 2.5;
RDisp_all1_9 = RandDispGen(duration, dt, zerotime, ramptime, wnDisp9, Disp, Freq, 0, 'RDisp_all1_9', 1);
```

```
Disp = 180;         Freq = 2.2;
RDisp_all1_10 = RandDispGen(duration, dt, zerotime, ramptime, wnDisp10, Disp, Freq, 0, 'RDisp_all1_10', 1);

%     Concatenate all data
RDisp_all1 = [RDisp_all1_1 RDisp_all1_2 RDisp_all1_3 RDisp_all1_4 RDisp_all1_5 RDisp_all1_6 RDisp_all1_7...
    RDisp_all1_8 RDisp_all1_9 RDisp_all1_10];
clear wnDisp1 wnDisp2 wnDisp3 wnDisp4 wnDisp5 wnDisp6 wnDisp7 wnDisp8 wnDisp9 wnDisp10;
clear RDisp_all1_1 RDisp_all1_2 RDisp_all1_3 RDisp_all1_4 RDisp_all1_5 RDisp_all1_6 RDisp_all1_7 RDisp_all1_8
RDisp_all1_9 RDisp_all1_10;
ExDispPlot(dt, RDisp_all1, 'R_25_125', 'plot2', 1);

disp('Press any key to run next data set...');
pause;      close all;


%%%%%%%%%%%%%%%%%%%%%%%%%%%%%%%%%%%%%%%%%%%%%%%%%%%%%%%%%%%%%%%%%%%%%%%%%%%%%
%%%%%
% --> 2nd data set
disp('2nd data set');
disp(' ');

Disp = 25;         Freq = 1.0;
RDisp_25_1 = RandDispGen(duration, dt, zerotime, ramptime, wnDisp11, Disp, Freq, 1, 'RDisp_25_1', 1);

Disp = 25;         Freq = 2.0;
RDisp_25_2 = RandDispGen(duration, dt, zerotime, ramptime, wnDisp12, Disp, Freq, 0, 'RDisp_25_2', 1);

Disp = 25;         Freq = 3.0;
RDisp_25_3 = RandDispGen(duration, dt, zerotime, ramptime, wnDisp13, Disp, Freq, 0, 'RDisp_25_3', 1);

Disp = 25;         Freq = 4.0;
RDisp_25_4 = RandDispGen(duration, dt, zerotime, ramptime, wnDisp14, Disp, Freq, 0, 'RDisp_25_4', 1);

Disp = 25;         Freq = 4.5;
RDisp_25_5 = RandDispGen(duration, dt, zerotime, ramptime, wnDisp15, Disp, Freq, 0, 'RDisp_25_5', 1);
%     Concatenate all data
RDisp_25 = [RDisp_25_1 RDisp_25_2 RDisp_25_3 RDisp_25_4 RDisp_25_5];
clear  wnDisp11 wnDisp12 wnDisp13 wnDisp14 wnDisp15;
clear RDisp_25_1 RDisp_25_2 RDisp_25_3 RDisp_25_4 RDisp_25_5;
ExDispPlot(dt, RDisp_25, 'R_25', 'plot2', 1);

disp('Press any key to run next data set...');
pause;      close all;


%%%%%%%%%%%%%%%%%%%%%%%%%%%%%%%%%%%%%%%%%%%%%%%%%%%%%%%%%%%%%%%%%%%%%%%%%%%%%
%%%%%
% --> 3rd data set
disp('3rd data set');
disp(' ');

Disp = 75;         Freq = 0.5;
RDisp_50_1 = RandDispGen(duration, dt, zerotime, ramptime, wnDisp16, Disp, Freq, 1, 'RDisp_50_1', 1);

Disp = 75;         Freq = 1.0;
RDisp_50_2 = RandDispGen(duration, dt, zerotime, ramptime, wnDisp17, Disp, Freq, 0, 'RDisp_50_2', 1);

Disp = 75;         Freq = 1.5;
RDisp_50_3 = RandDispGen(duration, dt, zerotime, ramptime, wnDisp18, Disp, Freq, 0, 'RDisp_50_3', 1);

Disp = 75;         Freq = 2.2;
RDisp_50_4 = RandDispGen(duration, dt, zerotime, ramptime, wnDisp19, Disp, Freq, 0, 'RDisp_50_4', 1);

Disp = 75;         Freq = 3.5;
RDisp_50_5 = RandDispGen(duration, dt, zerotime, ramptime, wnDisp20, Disp, Freq, 0, 'RDisp_50_5', 1);
```

```
%     Concatenate all data
RDisp_50 = [RDisp_50_1 RDisp_50_2 RDisp_50_3 RDisp_50_4 RDisp_50_5];
clear  wnDisp16 wnDisp17 wnDisp18 wnDisp19 wnDisp20;
clear RDisp_50_1 RDisp_50_2 RDisp_50_3 RDisp_50_4 RDisp_50_5;
ExDispPlot(dt, RDisp_50, 'R_50', 'plot2', 1);

disp('Press any key to run next data set...');
pause;      close all;


%%%%%%%%%%%%%%%%%%%%%%%%%%%%%%%%%%%%%%%%%%%%%%%%%%%%%%%%%%%%%%%%%%%%%%%%%%%%
%%%%%
% --> 4th data set
disp('4th data set');
disp(' ');

Disp = 150;         Freq = 0.6;
RDisp_75_1 = RandDispGen(duration, dt, zerotime, ramptime, wnDisp21, Disp, Freq, 1, 'RDisp_75_1', 1);

Disp = 150;         Freq = 0.9;
RDisp_75_2 = RandDispGen(duration, dt, zerotime, ramptime, wnDisp22, Disp, Freq, 0, 'RDisp_75_2', 1);

Disp = 150;         Freq = 1.4;
RDisp_75_3 = RandDispGen(duration, dt, zerotime, ramptime, wnDisp23, Disp, Freq, 0, 'RDisp_75_3', 1);

Disp = 150;         Freq = 2.0;
RDisp_75_4 = RandDispGen(duration, dt, zerotime, ramptime, wnDisp24, Disp, Freq, 0, 'RDisp_75_4', 1);

Disp = 150;         Freq = 4.1;
RDisp_75_5 = RandDispGen(duration, dt, zerotime, ramptime, wnDisp25, Disp, Freq, 0, 'RDisp_75_5', 1);
%     Concatenate all data
RDisp_75 = [RDisp_75_1 RDisp_75_2 RDisp_75_3 RDisp_75_4 RDisp_75_5];
clear  wnDisp21 wnDisp22 wnDisp23 wnDisp24 wnDisp25;
clear RDisp_75_1 RDisp_75_2 RDisp_75_3 RDisp_75_4 RDisp_75_5;
ExDispPlot(dt, RDisp_75, 'R_75', 'plot2', 1);

disp('Press any key to run next data set...');
pause;      close all;


%%%%%%%%%%%%%%%%%%%%%%%%%%%%%%%%%%%%%%%%%%%%%%%%%%%%%%%%%%%%%%%%%%%%%%%%%%%%
%%%%%
% --> 5th data set
disp('5th data set');
disp(' ');

Disp = 300;         Freq = 0.6;
RDisp_100_1 = RandDispGen(duration, dt, zerotime, ramptime, wnDisp26, Disp, Freq, 1, 'RDisp_100_1', 1);

Disp = 300;         Freq = 1.7;
RDisp_100_2 = RandDispGen(duration, dt, zerotime, ramptime, wnDisp27, Disp, Freq, 0, 'RDisp_100_2', 1);

Disp = 300;         Freq = 3.7;
RDisp_100_3 = RandDispGen(duration, dt, zerotime, ramptime, wnDisp28, Disp, Freq, 0, 'RDisp_100_3', 1);

Disp = 300;         Freq = 2.8;
RDisp_100_4 = RandDispGen(duration, dt, zerotime, ramptime, wnDisp29, Disp, Freq, 0, 'RDisp_100_4', 1);

Disp = 300;         Freq = 1.0;
RDisp_100_5 = RandDispGen(duration, dt, zerotime, ramptime, wnDisp30, Disp, Freq, 0, 'RDisp_100_5', 1);
%     Concatenate all data
RDisp_100 = [RDisp_100_1 RDisp_100_2 RDisp_100_3 RDisp_100_4 RDisp_100_5];
clear  wnDisp26 wnDisp27 wnDisp28 wnDisp29 wnDisp30;
clear RDisp_100_1 RDisp_100_2 RDisp_100_3 RDisp_100_4 RDisp_100_5;
ExDispPlot(dt, RDisp_100, 'R_100', 'plot2', 1);
```

```
disp('Press any key to run next data set...');
pause;      close all;


%%%%%%%%%%%%%%%%%%%%%%%%%%%%%%%%%%%%%%%%%%%%%%%%%%%%%%%%%%%%%%%%
%%%%%
% --> 6th data set
disp('6th data set');
disp(' ');

Disp = 220;         Freq = 0.3;
RDisp_125_1 = RandDispGen(duration, dt, zerotime, ramptime, wnDisp31, Disp, Freq, 1, 'RDisp_125_1', 1);

Disp = 220;         Freq = 0.9;
RDisp_125_2 = RandDispGen(duration, dt, zerotime, ramptime, wnDisp32, Disp, Freq, 0, 'RDisp_125_2', 1);

Disp = 220;         Freq = 2.5;
RDisp_125_3 = RandDispGen(duration, dt, zerotime, ramptime, wnDisp33, Disp, Freq, 0, 'RDisp_125_3', 1);

Disp = 220;         Freq = 3.6;
RDisp_125_4 = RandDispGen(duration, dt, zerotime, ramptime, wnDisp34, Disp, Freq, 0, 'RDisp_125_4', 1);

Disp = 220;         Freq = 1.7;
RDisp_125_5 = RandDispGen(duration, dt, zerotime, ramptime, wnDisp35, Disp, Freq, 0, 'RDisp_125_5', 1);
%     Concatenate all data
RDisp_125 = [RDisp_125_1 RDisp_125_2 RDisp_125_3 RDisp_125_4 RDisp_125_5];
clear  wnDisp31 wnDisp32 wnDisp33 wnDisp34 wnDisp35;
clear RDisp_125_1 RDisp_125_2 RDisp_125_3 RDisp_125_4 RDisp_125_5;
ExDispPlot(dt, RDisp_125, 'R_125', 'plot2', 1);

% END OF INSERTED FILE RandDisp.m
%%%%%%%%%%%%%%%%%%%%%%%%%%%%%%%%%%%%%%%%%%%%%%%%%%%%%%%%%%%%%%%%
%%%%%%%

% Concatenate random displacement data, convert from mm to m
% Random displacement record in m
dispRand = cat(2,RDisp_all1/1000,RDisp_25/1000,RDisp_50/1000,RDisp_75/1000,RDisp_100/1000,RDisp_125/1000);
timeRand = duration*7*5 + 0.005;

% Make a vector of the time values
disp = dispRand;
t = 0:dt:timeRand;
tmax = max(t);
numPts = length(t);

% Determine horizontal velocity using backwards difference method
% equation from Chapra and Canale 1998 - published in Numerical Methods
% textbook McGraw-Hill, 1998
% Initialize a vector of velocities with all zeros.  Speeds up
% calculations.
vel = zeros(size(disp));
for i = 5:numPts
   vel(i) = (3*disp(i-4) - 16*disp(i-3) + 36*disp(i-2) - 48*disp(i-1) + 25*disp(i))/(12*dt);
end

% To avoid having the first four velocity values being zero, set them
% equal
% to the 5th velocity
for i = 1:4
   vel(i) = vel(5);
end

%Values in terms of N and m
%Values from Jankowski (2003) example 2
% HDRB diameter 22.3 cm, axial load = 12.5 tonnes, freq = 0.5 Hz
b1 = 21.239*9.80665*1000;
```

```
b2 = 343.10*9.80665*1000;
b3 = -876.70*9.80665*1000;
b4 = 51.829*9.80665*1000;
b5 = 4.3595;
b6 = 58.676*9.80665*1000;
b7 = 3.9664;
b8 = 91.482;
b9 = 1.5377*9.80665*1000;
b10 = 40.868*9.80665*1000;
b11 = 0.13985;

F1 = zeros(size(disp));
F2 = zeros(size(disp));
F = zeros(size(disp));


   for i = 1:1:numPts
   %Pan and Yang Eq. 1 (Hwang eq. 2)
   F1(i) = (b1 + b2*disp(i)^2 + b3*disp(i)^4 + b4/(cosh(b5*vel(i))^2)…
   + b6/(cosh(b7*vel(i))*cosh(b8*disp(i))))*disp(i);

   %Pan and Yang Eq. 2 (Hwang eq. 3)
   F2(i) = ((b9 + b10*disp(i)^2)/sqrt(b11^2 + vel(i)^2))*vel(i);

   %Pan and Yang Eq. 3 (Hwang eq. 1)
   F(i) = F1(i) + F2(i);
   end

%Convert force values from N to kN
F1(1,:) = F1(1,:)/1000;
F2(1,:) = F2(1,:)/1000;
F(1,:) = F(1,:)/1000;

%Convert disp and vel from m to cm
disp(1,:) = disp(1,:)*100;
vel(1,:) = vel(1,:)*100;

%Save parameters for use in HDRB FIS
save HDRB_Jankowski_ex2_30cm_dispcm_freq.mat disp  %cm
save HDRB_Jankowski_ex2_30cm_velcmps_freq.mat vel    %cm/s
save HDRB_Jankowski_ex2_30cm_forcekN_freq.mat F    %kN
save HDRB_Jankowski_ex2_30cm_time_freq.mat t %sec
```

scale_HDRB_parameters_circle_ex2.m

```
%Written by Rachel Husfeld
%August 2007

%This program uses a given force-displacement relationship for a HDRB %and scales it for a different sized HDRB, keeping the shear stress-%strain magnitude and relationship the same, and the normal stress the %same as that tested

clear all

load HDRB_Jankowski_ex2_30cm_dispcm_freq.mat  %variable name: disp  %cm
load HDRB_Jankowski_ex2_30cm_velcmps_freq.mat %variable name: vel %cm/s
load HDRB_Jankowski_ex2_30cm_forcekN_freq.mat %variable name: F    %kN
load HDRB_Jankowski_ex2_30cm_time_freq.mat %variable name: t    %sec

%22.3 cm diameter HDRB from Jankowski ex. 2
%normal stress = 0.314 kN/cm2 = 3.14 MPa
L = 17.65; %height of RB in cm
gamma = disp(1,:)/L; %shear strain cm/cm
diam = 22.3; %diameter in cm
A = pi()*diam^2/4; %area in cm2
```

```
tau = F(1,:)/A; %shear stress in kN/cm2
N = 122.6; %vertical load in kN

%Good rule of thumb vertical pressure is 100 kgf/cm2 = 0.9807 kN/cm2
'Vertical pressure of this bearing (kN/cm2) = '
stress = N/A

%Based on this pressure, area of cross-sxn is:
%100 kN vertical load
Q = input('Vertical load on bearing (kN) : ');

A_ideal = Q/stress;

'Ideal diameter of bearing (cm) = '
diam_ideal = sqrt((Q/stress)*4/pi())

diam_new = input('Diameter of bearing to be used (cm) :');

A_new = pi()*diam_new^2/4;

F_new = tau*A_new;
tau_new = F_new/A_new;
disp_new = gamma*L;
gamma_new = disp_new/L;

numPts = length(t);
dt = t(3) - t(2);

% determine horizontal velocity using backwards difference method
% equation from Chapra and Canale 1998 - published in Numerical
% Methods textbook McGraw-Hill, 1998
% Initialize a vector of velocities with all zeros.  Speeds up
% calculations.
vel_new = zeros(size(disp_new));
for i = 5:numPts
   vel_new(i) = (3*disp_new(i-4) - 16*disp_new(i-3) + 36*disp_new(i-2) - 48*disp_new(i-1) + 25*disp_new(i))/(12*dt);
end

% To avoid having the first four velocity values being zero, set them equal
% to the 5th velocity
for i = 1:4
   vel_new(i) = vel_new(5);
end

save HDRB_ex2_20cmdiam_30cmdisp_disp_new disp_new    %cm
save HDRB_ex2_20cmdiam_30cmdisp_vel_new vel_new      %cm/s
save HDRB_ex2_20cmdiam_30cmdisp_force_new F_new  %kN
```

loadRawData_HDRB_Jankowski.m

```
% Written by Rachel Husfeld
% September 2007

% This file prepares the data to create a FIS of the HDRB device
% described by Jankowski, 2004 - ex. 1 - 3

% Store displacement and velocity data for inputs to FIS
% Store force data for output of FIS

% This data is created analytically using the equations formulated by
% Pan and Yang

clear all
```

```
% load vector of concatenated displacement data (cm)
% maximum displacement is +/- 30 cm
% variable name is disp_new
load HDRB_ex2_20cmdiam_30cmdisp_disp_new
disp = disp_new';

% load vector of velocity data (cm/s)
% variable name is vel_new
load HDRB_ex2_20cmdiam_30cmdisp_vel_new
vel = vel_new';

% load vector of force data (kN)
% variable name is F_new
load HDRB_ex2_20cmdiam_30cmdisp_force_new
F = F_new'; %Force in kN

% define input and output vectors (in column form) for training of
% fuzzy inference system
input_HDRB = [disp vel];    % displacement (cm) and velocity (cm/s)
output_HDRB = [F];   % horizontal restoring force of device (kN)

% save input and output vectors for use with ANFIS
save input_HDRB_Jankowski_ex2_20cmdiam_30cmdisp.mat input_HDRB
save output_HDRB_Jankowski_ex2_20cmdiam_30cmdisp.mat output_HDRB
```

HDRB_FIS_two_inputs_random.m

```
% Written by Rachel Husfeld
% July 2007
% Training neuro-fuzzy model of HDRB device corresponding to Jankowski
% 2004 paper

% Uses training data that includes RANDOM data only

% Before running this file, execute loadRawData.m so that
% input_HDRB.mat and output_HDRB.mat are
% available to this program.

%   input:  [displacement (cm) velocity (cm/s)]
%   output:  [force (kN)]

clear all
close all

load input_HDRB_Jankowski_ex2_20cmdiam_30cmdisp.mat
%variable is called input_HDRB
load output_HDRB_Jankowski_ex2_20cmdiam_30cmdisp.mat
%variable is called output_HDRB

      %%%%%%%%%%%%%%%%%%%
      %               %
        interval = 3   ;%INPUT INTERVAL OF DATA TO BE USED.
      %               %
      %%%%%%%%%%%%%%%%%%%


data = [input_HDRB output_HDRB];
data = data(1:interval:length(data),:);
numPts = length(data);

% define the training and checking data
trn_data = data(1:2:numPts,:);
chk_data = data(2:2:numPts,:);
clear data
```

```
%Change # of MF and SS
mf_n = [3 2];           % number of MFs for each input variable
mf_type = 'dsigmf';     % type of MF
epoch_n = 100;          % number of training epochs
ss = 0.1;               % initial step size
ss_dec_rate = 0.8;      % step size modification rates
ss_inc_rate = 1.2;

% generate FIS matrix
%to use genfis1, all columns of trn_data must be input, except the last
%column must be a single output
in_fismat = genfis1(trn_data, mf_n, mf_type);

tic   % time the training session
% start training
[trn_out_fismat trn_error step_size chk_out_fismat chk_error] = ...
    anfis(trn_data, in_fismat, [epoch_n nan ss ss_dec_rate ss_inc_rate], ...
   [1,1,1,1], chk_data);
disp('lowest checking error: ')
min(chk_error)

%%%%%%%%%%%%%%%%%%%%%%%%%%%%%%%%%%%%%%%%%%%%%%%%%%%%%%%%%%%%%%%%
%%%%%

HDRB_two_inputs = chk_out_fismat;       % rename final FIS
writefis(HDRB_two_inputs,'HDRB_two_inputs_Jankowski_ex2_20cmdiam_30cmdisp_MF32_1');     % save it to the hard drive
toc/60                      % finish timing session (minutes)

t = 0:0.001:(length(trn_data)*0.001-0.001);
```

validation_file_random_only_20cm_ex2.m

```
%Written by Rachel Husfeld
%July 2007

% This file carries out numerical validation of fuzzy model of a
% HDRB/LRB
% Before running this file, HDRB_FIS_two_inputs_random.m or
% LRB_FIS_two_inputs_random.m needs to be run to create a fis

clear all
close all

%New data is generated analytically that was not used for training

%%%%%%%%%%%%%%%%%%%%%%%%%%%%%%%%%%%%%%%%%%%%%%%%%%%%%%%%%%%%%%%%
%%%%
%EXCERPT FROM RandDisp.m file
%generates random displacement record

duration = input('Duration of each subset of data (sec) : ');
dt       = input('Time step (sec) : ');
disp(' ');
zerotime = input('Enter time for zero data (sec) : ');
ramptime = input('Enter time for ramp (sec)      : ');
disp(' ');

%%%%%%%%%%%%%%%%%%%%%%%
% Generate Random Data %
%%%%%%%%%%%%%%%%%%%%%%%

% Generate variables with random white noise signal
% Note that the prefix 'wn' of variables implies 'random white noise'.
```

```
%
% 5 levels of maximum stroke are considered

% Generate random data
% Note that each random data must be created separately to prevent
% repetition
tout  = duration + 3.0;
% extend 3 seconds longer (will be truncated later to prevent noise)
tout1 = [0:dt:tout];
rand('state',0);
wnDisp1 = rand(size(tout1));
wnDisp2 = rand(size(tout1));
wnDisp3 = rand(size(tout1));
wnDisp4 = rand(size(tout1));
wnDisp5 = rand(size(tout1));
wnDisp6 = rand(size(tout1));
wnDisp7 = rand(size(tout1));
wnDisp8 = rand(size(tout1));
wnDisp9 = rand(size(tout1));
wnDisp10 = rand(size(tout1));
wnDisp11 = rand(size(tout1));
wnDisp12 = rand(size(tout1));
wnDisp13 = rand(size(tout1));
wnDisp14 = rand(size(tout1));
wnDisp15 = rand(size(tout1));
wnDisp16 = rand(size(tout1));
wnDisp17 = rand(size(tout1));
wnDisp18 = rand(size(tout1));
wnDisp19 = rand(size(tout1));
wnDisp20 = rand(size(tout1));
wnDisp21 = rand(size(tout1));
wnDisp22 = rand(size(tout1));
wnDisp23 = rand(size(tout1));
wnDisp24 = rand(size(tout1));
wnDisp25 = rand(size(tout1));
wnDisp26 = rand(size(tout1));
wnDisp27 = rand(size(tout1));
wnDisp28 = rand(size(tout1));
wnDisp29 = rand(size(tout1));
wnDisp30 = rand(size(tout1));
wnDisp31 = rand(size(tout1));
wnDisp32 = rand(size(tout1));
wnDisp33 = rand(size(tout1));
wnDisp34 = rand(size(tout1));
wnDisp35 = rand(size(tout1));

clear tout tout1;

%%%%%%%%%%%%%%%%%%%%%%%%%%%%%
% Generate random data files %
%%%%%%%%%%%%%%%%%%%%%%%%%%%%%

%%%%%%%%%%%%%%%%%%%%%%%%%%%%%%%%%%%%%%%%%%%%%%%%%%%%%%%%%%%%%%%%
%%%%%
% --> 1st data set
disp('1st data set');
disp(' ');

Disp = 30;        Freq = 1.0;
RDisp_all1_1 = RandDispGen(duration, dt, zerotime, ramptime, wnDisp1, Disp, Freq, 1, 'RDisp_all1_1', 1);

Disp = 80;        Freq = 1.5;
RDisp_all1_2 = RandDispGen(duration, dt, zerotime, ramptime, wnDisp2, Disp, Freq, 0, 'RDisp_all1_2', 1);

Disp = 150;        Freq = 0.9;
RDisp_all1_3 = RandDispGen(duration, dt, zerotime, ramptime, wnDisp3, Disp, Freq, 0, 'RDisp_all1_3', 1);
```

```
Disp = 90;        Freq = 0.5;
RDisp_all1_4 = RandDispGen(duration, dt, zerotime, ramptime, wnDisp4, Disp, Freq, 0, 'RDisp_all1_4', 1);

Disp = 200;        Freq = 1.4;
RDisp_all1_5 = RandDispGen(duration, dt, zerotime, ramptime, wnDisp5, Disp, Freq, 0, 'RDisp_all1_5', 1);
%     Concatenate all data
RDisp_all1 = [RDisp_all1_1 RDisp_all1_2 RDisp_all1_3 RDisp_all1_4 RDisp_all1_5];
clear wnDisp1 wnDisp2 wnDisp3 wnDisp4 wnDisp5;
clear RDisp_all1_1 RDisp_all1_2 RDisp_all1_3 RDisp_all1_4 RDisp_all1_5;

ExDispPlot(dt, RDisp_all1, 'R_25_125', 'plot2', 1);

%END EXCERPT FROM RandDisp.m file %%%%%%%%%%%%%%%%%%%%%%%%%%%%%%%%%%%%%%%%%%%%%%%%%%%%%%%%

dispRand = RDisp_all1/1000; %random displacement record in m

timeRand = duration*5;
%END DEFINITION FOR RANDOM DISPLACEMENT DATA %%%%%%%%%%%%%%%%%%%%%%%%%%%%%%%%%%%%%%%%%%%%

totaltime = timeRand;

disp = dispRand;

t = 0:dt:totaltime;
tmax = max(t);
numPts = length(t);
tbegin = 0;


% % determine horizontal velocity using backwards difference method
% % equation from Chapra and Canale 1998 - published in Numerical Methods
% % textbook McGraw-Hill, 1998
% Initialize a vector of velocities with all zeros.  Speeds up
% calculations.
vel = zeros(size(disp));
for i = 5:numPts
   vel(i) = (3*disp(i-4) - 16*disp(i-3) + 36*disp(i-2) - 48*disp(i-1) + 25*disp(i))/(12*dt);
end

% To avoid having the first four velocity values being zero, set them equal
% to the 5th velocity
for i = 1:4
   vel(i) = vel(5);
end

%Values in terms of N and m
%Values from Jankowski (2003) example 2
% HDRB diameter 22.3 cm, axial load = 12.5 tonnes, freq = 0.5 Hz
b1 = 21.239*9.80665*1000;
b2 = 343.10*9.80665*1000;
b3 = -876.70*9.80665*1000;
b4 = 51.829*9.80665*1000;
b5 = 4.3595;
b6 = 58.676*9.80665*1000;
b7 = 3.9664;
b8 = 91.482;
b9 = 1.5377*9.80665*1000;
b10 = 40.868*9.80665*1000;
b11 = 0.13985;

F1 = zeros(size(disp));
F2 = zeros(size(disp));
F = zeros(size(disp));
```

```
    for i = 1:1:numPts
    %Pan and Yang Eq. 1 (Hwang eq. 2)
    F1(i) = (b1 + b2*disp(i)^2 + b3*disp(i)^4 + b4/(cosh(b5*vel(i))^2)…
    + b6/(cosh(b7*vel(i))*cosh(b8*disp(i))))*disp(i);

    %Pan and Yang Eq. 2 (Hwang eq. 3)
    F2(i) = ((b9 + b10*disp(i)^2)/sqrt(b11^2 + vel(i)^2))*vel(i);

    %Pan and Yang Eq. 3 (Hwang eq. 1)
    F(i) = F1(i) + F2(i);
    end

%Convert force values from N to kN
F1(1,:) = F1(1,:)/1000;
F2(1,:) = F2(1,:)/1000;
F(1,:) = F(1,:)/1000;

%Convert disp and vel from m to cm
disp(1,:) = disp(1,:)*100;
vel(1,:) = vel(1,:)*100;

%Ex. 2 bearing
L = 17.65; %height of RB in cm
gamma = disp(1,:)/L; %shear strain cm/cm
diam = 22.3; %diameter in cm
A = pi()*diam^2/4; %area in cm2
tau = F(1,:)/A; %shear stress in kN/cm2
N = 122.6; %vertical load in kN

%Desired vertical pressure is 100 kgf/cm2 = 0.9807 kN/cm2
%'Vertical pressure of this bearing (kN/cm2) = '
stress = N/A;

%Based on this pressure, area of cross-sxn is:
%100 kN vertical load
Q = 100; %kN

A_ideal = Q/stress;

diam_new = 20; %cm

A_new = pi()*diam_new^2/4;

F_new = tau*A_new;
tau_new = F_new/A_new;
disp_new = gamma*L;
gamma_new = disp_new/L;

numPts = length(t);
dt = t(3) - t(2);

% determine horizontal velocity using backwards difference method
% equation from Chapra and Canale 1998 - published in Numerical Methods
% textbook McGraw-Hill, 1998
% Initialize a vector of velocities with all zeros.  Speeds up
% calculations.   % cm/s
vel_new = zeros(size(disp_new));
for i = 5:numPts
    vel_new(i) = (3*disp_new(i-4) - 16*disp_new(i-3) + 36*disp_new(i-2) - 48*disp_new(i-1) + 25*disp_new(i))/(12*dt);
end

% To avoid having the first four velocity values being zero, set them equal
% to the 5th velocity
for i = 1:4
    vel_new(i) = vel_new(5);
end
```

```
% Disp in cm
disp1(1,:) = t(1,:);
disp1(2,:) = disp_new(1,:);

%Vel in cm/s
vel1(1,:) = t(1,:);
vel1(2,:) = vel_new(1,:);

% Force in kN
F1(1,:) = t(1,:);
F1(2,:) = F_new(1,:);

save disp_check_20cm_ex2_MF32_1.mat disp1
save vel_check_20cm_ex2_MF32_1.mat vel1
save force_check_20cm_ex2_MF32_1.mat F1

%  for the input variables, displacement (cm) and velocity (cm/sec)
HDRB_two_inputs_Jankowski_random = readfis('HDRB_two_inputs_Jankowski_ex2_20cmdiam_30cmdisp_MF32_1');

fis_sat_limits = getfis(HDRB_two_inputs_Jankowski_random, 'inrange');
fis_disp_sat_min = fis_sat_limits(1,1)
fis_disp_sat_max = fis_sat_limits(1,2)
fis_vel_sat_min = fis_sat_limits(2,1)
fis_vel_sat_max = fis_sat_limits(2,2)

%End of closed-form solution

sim('checkmodel_rev')

%Results from Simulink
load force_check_FIS.mat % Force in N

time = F_FIS(1,:);
F_fuz = F_FIS(2,:)/1000;

F_exp = F_new(1,:);

eta_t = sqrt(sum((F_exp - F_fuz).^2));
eta_x = sqrt(sum((F_exp - F_fuz).^2.*abs(disp)));
eta_v = sqrt(sum((F_exp - F_fuz).^2.*abs(vel)));

mu_F = mean(F_fuz);

sigma_F = sqrt(sum((F_exp - mu_F).^2));

% Error measured between the fuzzy predicted force and the analytical %model

E_t = eta_t/sigma_F;    % as a function of time
E_x = eta_x/sigma_F;    % as a function of displacement
E_v = eta_v/sigma_F;    % as a function of velocity

Errors = [E_t E_x E_v]
```

checkmodel_rev.mdl

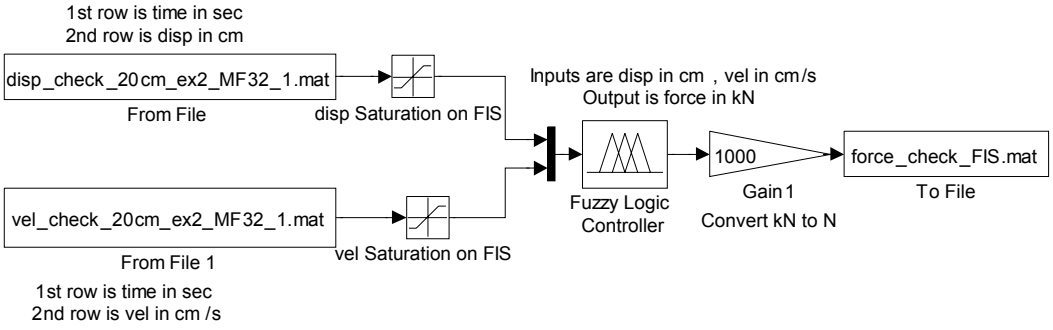
1st row is time in sec
2nd row is disp in cm
disp_check_20cm_ex2_MF32_1.mat
From File
disp Saturation on FIS
Inputs are disp in cm , vel in cm/s
Output is force in kN
1000
Gain1
Convert kN to N
force_check_FIS.mat
To File
Fuzzy Logic
Controller
vel_check_20cm_ex2_MF32_1.mat
From File 1
vel Saturation on FIS
1st row is time in sec
2nd row is vel in cm /s

APPENDIX F

MATLAB CODE FOR DYNAMIC ANALYSIS

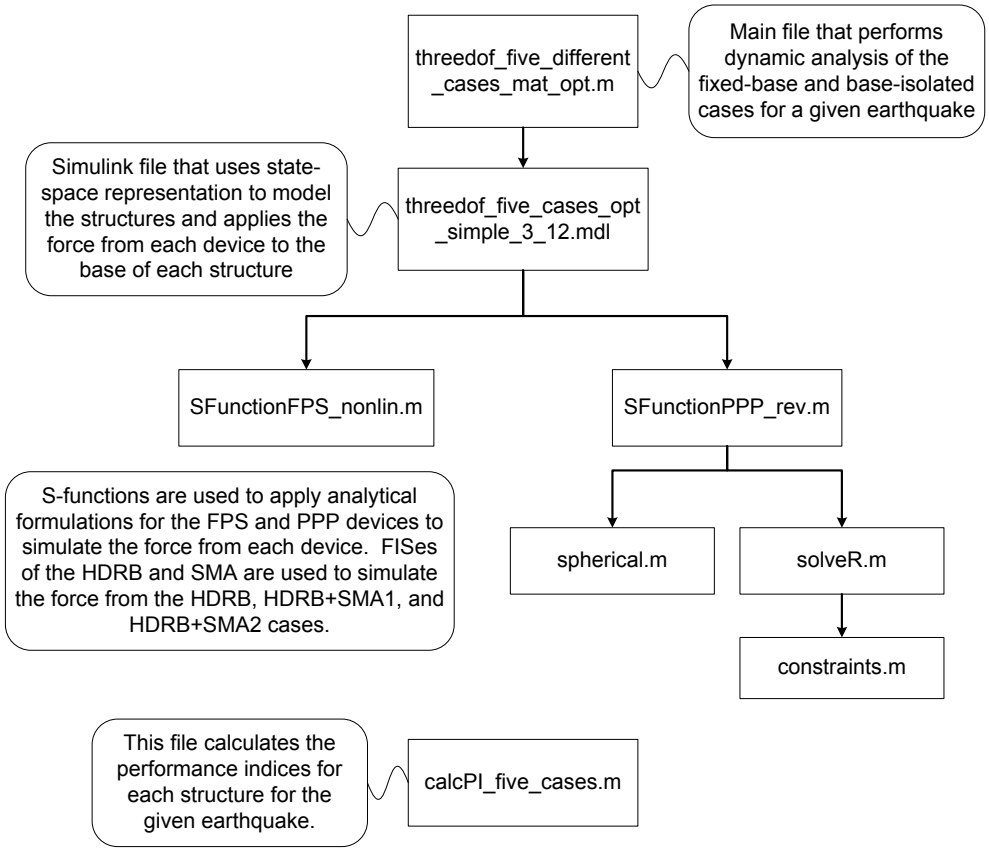

threedof_five_different_cases_mat_opt.m

```
%Written by Rachel Husfeld
%August 2007

%Dynamic analysis of three DOF MODEL of case study structure –
%two-family house
%Performs analysis on FPS, HDRB, HDRB+SMA1, HDRB+SMA2, and PPP cases
%Motion in North-South direction (along longer side of structure)

close all;
clear all

global w5 uc qd drebar QI QD Qi To1 R Lp1 ke1 Qs R1 mu mass_each
global a b c d e
```

```
a = 8 %number of FPS devices
b = 8 %number of HDRB
c = 8 %number of HDRB+SMA1
d = 8 %number of HDRB+SMA2
   f = 4; %number of braces in HDRB+SMA2
e = 8 %number of PPP

%Mass matrix is the same for uncontrolled and controlled cases
%Lumped mass matrix
mb = 27018; %kg %slab-on-grade INCLUDING 25% of live load
m1 = 40711; %kg %first floor slab level
m2 = 16148; %kg %roof diaphragm level
massvec = [mb;m1;m2];
m = [mb 0 0; 0 m1 0; 0 0 m2];

%Controlled case %%%%%%%%%%%%%%%%%%%%%%%%%%%%%%%%%%%%%%%%%%%%%%%%%%%%%
%Stiffness matrix
kb = 0; %N/m %given stiffness to represent 3DOF model
% see solve_stiffnesses.m program
k1 = 433009236; %N/m
k2 = 323999918; %N/m
k = [kb+k1 -k1 0; -k1 k1+k2 -k2; 0 -k2 k2];

%Damping matrix
%USE STIFFNESS PROPORTIONAL DAMPING to avoid contribution of base to
%damping of structure
zeta = 0.0382; %percent damping from structure for mode 1
w1 = 0.5*2*pi; %rad/sec based on Tiso = 2 sec desired
beta = 2*zeta/w1;
damping = beta*k;

%Define state space matrices A,B,C,D
nDOF = 3;
A = [zeros(nDOF) eye(nDOF); -inv(m)*k -inv(m)*damping];
B = [zeros(nDOF); inv(m)];
C = [eye(nDOF) zeros(nDOF); zeros(nDOF) eye(nDOF); -inv(m)*k -inv(m)*damping];
D = [zeros(nDOF); zeros(nDOF); inv(m)];
%End definition of controlled case %%%%%%%%%%%%%%%%%%%%%%%%%%%%%%%%%%

%Uncontrolled case 2DOF- existing construction %%%%%%%%%%%%%%%%%%%%%%

massvecuc = [m1;m2];

%Stiffness matrix
%Use 2DOF model
k1uc = 433009236; %N/m
k2uc = 323999918; %N/m
kuncontrolled = [k1uc+k2uc -k2uc; -k2uc k2uc];

%Damping matrix - Stiffness proportional damping
muc = [m1 0; 0 m2];
zeta1 = 0.0382; %percent damping from structure for mode 1
w1uc = 81.68; %rad/sec From microvibration testing
betauc = 2*zeta1/w1uc;
damping_uncont = betauc*kuncontrolled;

%Define state space matrices
nDOF = 2;
Auc = [zeros(nDOF) eye(nDOF); -inv(muc)*kuncontrolled -inv(muc)*damping_uncont];
Buc = [zeros(nDOF); inv(muc)];
Cuc = [eye(nDOF) zeros(nDOF); zeros(nDOF) eye(nDOF); -inv(muc)*kuncontrolled -inv(muc)*damping_uncont];
Duc = [zeros(nDOF); zeros(nDOF); inv(muc)];
%End definition of uncontrolled case %%%%%%%%%%%%%%%%%%%%%%%%%%%%%%%

%%%%%%%%%%%%%%%%%%%%%%%%%%%%%%%%%%%%%%%%%%%%%%%%%%%%%%%%%%%%%%%%
%%%%
%Parameters for FPS S-function%%%%%%%%%%%%%%%%%%%%%%%%%%%%%%%%%%%%%%
```

```
R1 = 3.5; %radius of curvature in meters
mu = 0.03; %coefficient of friction (decimal form)
mass_each = 84/a; %mass on each bearing

%%%%%%%%%%%%%%%%%%%%%%%%%%%%%%%%%%%%%%%%%%%%%%%%%%%%%%%%%%%%%%%%
%%%%
%Parameters for HDRB%%%%%%%%%%%%%%%%%%%%%%%%%%%%%%%%%%%%%%%%%%%%%%%
%Jankowski ex. 2, 30 cm displacement, 20 cm diameter HDRB (scaled)
fismat2 = readfis('HDRB_two_inputs_Jankowski_ex2_20cmdiam_30cmdisp_MF32_1.fis');

% Get limits of saturation for fuzzy model of the HDRB
% These are equivalent to the extreme limits of the universes of
% discourse
% for the input variables, displacement (cm) and velocity (cm/sec)
fis2_sat_limits       = getfis (fismat2, 'inrange');
fis2_disp_sat_min = fis2_sat_limits(1,1)*(1/100) %convert cm to m
fis2_disp_sat_max = fis2_sat_limits(1,2)*(1/100) %convert cm to m
fis2_vel_sat_min = fis2_sat_limits(2,1)*(1/100) %convert cm/s to m/s
fis2_vel_sat_max   = fis2_sat_limits(2,2)*(1/100) %convert cm/s to m/s

%%%%%%%%%%%%%%%%%%%%%%%%%%%%%%%%%%%%%%%%%%%%%%%%%%%%%%%%%%%%%%%%
%%%%%
%Read SMA FIS  - 1 mm diameter Nitinol, AERO Lab testing
%  Inputs are strain (decimal),  strain rate (decimal)
%  Output is Stress (MPa)
fismat3 = readfis('SMA_Nitinol_2sided.fis');

%Parameters for HDRB+SMA1 (SMA connected diagonally in individual
%bearing)
diam_wire = 1; %diameter of each wire (mm)
height = 0.1765; %(m) height of bearing

width = 0.25; %(m) horizontal dimension of connected SMA
            %(larger than diam of bearing due to cover plates)
numwires = 60; %number of SMA wires in each diagonal

alpha = atan(height/width); %angle of SMA in radians
L = sqrt(height^2 + width^2); %length of wire (m)

%%%%%%%%%%%%%%%%%%%%%%%%%%%%%%%%%%%%%%%%%%%%%%%%%%%%%%%%%%%%%%%%
%%%%
%Parameters for HDRB+SMA2 case (Adjacent HDRBs connected by SMA)
diam_wire2 = 1; %diameter of each wire (mm)
width2 = 4.5; %(m) horizontal dimension
height2 = 0.1765; %(m) height of bearing
beta = atan(height2/width2); %angle of SMA in radians
Ltot = sqrt(height2^2 + width2^2); %total length of diagonal

numwires2 = 40; %number of SMA wires in each diagonal
L2 = 4; %(m) %length of SMA wire in diagonal

Lrigid = Ltot - L2; %total length of rigid elements

% Get limits of saturation for fuzzy model of the SMA FIS
% These are equivalent to the extreme limits of the universes of
% discourse
% for the input variables, strain and strain rate (both in decimal
% form)
fis3_sat_limits       = getfis (fismat3, 'inrange');
fis3_disp_sat_min  = fis3_sat_limits(1,1)
fis3_disp_sat_max = fis3_sat_limits(1,2)
fis3_vel_sat_min    = fis3_sat_limits(2,1)
fis3_vel_sat_max   = fis3_sat_limits(2,2)

%%%%%%%%%%%%%%%%%%%%%%%%%%%%%%%%%%%%%%%%%%%%%%%%%%%%%%%%%%%%%%%%
%%
```

```
% Parameters for PPP %%%%%%%%%%%%%%%%%%%%%%%%%%%%%%%%%%%%%%%%%%%%%%%%
Qs = -84/e; %tonf : vertical applied load on each PPP

To1 = 7.4; %tonf initial prestress in central cable
R = 50; %cm radius of top and bottom spherical rolling surfaces
Lp1 = 165; %cm length of pile
ke1 = 10.6; %tonf/cm elastic stiffness of cable
drebar = 3.6; %cm diameter of each rebar in base

%Geometry of top (U) rolling surface
shapeU = 'spherical';
ParamU = [R]; %radius R (cm)

%Geometry of bottom (D) rolling surface
shapeD = 'spherical';
ParamD = [R];

%Set up matrices for dependent and independent force vectors
QD = [];
QI = [];

Lp = Lp1;
To = To1;
ke = ke1;

%Give PPP an initial value
rec(1) = 0.00001;
rec(2) = 0.00002;
qi = [rec(1); 0; 0; 0; 0];
%for first displacement value, solveR makes initial guess for qd
qi_ant = 2*qi - [rec(2); 0; 0; 0; 0];
[qd,Qi] = solveR(qi,qi_ant,Qs,Lp,shapeU,ParamU,shapeD,ParamD,ke,To);

QD = [qd];
QI = [Qi];

%%%%%%%%%%%%%%%%%%%%%%%%%%%%%%%%%%%%%%%%%%%%%%%%%%%%%%%%%%%%%%%%%%%%
%
%Time definition for use in Simulink
%Load earthquake acceleration-time history
load eq1981_LPAN_1p0

eq_mat_file = eq_accel;

save eq eq_mat_file

dt = eq_mat_file(1,3)-eq_mat_file(1,2);

tbegin = min(eq_mat_file(1,:))+dt;
tend = max(eq_mat_file(1,:));

%Time step for Simulink simulation
delt = 0.0029; %sec
t = tbegin:delt:tend;

%Start Simulink model
sim('threedof_five_cases_opt_simple_3_12')

%Load solution from Simulink
load('mdof_general')
load('mdof_general_fps2')
load('mdof_general_fps3')
load('mdof_general_fps4')
load('mdof_general_fps5')
load('mdof_general_uc')
load strain.mat
```

```
load strain2.mat
load stress.mat
load stress2.mat
load strainrate.mat
load strainrate2.mat
```

threedof_five_cases_opt_simple_3_12.mdl

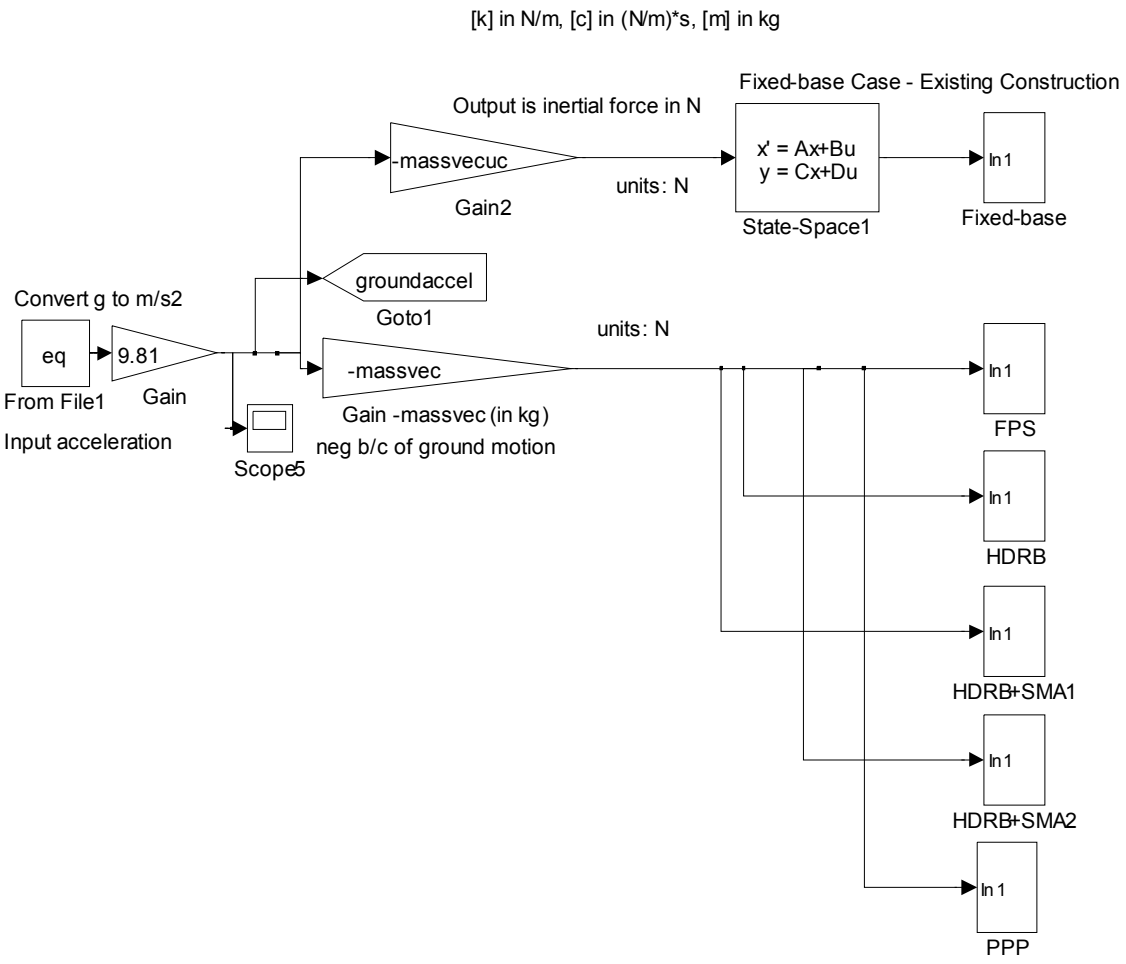

threedof_five_cases_opt_simple_3_12/Fixed-base

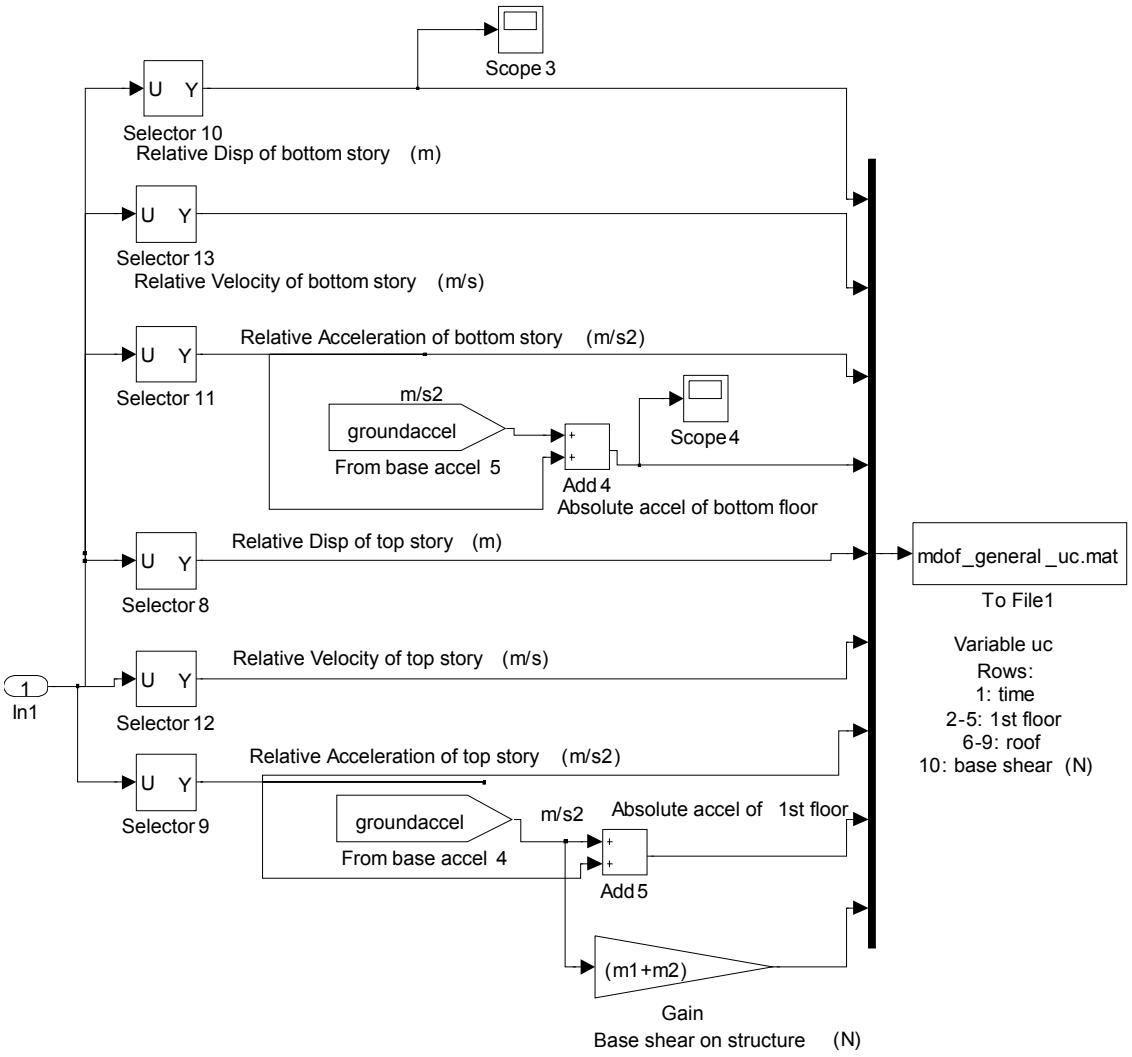

threedof_five_cases_opt_simple_3_12/FPS

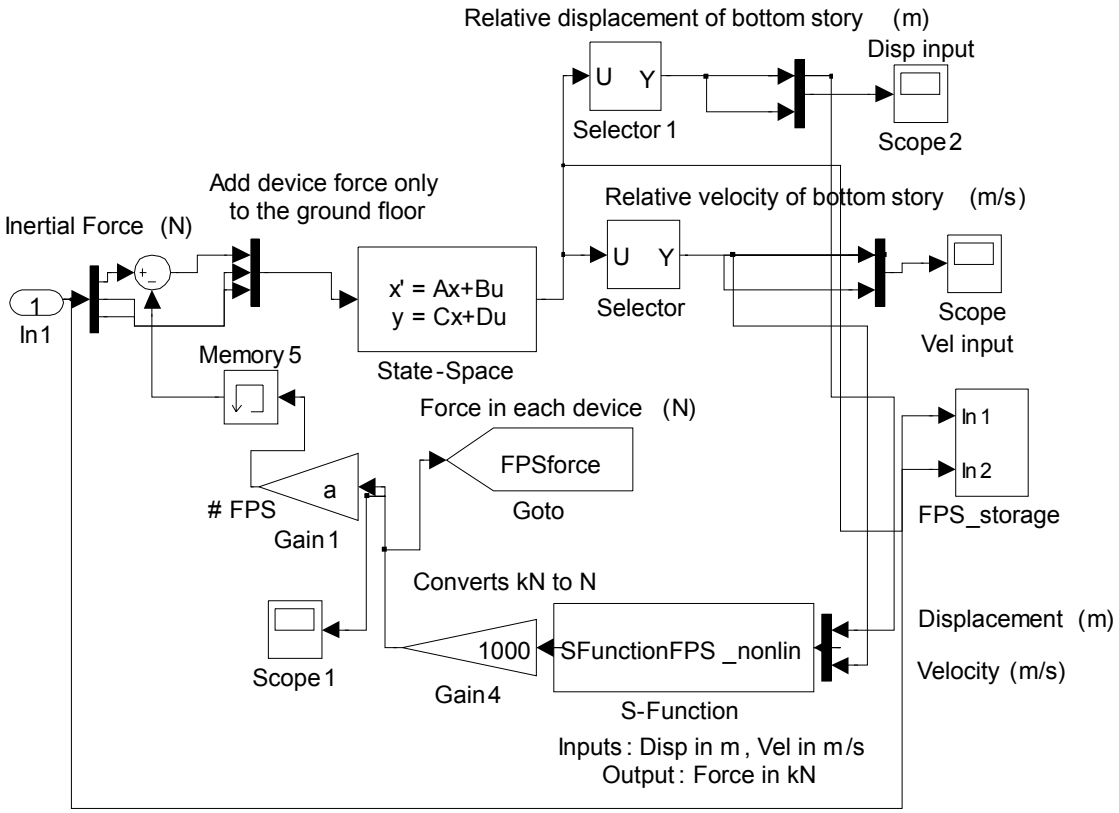

threedof_five_cases_opt_simple_3_12/FPS/FPS_storage

Note: This storage subsystem is typical for each of the isolation devices.

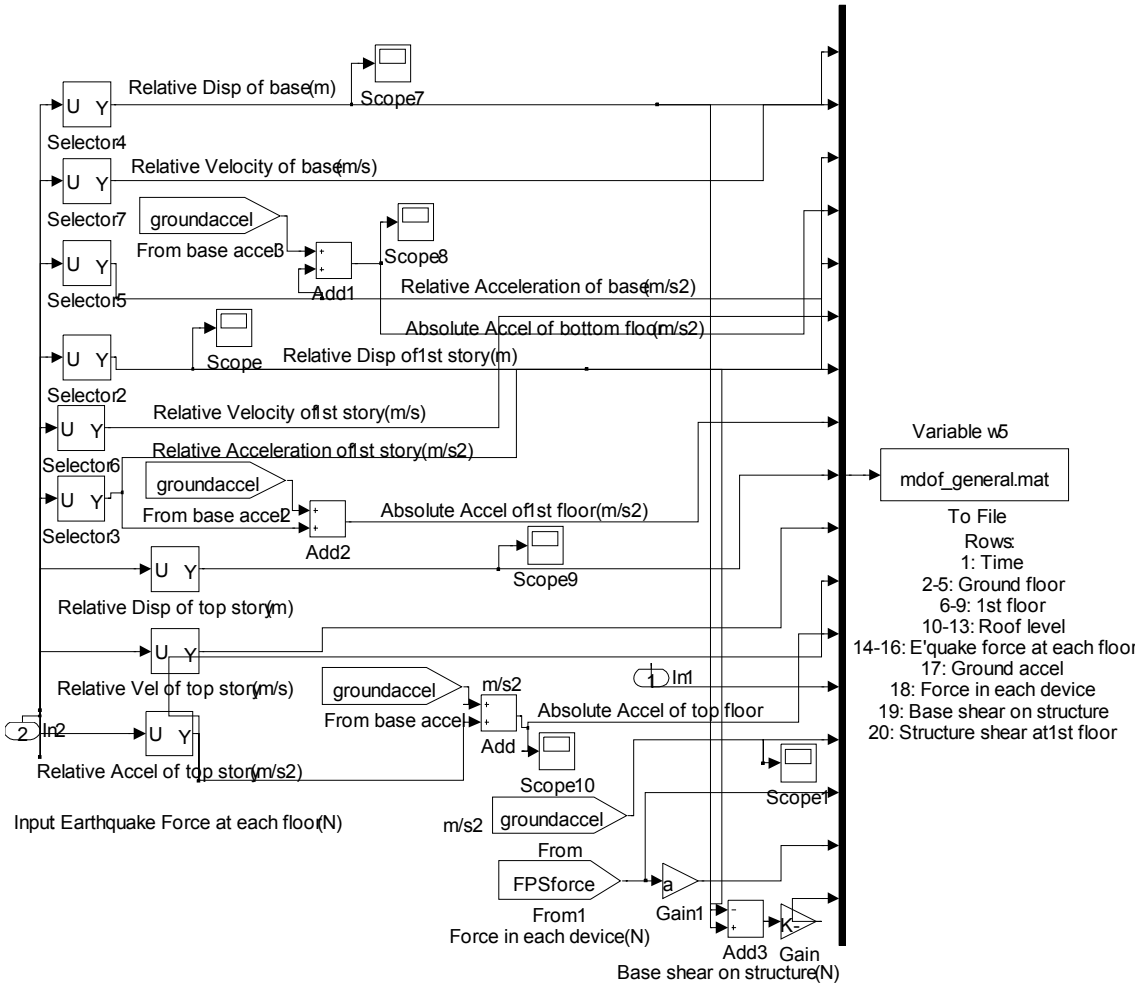

threedof_five_cases_opt_simple_3_12/HDRB

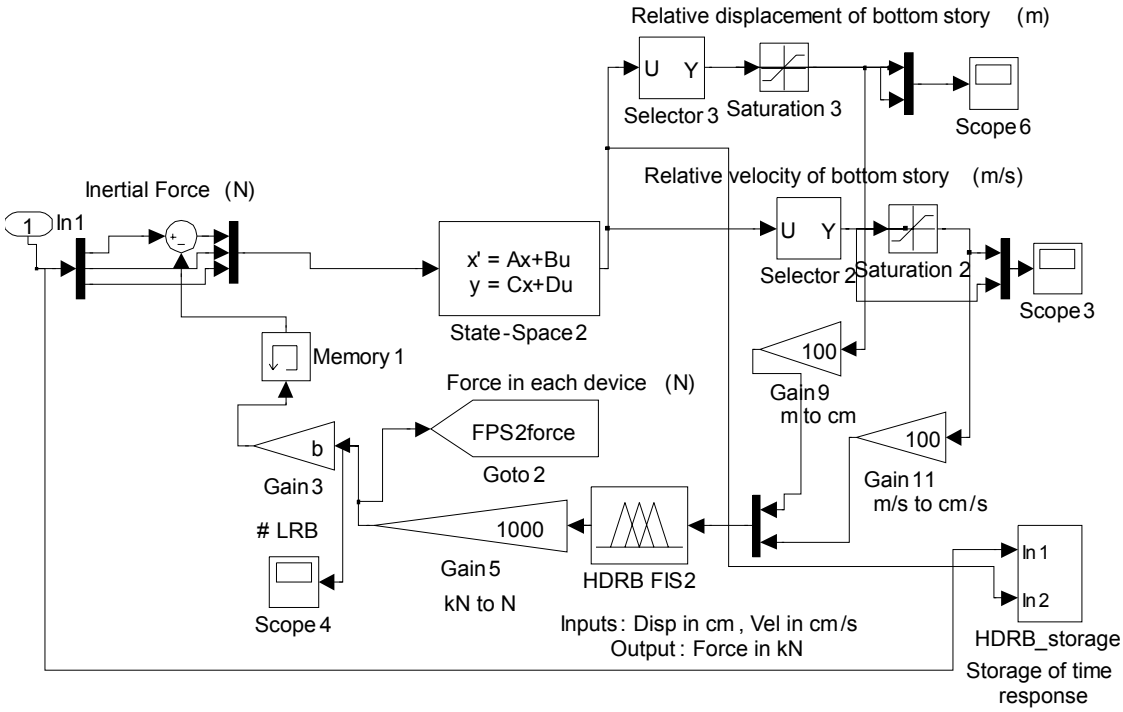

threedof_five_cases_opt_simple_3_12/HDRB+SMA1

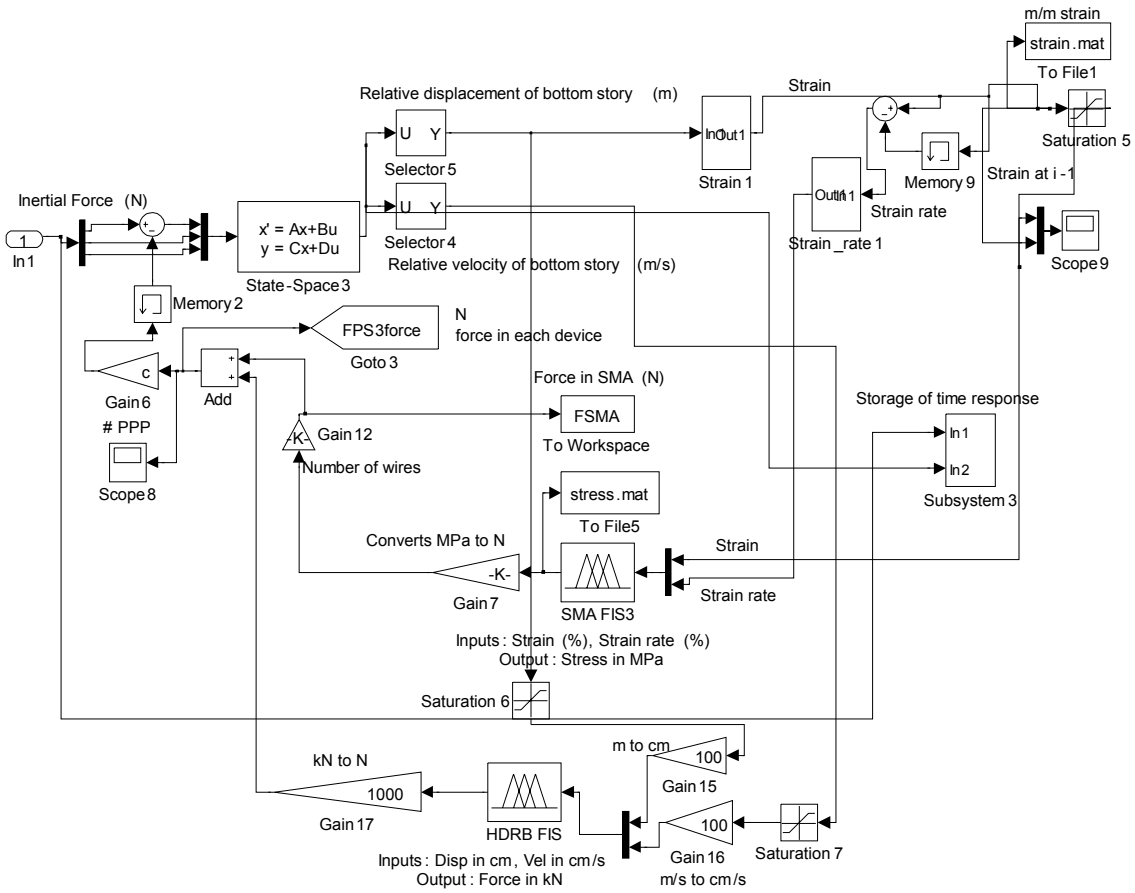

threedof_five_cases_opt_simple_3_12/HDRB+SMA1/Strain1

Note: This strain calculation subsystem is typical for the HDRB+SMA1 and HDRB+SMA2 isolation systems.

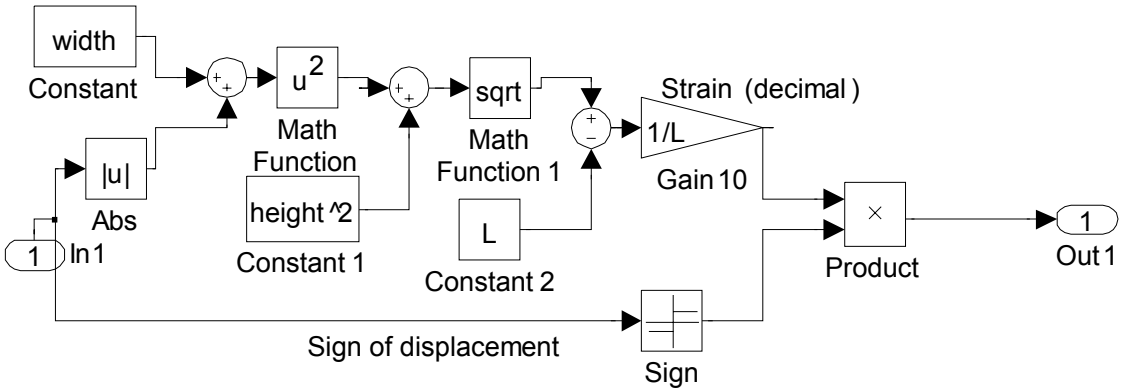

threedof_five_cases_opt_simple_3_12/ HDRB+SMA1/Strain_rate1

Note: This strain rate calculation subsystem is typical for the HDRB+SMA1 and HDRB+SMA2 isolation systems.

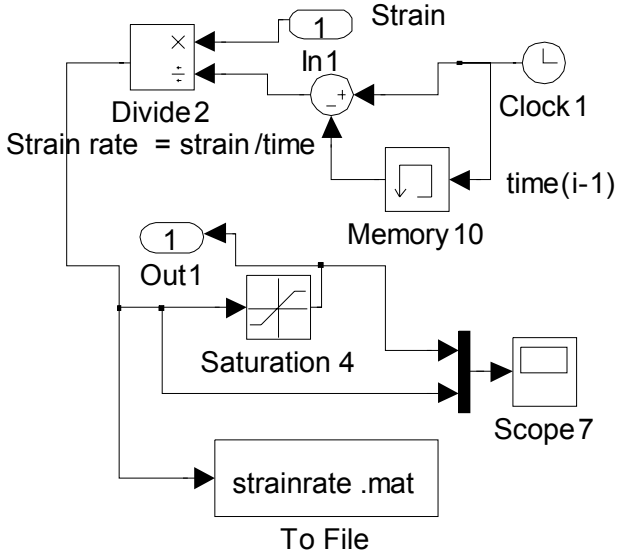

threedof_five_cases_opt_simple_3_12/ HDRB+SMA2

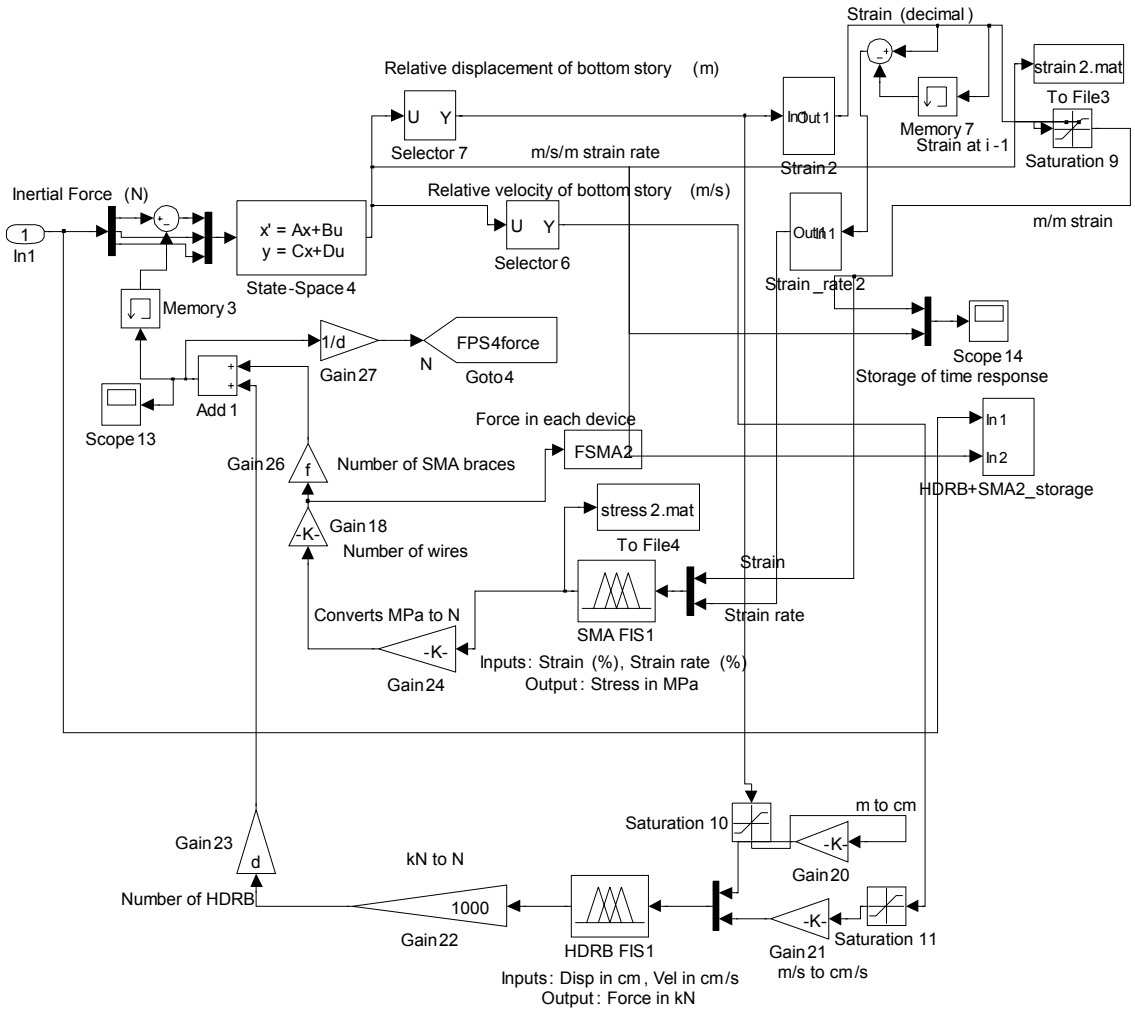

threedof_five_cases_opt_simple_3_12/PPP

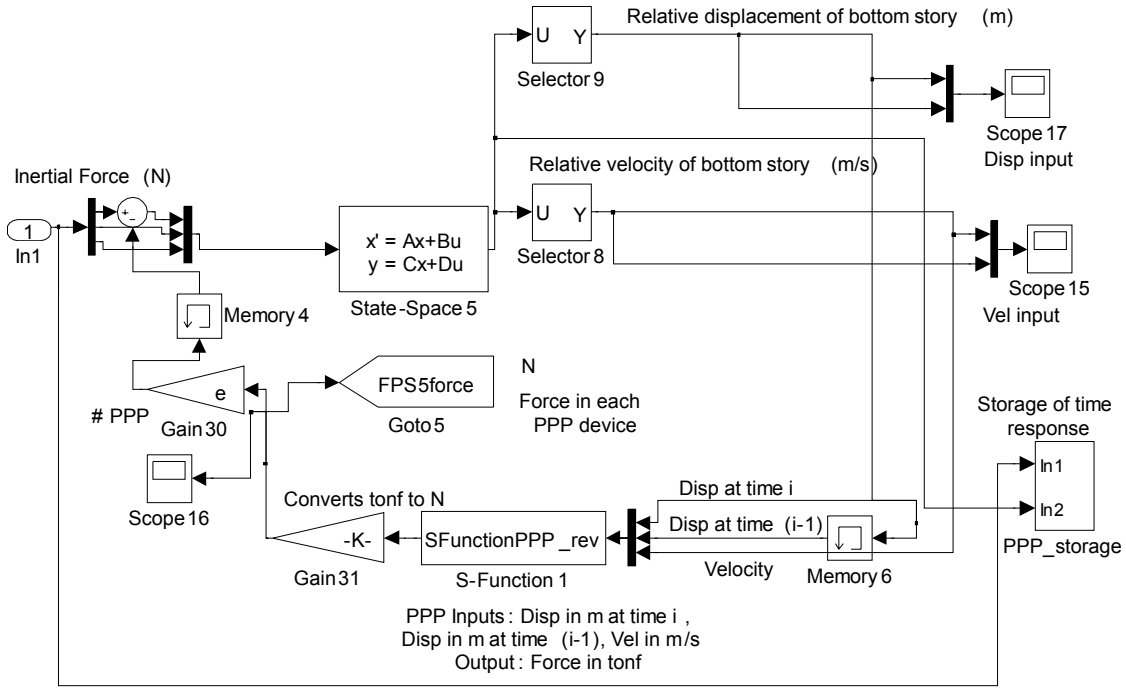

SFunctionFPS_nonlin.m

```
function [sys,x0,str,ts] = SFunctionFPS_nonlin(t,x,u,flag)
%
%   Created 12 January 2002.  Prof. Roschke
%   Modified 20 November 2007 RLH

%   This S-Function works with a Simulink file that is named
%   "threedof_five_cases_opt_simple_3_12.mdl"
%
%   Input variables are called u(1), u(2) - disp and velocity at base
%   Output force from this S-Function is returned to the Simulink file
%   through the variable "sys" (see below).

% Dispatch the flag. The switch function controls the calls to
% S-function routines at each simulation stage.
switch flag,
  case 0
    [sys,x0,str,ts] = mdlInitializeSizes; % Initialization
  case 3
    sys = mdlOutputs(t,x,u); % Calculate outputs
  case { 1, 2, 4, 9 }
    sys = []; % Unused flags
  otherwise
    error(['Unhandled flag = ',num2str(flag)]); % Error handling
end;
% Below are the S-function subroutines
%=============================================================
%          mdlDerivatives
%=============================================================
```

```
function sys=mdlDerivatives(t,x,u)
% Compute derivatives of continuous states
sys = [];
%=============================================================
%           mdlUpdate
%=============================================================
function sys=mdlUpdate(t,x,u)
% Compute update for discrete states. If necessary, check for
% sample time hits.
sys = [];   % Empty since this model has no discrete states.

%=============================================================
% Function mdlInitializeSizes initializes the states, sample
% times, state ordering strings (str), and sizes structure.
%=============================================================
function [sys,x0,str,ts] = mdlInitializeSizes
% Call function simsizes to create the sizes structure.
sizes = simsizes;
% Load the sizes structure with the initialization information.
sizes.NumContStates= 0;
sizes.NumDiscStates= 0;
sizes.NumOutputs=    1;
sizes.NumInputs=     2; %%%%%%%%%%%%%%%%%%
sizes.DirFeedthrough=1;
sizes.NumSampleTimes=1;
% Load the sys vector with the sizes information.
sys = simsizes(sizes);
%
x0 = []; % No continuous states
%
str = []; % No state ordering
%
ts = [-1 0]; % Inherited sample time
% End of mdlInitializeSizes.
%=============================================================
% Function mdlOutputs performs the calculations desired by the user.
%=============================================================
function sys = mdlOutputs(t,x,u)

global R1 mu mass_each

R = R1;

radius = R; %radius of curvature in meters
coeff_friction = mu; %coeff of friction in decimal form

% Define the gravity constant (m/s^2)
gravity = 9.80665 ;

% Compute the weight (kN)
weight = mass_each * gravity ;

xdisp = u(1); %m
xvel = u(2); % m/s2

% Compute the nonlinear horizontal force acting on the FPS required to % give equilibrium
numerator = xdisp + sign(xvel) * coeff_friction * (radius^2 -xdisp^2)^0.5 ;
denominator = (radius^2 - xdisp^2)^0.5 - sign(xvel) * coeff_friction * xdisp ;
force_nonlin = weight * (numerator / denominator) ;

sys = force_nonlin;

% End of mdlOutputs.
%
%=============================================================
%           mdlGetTimeOfNextVarHit
```

```
%=============================================================
function sys=mdlGetTimeOfNextVarHit(t,x,u)
% Return the time of the next hit for this block. Note that
% the result is absolute time.  Note that this fuction is
% only used when you specify a Variable discrete-time sample
% time [-2 0] in the sample time array in sampleTime = 1;
sys = [];
%=============================================================
%           mdlTerminate
%=============================================================
function sys=mdlTerminate(t,x,u)
% perform any necessary tasks at the end of the simulation
sys = [];
```

SFunctionPPP_rev.m

```
function [sys,x0,str,ts] = SFunctionPPP_rev(t,x,u,flag)
%
%   S-function format created 12 January 2002.  Prof. Roschke
%   Modified for PPP device 20 November 2007 RLH
%   Modified 6 December 2007 RLH

%   This S-Function works with a Simulink file that is named
%   "threedof_five_cases_opt_simple_3_12.mdl"
%
%   Input variables are called u(1), u(2), u(3) - disp(i), disp(i-1),
%   and vel(i) at base
%   Output force from this S-Function is returned to the Simulink file
%   through the variable "sys" (see below).

% Dispatch the flag. The switch function controls the calls to
% S-function routines at each simulation stage.
switch flag,
  case 0
    [sys,x0,str,ts] = mdlInitializeSizes; % Initialization
  case 3
    sys = mdlOutputs(t,x,u); % Calculate outputs
  case { 1, 2, 4, 9 }
    sys = []; % Unused flags
  otherwise
    error(['Unhandled flag = ',num2str(flag)]); % Error handling
end;
% Below are the S-function subroutines
%=============================================================
%           mdlDerivatives
%=============================================================
function sys=mdlDerivatives(t,x,u)
% Compute derivatives of continuous states
sys = [];
%=============================================================
%           mdlUpdate
%=============================================================
function sys=mdlUpdate(t,x,u)
% Compute update for discrete states. If necessary, check for
% sample time hits.
sys = [];   % Empty since this model has no discrete states.

%=============================================================
% Function mdlInitializeSizes initializes the states, sample
% times, state ordering strings (str), and sizes structure.
%=============================================================
function [sys,x0,str,ts] = mdlInitializeSizes
% Call function simsizes to create the sizes structure.
sizes = simsizes;
% Load the sizes structure with the initialization information.
```

```
sizes.NumContStates= 0;
sizes.NumDiscStates= 0;
sizes.NumOutputs=    1;
sizes.NumInputs=     3; %%%%%%%%%%%%%%%%
sizes.DirFeedthrough=1;
sizes.NumSampleTimes=1;
% Load the sys vector with the sizes information.
sys = simsizes(sizes);
%
x0 = []; % No continuous states
%
str = []; % No state ordering
%
ts = [-1 0]; % Inherited sample time
% End of mdlInitializeSizes.
%==============================================================
% Function mdlOutputs performs the calculations desired by the user.
%==============================================================
function sys = mdlOutputs(t,x,u)

global qd QI QD Qi To1 R Lp1 ke1 Qs

%Based on main.m file for PPP originally from de la Llera

%Geometry of top (U) rolling surface
shapeU = 'spherical';
ParamU = [R]; %radius R (cm)

%Geometry of bottom (D) rolling surface
shapeD = 'spherical';
ParamD = [R];

rec(2) = u(1)*100; %horizontal displacement of top of PPP (cm) at time(i)
rec(1) = u(2)*100; %horizontal displacement of top of PPP (cm) at time(i-1)

vel(1) = u(3)*100; %velocity at time(i) in cm/s

%To prevent complex numbers
if rec(2)==0 && rec(1)==0
    rec(1) = 0.00001;
    rec(2) = 0.00002;
end

Lp = Lp1;
To = To1;
ke = ke1;

%Calculate force vectors for the displacement value
%Independent coordinate vector - see Eq. 1 (Pinochet et al. 2006)
%Subject device to initial horizontal displacement
qi = [rec(2); 0; 0; 0; 0];

%Call solveR function
qi_ant = [rec(2-1); 0; 0; 0; 0]; %Uses previous value of force
[qd,Qi] = solveR(qi,qi_ant,Qs,Lp,shapeU,ParamU,shapeD,ParamD,ke,To,qd);

%Store dependent and independent force and coordinate vectors
QD = [qd];
QI = [Qi];

%%%%%%%%%%%%%%%%%%%%%%%%%%%%%%%%%%%%%%%%%%%%%%%%%%%%%%%%%%%%%%%%
%%%%%
%The following accounts for friction between PS cable and duct
%(Besa et al. 2008 change #3)

%Calculate change in length of PS cable
```

```
delta = 2*((rec(2)-QD(5,1)).^2+(QD(1,1)-QD(6,1)).^2).^.5;

%Calculate tension in PS cable for each value of displacement
T = ke*delta + To;

%Prevent complex numbers
if (QD(1,1)-QD(6,1)) == 0
   QD(6,1) = QD(6,1) - 0.0000001;
end

%Calculate angle of the cable with respect to the vertical
phis = atan((rec(2)-QD(5,1))./(QD(1,1)-QD(6,1)));

%Calculate normal force at contact point of top capital
Ns(1,1) = T(1,1)*cos(phis(1,1));

%Corrective friction coefficient = 1.8%
mu = 0.018;

qdot = vel;

%Force corrected by taking friction between PS cable and duct into account
Fcorr(1,1) = QI(1,1) + mu*Ns(1,1)*sign(qdot(1,1));

%Force is the output (in tonf)
Force = Fcorr(1,1);
sys = Force;
% End of mdlOutputs.
%
%=============================================================
%           mdlGetTimeOfNextVarHit
%=============================================================
function sys=mdlGetTimeOfNextVarHit(t,x,u)
% Return the time of the next hit for this block. Note that
% the result is absolute time.  Note that this fuction is
% only used when you specify a Variable discrete-time sample
% time [-2 0] in the sample time array in sampleTime = 1;
sys = [];
%=============================================================
%           mdlTerminate
%=============================================================
function sys=mdlTerminate(t,x,u)
% perform any necessary tasks at the end of the simulation
sys = [];
```

spherical.m

```
% Written by J. Pinochet (2006)
% [r,rp,rpp,Arc] = spherical(Param,psi)
%
% DESCRIPTION:  Defines the spherical ending shape of radius 'r'
%               for a polar angle 'psi'.
%
% INPUT:   Param    = shape parameters = [R]
%            R      = spherical ending radius
%          psi      = angle (not used in this shape)
%
% OUTPUT:   r       = radius for an angle 'psi'
%          rp       = Derivative of the radius for an angle 'psi'
%          rpp      = Second derivative of the radius for an
%                     angle 'psi'
%          Arc      = Rolled arc from 0 to 'psi'
% ------------------------------------------------------------------
function [r,rp,rpp,Arc] = spherical(Param,psi)
```

```
% Extract parameters
R = Param(1);

% Define ending shape
r = R;
rp = 0;
rpp = 0;
Arc = R*psi;

return
```

solveR.m

```
% Written by J. Pinochet (2006)
% Modified by R. Husfeld 2008

% This file follows the analytical formulation for the PPP device
% described by Pinochet et al. (2006)

% [qd, Qi] = solveR(qi,Qs,Lp,shapeU,ParamU,shapeD,ParamD,ke,qd0)
%
% DESCRIPTION:  Solves the 'prestressed rod' state to obtain the
%               dependent dofs values and the independent dofs
%               forces.
%
% INPUT:    qi      = Independent dof values
%           Qs      = Known external force
%           Lp      = Total rod length
%           shapeU  = 'Up' (or top) ending shape function name
%           ParamU  = 'Up' (or top) ending shape parameters
%           shapeD  = 'Down' (bottom) ending shape function name
%           ParamD  = 'Down' (bottom) ending shape parameters
%           ke      = Elastic element stiffness
%           [qd0]   = Initial dependent dofs value for iteration
%
% OUTPUT:   qd      = Dependent dofs values
%           Qi      = Independent dofs forces
% ------------------------------------------------------------------

function [qd, Qi] = solveR(qi,qi_ant,Qs,Lp,shapeU,ParamU,shapeD,ParamD,ke,To,qd0)

global drebar
global qd QD QI Qi

narg = nargin;

% Independent variables initialization
xsu = qi(1);
thsu = qi(2);
xsd = qi(3);
ysd = qi(4);
thsd = qi(5);

% Dependent variables initial aproximation if not defined
if narg < 11
   ysu = ysd+Lp;
   xp = (xsu+xsd)/2;
   yp = (ysu+ysd)/2;
   thp = atan((xsd-xsu)/Lp);
   xeu = xsu;
   yeu = ysu;
   theu = thp;
   xed = xsd;
   yed = ysd;
   thed = thp;
```

```
    lu = thp;
    psiu = thp;
    ld =thp;
    psid = thp;
    qd0 = [ysu, xp, yp, thp, xeu, yeu, theu, xed, yed, thed, lu, psiu, ld, psid]';
end

% Find qd from constraints using Newton's Method.
qd = qd0;
[PHI,PHI_qi,PHI_qd] = constraints(qi,qd,Lp,shapeU,ParamU,shapeD,ParamD);

%tol = Lp*1e-8;
%Made tolerance larger
tol = Lp*1e-5;

%Iterate until shape parameters/position are accurate
err = tol+1;
while err>tol
    qd = qd-PHI_qd\PHI;
    qd(4) = atan(tan(qd(4)));
    qd(7) = atan(tan(qd(7)));
    qd(10) = atan(tan(qd(10)));
    qd(12) = atan(tan(qd(12)));
    qd(14) = atan(tan(qd(14)));
    [PHI,PHI_qi,PHI_qd] = constraints(qi,qd,Lp,shapeU,ParamU,shapeD,ParamD);
    err = norm(PHI);
end

% Potential energy Jacobian
ysu = qd(1);
xeu = qd(5);
yeu = qd(6);
xed = qd(8);
yed = qd(9);
deltaU = sqrt((xsu-xeu)^2+(ysu-yeu)^2);
deltaD = sqrt((xsd-xed)^2+(ysd-yed)^2);
V_qi = [ke*(xsu-xeu)*(1+deltaD/deltaU)+To*(xsu-xeu)/deltaU;
        0;
        ke*(xsd-xed)*(1+deltaU/deltaD)+To*(xsd-xed)/deltaD;
        ke*(ysd-yed)*(1+deltaU/deltaD)+To*(ysd-yed)/deltaD;
        0];
V_qd = [ke*(ysu-yeu)*(1+deltaD/deltaU)+To*(ysu-yeu)/deltaU;
        0; 0; 0;
        -ke*(xsu-xeu)*(1+deltaD/deltaU)-To*(xsu-xeu)/deltaU;
        -ke*(ysu-yeu)*(1+deltaD/deltaU)-To*(ysu-yeu)/deltaU;
        0;
        -ke*(xsd-xed)*(1+deltaU/deltaD)-To*(xsd-xed)/deltaD;
        -ke*(ysd-yed)*(1+deltaU/deltaD)-To*(ysd-yed)/deltaD;
        0; 0; 0; 0; 0];

%The following is to avoid the occurrence of complex numbers
TestVqi = isnan(V_qi);

if TestVqi(1,1) ==1
    V_qi(1,1) = 0;
end

if TestVqi(3,1) ==1
    V_qi(3,1) = 0;
end

if TestVqi(4,1) ==1
    V_qi(4,1) = 0;
end

TestVqd = isnan(V_qd);
```

```
if TestVqd(1,1) ==1
   V_qd(1,1) = 0;
end

if TestVqd(5,1) ==1
   V_qd(5,1) = 0;
end

if TestVqd(6,1) ==1
   V_qd(6,1) = 0;
end

if TestVqd(8,1) ==1
   V_qd(8,1) = 0;
end

if TestVqd(9,1) ==1
   V_qd(9,1) = 0;
end

% Vector of external forces
Qd = [Qs zeros(1,13)]';

% Vector of inelastic forces - see equation (15) in Pinochet paper
% Fp : dissipative forces due to rebar yielding
Arebar = (pi*(drebar^2))/4; %cm^2
fy = 2.4; %tonf/cm2
Fp = Arebar*fy; %tonf - This is the yield force for ONE rebar
fn = Fp*[1; 1]*sign((qi(1)-qi_ant(1))*qi(1));
G_qi = zeros(2,5);
G_qd = zeros(2,14);

%Eccentricity (d) of the ductile rebars
d = 5; %cm

thed = qd(10);

% Extension of the bars
delt1 = sqrt((xed-d*cos(thed)-xsd+d*cos(thsd))^2+(yed-d*sin(thed)-ysd+d*sin(thsd))^2);
delt2 = sqrt((xed+d*cos(thed)-xsd-d*cos(thsd))^2+(yed+d*sin(thed)-ysd-d*sin(thsd))^2);

% Jacobian of G relative to the independent coordinates
G_qi = zeros(2,5); %added this from genforset.m
G_qi(1,3) = -(xed-d*cos(thed)-xsd+d*cos(thsd))/delt1;
G_qi(2,3) = -(xed+d*cos(thed)-xsd-d*cos(thsd))/delt2;
G_qi(1,4) = -(yed-d*sin(thed)-ysd+d*sin(thsd))/delt1;
G_qi(2,4) = -(yed+d*sin(thed)-ysd-d*sin(thsd))/delt2;
G_qi(1,5) = -G_qi(1,3)*d*sin(thsd)+G_qi(1,4)*d*cos(thsd);
G_qi(2,5) = G_qi(2,3)*d*sin(thsd)-G_qi(2,4)*d*cos(thsd);

% Jacobian of G relative to the dependent coordinates
G_qd = zeros(2,14); %added this from genforset.m
G_qd(1,8) = -G_qi(1,3);
G_qd(2,8) = -G_qi(2,3);
G_qd(1,9) = -G_qi(1,4);
G_qd(2,9) = -G_qi(2,4);
G_qd(1,10) = G_qd(1,8)*d*sin(thed)-G_qd(1,9)*d*cos(thed);
G_qd(2,10) = -G_qd(1,8)*d*sin(thed)+G_qd(1,9)*d*cos(thed);

%%%%%%%%%%%%%%%%%%%%%%%%%%%%%%%%%%%%%%%%%%%%%%%%%%%%%%%%%%%%%%%%%%%%%%%%
%%%%%
% Code added to avoid the singular matrix error in calculating Qi
[m,n] = size(PHI_qd);

for i=1:1:m
```

```
   for j=1:1:n
     if PHI_qd(i,j)==0
         PHI_qd(i,j)=1*(10^-10);
     end
   end
end
%%%%%%%%%%%%%%%%%%%%%%%%%%%%%%%%%%%%%%%%%%%%%%%%%%%%%%%%%%%%%%%%%
%%%%%

% Calculate forces in independent dofs
Qi = V_qi + ((PHI_qi')/(PHI_qd'))*(Qd - V_qd) + (G_qi'-((PHI_qi')/(PHI_qd'))*G_qd')*fn;

% Code added to prevent complex numbers
Test = isnan(Qi);

if Test(1,1) ==1
    Qi(1,1) = 0;
end
if Test(2,1) ==1
    Qi(2,1) = 0;
end
if Test(3,1) ==1
    Qi(3,1) = 0;
end
if Test(4,1) ==1
    Qi(4,1) = 0;
end
if Test(5,1) ==1
    Qi(5,1) = 0;
end

return
```

constraints.m

```
% Written by J. Pinochet (2006)

% This file follows the analytical formulation for the PPP device
% described by Pinochet et al. (2006)

% [PHI,PHI_qi,PHI_qd] = constraints(qi,qd,Lp,shapeU,ParamU,shapeD,ParamD)
%
% DESCRIPTION:  Returns the 'prestressed rod' constraints vector and
%               the constraints Jacobian to independent and
%               dependent dofs.
%
% INPUT:    qi      = Independent dofs values
%           qd      = Dependent dofs values
%           Lp      = Total rod length
%           shapeU  = 'Up' (or top) ending shape function name
%           ParamU  = 'Up' (or top) ending shape parameters
%           shapeD  = 'Down' (bottom) ending shape function name
%           ParamD  = 'Down' (bottom) ending shape parameters
%
% OUTPUT:   PHI     = Constraints vector
%           PHI_qi  = Constraints Jacobian to independent dofs
%           PHI_qd  = Constraints Jacobian to dependent dofs
% ------------------------------------------------------------------

function [PHI,PHI_qi,PHI_qd] = constraints(qi,qd,Lp,shapeU,ParamU,shapeD,ParamD)

% Initialize independent dofs
xsu = qi(1);
thsu = qi(2);
xsd = qi(3);
```

```
ysd = qi(4);
thsd = qi(5);

% Initialize unknown dofs
qs = qd(1);
ysu = qs(1);

% Initialize rod dofs
qr = qd(2:10);
xp = qr(1);
yp = qr(2);
thp = qr(3);
xeu = qr(4);
yeu = qr(5);
theu = qr(6);
xed = qr(7);
yed = qr(8);
thed = qr(9);

% Initialize auxiliary variables
qa = qd(11:14);
lu = qa(1);
psiu = qa(2);
ld = qa(3);
psid = qa(4);

% Radius shape evaluation
rou = feval(shapeU,ParamU,0);
rod = feval(shapeD,ParamD,0);
[ru, rup, rupp, Arcu] = feval(shapeU,ParamU,psiu);
[rd, rdp, rdpp, Arcd] = feval(shapeD,ParamD,psid);

% Rod constraints
PHIr = [xp-Lp/2*sin(thp)-xeu;
       yp+Lp/2*cos(thp)-yeu;
       thp-theu;
       xp+Lp/2*sin(thp)-xed;
       yp-Lp/2*cos(thp)-yed;
       thp-thed];
% Rod constraints Jacobian to independent dofs
PHIr_qi = zeros(6,5);
% Rod constraints Jacobian to slave dof
PHIr_qs = [0 0 0 0 0 0]';
% Rod constraints Jacobian to rod dofs
PHIr_qr = [1 0 -Lp/2*cos(thp) -1 0 0 0 0 0;
          0 1 -Lp/2*sin(thp) 0 -1 0 0 0 0;
          0 0 1 0 0 -1 0 0 0;
          1 0 Lp/2*cos(thp) 0 0 0 -1 0 0;
          0 1 Lp/2*sin(thp) 0 0 0 0 -1 0;
          0 0 1 0 0 0 0 0 -1];
% Rod constraints Jacobian to auxiliary variable
PHIr_qa = zeros(6,4);

% Ending rolling constraints
PHIe = [xeu+rou*sin(thp)-ru*sin(thp-psiu)-lu*cos(thsu)-xsu;
       yeu-rou*cos(thp)+ru*cos(thp-psiu)-lu*sin(thsu)-ysu;
       xed-rod*sin(thp)+rd*sin(thp-psid)+ld*cos(thsd)-xsd;
       yed+rod*cos(thp)-rd*cos(thp-psid)+ld*sin(thsd)-ysd];
% Ending rolling constraints Jacobian to independent dofs
PHIe_qi = [-1 lu*sin(thsu) 0 0 0;
          0 -lu*cos(thsu) 0 0 0;
          0 0 -1 0 -ld*sin(thsd);
          0 0 0 -1 ld*cos(thsd)];
% Ending rolling constraints Jacobian to slave dof
PHIe_qs = [0 -1 0 0]';
% Ending rolling constraints Jacobian to rod dofs
```

```
PHIe_qr = [0 0 rou*cos(thp)-ru*cos(thp-psiu) 1 0 0 0 0 0;
   0 0 rou*sin(thp)-ru*sin(thp-psiu) 0 1 0 0 0 0;
   0 0 -rod*cos(thp)+rd*cos(thp-psid) 0 0 0 1 0 0;
   0 0 -rod*sin(thp)+rd*sin(thp-psid) 0 0 0 0 1 0];
% Ending rolling constraints Jacobian to auxiliary variable
PHIe_qa = [-cos(thsu) -rup*sin(thp-psiu)+ru*cos(thp-psiu) 0 0;
   -sin(thsu) rup*cos(thp-psiu)+ru*sin(thp-psiu) 0 0;
   0 0 cos(thsd) rdp*sin(thp-psid)-rd*cos(thp-psid);
   0 0 sin(thsd) -rdp*cos(thp-psid)-rd*sin(thp-psid)];

% Auxiliary constraints
PHIa = [tan(thsu-theu+psiu)-rup/ru;
       lu-Arcu;
       tan(thsd-thed+psid)-rdp/rd;
       ld-Arcd];
% Auxiliary constraints Jacobian to independent dofs
PHIa_qi = [0 1+tan(thsu-theu+psiu)^2 0 0 0;
         0 0 0 0 0;
         0 0 0 0 1+tan(thsd-thed+psid)^2;
         0 0 0 0 0];
% Auxiliary constraints Jacobian to slave dof
PHIa_qs = [0 0 0 0]';
% Auxiliary constraints Jacobian to rod dofs
PHIa_qr = [0 0 0 0 0 -1-tan(thsu-theu+psiu)^2 0 0 0;
         0 0 0 0 0 0 0 0 0 0;
         0 0 0 0 0 0 0 0 -1-tan(thsd-thed+psid)^2;
         0 0 0 0 0 0 0 0 0 0];
% Auxiliary constraints Jacobian to auxiliary variable
PHIa_qa = [0 1+tan(thsu-theu+psiu)^2-rupp/ru+(rup/ru)^2 0 0;
         1 -sqrt(ru^2+rup^2) 0 0;
         0 0 0 1+tan(thsd-thed+psid)^2-rdpp/rd+(rdp/rd)^2;
         0 0 1 -sqrt(rd^2+rdp^2)];

% Constraints vector
PHI = [PHIr;PHIe;PHIa];

% Constraints Jacobian to dependent dofs
PHI_qi = [PHIr_qi; PHIe_qi; PHIa_qi];

% Constraints Jacobian to dependent dofs
PHI_qd = [PHIr_qs PHIr_qr PHIr_qa;
        PHIe_qs PHIe_qr PHIe_qa;
        PHIa_qs PHIa_qr PHIa_qa];
return
```

calcPI_five_cases.m

```
%Written by R. Husfeld June 19, 2007
%Modified Sept. 25, 2007

%This file calculates performance indices for each isolated case of
%the 3DOF base-isolated model and
%the 2DOF fixed-base model of a two family Chilean low-cost house

%The order of saved variables in Simulink is:

%TRADITIONAL CONSTRUCTION CASE
%mdof_general_uc.mat: variable name uc
%1st row is time
%2-5 rows are relative disp, veloc, and accel, and abs accel of 1st
%floor
%6-9 rows are relative disp, veloc, and accel, and abs accel of 2nd
%floor
%10 base shear
```

```
%CONTROLLED CASE
%mdof_general.mat: variable name w5, fps2, fps3, fps4
%1st row is time
%2-5 rows are relative disp, veloc, and accel, and abs accel of base %level
%6-9 rows are relative disp, veloc, and accel, and abs accel of 1st %floor
%10-13 rows are relative disp, veloc, and accel, and abs accel at 2nd %floor
%14-16 are e'quake force at base, 1st, & 2nd floor levels
%17 ground accel
%18 force in device
%19 base shear
%20 structure shear at 1st floor

%Do not clear the workspace after running
%"threedof_five_different_cases_mat_opt.m"
%This file uses variables created upon execution of that .m file

%Global variables are number of each device
global a b c d e

%Input parameters required
k1 = 433009236; %N/m
k2 = 323999918; %N/m
k1uc = 433009236; %N/m
k2uc = 323999918; %N/m

mb = 27018; %kg %slab-on-grade %INCLUDING 25% of live load
m1 = 40711; %kg %first floor slab level
m2 = 16148; %kg %roof diaphragm level

mass_total = mb + m1 + m2; %kg - total mass of structure

%UNCONTROLLED (UC) (or fixed-base) - FIRST FLOOR
%Collect 1st floor drift & abs. accel & peak base shear
uc_peak_accel_1 = max(abs(uc(5,:))); %abs accel of 1st floor

uc_peak_drift_1 = max(abs(uc(2,:)));
%disp of 1st floor relative to ground
uc_peak_base_shear = max(abs(uc(10,:))); % in Newtons

%Interstory drift between 1st floor and ground
uc_interstory_drift_1 = abs(uc(2,:));
%disp of 1st floor relative to ground
uc_peak_interstory_drift_1 = max(uc_interstory_drift_1(1,:));

%Interstory drift between 2nd floor and 1st floor
uc_interstory_drift_2 = abs(uc(6,:) - uc(2,:));
%disp of 2nd floor relative to 1st
uc_peak_interstory_drift_2 = max(uc_interstory_drift_2(1,:));

uc_peak_story_shear_1 = max(k1uc*uc(2,:));

%RMS absolute accel
uc_n_accel_1 = length(uc(5,:));
uc_rms_accel_1 = norm(uc(5,:))/sqrt(uc_n_accel_1); %RMS accel


%UNCONTROLLED (UC) - SECOND FLOOR (ROOF LEVEL)
%Collect 2nd floor drift & abs. accel
uc_peak_drift_2 = max(abs(uc(6,:))); %disp rel to ground
uc_peak_accel_2 = max(abs(uc(9,:))); %abs accel

%Interstory drift between 2nd and 1st floors
uc_interstory_drift_2 = abs(uc(6,:) - uc(2,:));
uc_peak_interstory_drift_2 = max(uc_interstory_drift_2(1,:));

%RMS interstory drift and RMS absolute accel
```

```
uc_n_is_drift_2 = length(uc_interstory_drift_2);
uc_rms_is_drift_2 = norm(uc_interstory_drift_2)/sqrt(uc_n_is_drift_2); %Calc RMS drift by norm(x)/sqrt(n)
uc_n_accel_2 = length(uc(9,:));
uc_rms_accel_2 = norm(uc(9,:))/sqrt(uc_n_accel_2); %RMS accel
```

Note: the following code is typical for each of the base isolation systems

```
%%%%%%%%%%%%%%%%%%%%%%%%%%%%%%%%%%%%%%%%%%%%%%%%%%%%%%%%%%%%%%%%
%%%
%Related to base-isolated case #1
%CONTROLLED (CONT) - BASE LEVEL
%Collect base level drift & abs. accel
cont_peak_drift_0 = max(abs(w5(2,:)));
%displacement of base relative to ground
cont_peak_drift_1 = max(abs(w5(6,:))); %disp of 1st floor rel to ground
cont_peak_accel_0 = max(abs(w5(5,:))); %abs accel of base

cont_peak_device_force = max(abs(w5(18,:)));
cont_peak_base_shear_0 = max(abs(w5(19,:)));

%RMS abs accel
cont_n_accel_0 = length(w5(5,:));
cont_rms_accel_0 = norm(w5(5,:))/sqrt(cont_n_accel_0); %RMS accel

%RMS base displacement
cont_n_base_0 = length(w5(2,:));
cont_rms_base_disp = norm(w5(2,:))/sqrt(cont_n_base_0);

%Peak base shear at isolation level
J1FIS1 = abs(cont_peak_base_shear_0)/uc_peak_base_shear;

%Peak base displacement at isolation level
J3FIS1 = cont_peak_drift_0;

%Peak force summed from all devices divided by peak base shear in
%controlled structure
%MULTIPLY BY a, the number of devices
J6FIS1 = abs(a*(cont_peak_device_force)/cont_peak_base_shear_0);

J7FIS1 = cont_rms_base_disp;

%CONTROLLED (CONT) - FIRST FLOOR
%Collect 1st floor drift & abs. accel & peak base shear
cont_peak_drift_1 = max(abs(w5(6,:))); %disp of 1st floor rel to ground
cont_peak_accel_1 = max(abs(w5(9,:))); %abs accel

%Interstory drift between 1st floor and base level
cont_interstory_drift_1 = abs(w5(6,:) - w5(2,:));
cont_peak_interstory_drift_1 = max(cont_interstory_drift_1(1,:));

%Interstory drift between 2nd floor and 1st floor
cont_interstory_drift_2 = abs(w5(10,:) - w5(6,:));
cont_peak_interstory_drift_2 = max(cont_interstory_drift_2(1,:));

cont_peak_story_shear_1 = max(k1*(w5(6,:)-w5(2,:)));

cont_n_accel_1 = length(w5(9,:));
cont_rms_accel_1 = norm(w5(9,:))/sqrt(cont_n_accel_1); %RMS accel

%Peak structure shear at 1st floor level
J2FIS1 = cont_peak_story_shear_1/uc_peak_story_shear_1;

%Peak Inter-story drift between 1st floor and base
J4FIS1_1 = cont_peak_interstory_drift_1/uc_peak_interstory_drift_1;

%Peak absolute floor acceleration between 1st floor and base
```

```
J5FIS1_1 = cont_peak_accel_1/uc_peak_accel_1;

%RMS Absolute Floor Accel
J8FIS1_1 = cont_rms_accel_1/uc_rms_accel_1;


%CONTROLLED (CONT) - SECOND FLOOR (ROOF LEVEL)
%Collect 2nd floor drift & abs. accel
cont_peak_drift_2 = max(abs(w5(10,:)));
%disp of 2nd floor rel to ground
cont_peak_accel_2 = max(abs(w5(13,:))); %abs accel

%Interstory drift between 2nd and 1st floors
cont_interstory_drift_2 = abs(w5(10,:) - w5(6,:));
cont_peak_interstory_drift_2 = max(cont_interstory_drift_2(1,:));

cont_n_accel_2 = length(w5(13,:));
cont_rms_accel_2 = norm(w5(13,:))/sqrt(cont_n_accel_2); %RMS accel

%Peak Inter-story drift between 2nd and 1st floors
J4FIS1_2 = cont_peak_interstory_drift_2/uc_peak_interstory_drift_2;

%Peak inter-story drift for any floor
J4FIS1 = max(J4FIS1_1,J4FIS1_2);

%Peak absolute floor acceleration between 2nd and 1st floors
J5FIS1_2 = cont_peak_accel_2/uc_peak_accel_2;

%Peak absolute floor acceleration for any floor
J5FIS1 = max(J5FIS1_1,J5FIS1_2);

%RMS Absolute Floor Accel
J8FIS1_2 = cont_rms_accel_2/uc_rms_accel_2;

%Max Absolute Floor Accel
J8FIS1 = max(J8FIS1_1,J8FIS1_2);
```

Note: After calculating PIs for the fixed-base case and each of the isolated cases, use the following code.

```
'Normalized peak base shear at isolation level for each FIS'
J1 = [J1FIS1, J1FIS2, J1FIS3, J1FIS4, J1FIS5]

'Normalized peak structure shear at first story level for each FIS'
J2 = [J2FIS1, J2FIS2, J2FIS3, J2FIS4, J2FIS5]

'(Not normalized) Peak base displacement at isolation level for each FIS'
J3 = [J3FIS1, J3FIS2, J3FIS3, J3FIS4, J3FIS5]

'Normalized peak inter-story drift for each FIS'
J4 = [J4FIS1, J4FIS2, J4FIS3, J4FIS4, J4FIS5]

'Normalized peak absolute floor acceleration for each FIS'
J5 = [J5FIS1, J5FIS2, J5FIS3, J5FIS4, J5FIS5]

'Peak force generated by all devices normalized by peak base shear for each FIS'
J6 = [J6FIS1, J6FIS2, J6FIS3, J6FIS4, J6FIS5]

'(Not normalized) RMS base displacement for each FIS'
J7 = [J7FIS1, J7FIS2, J7FIS3, J7FIS4, J7FIS5]

'Normalized peak RMS absolute floor acceleration for each FIS'
J8 = [J8FIS1, J8FIS2, J8FIS3, J8FIS4, J8FIS5]
```

VITA

Rachel Lynn Husfeld received her Bachelor of Science in civil engineering from Valparaiso University in May 2006. She entered the Zachry Department of Civil Engineering at Texas A&M University in August 2006 and completed her Master of Science degree in May 2008. During her study Ms. Husfeld worked with Dr. Paul N. Roschke to optimize several devices for use in base isolation of masonry housing structures. Her graduate study was funded by the National Science Foundation through a Graduate Research Fellowship. Ms. Husfeld may be reached at 1301 McKinney, Suite 1100, Houston, TX, 77010, or at Rachel.Husfeld@gmail.com.